Energy

FOSSIL

DOE/PC/90012-10
(DE91014240)

HYDRODYNAMICS OF THREE-PHASE SLURRY FISCHER-TROPSCH BUBBLE COLUMN REACTORS

Final Report

By
Dragomir B. Bukur
James G. Daly
Snehal A. Patel

September 1990

Work Performed Under Contract No. AC22-86PC90012

For
U.S. Department of Energy
Pittsburgh Energy Technology Center
Pittsburgh, Pennsylvania

By
Texas A&M University
College Station, Texas

DISCLAIMER

DOE/PC/90012-10

HYDRODYNAMICS OF THREE-PHASE SLURRY FISCHER-TROPSCH BUBBLE COLUMN REACTORS

FINAL REPORT

DRAGOMIR B. BUKUR, JAMES G. DALY AND SNEHAL A. PATEL

TEXAS A&M UNIVERSITY

DEPARTMENT OF CHEMICAL ENGINEERING

COLLEGE STATION, TX 77843

September 1990

Prepared for the Pittsburgh Energy Technology Center,

the United States Department of Energy Under Contract No. DE-AC22-86PC90012

George Cinquegrane, Project Manager (PETC)

John Shen, Program Manager (DOE/FE)

DOE/PC/90012--10

DE91 014240

HYDRODYNAMICS OF THREE-PHASE SLURRY FISCHER-TROPSCH BUBBLE COLUMN REACTORS

FINAL REPORT

DRAGOMIR B. BUKUR, JAMES G. DALY AND SNEHAL A. PATEL

TEXAS A&M UNIVERSITY

DEPARTMENT OF CHEMICAL ENGINEERING

COLLEGE STATION, TX 77843

September 1990

Prepared for the Pittsburgh Energy Technology Center,

the United States Department of Energy Under Contract No. DE-AC22-86PC90012

George Cinquegrane, Project Manager (PETC)

John Shen, Program Manager (DOE/FE)

DISCLAIMER

Printed in the United States of America, Office of Scientific and Technical Information, Oak Ridge , Tennessee

TABLE OF CONTENTS

Page

Page

LIST OF TABLES

Table Page

Table Page

Table Page

LIST OF FIGURES

Figure Page

Figure Page

Figure Page

Figure Page

Figure Page

Figure Page

Figure Page

Figure Page

ABSTRACT

This report describes results of a study on hydrodynamics of three-phase bubble columns for Fischer-Tropsch synthesis under a DOE Contract No. DE-AC22-86PC90012.

Experiments were conducted in two stainless steel bubble columns of 0.05 m and 0.21 m in diameter and 3 m tall, at 265°C and atmospheric pressure using nitrogen gas and two types of liquid medium (hydrotreated reactor wax designated FT-300, and raw reactor wax from fixed bed reactors at SASOL). The effects of solids type (iron oxide and silica), concentration (0-30 wt%), size (0-5 μm and 20-44 μm), and slurry (liquid) velocity (up to 0.02 m/s) on the gas holdup and axial solids concentration profiles, were investigated. Phase volume fractions were determined using conventional (differential pressure measurements together with determination of slurry concentration along the column) and novel (dual energy nuclear density gauge) experimental techniques. Bubble size distribution and the Sauter mean bubble diameter were obtained using the dynamic gas disengagement (DGD) method. Flow regime transitions in both columns were determined using statistical analysis of both pressure and density fluctuations.

Correlations for prediction of gas holdups and axial solids dispersion coefficient have been developed from experimental data obtained in this study. Data needed for calculation of the gas-liquid interfacial area (average gas holdup and Sauter mean bubble diameter) have been presented and can be used to estimate the mass transfer rate in slurry bubble column reactors. The results obtained in this study should be useful to those engaged in design and economic evaluations of slurry bubble column reactors for Fischer-Tropsch synthesis reaction.

Objective and Scope of Work

The overall objective of this contract is to determine the effects of bubble column diameter, solids loading and particle size, and operating conditions (temperature, gas and liquid flow rates) on hydrodynamics of slurry bubble columns for Fischer-Tropsch synthesis, using a molten wax as the liquid medium. To accomplish these objectives, the following specific tasks will be undertaken.

Task 1 - Project Work Plan

The objective of this task is to establish a detailed project work plan covering the entire period of performance of the contract, including a detailed program schedule, analytical procedures, and estimated costs and manhours expended by month for each task.

Task 2 - Design and Construction of the Experimental Apparatus

The existing stainless steel columns (0.05 m and 0.21 m in diameter, 3 m tall) that were constructed under our previous DOE contract (DE-AC22-84PC70027), will be modified and additions made in order to study the effect of continuous upward liquid flow. After the procurement of equipment and instrumentation, and construction of the unit is completed, a shakedown of test facilities will be made to verify achievement of planned operating conditions.

Task 3 - Measurement of Hydrodynamic Parameters by Conventional Techniques

In this task, the effects of operating conditions (liquid and gas superficial velocities), gas distributor, column diameter, and solids concentrations and particle size on hydrodynamic parameters in the stainless steel columns will be determined. All experiments will be conducted using nitrogen at atmospheric pressure. The hydrodynamic parameters that will be determined as a function of the independent variables mentioned above are: average gas hold-up, axial solids distribution, axial gas hold-

up, flow regime characterization, and qualitative information on bubble size distribution.

Task 4 - Application of a Gamma Radiation Density Gauge for Determining Hydrodynamic Parameters

The objective of this task is to determine hydrodynamic parameters for the three-phase system using a nuclear density gauge apparatus. A movable assembly mechanism and positioning racks for the two nuclear density gauges and detectors will be designed and constructed. Following the interfacing of the apparatus with an on-line microprocessor, the gauges will be calibrated using pure components (liquid wax and solid particles), and with known proportions of liquid and solid. After calibration, the following parameters will be obtained from experiments in the large stainless steel column: axial gas hold-up, axial concentration of solids, and qualitative information on flow regimes.

EXECUTIVE SUMMARY

Slurry phase Fischer-Tropsch (FT) processing is considered a potentially economic method to convert coal derived synthesis gas into liquid fuels. Largely due to its relatively simple reactor design, improved thermal efficiency, and ability to process CO-rich synthesis gas, the slurry process has several potential advantages over conventional vapor phase processes.

The scale-up of slurry bubble column reactors is subject to uncertainty because important hydrodynamic parameters change with the scale (i..e. with the reactor diameter, and, to smaller extent, with the height). These parameters have significant effect on the synthesis gas conversion and product selectivity. Commercial size reactors are expected to operate in a churn-turbulent flow regime, and it is essential to use a bubble column with sufficiently large diameter which will allow for operation in this flow regime. A glass bubble column with 0.23 m in diameter, 3 m tall was constructed at Texas A&M University (TAMU), under DOE Contract No. DE-AC22-84PC70027, for hydrodynamic studies of Fischer-Tropsch synthesis in the absence of solids. It was demonstrated that this column operates in the churn-turbulent flow regime under typical processing conditions for slurry Fischer-Tropsch synthesis reaction. This study has provided useful information on the effects of operating conditions, gas distributor design, column geometry, and oxygenated species on gas hold-up and bubble size distribution.

Slurry FT bubble column reactors operate with solid loadings up to 30 wt%, and part of slurry is removed from the reactor and returned to it as a concentrated slurry from a wax/catalyst separation unit. These factors (i.e. the presence of solids and small continuous liquid flow) may have significant effect on hydrodynamic parameters, and need to be evaluated. Therefore, TAMU proposed to conduct a systematic study of the effect of solids, and small upward liquid flow on hydrodynamic parameter in 0.05 m and 0.21 m diameter columns, under conditions which simulate the process conditions in industrial slurry bubble column reactors for Fischer-Tropsch synthesis. The following hydrodynamic parameters were determined: the average and axial gas holdups, axial solids concentration profiles, the axial solids

dispersion coefficient, Sauter mean bubble diameter in the absence of solids, flow regimes and flow regime transitions, by utilizing both conventional and novel experimental techniques.

SUMMARY OF RESULTS

Experiments were conducted in two stainless steel bubble columns (0.05 and 0.21 m in diameter, 3 m in height) in two modes of operation : (a) batch mode - continuous flow of gas, stationary liquid (slurry), and (b) continuous mode - both gas and liquid (slurry) in cocurrent upward flow. A total of 34 runs (28 with FT-300 wax, and 6 with SASOL reactor wax) were made in the small diameter column, whereas 35 runs (6 with FT-300 wax, and 29 with SASOL reactor wax) were made in the large diameter column. Two different types of solid particles were employed in these tests: iron oxide (0-5 μm and 20-44 μm) and silica (0-5 μm and 20-44 μm) to simulate typical catalysts and supports employed in Fischer-Tropsch synthesis. All experiments were conducted at 265°C and atmospheric pressure, using nitrogen as the gas. Experimental conditions for different runs are listed in Tables 2.4 and 2.5.

Gas Holdups by Conventional Techniques

Axial (between two measurement ports along the column height) and average (for the entire column) holdups were calculated from differential pressure and solids concentration measurements along the column height, as described in Chapter II. The effects of slurry (liquid) flow rate, solids concentration, type and size, column diameter, distributor type, and liquid medium on the average gas holdup are summarized below.

Effects of slurry (liquid) velocity. The gas holdup decreased with increasing slurry (liquid) velocity for experiments conducted with FT-300 wax (with and without solids) in the both columns. The decrease in holdup was most pronounced at gas velocities which favor the formation of foam, since a slight upward liquid (slurry) flow rate is sufficient to dissipate the foam layer. In the absence of foam, the effect of slurry flow rate on gas holdup is negligible.

SASOL reactor wax does not have tendency to foam, and the slurry velocity did not have significant effect on the gas holdup. The trends observed in our study are consistent with results reported in literature with other systems.

Effects of Solids Concentration. The addition of solids increased gas holdup in experiments conducted in the batch mode of operation with both FT-300 wax and SASOL reactor wax. This may be attributed either to reduction in bubble size with addition of small particles or to poor wettability of particles in the region of high gas holdups (upper portion of the column).

In continuous mode of operation addition of solids to FT-300 wax causes a slight decrease in the gas holdup; whereas, addition of solids to SASOL wax causes a slight increase in the gas holdup. This difference in the behavior of the two wax types might be due to differences in the wettability of the particles with respect to each wax type.

Effects of Solids Type and Size. In general, this effect was found to be insignificant, i.e. neither the particle size nor the solids type have marked effect on the gas holdup. However, in the presence of large axial concentration gradients of solids the holdup decreased with increase in particle size (e.g. experiments with large iron oxide particles in the batch mode of operation). In the latter case, the solids accumulate near the distributor increasing the apparent viscosity of the slurry which results in larger bubbles and thus lower gas holdups.

Effect of Column Diameter. From the limited data it appears that column diameter does not have significant effect on gas holdup when the foam is not present in the system.

Effect of Distributor Type. Two type of gas spargers were used for experiments in the 0.21 m ID column; (a) a perforated plate (19 holes of 2 mm in diameter), and (b) bubble cap distributor (7 caps, each with 3 holes of 2 mm in diameter). For both waxes, gas holdups in experiments with the bubble cap distributor were slightly higher than those obtained with the perforated plate distributor.

Effect of Liquid Medium. In the batch mode of operation and at low gas velocities gas holdups

obtained with the FT-300 wax were substantially higher than those obtained with the SASOL reactor wax, primarily due to foaming tendency of the former. However, in the absence of foam the holdups were similar.

Gas Holdup Correlation

Data from both our three-phase (present work) and two-phase studies (DOE Contract No. DE-AC22-84PC70027) were combined and the following general correlation was developed for prediction of gas holdups in Fischer-Tropsch slurry bubble column reactors in the absence of foam.

$$\varepsilon_g = 0.24\ (Fr_g^{0.28}\ Bo^{0.14})$$

where: $F\,r_g = \left(u_g^2 / gd_c\right)$; $Bo = \left(d_c^2\ \rho_{sL} g/\sigma_L\right)$; d_c = column diameter; g = gravity constant; u_g = superficial gas velocity; ρ_{sL} = density of slurry; σ_L = surface tension of the liquid medium.

The mean square error based on 514 data points was 7×10^{-4}, and approximately 94% of experimental data were within $\pm$ 30% of the predicted values by the above correlation.

Axial Solids Concentration Distributions

Axial solids concentration profiles were obtained during experiments conducted in both the 0.05 m and 0.21 m ID columns with 0 - 5 μm and 20 - 44 μm iron oxide and silica particles. Solids concentrations of 10, 20, and 30 wt% were employed throughout these studies. The small (0 - 5 μm) iron oxide and silica particles were completely suspended in both columns in the batch and continuous modes of operation. However, significant concentration gradients were observed with large (20 -44 μm) particles, in the small diameter column during batch experiments. In the large diameter column, the solids concentration gradient was smaller. The solids distribution became uniform with the introduction of upward slurry velocity (0.005 or 0.02 m/s), since the slurry velocity was greater than the terminal settling velocity of the largest particles. Axial solids dispersion coefficients were estimated from axial solids concentration profiles obtained in experiments conducted with large solids in both the batch mode and continuous mode

(the latter in the large diameter column only) of operation. The axial solids dispersion coefficients in the large diameter column were significantly greater than those obtained in the small diameter column. The following correlation for prediction of the particle Peclet number was obtained.

$$Pe_p = 8.4 \left[\frac{Fr_g^6}{Re_g} \right]^{0.107}$$

where: $Re_g = u_g d_c \rho_L / \mu_L$; $Pe_p = u_g d_c / E_s$; μ_L = viscosity of liquid; E_s = axial dispersion coefficient for solids. The above correlation was developed from data obtained with both large iron oxide and silica particles using both SASOL wax and FT-300 wax.

Nuclear Density Gauge Measurements

A dual energy gamma-ray densitometer was designed and constructed for the purpose of obtaining phase (i.e. gas, liquid, and solid) fractions in the large diameter column. The sources and detectors were placed on a movable platform so that measurements could be made at various axial and radial locations. Cesium-137 and Cobalt-60 radioactive sources were used. For the (Cesium-137) - (Cobalt-60) system, slight errors in various parameters (e.g. the distance through the column) cause significant errors in the measured phase fractions. This is due to similarities in the absorption coefficients for the various phases associated with the two sources. However, when a three-phase system was treated as a two-phase (slurry/gas) system, the measured volume fractions of gas and slurry were comparable to those obtained using conventional (i.e. DP cells) technique.

Bubble Size Measurements

Sauter mean bubble diameters were measured using the dynamic gas disengagement (DGD) technique. The DGD technique is based on the fact that the volumetric flow rate at which the liquid level decreases once the gas flow is shut-off is equal to the volumetric flow rate at which the bubbles exit the dispersion. In the past, the DGD measurements were made in clear columns, and the rate at which the

liquid level (or dispersion) dropped was recorded via a VCR/camera system. In this study, we utilized pressure measurements to determine the rate of disengagement. Pressure measurements not only remove some of the subjectivity associated with VCR/camera measurements, but also enable one to determine the effect of axial position on the bubble size distribution. Sauter mean bubble diameters for FT-300 wax were quantitatively similar in both the 0.05 m and 0.21 m ID bubble columns for the range of gas velocities employed in this study. The Sauter mean bubble diameter ranged from approximately 0.9 mm at a gas velocity of 0.02 m/s to a value of 1.4 mm at a gas velocity of 0.12 m/s. Sauter mean bubble diameters for the experiment conducted with SASOL wax (increasing gas velocities, 0.21 m ID column) were similar to those obtained with FT-300 wax. However, for the experiment conducted using a decreasing order of gas velocities, the Sauter mean bubble diameters were slightly higher (e.g., d_s=1.7 mm at a gas velocity of 0.12 m/s). For the experiment conducted with SASOL wax in the 0.05 m ID column, the Sauter mean bubble diameters ranged from 1.4 mm (u_g=0.02 m/s) to 2.2 mm (u_g=0.09 m/s).

Flow Regime Transitions

Statistical analysis of wall pressure and nuclear density gauge fluctuations was used to determine flow regime transitions in both columns. For experiments in the small diameter column, the transition from the bubbly to the slug flow regime occurred between gas velocities of 0.04 and 0.06 m/s, regardless of solids concentration or slurry velocity (up to 0.02 m/s). Likewise, in the large diameter column, the transition from the homogeneous bubbling regime to the churn-turbulent regime occurred between gas velocities of 0.04 and 0.06 m/s. In the small diameter column, slugs start forming at a height of 0.6 m above the distributor. The flow regime transitions obtained in this study are in agreement with those predicted using correlations presented by Taitel et al. (1981) and the flow regime map presented by Deckwer et al. (1980).

RECOMMENDATIONS FOR FUTURE WORK

On the basis of results obtained in this study the following recommendations are made:

- Continue work on development of nuclear densitometry for measurement of volume fractions and bubble rise velocities in three-phase systems.
- Continue work on refinements (theoretical and experimental) of the dynamic gas disengagement (DGD) method for determination of bubble size distribution. In particular, experiments should be conducted in which the bubble size distribution is measured by various techniques (e.g., photography, probes, DGD), and applicability of the DGD method should be extended to three-phase systems.

Future work in the area of hydrodynamic studies of Fischer-Tropsch slurry bubble column reactors should be directed towards measurement of additional parameters needed for design and scale-up slurry bubble column reactors, such as:

- Volumetric mass transfer coefficient ($k_L a$);
- Axial dispersion coefficients for the gas and the liquid phase by tracer studies;
- Heat transfer coefficient between the slurry and the immersed heat exchanger surfaces.

These measurements should be conducted under conditions similar to those that are planned for use in slurry bubble column reactors for Fischer-Tropsch synthesis (i.e., at reaction temperatures and pressures, and with wax as the liquid medium). Experiments should be conducted in a bubble column with sufficiently large column diameter to ensure operation in the churn-turbulent flow regime.

I. INTRODUCTION

Fischer–Tropsch (F–T) synthesis represents an important route for indirect coal liquefaction. During World War II, Germany utilized F–T synthesis to produce motor fuels. Currently, commercial size units are in operation at SASOL in South Africa. Fixed bed (Germany and SASOL) and entrained bed (SASOL) type of reactors have been used for conversion of synthesis gas into hydrocarbon products.

Interest in F–T synthesis has been renewed following the oil embargo in 1973. In particular, slurry phase F–T synthesis has received a great deal of attention. Slurry phase bubble column reactors offer several advantages over conventional reactors. These include better mixing, heat transfer, and temperature control. Also, fine catalyst particles, which minimize intraparticle diffusion effects, may be used in a slurry bubble column reactor. One of the major disadvantages of bubble column reactors is the uncertainty associated with scale–up from a laboratory size reactor to a commercial size reactor.

Recent studies by Gray et al. (1980) and Thompson et al. (1981) have shown that F–T synthesis in slurry phase bubble column reactors has significant advantages over other types of reactors that are currently employed. A number of slurry phase F–T pilot plant reactors have been constructed and operated by several U.S.A. and German companies (e.g., Air Products and Chemicals Inc., Mobil, Schering, and Rurhchemie). Also, a number of studies have been conducted by several academic institutions (e.g., MIT; University of California, Berkley; University of Oldenberg; and Texas A&M University). The majority of these studies, were conducted in relatively small diameter columns (less than 0.05 m ID) and superficial gas velocities less than 0.05 m/s. Under these conditions, either the homogeneous bubbly regime or slug flow regime will exist (Deckwer et al., 1980; Shah et al., 1982). However, commercial size reactors are expected to operate in the churn–turbulent flow regime, and extrapolation of results obtained in smaller

diameter columns may not be warranted. The specific gas–liquid interfacial area, as well as gas and liquid phase mixing differ in different flow regimes. Since construction and operating costs are expected to be high for large diameter bubble column reactors, hydrodynamic data obtained in large diameter columns operating in the churn–turbulent flow regime are needed to properly scale–up slurry phase F–T bubble column reactors.

The common procedure in the design and scale–up of multiphase reactors is to obtain hydrodynamic parameters in a non–reacting system, and kinetic parameters from a reactor system designed to eliminate physical transport resistances. Experiments in non–reacting systems are less expensive and provide information on scale–up effects. Results obtained in these two types of experiments are used as inputs into a mathematical model for the multiphase reactor. Computer simulated results then provide basis for economic evaluations, process optimization, and the reactor design and scale–up. This approach has been successfully used in the design of large scale fluidized bed reactors (e.g., Shell Chlorine process, de Vries et al., 1972; and Mobil's methanol to gasoline (MTG) process, Krambeck et al., 1985).

Many of the techniques commonly used to measure hydrodynamic parameters in laboratory scale bubble column reactors may not be used to monitor the hydrodynamics of large scale reactors. For example, gas holdups in laboratory reactors are usually measured by visual observations which involve terminating the gas flow to the column, or through differential pressure measurements. In an industrial application, the gas flow to the system cannot be shut–off during operation of the reactor. For applications which involve the use of small catalyst particles, pressure transducers are likely to plug, particularly in high pressure applications, giving rise to errors in volume fraction measurements. One technique which has found some success in industrial applications for

monitoring gas holdups is the nuclear density gauge technique. This technique is a non–intrusive technique and may be used with systems that operate at high temperatures and pressures.

Overview of Fischer-Tropsch Studies in Bubble Columns

Hydrodynamic studies of direct relevance to Fischer–Tropsch synthesis in slurry bubble column reactors are summarized in Table 1.1. These studies have provided useful information on the effects of superficial gas velocity, distributor design, liquid static height, solid concentration, pressure, gas and wax type, temperature, and column diameter on average gas holdup and to a limited extent on bubble size distribution. However, with the exception of the study conducted by Bukur et al. (1987a), these studies were limited to bubble columns with diameters less than 0.12 m, where the churn–turbulent flow regime could not be achieved. A systematic study of the hydrodynamics of two–phase F–T slurry bubble columns operating in the batch mode (i.e. no liquid circulation) was conducted at Texas A&M University (Bukur et al., 1987a,b,c; Bukur and Daly, 1987; Patel et al., 1990) in 0.05 m ID and 0.23 m ID bubble columns using various types of distributors and waxes. In particular, average and axial gas holdups were obtained together with bubble size distributions. The churn–turbulent flow regime was observed in the large diameter bubble column.

In order to model slurry bubble column reactors, the following hydrodynamic parameters are needed: specific gas–liquid interfacial area; axial solids dispersion coefficients; Sauter mean bubble diameter; axial dispersion coefficients for the gas and liquid; overall heat transfer coefficient between the slurry and immersed heat transfer internals; mass transfer coefficients for all species; gas holdups; and physico–chemical properties of the liquid medium. Axial dispersion coefficients have not been measured experimentally in systems with paraffin wax as the liquid medium. A limited amount of experimental data can be found in the literature on some of the other parameters mentioned above.

Table 1.1. Summary of Bubble Column Hydrodynamic Studies

Investigator	Column ID (m)	u_g (m/s)	ω_s (%)	T (°C)	P (MPa)	Liquid[a]	Quantity Measured
Calderbank et al. (1963)	0.051	0 - 0.055	0	265	0.1	KW	ϵ_g, a_g
Farley and Ray (1964)	0.25	0.03-0.073	13	265	0.15-1.1	KW	ϵ_g
Zaidi et al. (1979)	0.04-0.10	0-0.038	2-14	250-290	1.0	MP	ϵ_g, d_s
Deckwer et al. (1980)	0.04-0.10	0-0.04	0-16	143-270	0.4-1.1	MP	ϵ_g, d_s
Quicker and Deckwer (1981)	0.0.95	0.04	0	130-170	0.1	FT-300	ϵ_g, d_s
Kuo (1985)	0.032,0.053	0-0.05	0	200-230	0.1	FT-200,PW	ϵ_g
"	0.051	0-0.12	"	138-260	0.1-0.2	FT-200,PW	ϵ_g
"	0.102	0-0.065	"	260	0.1-0.2	FT-200,PW	ϵ_g
"	0.026	0-0.035	15	177	0.1-1.15	PW	ϵ_g
Sanders et al. (1986)	0.05	0-0.06	0-30	240	1.0	FT-300,PW	ϵ_g
O'Dowd et al. (1987)	0.022	0-0.02	0	250,280	1.5-2.2	PW,MP	ϵ_g, d_s
Bukur et al. (1987a,b,c)	0.05, 0.23	0-0.15	0	160-280	0.1	FT300,FT200 SASOL,PW	ϵ_g, a_g, d_s

[a] KW-Krupp wax; MP-Molten paraffin wax; PW-Product wax

Mass Transfer Coefficient

Zaidi et al. (1979) measured values of the the volumetric mass transfer coefficient, $k_\ell a_g$, for carbon monoxide in a small bubble column reactor. The mass transfer coefficient, k_ℓ, for carbon monoxide was calculated using the experimentally determined value of the specific gas–liquid interfacial area, a_g. The gas–liquid interfacial area was determined from measurements of the gas holdup and Sauter mean bubble diameter in a non–reacting system. The experimental value for the mass transfer coefficient of carbon monoxide agreed fairly well with the value predicted using the empirical correlations proposed by Hughmark (1967) and Calderbank and Moo–Young (1961).

More recent measurements of volumetric mass transfer coefficients were made using stirred tank reactors (Albal et al., 1984; Ledakowicz et al., 1984; Deimling et al., 1984). Only Deimling et al. determined mass transfer coefficients separately for hydrogen and carbon monoxide. These values agreed with those predicted using the correlation presented by Calderbank and Moo–Young. Thus, it appears that this correlation may be used to estimate mass transfer coefficients in F–T slurry bubble column reactors. Calderbank and Moo–Young's correlation requires an estimate for the Sauter mean bubble diameter, as well as, the physico–chemical properties of the liquid medium (i.e. density, viscosity, and diffusivity).

The physico–chemical properties of F–T derived waxes are available. Solubilities of hydrogen, carbon monoxide, water and carbon dioxide were measured by Peter and Weinert (1955), and subsequently by other investigators (e.g. Calderbank et al., 1963 – hydrogen only; Albal et al., 1984 – hydrogen and carbon monoxide; Ledakowicz et al., 1984 – carbon monoxide; Deimling et al., 1984 – hydrogen and carbon monoxide). Good agreement exists between the data obtained in different studies. Values of the liquid density and viscosity were reported by Calderbank et al., Deckwer et al. (1980), researchers at Mobil (e.g. Gupte et al., 1984), and Bukur et al. (1987a). The values

of density are in good agreement, while there is some variation in reported values of the liquid viscosity. The latter is caused by the fact that different waxes were used in the different studies. Apparently, the density does not vary appreciably with wax type. Liquid phase diffusivities of hydrogen, carbon monoxide, water and carbon dioxide were determined by Peter and Weinert (1955). Rodden (1988) and Rodden et al. (1988) measured the diffusion coefficients for several dilute solutes in Fischer–Tropsch wax.

Heat Transfer Coefficient

In F–T slurry bubble column reactors, internal heat transfer rods are used to maintain a constant temperature inside the reactor. The heat transfer coefficient between internal heat transfer rods and the slurry was determined by Deckwer et al. (1980). Deckwer et al. conducted experiments in a 0.10 m ID bubble column using paraffin wax as the liquid medium and up to 16 wt% alumina particles (less than 5 μm) as the solid phase.

Additional experimental studies in a larger diameter column with heat transfer internals are needed to minimize the risks in bubble column reactor scale–up. The effect of heat transfer internals on average gas holdup, bubble size distribution, and solids mixing needs to be determined for bubble columns which operate in the churn–turbulent flow regime.

Gas Holdup and Bubble Size Distribution

Average gas holdup in paraffin wax systems have been studied by several investigators. Calderbank et al. (1963) measured gas holdup and specific gas–liquid interfacial area in a 0.05 m ID column using a ball and cone distributor with Krupp wax as the liquid medium. The experiments were conducted at a temperature of 265 °C for gas velocities up to 0.055 m/s. Gas holdups from this study varied linearly with gas velocity, with gas holdups reaching approximately 0.2 at a gas velocity of 0.055 m/s. The specific gas–liquid interfacial area increased significantly with increasing gas velocity for

gas velocities less than 0.03 m/s. For gas velocities greater than 0.03 m/s, the specific gas–liquid interfacial area remained fairly constant ($\approx$ 400 m^2/m^3).

Deckwer et al. (1980) examined the effects of column diameter (0.041 m and 0.10 m), superficial gas velocity (up to 0.04 m/s), temperature (143 – 285 °C), pressure (400–1100 kPa) and solids concentration (up to 16 wt%) on gas holdup using a hard paraffin wax as the liquid medium. Both columns were equipped with a 75 μm sintered metal plate distributor. In their experiments, gas holdup was independent of temperature for temperatures greater than 240 °C, column diameter and pressure, and it decreased slightly with the addition of solids. The gas holdups obtained in this study were higher than those predicted using existing literature correlations, as well as those obtained in the Calderbank et al. study. Deckwer et al. also determined the Sauter mean bubble diameter using photography in a 0.05 m ID glass column. The Sauter mean bubble diameter was found to be independent of gas velocity and was approximately 0.7 mm. The Sauter mean bubble diameter and gas holdup were used to estimate the specific gas–liquid interfacial area. The interfacial area was approximately three times greater than that obtained in the study by Calderbank et al.

Quicker and Deckwer (1981) studied the effect of distributor design on gas holdup and Sauter mean bubble diameter in a 0.095 m ID column at temperatures of 130 °C and 170 °C. In their study, there was no effect of distributor type on bubble size; however, higher holdups were obtained with a single nozzle distributor (0.9 mm in diameter) than with a perforated plate distributor (19 holes x 1.1 mm in diameter). The holdups from this study with the single nozzle distributor were also higher than the holdups obtained in the study by Deckwer et al. (1980) with the 75 μm distributor.

Researchers at Mobil (Smith et al., 1984; Kuo, 1985) have conducted a comprehensive study of this system. They reported results illustrating the effects of distributor type, liquid static height, wax type, operating conditions, gas type, and column diameter

on average gas holdup. Wax type, distributor design, and temperature had a significant effect on gas holdup in their study. For experiments with sintered metal plate distributors, the effect of liquid static height was very pronounced, with higher holdups (up to 0.70) being observed as the liquid static height was decreased. The column diameter (0.032 – 0.12 m) had some effect on gas holdup, while the effects of pressure (0.1 to 1.48 mPa) and gas type (nitrogen, hydrogen, or hydrogen/carbon monoxide mixtures) on gas holdup were negligible. The bubbles produced by the orifice plate distributors were non–uniform in size and larger than the ones produced by the sintered metal plate distributors; however, bubble sizes were only reported for experiments conducted at low superficial gas velocities. The gas holdups from Mobil's studies with the sintered metal plate distributors were higher than those reported by Deckwer et al. (1980); whereas, the holdups obtained from the orifice plate distributors were lower than those reported by Deckwer et al.

Also, a systematic study of this system (two–phase) has been conducted in our laboratory (Bukur et al., 1987a,b; Bukur and Daly, 1987). Experiments were conducted in 0.05 and 0.23 m ID columns approximately 3 m in height using nitrogen as the gas phase and both FT–300 wax and various reactor waxes (primarily in the 0.05 m ID column) as the liquid medium. In experiments in the small diameter column (FT–300 wax) with the 40 μm sintered metal plate distributor and with 2 and 4 mm orifice plate distributors it was found that for a given temperature in the range 230 – 280 °C, there is a range of superficial gas velocities where one can have two values of gas holdup (Bukur et al., 1987a,b, Bukur and Daly 1987). The higher holdups are caused by the existence of a stable foam layer which exists at the top of the dispersion, and this is referred to as the "foamy" regime. In the slug flow regime, gas holdups are significantly lower than those observed in the foamy regime (i.e. approximately one half). In experiments conducted with reactor waxes (SASOL and Mobil) the foamy regime was not observed.

These findings may be used to explain the discrepancies reported in the previously reported values of gas holdup. If the data from different experiments are grouped together according to flow regime type, then they are well represented by two curves; one for the "foamy" flow regime and one for the slug flow regime (Bukur et al., 1987b).

The existence of the foamy flow regime has also been observed in the large diameter column with FT–300 wax at 265 °C (Bukur and Daly, 1987). However, the difference in gas holdups between the "foamy" and churn–turbulent regime is significantly less, and foam breakup usually occurs between gas velocities of 0.03 and 0.05 m/s. Foam was not observed during experiments at 200 °C. This was attributed to the fact that at lower temperatures, the viscosity of the liquid is greater which enhances bubble coalescence.

Bubble sizes were also measured in our laboratory (Bukur et al., 1987a,c; Patel et al., 1990) using various wax types in the 0.05 m ID column and with FT–300 wax in the 0.23 m ID column using both photography and the dynamic gas disengagement technique. Results obtained from the two techniques were comparable. Sauter mean bubble diameters in both the small diameter column and large diameter column with FT–300 wax were approximately 0.8 mm at gas velocities greater than 0.04 m/s. This value is in good agreement with the value of 0.7 mm reported by Deckwer et al. (1980). However, Sauter mean bubble diameters for reactor waxes were significantly higher (Bukur et al., 1987a,c). The Sauter mean bubble diameter for SASOL wax in the 0.05 m ID column approached a value of 2 mm at gas velocities greater than 0.05 m/s and for Mobil reactor wax in the 0.05 m ID column, the Sauter mean bubble diameter approached a value of 4 to 5 mm. Sauter mean bubble diameters estimated from the gas holdups and interfacial areas reported by Calderbank et al. (1963) range from approximately 3 to 5 mm. The important conclusion from our studies is that similar gas holdups do not imply similar Sauter mean bubble diameters.

Flow Regime Characterization

As mentioned previously, the majority of Fischer–Tropsch hydrodynamic studies have been conducted in small diameter columns where only the homogeneous bubbly and slug flow regimes occur. In the studies by Deckwer et al. (1980) and Quicker and Deckwer (1981), the bubble size distribution was found to be fairly uniform for the gas velocities (< 0.04 m/s) employed in their studies. A uniform bubble size distribution is characteristic of the homogeneous bubbly flow regime. In experiments conducted at Texas A&M (Bukur et al., 1987a) and by researchers at Mobil (Kuo, 1985) in 0.05 m ID columns, it was observed that slugs start developing between gas velocities of 0.02 and 0.03 m/s.

Experiments conducted at Texas A&M (Bukur et al., 1987a) in a 0.23 m ID glass column revealed that the homogeneous bubbly regime exists at gas velocities up to 0.02-0.04 m/s, and the churn–turbulent flow regime was observed at higher gas velocities (up to 0.15 m/s). The churn–turbulent flow regime was characterized by a wide bubble size distribution, with bubbles ranging in size from less than 1 mm to greater than 100 mm in diameter.

Effect of Solids

There have been very few studies on the effect of solids on hydrodynamic parameters in bubble columns with wax as the liquid medium. Deckwer et al. (1980) examined the effect of solids (up to 16 wt%) on gas holdup in a 0.10 m ID bubble column. Their work showed than the presence of solids causes a slight decrease in the gas holdup; however, they did not observe any difference in the gas holdup between solids loadings of 5 and 16 wt %. Researchers at Mobil (Kuo, 1985) monitored solids concentrations in a 0.05 m ID by 9 m tall Fischer–Tropsch slurry bubble column reactor. In some of their studies, they observed catalyst settling near the distributor which resulted in a non–uniform temperature distribution. Non–uniform catalyst distribution may have a

detrimental effect on bubble column reactor performance as shown by Bukur and Kumar (1986). Since Fischer–Tropsch slurry bubble column reactors are characterized by low space–time yields due to low catalyst concentrations, it is necessary to determine the upper limit of catalyst concentration. This has not been investigated in a systematic way.

Smith et al. (1984) determined the axial solids dispersion coefficient for ethanol–water mixtures. They found that under foamy conditions (1.8 wt% ethanol) the axial dispersion coefficient was significantly lower than that under nonfoamy conditions (pure water). Since Fischer–Tropsch derived paraffinic waxes have a tendency to foam, it is possible that under foamy conditions, catalyst distribution profiles may be significantly greater than those under nonfoamy conditions.

Effect of Liquid Velocity

During Fischer–Tropsch synthesis, high molecular weight compounds (reactor wax) are formed. As these compounds are formed, they remain in the reactor and as a result, there is a continuous increase in the slurry volume with time on stream. Thus, during actual operations, some of the slurry must be removed without loosing much of the dispersed catalyst. Researchers at Mobil (Kuo, 1985) accomplished this by withdrawing slurry from the reactor and transferring it to a catalyst/wax separation unit where the slurry was separated into two streams. The stream with high catalyst concentration was returned to the reactor and the stream with low catalyst concentration (less than 1 wt% solids) was sent to a filtration system for separation. The effect of slurry removal and return of concentrated slurry to the reactor may be simulated in a non–reacting system by using a continuous slurry flow. No studies of this nature have been conducted in bubble columns with paraffin derived waxes as the liquid medium.

Continuous liquid flow may have a pronounced effect on gas holdup in bubble columns with foaming systems as shown by Shah et al. (1985). They studied the

aqueous ethanol mixture and observed that a small upward liquid flow (0.0077 m/s) was sufficient to significantly reduce the gas holdup (e.g. at u_g =0.15 m/s ϵ_g= 0.80 in the absence of liquid flow and ϵ_g=0.2 with $u_{s\ell}$ = 0.0077 m/s).

Overview of Nuclear Density Gauge Studies

With an increase in the utilization of multiphase reactor systems, there is a need to develop techniques or methods to measure various component properties. In order to properly design and scale–up multiphase reactors such as fluidized beds and bubble columns, hydrodynamic parameters (e.g. gas hold–up, bubble size distribution, solids concentration profiles, and flow regime transitions) are needed. Many fluidized beds and bubble columns operate at high pressures and high temperatures and extrapolation of results obtained at lower pressures and lower temperatures may not be warranted. Therefore, there is a need to develop techniques which may be used to measure hydrodynamic parameters at operating conditions. Another problem that exists with conventional techniques that are currently used to measure some of these properties is the fact that the system is disturbed either by altering the gas and/or liquid flow patterns or removing samples of the slurry. Therefore, it would be advantageous to design a system which is capable of obtaining hydrodynamic parameters without interfering with the reaction environment. An attractive technique for measuring holdups and flow regime transitions is absorption of radiation.

Radiation absorption has been used since the early 1950's. It was first used to measure liquid levels in opaque tanks. Two different types of methods were used: (1) A radioactive source was allowed to float on the liquid surface, and a detector was placed on the outside of the vessel. (2) A beam of radiation located from a source on the outside of the vessel was passed through the vessel to a detector on the opposite side. A change in the amount of radiation absorbed by the detector indicated the top of the liquid level (Gibson et al., 1957). The second method is capable of providing

more information than just the liquid level. The amount of radiation that is absorbed as it passes through a medium is a function of several things including the mass of the medium. Through proper calibrations, one can obtain mean densities or void fractions of the various components which comprise the medium. A device such as the second one is called a nuclear density gauge. Nuclear density gauges have been used in numerous two–phase studies; however, most of these studies, were directed towards studying a particular property.

The majority of previous investigations which utilized gamma–ray absorption were conducted in two–phase fluidized beds and are summarized in Table 1.2. Bartholemew and Casagrande (1957) used Cobalt–60 to measure radial solids concentration profiles in a two–phase fluidized system. Fan et al. (1962) measured axial density profiles in a fluidized bed using gamma–ray absorption. El Halwagi and Gomezplata (1967) also used a nuclear density gauge to measure the solids concentration in a fluidized bed. Baumgarten and Pigford (1960) used Thalium–170 to study density fluctuations in a fluidized bed. Their measurements allowed bubble size, frequency and velocity to be determined. Orcutt and Carpenter (1971) used a dual energy nuclear density gauge (Cesium–137 and Cobalt–60) to measure steady state bubble coalescence. From their measurements, they were able to determine bubble diameters. Gidaspow et al. (1983) utilized a movable nuclear density gauge to obtain density profiles in a fluidized bed. As is evident, the majority of the previous studies were directed toward studying a certain aspect or property of two–phase fluidized beds. However, Weimer et al. (1981) measured expanded bed height , dense phase voidage, dense phase superficial gas velocity, bubble volume fraction, bubble size, and bubble frequency using a single source (Cesium–137) nuclear density gauge. Their study dealt primarily with the performance of the density gauge system and the techniques used to analyze data obtained from the nuclear density gauge.

Table 1.2. Summary of Nuclear Density Gauge Studies

Investigator	Source	System
Bernatowicz et al. (1987)	Cesium–137 Americium–241	3–phase, 1 inch pipe phase fractions and bubble length
Weimer et al. (1985)	Cesium–137	2–phase fluidized bed, 0.292 m cast acrylic and 0.128 m steel hold–up, bubble size, bubble velocity, bubble frequency
Gidaspow et al. (1983)	Cesium–137	2–phase fluidized bed, .40 by 0.0381 m bed porosity distributions above gas jets
Abouelwafa and Kendall (1980)	Barium–133 Cobalt–57 Radium–226	3–phase, no flow, 10 cm thick volume fractions
Lassahn (1975)	Cesium–137	2–phase vertical pipe 16 mm, bubble flow rate
Orcutt and Carpenter (1971)	Cesium–137 Cobalt–60	2–phase fluid bed, bubble coalescence
Basov et al. (1969)	Cesium–137	2–phase, height of gas jets
Farley and Ray (1964)	Cesium–137	3–phase bubble column (0.247 m ID), gas hold–up
Baumgarten and Pigford (1960)	Thulium–170	2–phase fluid bed 3 x 6 inch, density fluct
Bartholemew and Casagrande (1957)	Cobalt–60	2–phase 20.4 in catalyst riser, catalyst density
Gibson et al. (1957)	Cesium–137	3–phase 10 in BC, gas hold–up

Nuclear density gauges have also been used for studies involving bubble column reactors. Gibson et al. (1957) used gamma–ray absorption to determine the liquid level in a batch operated two–phase bubble column operating between 160 and 250 °C and pressures between 3 and 20 atm. Farley and Ray (1964) used a single source nuclear density gauge to measure axial gas hold–up and density profiles in a three–phase bubble column reactor. They treated a three–phase system as a two–phase system by assuming that the liquid and solid phases remained in the same proportions throughout the entire column.A nuclear density gauge has also been used to measure the slurry density in LaPorte's liquid phase methanol reactor (0.572 m in diameter) operated by Air Products (Tsao, 1984).

Abouelwafa and Kendall (1980) proposed the concept of using a dual source nuclear density gauge to measure component fractions in three–phase systems. They reported results for component fractions in a three–phase liquid–liquid–gas pipeline. The difference between measured component fractions and known component fractions was small. Bernatowicz et al. (1987) used a dual source nuclear density gauge to monitor in real–time the ratio of solids to liquid to gas in a process stream at the Solvent Refined Coal facility in Wilsonville, Alabama. They were able to monitor density changes in the process stream, and determine bubble lengths in the stream.

Seo and Gidaspow (1987) have used a dual energy nuclear density gauge to measure volume fractions in a three–phase two–dimensional fluidized bed (2.54 cm wide). They used a Cs–137 source and an X-ray source to measure the volume fraction of solids (two types) and gas.

The results obtained by Abouelwafa and Kendall (1980), Bernatowicz et al. (1987), and Seo and Gidaspow (1987) indicate that dual source nuclear density gauges can provide information regarding component fractions and bubble lengths in three–phase systems. However, a systematic study of the use of dual energy nuclear density gauges in

large diameter three–phase systems, including further applications and means of analysis is needed.

Objectives of This Study

As shown above, very few hydrodynamic studies of direct relevance to the Fischer–Tropsch synthesis have been conducted in large diameter columns which are of practical industrial importance. One of the goals of this research is to conduct a systematic study of the effect of solids type, size and concentration and superficial liquid flow rate on gas holdup and solids concentration profiles in a relatively large diameter column (0.21 m ID) in the churn–turbulent flow regime. Another goal of this project is to assess the possibility of using a dual energy nuclear density gauge to measure volume fractions in a large diameter bubble column. Also, an attempt will be made to obtain information regarding bubble size distribution and flow regime transitions. The results from this study should provide useful information necessary to properly design and scale–up large diameter bubble column reactors for Fischer–Tropsch synthesis, as well as, information on the applicability of dual energy nuclear density gauges for determination of hydrodynamic parameters in large diameter multiphase systems.

II. MEASUREMENT OF GAS HOLDUPS BY CONVENTIONAL TECHNIQUES

Gas holdups and solids concentration profiles were measured using conventional techniques. In particular, gas holdup was calculated from visual observations of the expanded and static liquid height in the glass columns, and from measurements of differential pressures and solids concentrations in the stainless steel columns. The experimental apparatus, operating conditions, data reduction procedures, and results from both two–phase and three–phase experiments are described below. Also, empirical correlations which may be used to predict overall (or average) gas holdup in a Fischer–Tropsch slurry bubble column reactor are presented.

Experimental Apparatus and Operating Procedure

Figure 2.1 is a schematic representation of the slurry bubble column apparatus which was constructed for these studies. The majority of experiments were conducted in 0.05 and 0.21 m ID by 3 m tall stainless steel columns. Experiments in both the batch mode (i.e. without slurry circulation) and continuous mode (i.e. with slurry circulation) of operation were conducted in the stainless steel columns. Five pressure transducers (Valydine Model DP 15) and five slurry sampling valves (1/4" Whitey ball valves) with pneumatic actuators were located along the column (see Figure 2.9 for their locations).

The flow rate of prepurified nitrogen from gas cylinders was measured and controlled by a Brooks Model 5816 mass flow meter for experiments conducted in the 0.05 m ID column. A Sierra Series 840 mass flow meter was used to measure the gas flow rate during experiments conducted in the 0.21 m ID column. For the 0.21 m ID column, the flow rate was controlled manually by adjusting the outlet pressure from the nitrogen cylinder (cryogenic). Prior to each series of experiments, the mass flow

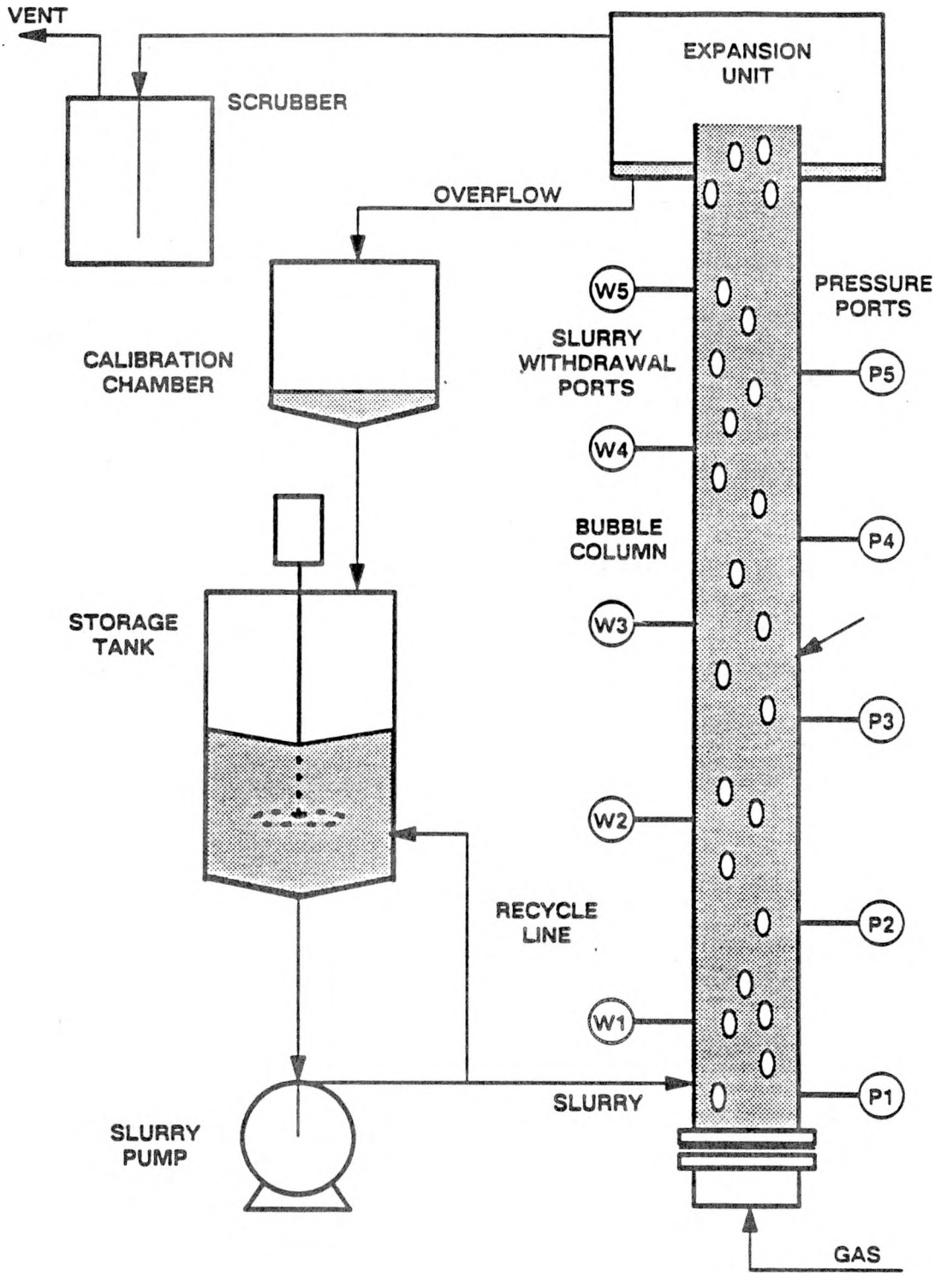

Figure 2.1. Schematic of the slurry bubble column apparatus.

meters were calibrated. The Brooks mass flow meter was calibrated using a wet test meter, and the Sierra mass flow meter was calibrated using a flow prover (i.e. an orifice meter). The metered gas entered the bubble column through the distributor which was located between two flanges at the bottom of the column. For experiments in the 0.21 m ID column, the gas was passed through an electrically heated U–shaped preheater before entering the column at the distributor. The gas inlet temperature was manually controlled using two variable voltage transformers. The temperature of the gas was monitored by three thermocouples (one located in the middle of the preheater – 0.21 m ID column only; one located after the preheater; and one located just below the distributor). The thermocouples were connected to an Omega (Model 199) ten channel temperature indicator.

The wax was charged in the storage tank and the tank was electrically heated to bring the wax to the desired temperature. The wax storage tank for the large diameter column was 0.61 m in diameter and 0.91 m long; and the wax storage tank for the small diameter column was 0.3 m in diameter and 0.46 m long. The slurry inlet systems for the large and small diameter columns are shown in Figures 2.2 and 2.3, respectively. Once the solid wax was melted ($\approx$ 150 °C), the stirrer was switched on to improve the heating process. For experiments conducted with solids, the solids were added to the storage tank once the wax was at the desired temperature (220 °C for batch experiments and 265 °C for continuous experiments). The column was heated to the desired operating temperature (265 °C) before the slurry was introduced. The column temperature was controlled using two temperature controllers, one for the bottom half of the column and one for the top half of the column. For all experiments, batch and continuous, the wax was transported to the column using a slight nitrogen overpressure in the storage tank. For the continuous mode experiments, the pump (Pulsafeeder, Model G12 – 0.05 m ID column; Tuthill Corporation, Model 3A – 0.21 m ID column) was not switched on

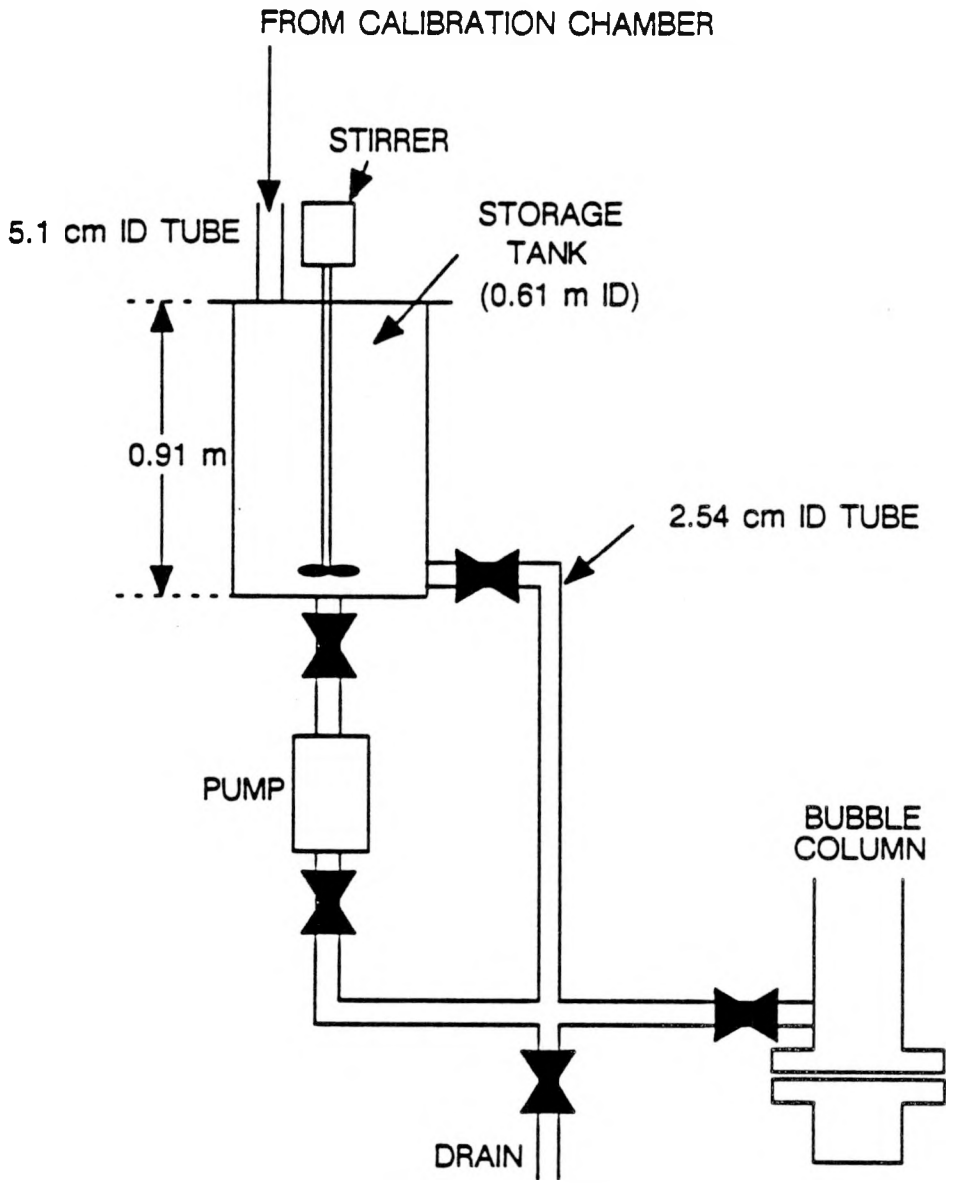

Figure 2.2. Schematic representation of the slurry inlet system for the large diameter stainless steel column.

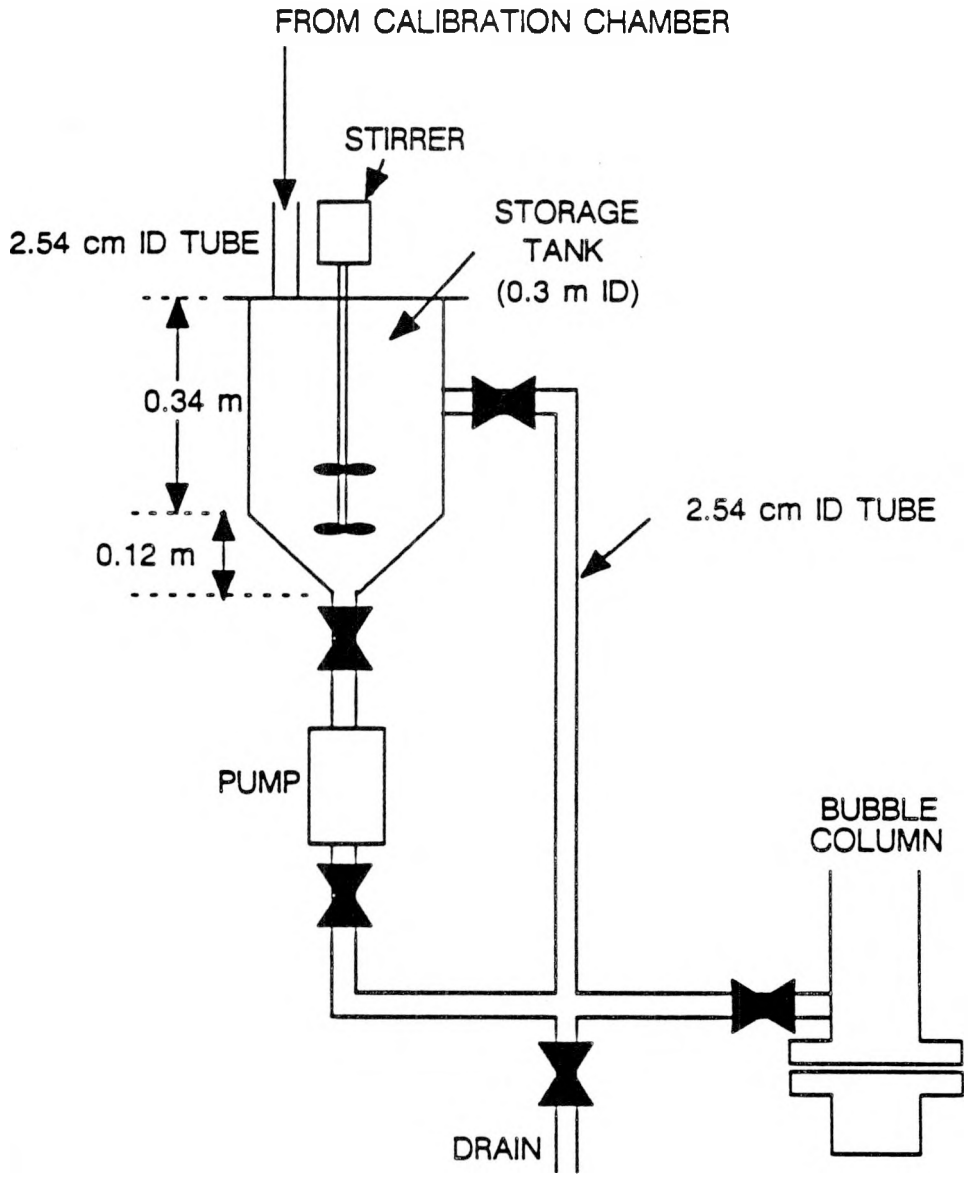

Figure 2.3. Schematic representation of the slurry inlet system for the small diameter stainless steel column.

until the column was at least half filled with wax. This was done to prevent clogging of the pump by solids which might have settled in the storage tank. Throughout the preheating period and during the transportation of wax to the column, nitrogen flowed through the column. Once the wax was in the column, the temperatures of the various units were allowed to stabilize before the actual run was started. For experiments in the batch mode of operation, only the column was maintained at the desired operating temperature. The exit lines and expansion unit were maintained at a temperature of approximately 200 °C. The hot gas leaves the separator and passes through the scrubber which is filled with Varsol (mineral spirits), before it is vented to the atmosphere. The scrubber is used to recover components of the wax that evaporate from the column and is maintained at approximately 70 °C. The lines connected to the pressure transducers and slurry sampling valves were maintained at 200 °C. For experiments in the continuous mode of operation, all lines and vessels carrying the slurry were maintained at the operating temperature. The remaining temperatures were the same as those used for batch experiments. All temperatures were monitored regularly, every half hour during the preheat period and every hour during the experiment.

Once the column reached the desired temperature, the experiment was initiated. Superficial gas velocities in the range 0.02 – 0.12 m/s were employed in all runs. A duration of at least one and a half hours was used for each velocity. Pressure measurements were made three times for every gas velocity (i.e. approximately every half hour), with the first measurement made one half hour after the gas velocity was changed. Slurry samples were withdrawn at the five different locations after the final pressure measurement. The gas flow rate was then changed to the next setting. For experiments conducted in the continuous mode of operation, the superficial slurry velocity was monitored using the calibration chamber. The calibration chamber for the large diameter column was a 0.46 m ID cylindrical tank with an internal volume of approximately

50000 cm^3, and for the small diameter column, the calibration chamber was a 0.23 m ID cylindrical tank with an internal volume of approximately 4000 cm^3. Figures 2.4 and 2.5 are schematic representations of the circulation loops associated with the large and small diameter columns, respectively. The desired slurry flow rate was set by varying the pump speed, and slurry flow rate checks were made prior to each pressure reading (i.e. three times per gas velocity).

For three–phase experiments, slurry samples were withdrawn from the storage tank at the beginning and end of each experiment; as well as, at the end of each gas velocity for experiments conducted in the continuous mode of operation. In order to determine the volume of slurry in the storage tank, a dipstick, similar to that used to determine the oil level in an automobile, was designed (see Figure 2.6). The dipstick assembly consisted of a casing (2.54 cm diameter tube), which was welded to the lid of the storage tank, and the dipstick (0.635 cm diameter shaft). The casing extended half way into the storage tank and had vent holes at the top to allow any gas which might be trapped in the casing to disengage.

Following the completion of a run, the slurry was withdrawn into the storage tank using a slight vacuum (the pump was switched off for runs conducted in the continuous mode of operation). After each run, solids and wax inventories were made to check for any losse losses, particularly losses in solids due to settling in the various lines and process vessels. Solids and wax inventories are discussed in Chapter IV.

Following the completion of a series of experiments, the bubble column apparatus was cleaned . Any slurry which may have remained in the system was collected and weighed, so that an overall mass balance (solids + wax) could be obtained (see Chapter IV).

Two–phase experiments were also conducted in two columns (0.05 m ID and 0.23 m ID by 3 m tall) made of borosilicate glass. A detailed description of these columns has

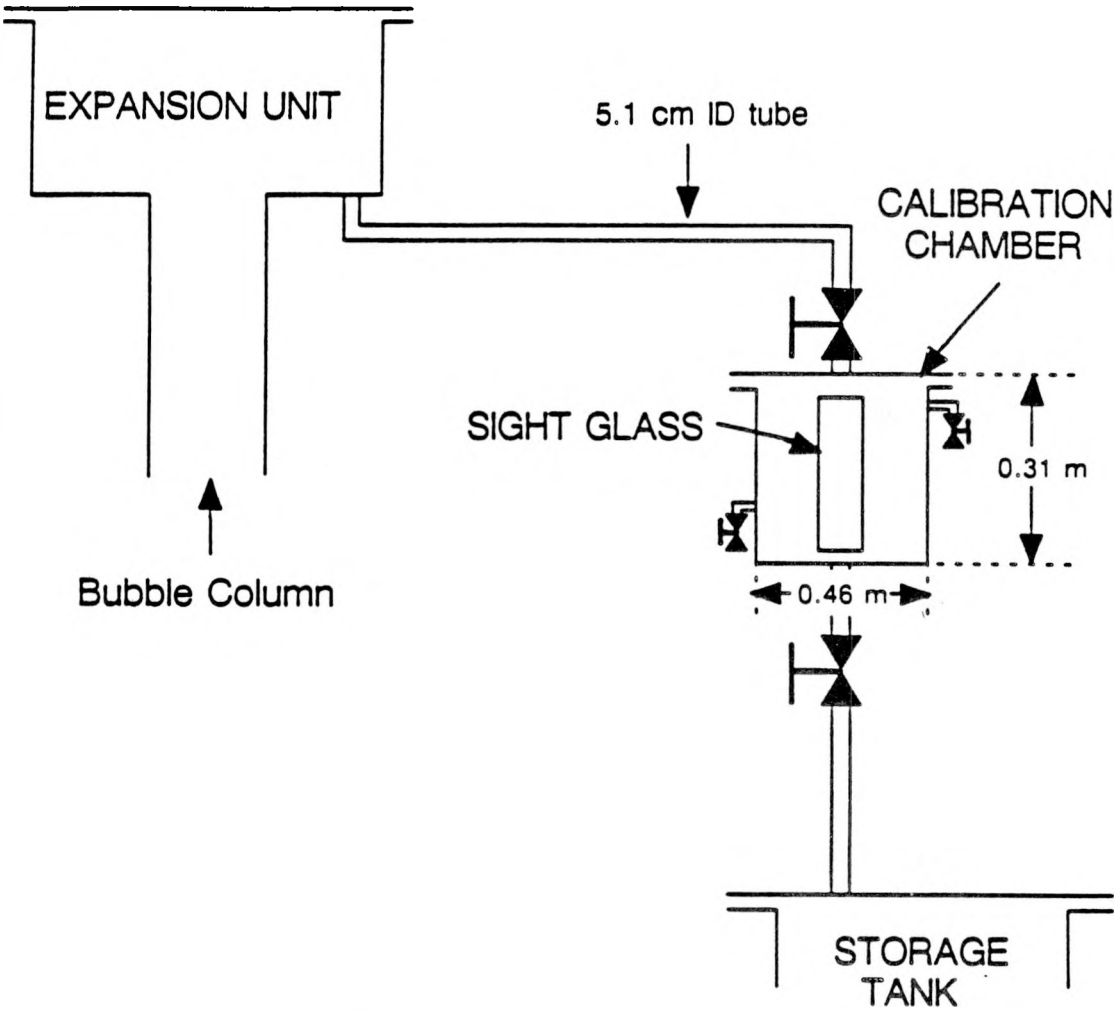

Figure 2.4. Schematic representation of the circulation loop for the large diameter stainless steel column.

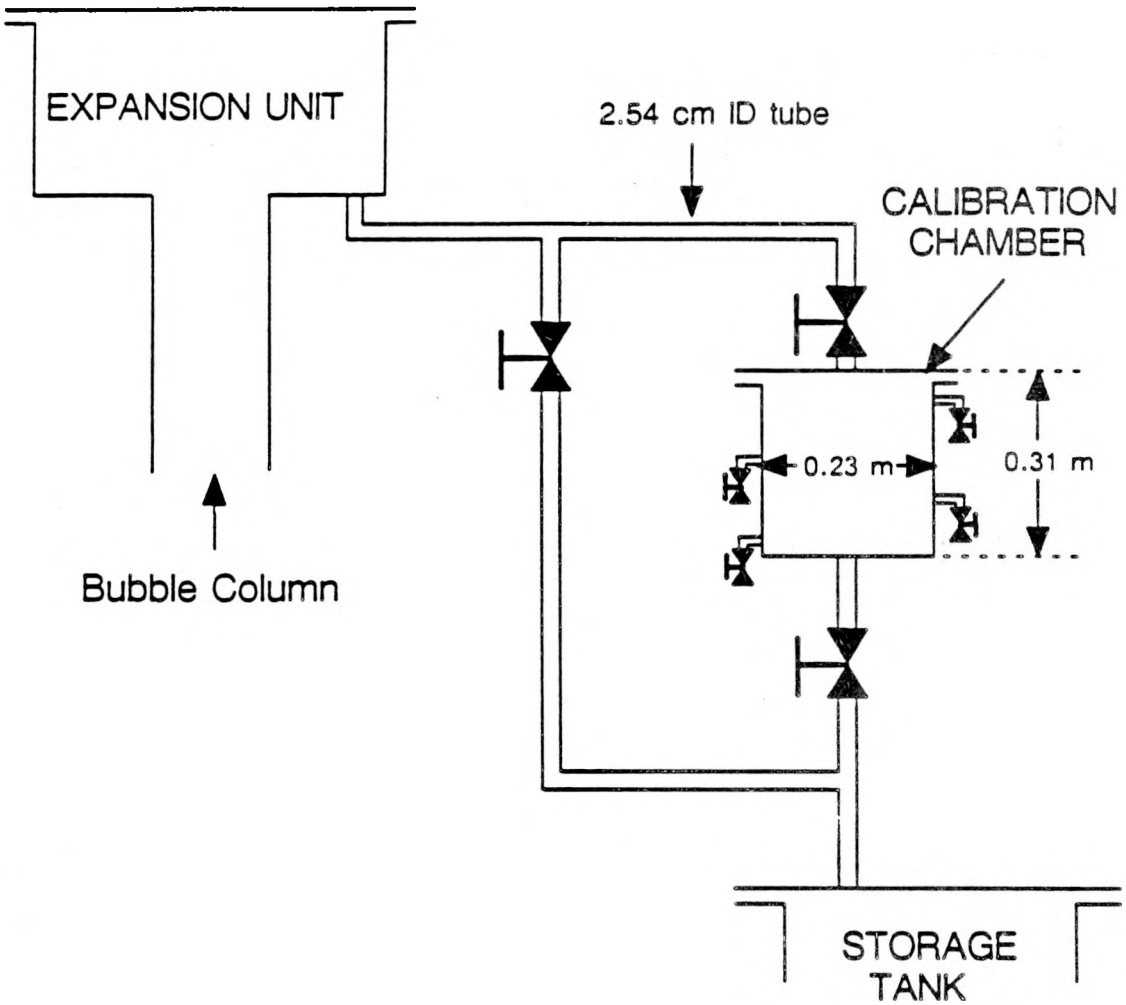

Figure 2.5. Schematic representation of the circulation loop for the small diameter stainless steel column.

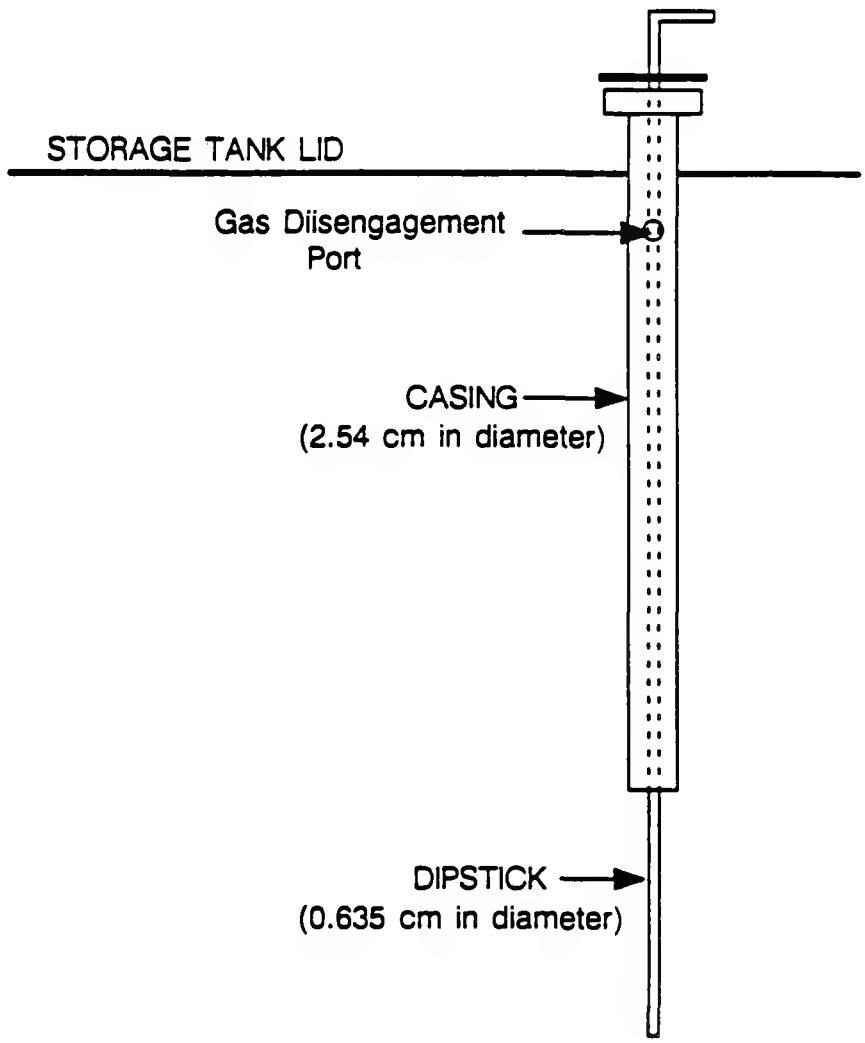

Figure 2.6. Schematic representation of the dipstick assembly.

been given elsewhere (Bukur et al., 1987a,b,c). All experiments in the glass columns were conducted in the batch mode of operation. The glass columns were used to obtain average gas holdups and bubble size distributions.

Experimental Conditions

The effects of operating conditions (slurry and gas superficial velocity), gas distributor design, column diameter, and solids concentration, type, and size were studied. Table 2.1 summarizes the experimental conditions employed in the stainless steel bubble columns. Experiments were conducted with SASOL's Arge reactor wax and FT–300 wax. SASOL reactor wax consists of high molecular weight products of the Fischer–Tropsch synthesis. FT–300 wax (also known as SH–105) is a hard paraffin wax obtained by hydrotreating and fractionation of reactor wax and it has an average molecular weight of 730 (Dura Commodities, New York).

Nitrogen was used as the gas for all experiments because it is inert, non–toxic, and inexpensive. Also, in earlier studies, it was found that the effect of gas type on the average gas holdup is small (Deckwer et al., 1980; Kuo, 1985). Superficial gas velocities in the range 0.02 – 0.12 m/s were employed in all experiments. With this range of gas velocities in the two columns, all important flow regimes were observed. A superficial gas velocity of 0.095 m/s was employed in the Rheinpreussen demonstration plant unit (Kolbel and Ralek, 1980), and thus, the higher velocities (0.08 – 0.12 m/s) chosen in this study are representative of gas velocities employed in large diameter reactors.

All of the experiments in the stainless steel bubble columns were conducted at a temperature of 265 °C, which is a typical temperature for the Fischer–Tropsch synthesis with precipitated iron catalysts. In our previous studies (Bukur et al., 1987a,b,c) some experiments were conducted in the small diameter column at other temperatures (160-280 °C) in order to study the effect of liquid viscosity on gas holdup.

Table 2.1. Bubble Column Dimensions and Experimental Conditions

COLUMN DIMENSIONS		
DIAMETER (m)	0.05	0.21
HEIGHT (m)	3.0	3.0
GAS DISTRIBUTOR	2 mm ORIFICE	PERFORATED PLATE BUBBLE CAPS
GAS	NITROGEN	NITROGEN
LIQUID	FT-300 and SASOL	FT-300 and SASOL
SOLIDS	IRON OXIDE (< 44 μm)	IRON OXIDE (< 44 μm)
	SILICA (< 44 μm)	SILICA (< 44 μm)
VARIABLES		
PRESSURE (atm)	1	1
TEMPERATURE (^{o}C)	265	265
SUPERFICIAL GAS VELOCITY (m/s)	0.02 - 0.12	0.02 - 0.12
LIQUID UPFLOW VELOCITY (m/s)	0.0 - 0.02	0.0 - 0.02
SOLIDS CONCENTRATION (wt%)	0 - 30	0 - 30

A 2 mm single hole orifice plate distributor was used for experiments conducted in the 0.05 m ID column. Whereas, for experiments in the 0.21 m ID column, both a 19 x 2 mm perforated plate and bubble cap distributor were used (see Figures 2.7 and 2.8, respectively). Perforated plates and bubble caps are commonly used in slurry bubble columns.

Solids concentrations in the range 0 – 30 wt% were employed throughout this work. This range of concentrations encompasses the range of catalyst concentrations used in slurry bubble column reactors for Fischer–Tropsch synthesis. Iron oxide particles (0 – 5 μm and 20 – 44 μm) were used as the primary solid. Some experiments were also conducted with silica particles (0 – 5 μm and 20 – 44 μm) to study the effect of solid density on the hydrodynamics of the system. The two types of solids used, iron oxide and silica, simulate typical catalysts and supports, respectively, employed in Fischer–Tropsch synthesis.

Data Acquisition and Reduction Procedures for Gas Holdups and Solids Concentration Profiles

Average gas holdups, axial gas holdups, and axial solid concentration profiles were measured experimentally. Experiments in the glass column were limited to two–phase (i.e. liquid/gas systems) batch studies; whereas, experiments in the stainless steel columns were conducted using both two–phase and three–phase systems with and without slurry circulation.

Average Gas Holdup – Glass Columns

For experiments conducted in the glass columns, only average (or overall) gas holdups were measured. The average gas holdup, which is the volume fraction of gas in the suspended slurry, is calculated from visual observations of the expanded and

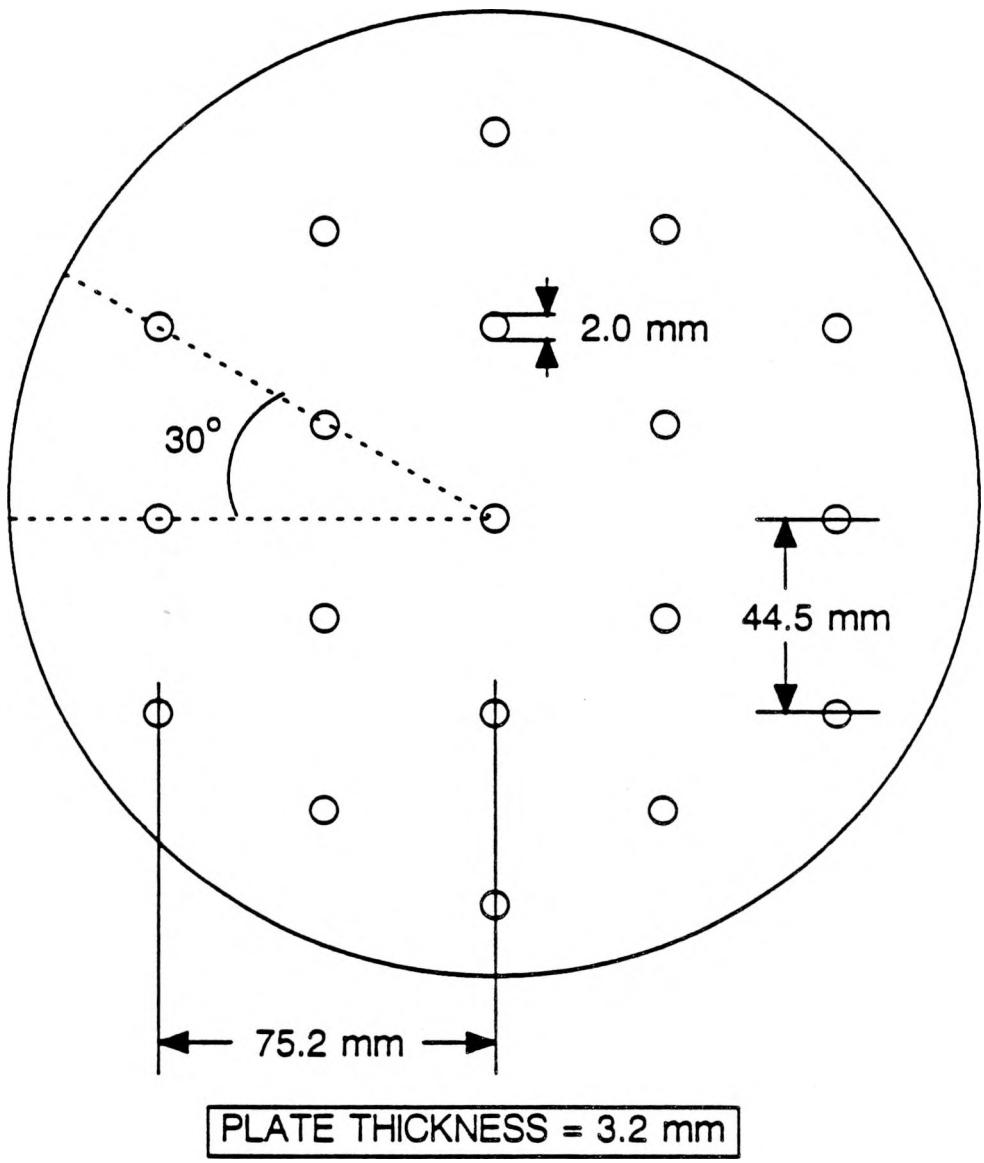

Figure 2.7. Schematic representation of the perforated plate distributor.

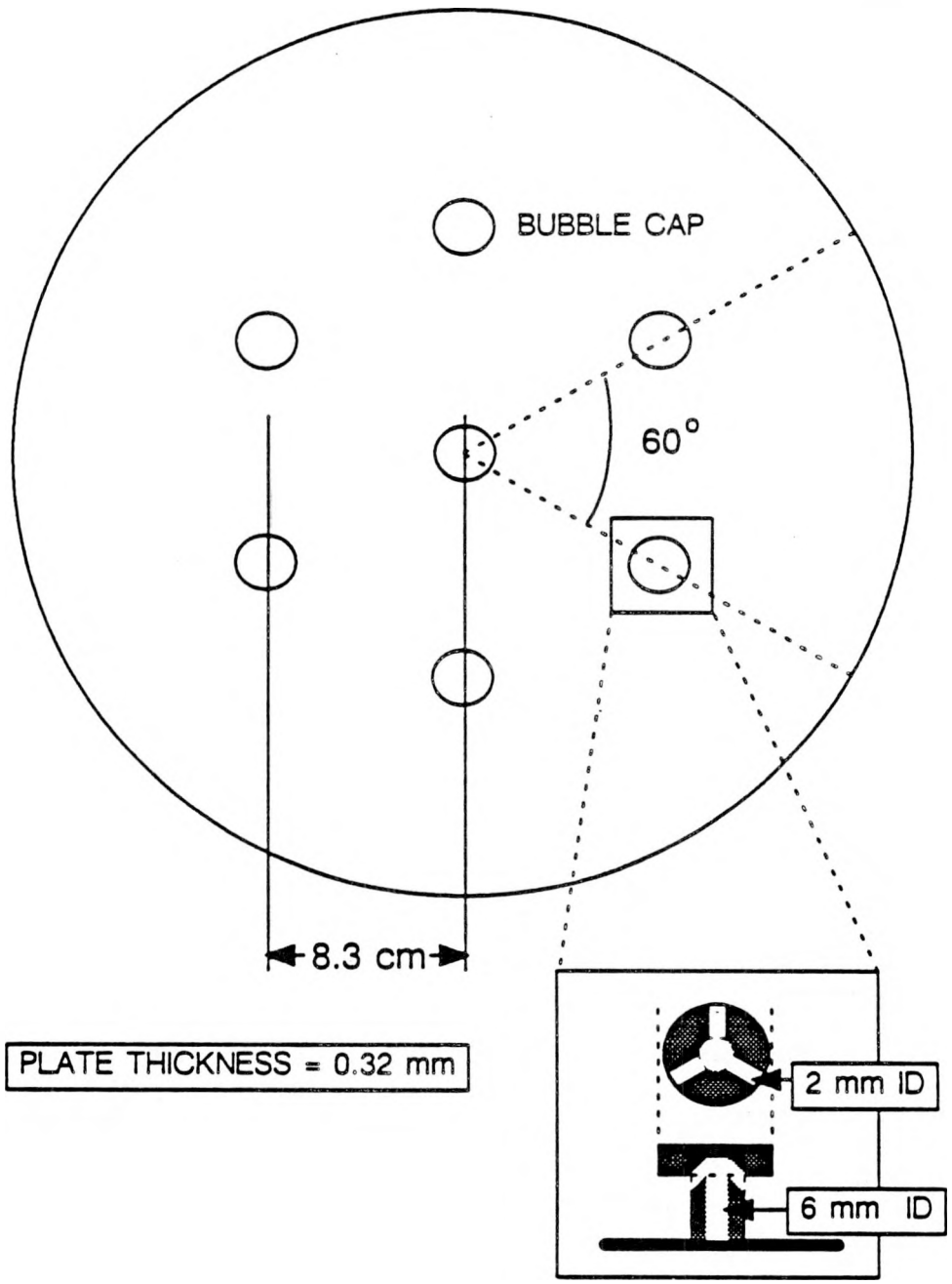

Figure 2.8. Schematic representation of the bubble cap distributor plate.

static liquid heights, i.e.

$$\epsilon_g = 1 - \frac{h_s}{h_{exp}} \tag{2.1}$$

where h_s is the static liquid height and h_{exp} is the expanded height of the slurry, and the quantity h_s/h_{exp} is the volume fraction of liquid in the gas/liquid dispersion. The expanded height was recorded three times per gas velocity at intervals of approximately 30 minutes. Once the expanded height was recorded three times, the gas flow was shut off and the static liquid height was recorded.

Phase Fractions – Stainless Steel Columns

In the stainless steel columns, axial gas holdups, axial solids concentrations, and average gas holdups were obtained. Axial pressure measurements and axial solids concentrations were used to calculate gas holdups (average and axial). Figure 2.9 is a schematic representation of the locations of the five pressure transducers and five slurry sampling ports.

Pressure Measurements

During experiments in the stainless steel columns, the pressure drop across the column and the weight fractions of solids were measured at various axial locations. A purgeless pressure transducer system was designed which prevents hot slurry from coming in contact with the DP cell (see Figure 2.10). The system consisted of a 0.635 cm diameter tube attached to the column wall and a 20 cm^3 chamber. When the column is filled with slurry, the nitrogen trapped in the chamber serves as a buffer between the hot slurry in the column and the low temperature DP cell. The chamber also serves as a trap for any slurry that flows into the 0.635 cm tube. A drain located at the bottom of the chamber is used to clean the trap between runs. A ball valve located in the 0.635 cm line serves to isolate the system from the column, in case the

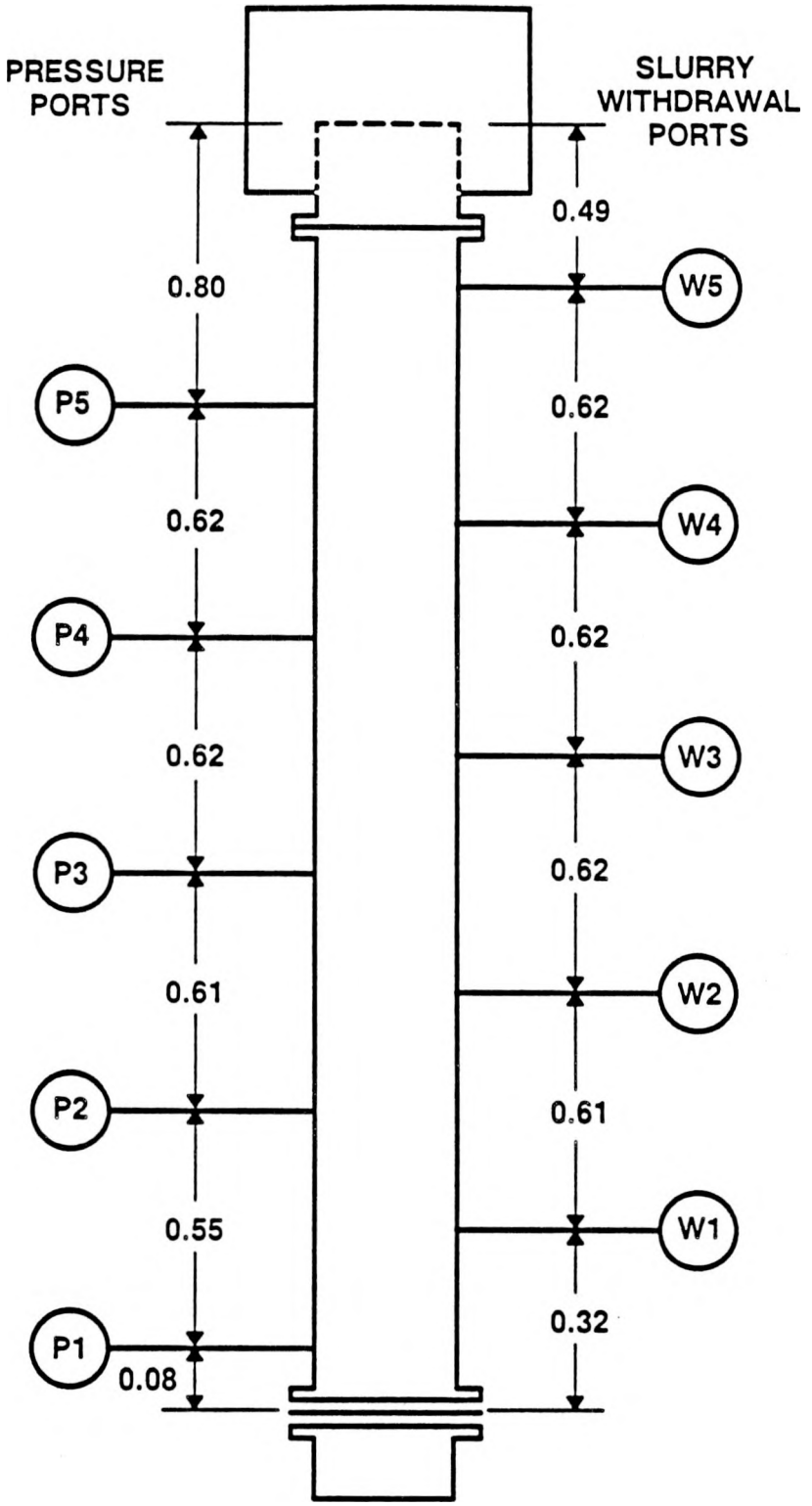

Figure 2.9. Schematic diagram of the pressure ports and slurry sampling ports locations (all dimensions in m).

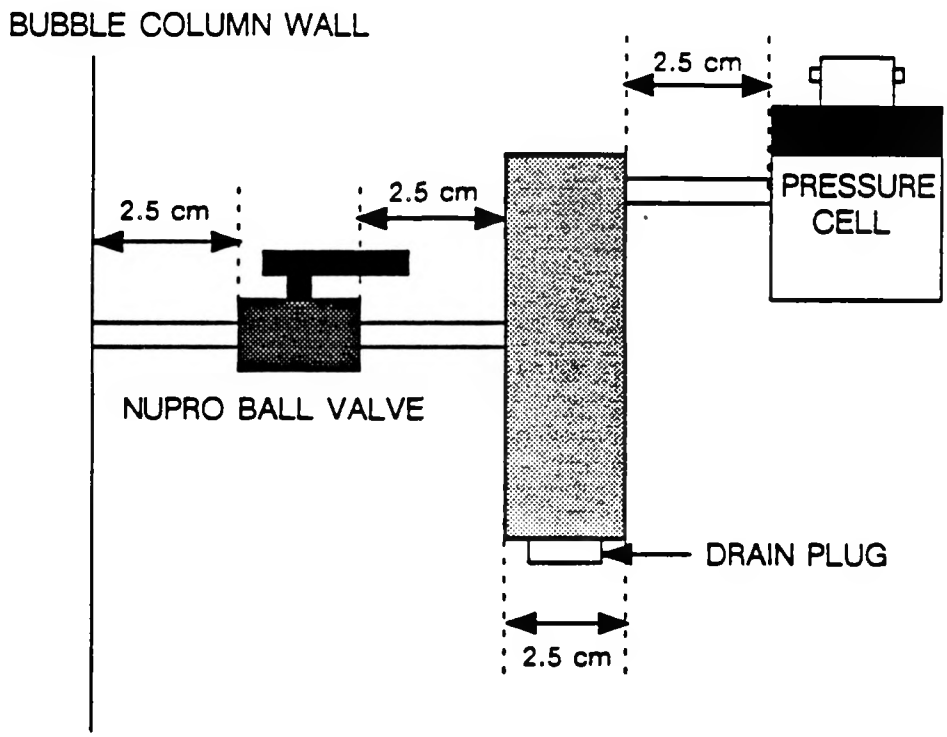

Figure 2.10. Schematic representation of the pressure transducer system.

trap has to be emptied during a run. The 0.635 cm line and chamber are heat traced and insulated to prevent solidification of slurry in this section.

The pressure transducers (Valydine Model DP–15) were connected to dual channel indicators (Valydine Model CD–223). The indicators have a digital display, as well as a 0 – 15 volt DC output. A data acquisition system which consisted of an A/D converter (Metrabyte Model DAS–16G), associated software, and a Zenith 286 personal computer was used to record the output voltage from the pressure transducer indicators. The pressure transducer indicators were adjusted so that the output voltage (proportional to pressure in inches of water) was scaled down by a factor of 10 before being sent to the data acquisition system. Thus, an output voltage of 1 corresponded to a height of approximately 10 inches of water. The calibration procedure for a single pressure transducer is outlined below. All pressure transducers were calibrated using the same procedure.

Before beginning each series of experiments, the pressure transducers were calibrated using tap water. The density of water was assumed to be 1000 kg/m^3. Initially, the output voltage from the pressure transducer indicator was set to zero. In order to calibrate a pressure transducer, the column was filled with water. The height of water above the transducer is the height of water in the column minus the height of the pressure transducer (both measured from the bottom of the column). The output voltage from the transducer indicator was forced to be 1/10th of the height of water (in inches) above the transducer by adjusting the span. The column was then drained and the zero was readjusted if necessary. Next, the column was filled with water again, and the output voltage was recorded. By making several measurements with different amounts of water in the column once the zero and span were set, a calibration curve of height of water (in inches) above the pressure transducer versus output voltage from the

pressure transducer indicator was obtained. Figure 2.11 is a sample calibration curve. The form of the calibration equation for a given pressure transducer is:

$$\text{Pressure (inches of water)} = \text{slope} * (\text{output voltage}) + \text{intercept} \qquad (2.2)$$

For all pressure transducers, the slope of the calibration curve was in the range 9.9 to 10.1 and the intercept was in the range -0.6 to 0.6.

Data acquisition software was written which would display a "running" average of the pressure indicator output voltage. During the experiments, data was collected at a rate of 50 Hz for a period of 2 to 3 minutes. As previously described, measurements were made three times per gas velocity (i.e. approximately every 30 minutes), and the average of the three values (output voltage) was used to calculate the pressure, in inches of water, above a given pressure transducer using Eq. 2.2.

Solid Concentration Measurements

For three–phase systems, both pressure measurements and weight fractions of solids are needed to determine the phase holdups (i.e. gas, liquid, and solids holdup). The weight fraction of solids in the slurry samples withdrawn at the various axial locations (see Figure 2.9) was measured using the Archimedean principle (the apparent loss in weight of a solid body, when completely immersed in a liquid, equals the weight of the displaced fluid). The procedure used is outlined below.

The slurry withdrawn into the sampling cylinder is allowed to cool and solidify. The solid slurry plug is then removed for solids fraction determination. The sample is first weighed on a precision balance ($m_{s\ell}$). It is then suspended with a thin wire from a support structure placed on the balance and the combined weight of the support structure and sample recorded (m_1). The sample, while still suspended from the support structure, is then completely immersed in a beaker of acetone and the balance reading recorded (m_2). The three measured quantities, along with the known densities of

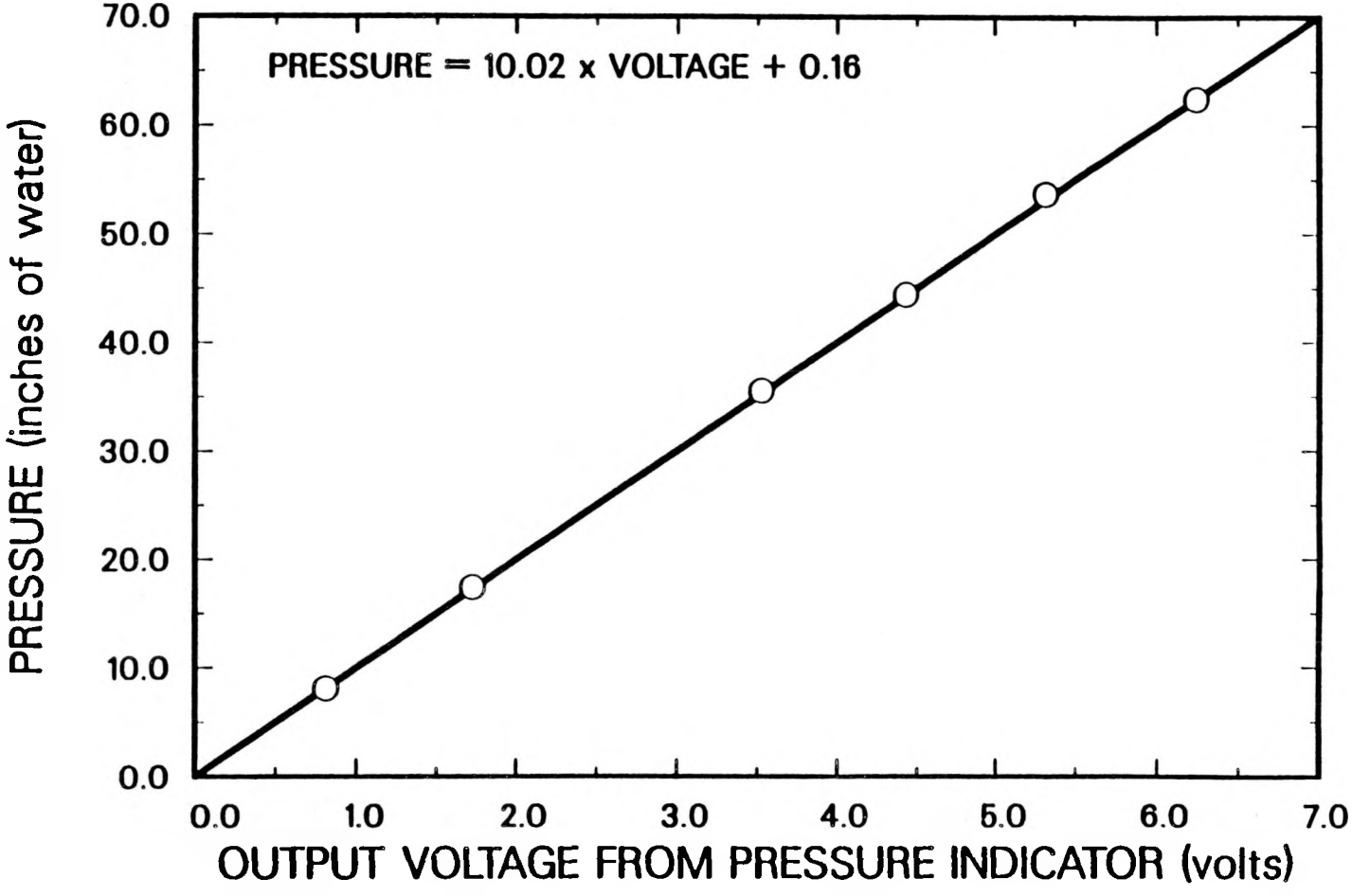

Figure 2.11. Typical pressure transducer calibration curve.

solidified wax (ρ_w), solids (ρ_s), and acetone (ρ_{acet}), were used to determine the weight fraction of solids (ω_s) in the slurry sample. By the definition of the Archimedean principle,

$$W_{acet} = m_1 - m_2 \tag{2.3}$$

where W_{acet} is the weight of acetone displaced. The volume of acetone displaced, which is the same as the volume of the slurry sample, is given by

$$V_{s\ell} = \frac{W_{acet}}{\rho_{acet}} \tag{2.4}$$

By substituting Eq. 2.3 into Eq. 2.4 and dividing the weight of the slurry sample ($m_{s\ell}$) by the volume of the sample ($V_{s\ell}$), the following expression is obtained for the density of the slurry sample

$$\rho_{s\ell} = \frac{m_{s\ell}\rho_{acet}}{m_1 - m_2} \tag{2.5}$$

The density of the sample may be expressed in terms of ω_s as follows

$$\rho_{s\ell} = \frac{1}{\frac{\omega_s}{\rho_s} + \frac{(1-\omega_s)}{\rho_w}} \tag{2.6}$$

Equating Eqs. 2.5 and 2.6 to eliminate $\rho_{s\ell}$, and rarranging the terms, yields the following expression for ω_s

$$\omega_s = \frac{\rho_s - \left(\frac{\rho_w\rho_s}{\rho_{acet}}\right)\left(\frac{m_1-m_2}{m_{s\ell}}\right)}{\rho_s - \rho_w} \tag{2.7}$$

The density of solidified wax was determined experimentally. The density of fresh FT–300 wax is 950 kg/m^3, and the density of fresh SASOL wax is 930.5 kg/m^3. Acetone was selected as the liquid medium for this procedure because it has a lower density than wax (ρ_{acet} = 792 kg/m^3), it evaporates quickly from the sample surface, and the solubility of wax in acetone at room temperature is negligible. The procedure was tested using both FT–300 and SASOL wax containing known quantities of solids. Samples containing 3, 7, 10, 15, 20, 25, 30, and 35 wt.% solids in wax were prepared. Samples

with 0–5 μm iron oxide, 20–44 μm iron oxide and 0–5 μm silica were used with FT–300, and samples with 0–5 μm iron oxide and 20–44 μm silica were used with SASOL wax. Solid densities of 5100 kg/m^3 for iron oxide and 2650 kg/m^3 for silica were employed. Tables 2.2a, 2.2b, and 2.2c show results obtained with slurries of 0 – 5 μm iron oxide particles, 20 – 44 μm iron oxide particles, and 0 – 5 μm silica particles in FT–300 wax, respectively. For these samples, the relative error between the calculated (Eq. 2.7) and the actual weight fraction of solids was highest for the sample containing 3 wt% 0 – 5μm silica particles (6.5 %). For all other solids concentrations, the relative error between the actual and calculated weight fractions was less than 2.2 %. Tables 2.3a and 2.3b show results from measurements with 0 – 5 μm iron oxide and 20 – 44μm silica particles in SASOL wax, respectively. For all samples analyzed, the calculated weight fractions of solids were within 1.02 % (relative) of the actual weight fraction of solids.

Sensitivity analysis of Eq. 2.7 revealed that the results were very sensitive to small variations in the density of solidified wax. A variation of only 1 % in the density of wax caused a 12 % change in ω_s; whereas, a 5 % change in the density of solids caused only a 2 % change in ω_s for slurries containing iron oxide, and a 4 % change in ω_s for slurries containing silica. Because of the high sensitivity to wax density, we determined the density of fresh wax and used wax. For FT–300, the density of fresh wax and used wax (100 hours on stream) was the same. However, the density of SASOL wax varied with time on stream. The density of fresh SASOL wax was 930.5 kg/m^3 and the density of used SASOL wax (72 hours on stream) was 941.2 kg/m^3. There was less than 0.07 % difference in the density of SASOL wax between 72 hours on stream and 144 hours on stream. The change in density between fresh and used SASOL wax was probably caused by changes in the composition of SASOL wax with time on stream. SASOL wax contains a significantly higher concentration of lower molecular weight components

Table 2.2a. Results from Archimedean Procedure (0 – 5 μm iron oxide in FT–300)[a]

Nominal	Actual wt.%	Measured wt.%	% Error
3	2.94	2.96	0.74
7	6.61	6.60	-0.13
10	9.15	9.09	-0.61
15	13.13	12.92	-1.59
20	20.20	20.26	0.31
25	25.15	24.95	-0.78
30	30.25	30.04	-0.68
35	35.22	34.90	-0.91

[a] densities used: ρ_w = 0.9495 g/cc, ρ_s = 5.1 g/cc, ρ_{acet} = 0.792 g/cc

Table 2.2b. Results from Archimedean Procedure (20 – 44 μm iron oxide in FT–300)[b]

Nominal	Actual wt.%	Measured wt.%	% Error
3	3.09	2.89	-6.54
7	7.11	7.25	2.02
10	10.24	10.01	-2.21
15	15.13	15.17	0.26
20	20.00	20.02	0.10
25	25.13	25.25	0.49
30	30.33	30.43	0.32
35	35.03	35.07	0.11

[a] densities used: ρ_w = 0.9495 g/cc, ρ_s = 5.1 g/cc, ρ_{acet} = 0.792 g/cc

Table 2.2c. Results from Archimedean Procedure (0 – 5 μm silica in FT–300)[c]

Nominal	Actual wt.%	Measured wt.%	% Error
3	3.04	3.09	1.54
7	7.06	7.04	-0.39
10	10.04	10.07	0.27
15	15.10	15.07	-0.23
20	20.09	20.00	-0.44
25	25.09	24.93	-0.67
30	30.15	30.05	-0.32
35	35.05	34.87	-0.51

[a] densities used: ρ_w = 0.9495 g/cc, ρ_s = 2.65 g/cc, ρ_{acet} = 0.792 g/cc

Table 2.3a. Results from Archimedean Procedure (0 – 5 μm iron oxide in SASOL)[a]

Nominal	Actual wt.%	Measured wt.%	% Error
3	3.03	3.02	-0.34
7	6.78	6.74	-0.65
10	9.81	9.89	0.77
15	14.94	14.99	0.31
20	20.26	20.05	-1.02
25	24.63	24.45	-0.72
30	28.95	29.04	0.32
35	35.21	34.90	-0.89

[a] densities used: $\rho_w = 0.9305$ g/cc, $\rho_s = 5.1$ g/cc, $\rho_{acet} = 0.792$ g/cc

Table 2.3b. Results from Archimedean Procedure (20 – 44 μm silica in SASOL)[b]

Nominal	Actual wt.%	Measured wt.%	% Error
3	2.97	2.97	0.0
7	7.02	6.97	-0.71
10	9.94	10.00	0.06
15	15.03	14.91	-0.83
20	19.94	19.86	-0.41
25	24.81	24.91	0.39
30	29.88	29.93	0.18
35	35.12	35.08	-0.10

[a] densities used: $\rho_w = 0.9305$ g/cc, $\rho_s = 2.65$ g/cc, $\rho_{acet} = 0.792$ g/cc

than FT–300 wax. These low molecular weight components evaporate when the slurry is held at 265 °C for extended periods of time. As mentioned previously, slight errors (or changes) in wax density result in large errors of the estimated solids concentration. In order to compensate for changes in wax density (SASOL wax) with time on stream, the density of used wax (i.e. 941.2 kg/m^3) was used to calculate the solids concentration once the wax had been on stream for over 72 hours, and the density of fresh wax (930.5 kg/m^3) was used prior to that.

Holdup Calculations

The system constants used to determine the gas holdup, liquid holdup, and solid holdup include the densities of solids (ρ_s), liquid (ρ_ℓ), solidified wax (ρ_w) and acetone (ρ_{acet}), heights of the five pressure ports above the distributor (h_1 to h_5), and the distance between the distributor (bottom of the column) and the top of the column (h_t). The measured quantities include the meter readings (i.e. average output voltages, OV_1 to OV_5), the weights of solidified slurry samples ($m_{s\ell_{ij}}$), the weight of the slurry sample suspended in air ($m_{1_{ij}}$), and its weight when immersed in acetone (m_{2ij}). For simplicity, the measured quantities have been replaced with the primary derived quantities, i.e. the differential pressure across section i–j (ΔP_{ij}), and the average weight fraction of solids for the section i–j ($< \omega_s >_{ij}$).

The differential pressure is defined by

$$\Delta P_{ij} = P_i - P_j = (a_i OV_i + b_i) - (a_j OV_j + b_j) \qquad i = 1 \text{ to } 5 \text{ and } j = i + 1 \qquad (2.8)$$

where a_i and a_j are the slopes of the calibration curves relating the meter readings to pressure (in inches of water) for transducers at ports i and j, respectively, and b_i and b_j are the intercepts of the two curves (see Eq. 2.2). Note, j = 6 corresponds to the top

of the column, and the pressure at the top of the column is assumed to be atmospheric pressure. The distance between pressure ports i and j is defined as

$$\Delta h_{ij} = h_j - h_i \qquad i = 1 \text{ to } 5 \text{ and } j = i + 1 \tag{2.9}$$

The average weight fraction of solids (see Eq. 2.7) between pressure ports i and j is given by

$$< \omega_s >_{ij} = \frac{\rho_s - \left(\frac{\rho_w \rho_s}{\rho_{acet}}\right)\left(\frac{m_{1_{ij}} - m_{2_{ij}}}{m_{s\ell_{ij}}}\right)}{\rho_s - \rho_w} \qquad i = 1 \text{ to } 5 \text{ and } j = i + 1 \tag{2.10}$$

The gas holdup in a three–phase (gas/liquid/solid) system may be expressed in terms of the slurry (liquid/solid) density, $\rho_{s\ell}$ and the density of the gas–liquid–solid dispersion, ρ_d (i.e. density of the expanded slurry) as,

$$\epsilon_g = \frac{\rho_{s\ell} - \rho_d}{\rho_{s\ell} - \rho_g} \approx 1 - \frac{\rho_d}{\rho_{s\ell}} \tag{2.11}$$

since the density of the gas, ρ_g is small in comparison to the density of the slurry at low pressures.

The density of the expanded slurry between any two pressure ports, i and j may be calculated from the measured pressure drop ΔP_{ij} and the known distance between the pressure taps, Δh_{ij},

$$s_{d_{ij}} = \frac{\Delta P_{ij}}{\Delta h_{ij}} \text{ and } \rho_{d_{ij}} = s_{d_{ij}} \rho_{water} \qquad i = 1 \text{ to } 5 \text{ and } j = i + 1 \tag{2.12}$$

where $s_{d_{ij}}$ is the specific gravity of the dispersion between pressure ports i and j. Substituting this expression into Eq. 2.11, yields:

$$< \epsilon_{g_{ij}} > = 1 - \frac{\Delta P_{ij}}{s_{s\ell_{ij}} \Delta h_{ij}} \tag{2.13}$$

where $s_{s\ell_{ij}}$ is the specific gravity of the slurry (liquid/solid) in the i–j section. The specific gravity of the slurry between pressure ports i and j can be calculated from the

weight fraction of solids between pressure ports i and j, the density of the solid, and the density of the liquid using the following expression

$$s_{s\ell_{ij}} = \frac{1}{\rho_{water}} \frac{1}{\left[\frac{<\omega_s>_{ij}}{\rho_s} + \frac{1-<\omega_s>_{ij}}{\rho_\ell}\right]} \qquad i = 1 \text{ to } 5 \text{ and } j = i+1 \tag{2.14}$$

Substituting Eq. 2.14 into Eq. 2.13 yields

$$< \epsilon_g >_{ij} = 1 - \left(\frac{\Delta P_{ij} \rho_{water}}{\Delta h_{ij}}\right) \left[\frac{< \omega_s >_{ij}}{\rho_s} + \frac{1- < \omega_s >_{ij}}{\rho_\ell}\right] \qquad i = 1 \text{ to } 5,\ j = i+1 \tag{2.15}$$

The latter expression was used to calculate the gas holdup between pressure ports i and j.

The liquid holdup may be expressed in terms of ρ_ℓ, ρ_d, ρ_s, ϵ_g, and ϵ_s as follows:

$$\epsilon_\ell = \frac{\rho_d - \epsilon_g \rho_g - \epsilon_s \rho_s}{\rho_\ell} \tag{2.16}$$

where ϵ_s is the volume fraction of solids (i.e. solids holdup) in the dispersion. Assuming $\epsilon_g \rho_g$ is negligible, Eq. 2.16 may be rewritten as:

$$\epsilon_\ell = \frac{\rho_d - \epsilon_s \rho_s}{\rho_\ell} \tag{2.17}$$

The volume fraction of solids in the dispersion may be expressed in terms of the weight fraction of solid in the dispersion using

$$\epsilon_s = \frac{\omega_s \rho_d}{\rho_s} \tag{2.18}$$

Substituting Eq. 2.18 into Eq. 2.17 upon rearrangement yields the following expression for ϵ_ℓ

$$\epsilon_\ell = \frac{\rho_d (1 - \omega_s)}{\rho_\ell} \tag{2.19}$$

Thus the liquid holdup in the section i–j is given by

$$< \epsilon_{\ell_{ij}} >= \frac{\rho_{d_{ij}} (1 - < \omega_{s_{ij}} >)}{\rho_\ell} \qquad i = 1 \text{ to } 5 \text{ and } j = i+1 \tag{2.20}$$

Substituting the expression for $\rho_{d_{ij}}$ (Eq. 2.12) into Eq. 2.20 the following expression is obtained for the average liquid holdup between pressure ports i and j

$$< \epsilon_\ell >_{ij} = \left(\frac{\Delta P_{ij} \rho_{water}}{\Delta h_{ij}}\right)\left(\frac{1 - < \omega_s >_{ij}}{\rho_\ell}\right) \qquad i = 1 \text{ to } 5, \quad j = i + 1 \qquad (2.21)$$

Since the sum of the volume fractions of gas, liquid and solids equals one, the volume fraction of solids in the dispersion between pressure ports i and j may be expressed as:

$$< \epsilon_{s_{ij}} > = 1 - < \epsilon_{\ell_{ij}} > - < \epsilon_{g_{ij}} > \qquad i = 1 \text{ to } 5 \text{ and } j = i + 1 \qquad (2.22)$$

Substituting Eqs. 2.15 and 2.21 into Eq. 2.22 yields the following expression for the average volume fraction of solids in the i–j section

$$< \epsilon_s >_{ij} = \left(\frac{\Delta P_{ij} \rho_{water}}{\Delta h_{ij}}\right)\left(\frac{< \omega_s >_{ij}}{\rho_s}\right) \qquad i = 1 \text{ to } 5, \quad j = i + 1 \qquad (2.23)$$

Equations 2.15, 2.21, and 2.23 were used to estimate holdups of the three phases in the section between any two adjacent pressure ports; however, for the equations to be valid the entire section must be filled with the dispersion. For runs conducted in the continuous mode of operation, all five sections are always full, since the dispersion fills the entire column. For runs conducted in the batch mode of operation, Eqs. 2.15, 2.21, and 2.23 may be used for those sections that are full, i.e. all sections below the top most non-zero pressure port. The section just above this pressure port (say section n) is only partially full, therefore the height of the dispersion in this section (Δh_n) is not known. However, the differential pressure for this section (ΔP_n) is known. If a slurry sample was not withdrawn from this section, $< \omega_s >_n$ would also be an unknown quantity. For such cases, the gas holdup and if necessary, the weight fraction of solids in this section are either estimated by extrapolation of the $< \epsilon_g >$ and $< \omega_s >$ profiles or they are assumed to have the same values as in the section below (i.e. $< \epsilon_{g_{n,n+1}} > = < \epsilon_{g_{n-1,n}} >$

and $< \omega_{s_{n,n+1}} >=< \omega_{s_{n-1,n}} >$). The height of the dispersion in this section is then calculated using (see Eq. 2.15)

$$\Delta h_n = \left(\frac{\Delta P_n \rho_{water}}{1- < \epsilon_g >_n}\right)\left[\frac{< \omega_s >_n}{\rho_s} + \frac{1- < \omega_s >_n}{\rho_\ell}\right] \qquad (2.24)$$

Equations 2.21 and 2.23 can then be used to estimate the liquid and solids holdups for this section. For all runs, no measurements are made between the distributor and pressure port 1 (see Figure 2.9). It is assumed that the volume fractions of the three phases in this section are the same as those in the section above (i.e. section 1-2).

The average gas holdup for the entire dispersion can be obtained using a weighted (volume) average of the gas holdups in the individual sections and is expressed as

$$< \epsilon_g >= \sum_{i=1}^{n} f_{d_{ij}} < \epsilon_{g_{ij}} > \qquad j = i+1 \qquad (2.25)$$

where $f_{d_{ij}}$ is the volume fraction of the dispersion between pressure ports i and j and is given by

$$f_{d_{ij}} = \frac{\Delta h_{ij}}{\sum_i \Delta h_{ij}} \qquad i = 1 \text{ to } 5 \text{ and } j = i+1 \qquad (2.26)$$

Substituting Eqs. 2.15 and 2.26 into Eq. 2.25 yields

$$< \epsilon_g >= 1 - \frac{\sum_{i=0}^{n}\left(\Delta P_{ij}\rho_{water}\right)\left[\frac{< \omega_s >_{ij}}{\rho_s} + \frac{1- < \omega_s >_{ij}}{\rho_\ell}\right]}{\sum_{i=0}^{n} \Delta h_{ij}} \qquad j = i+1 \qquad (2.27)$$

where $\Delta P_{01} = \Delta P_{12}\Delta h_{01} / \Delta h_{12}$, and $< \omega_s >_{01}=< \omega_s >_{12}$. For the continuous mode of operation n = 5; whereas, for the batch mode of operation, n is dependent on the location of the top of the dispersion.

For two–phase experiments in the stainless steel column, the same procedure was used to calculate gas holdups and liquid holdups. However, the weight fraction of solids, ω_s, was set equal to 0.

Results and Discussion

Average and axial gas holdups obtained from experiments in the stainless steel columns are presented here. Axial solids concentration profiles will be discussed in Chapter IV. The discussion is divided into three main sections. In the first part, definitions and descriptions of the various flow regimes which were observed are presented. Following this, the effect of various operating conditions and column diameter on gas holdups are discussed. Finally, various correlations which may be used to predict average gas holdup in a three–phase Fischer–Tropsch bubble column reactors are presented.

Description of the Flow Field

The hydrodynamics (e.g. mixing characteristics, bubble size distribution, etc.) of a bubble column is significantly affected by the flow regime prevailing in the column. Ample evidence of this dependency is available in the literature (e.g. Shah et al., 1982) and various criteria have been proposed by different researchers to delineate the flow regimes (e.g. Taitel et al., 1981; Deckwer et al., 1980). Deckwer et al. presented a flow regime map (see Figure 2.12) which qualitatively characterizes the dependence of flow regimes on column diameter and superficial gas velocity. At low gas velocities, regardless of column diameter, the homogeneous (or homogeneous bubbling) regime exists. This regime is characterized by a uniform bubble size distribution in which there is very little interaction between neighboring bubbles. As the gas velocity increases, bubble coalescence and breakup occur. In columns less than 0.10 m in diameter, the large bubbles may fill the entire column diameter forming slugs; this is known as the slug flow regime. In larger diameter columns, large bubbles are formed without producing slugs. As these large bubbles rise through the column, there is an increase in turbulence; hence, this is called the churn–turbulent flow regime. The shaded regions in Figure 2.12

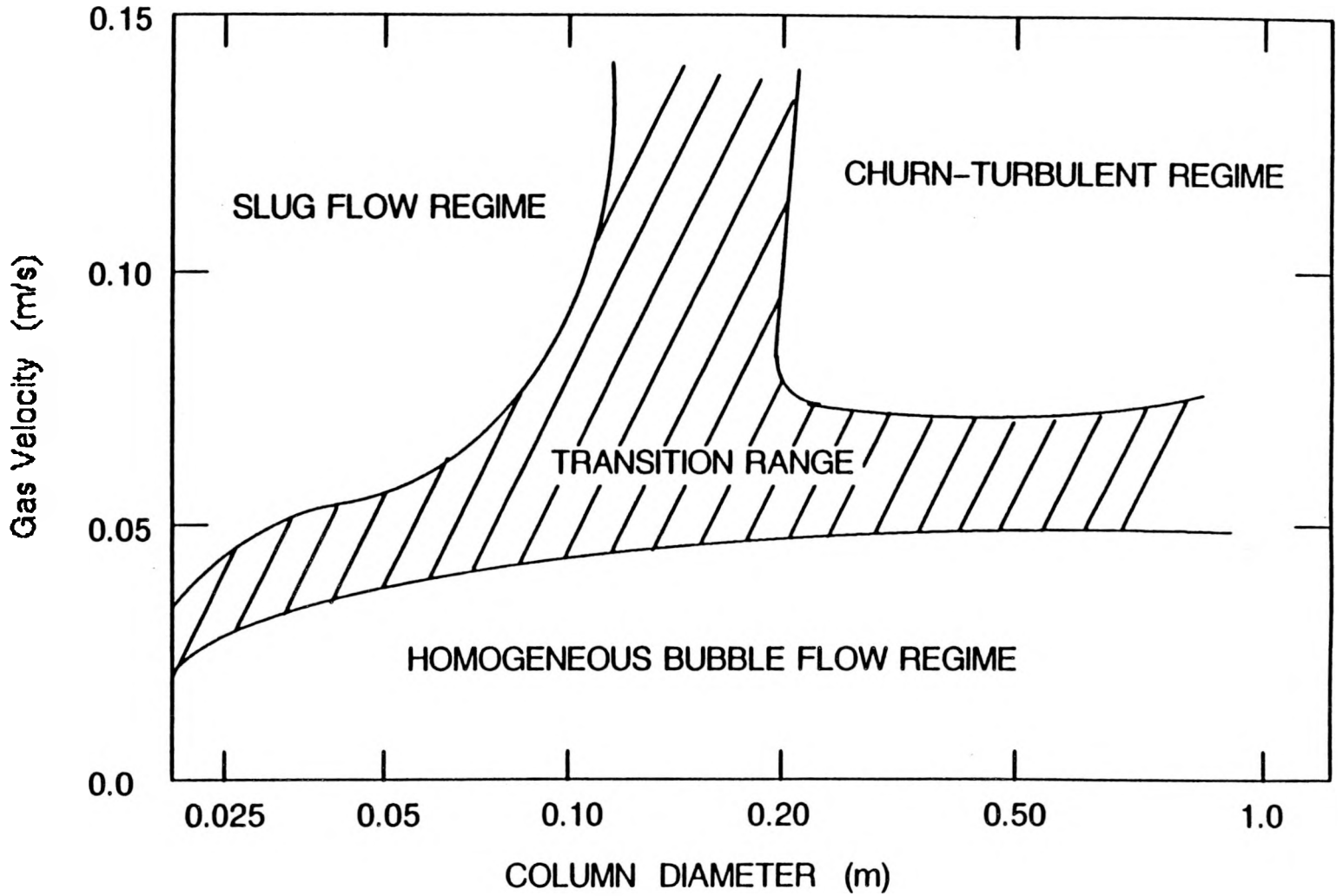

Figure 2.12. Bubble column flow regime map (adopted from Deckwer et al., 1980).

indicate the transition regions between the various flow regimes. The exact boundaries associated with the transition regions will probably vary with the system studied.

The flow regimes described above are typically associated with nonfoaming systems. For foaming systems, Shah et al. (1985) include an additional flow regime called the foaming (or foamy) regime. The foamy regime overlaps the previously described regimes and is characterized by high gas holdups and substantial recirculation of bubbles.

In our experiments, all of the flow regimes described above were observed. In the 0.05 m ID column, the homogeneous bubbly regime prevailed at superficial gas velocities less than 0.04 m/s and the slug flow regime at higher gas velocities. For experiments conducted with FT–300 wax, the foamy regime was also observed; however, with SASOL reactor wax, very little foam, if any, was present. In the 0.21 m ID column, the homogeneous bubbling regime was observed at low gas velocities (u_g <0.04 m/s) and the churn–turbulent regime at higher gas velocities. The amount of foam observed in experiments with FT–300 wax in the large diameter column was significantly less than that observed under similar operating conditions in the small diameter column. As in the 0.05 m ID column, little or no foam was observed during experiments conducted with SASOL wax in the 0.21 m ID column.

Gas Holdup Results

FT–300 and SASOL wax were used for experiments in both the small (0.05 m ID) and large (0.21 m ID) diameter columns. The majority of experiments in the small diameter column were conducted with FT–300 wax, since SASOL wax was not available during the initial stages of this study. Once SASOL wax became available, some experiments were preformed in order to study the effect of wax type on gas holdup and solid concentration profiles. Table 2.4 summarizes experimental conditions used in the small diameter column. An increasing order of gas velocities was employed for all

Table 2.4. Summary of Runs in the Small Stainless Steel Column

EXP. No.	WAX TYPE	T (°C)	d_p (μm)	ω_s (%)	SOLIDS TYPE	u_ℓ (m/s)	TOS (hr)	TIME HOT (hr)
1	FT-300	265	–	–	—	0.0	0	12
2	FT-300	265	–	–	—	0.005	8	36
3	FT-300	265	–	–	—	0.02	16	60
4	FT-300	265	0 – 5	10	IRON OX	0.005	24	84
5	FT-300	265	0 – 5	10	IRON OX	0.02	32	108
6	FT-300	265	0 – 5	10	IRON OX	0.0	40	132
7	FT-300	265	0 – 5	20	IRON OX	0.005	0	12
8	FT-300	265	0 – 5	20	IRON OX	0.02	8	36
9	FT-300	265	0 – 5	20	IRON OX	0.0	16	60
10	FT-300	265	0 – 5	30	IRON OX	0.005	24	84
11	FT-300	265	0 – 5	30	IRON OX	0.02	32	108
12	FT-300	265	0 – 5	30	IRON OX	0.0	40	132
13	FT-300	265	20 – 44	10	IRON OX	0.005	0	12
14	FT-300	265	0 – 5	10	SILICA	0.005	0	12
15	FT-300	265	0 – 5	20	SILICA	0.005	8	36
16	FT-300	265	0 – 5	20	SILICA	0.02	16	60
17	FT-300	265	0 – 5	20	SILICA	0.0	24	84
18	FT-300	265	0 – 5	30	SILICA	0.005	32	108
19	FT-300	265	20 – 44	10	IRON OX	0.005	0	12
20	FT-300	265	20 – 44	10	IRON OX	0.02	8	36
21	FT-300	265	20 – 44	20	IRON OX	0.0	16	84
22	FT-300	265	20 – 44	20	SILICA	0.0	0	36
23	FT-300	265	–	–	—	0.0	0	12
24	FT-300	265	–	–	—	0.005	8	36
25	FT-300	265	20 – 44	20	IRON OX	0.0	16	60
26	FT-300	265	20 – 44	20	IRON OX	0.02	24	84
27	FT-300	265	20 – 44	20	IRON OX	0.005	32	108
28	FT-300	265	20 – 44	20	SILICA	0.0	0	12
29	SASOL	265	–	–	—	0.0	0	12
30	SASOL	265	–	–	—	0.005	8	36
31	SASOL	265	0 – 5	20	IRON OX	0.005	16	60
32	SASOL	265	20 – 44	20	IRON OX	0.0	0	12
33	SASOL	265	20 – 44	20	IRON OX	0.005	8	36
34	SASOL	265	20 – 44	20	IRON OX	0.005	12	60

Note: Horizontal lines separate batches
TOS – Time on stream
TIME HOT – Total time heated

experiments in the small diameter column, with the exception of the two batch experiments conducted with 20–44 μm silica particles (experiments 22 and 28 in Table 2.4) and the last two continuous experiments with large iron oxide particles suspended in FT–300 wax (experiments 26 and 27 in Table 2.4). For these experiments, a decreasing order of gas velocities was used. Experiments in the large diameter column were conducted once all experiments in the small diameter column were completed. SASOL wax was chosen as the primary fluid for experiments in the 0.21 m ID column since it is more representative of the reactor wax present in a slurry bubble column reactor during Fischer–Tropsch synthesis. Also, a limited number of experiments was conducted with FT–300 wax in the 0.21 m ID column. A summary of the experiments conducted in the large diameter column is presented in Table 2.5. The 19 x 2 mm perforated plate (PP) was used for majority of these experiments. With the exception of a few experiments without solids (i.e. experiments 1 – 4 in Table 2.5), all experiments in the large diameter column were performed using a decreasing order of gas velocities. The effect of slurry flow rate, solids concentration, type and size, liquid medium, temperature, distributor type, and column diameter on gas holdup is discussed below.

Effect of Slurry Velocity

Figures 2.13a and 2.13b show the effect of slurry velocity on average gas holdup for experiments conducted with FT–300 wax in the small and large diameter columns, respectively. A substantial amount of foam was produced during the batch (i.e. $u_{s\ell} = 0$) experiment in the 0.05 m ID column, with gas holdup values as high as 0.29 at a gas velocity of 0.04 m/s (see Figure 2.13a). Gas holdups decreased significantly for gas velocities in the range 0.04 – 0.09 m/s when the superficial slurry velocity was increased to 0.005 m/s. A further decrease in gas holdup was observed when the slurry velocity was increased to 0.02 m/s. It should be noted that at higher gas velocities,

Table 2.5. Summary of Runs in the Large Stainless Steel Column

EXP. No.	WAX TYPE	T (°C)	d_p (μm)	ω_s (%)	SOLIDS TYPE	u_ℓ (m/s)	DIST —	TOS (hr)	TIME HOT (hr)
1	SASOL	265	—	—	—	0.0	PP	0	12
2	SASOL	265	—	—	—	0.005	PP	6	36
3	SASOL	265	—	—	—	0.02	PP	12	42
4	SASOL	265	—	—	—	0.005	BC	18	78
5	SASOL	265	—	—	—	0.0	PP	0	72
6	SASOL	265	0 – 5	IRON OX	10	0.0	PP	8	96
7	SASOL	265	0 – 5	IRON OX	20	0.0	PP	16	120
8	SASOL	265	0 – 5	IRON OX	20	0.005	PP	24	124
9	SASOL	265	0 – 5	IRON OX	20	0.02	PP	32	130
10	SASOL	265	0 – 5	IRON OX	20	0.0	BC	40	154
11	SASOL	265	0 – 5	IRON OX	20	0.005	BC	48	162
12	SASOL	265	0 – 5	IRON OX	20	0.0	PP	56	186
13	SASOL	265	0 – 5	IRON OX	30	0.0	PP	64	210
14	SASOL	265	0 – 5	IRON OX	30	0.005	PP	72	234
15	SASOL	265	20 – 44	IRON OX	10	0.005	PP	0	12
16	SASOL	265	20 – 44	IRON OX	10	0.02	PP	6	18
17	SASOL	265	20 – 44	IRON OX	20	0.0	PP	12	42
18	SASOL	265	20 – 44	IRON OX	20	0.005	PP	18	48
19	SASOL	265	20 – 44	IRON OX	20	0.02	PP	24	72
20	SASOL	265	20 – 44	IRON OX	20	0.0	BC	30	120
21	SASOL	265	20 – 44	IRON OX	20	0.0	PP	36	144
22	SASOL	265	20 – 44	IRON OX	30	0.0	PP	42	150
23	SASOL	265	20 – 44	IRON OX	30	0.005	PP	48	174
24	SASOL	265	20 – 44	IRON OX	30	0.02	PP	54	180
25	SASOL	265	—	—	—	0.005	BC	0	12
26	SASOL	265	20 – 44	SILICA	20	0.0	PP	6	36
27	SASOL	265	20 – 44	SILICA	20	0.005	PP	12	42
28	SASOL	265	20 – 44	SILICA	20	0.02	PP	18	48
29	SASOL	265	20 – 44	SILICA	30	0.005	PP	24	72
30	FT-300	265	—	—	—	0.0	PP	0	12
31	FT-300	265	—	—	—	0.005	PP	6	18
32	FT-300	265	—	—	—	0.02	PP	12	24
33	FT-300	265	20 – 44	IRON OX	20	0.0	PP	18	48
34	FT-300	265	20 – 44	IRON OX	20	0.005	PP	24	54
35	FT-300	265	20 – 44	IRON OX	20	0.005	BC	30	78

Note: Horizontal lines separate batches
TOS – Time on stream
TIME HOT – Total time heated
PP – Perforated plate distributor
BC – Bubble cap distributor

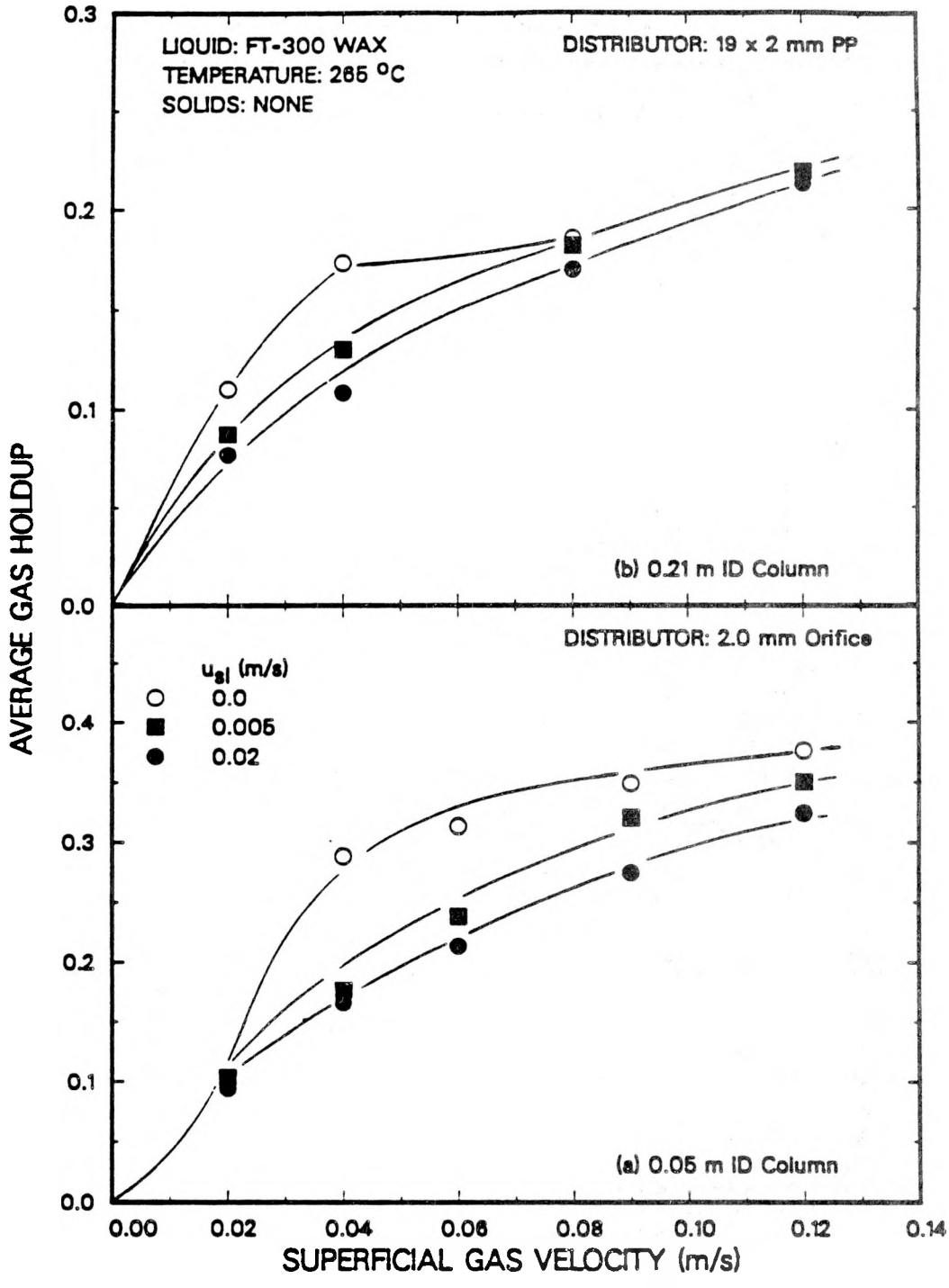

Figure 2.13. Effect of superficial slurry velocity on average gas holdup in the (a) small and (b) large diameter columns with FT-300 wax.

the difference in gas holdup between the batch experiment (i.e. $u_{s\ell}$=0.0 m/s) and the continuous experiments decreases. At a gas velocity of 0.02 m/s, the holdups from all three runs were similar (see Figure 2.13a). At this gas flow rate, the homogeneous bubbling regime exists, and one would expect holdups to be similar for all three slurry velocities.

Foam was also observed during the batch experiment in the large diameter column at a gas velocity of 0.04 m/s (see Figure 2.13b). At this gas velocity (i.e. 0.04 m/s), the amount of foam produced in the large diameter column was less than the amount of foam produced in the small diameter column (i.e. the gas holdup was 0.18 in the large diameter column as opposed to 0.29 in the small diameter column). Gas holdups during the continuous experiments at u_g = 0.04 m/s were lower than the gas holdups at this velocity during the batch experiment. Only a marginal decrease in gas holdup was observed when the slurry flow rate was increased from 0.005 to 0.02 m/s. At gas velocities of 0.08 and 0.12 m/s gas holdups from all three experiments were similar. At a gas velocity of 0.02 m/s, the gas holdup associated with the batch experiment was slightly higher than those from the continuous experiment. This was due to a slight increase in the gas holdup during the batch experiment in uppermost section of the column at this velocity (see Figure 2.14b).

Axial gas holdup profiles at gas velocities of 0.02, 0.04, and 0.12 m/s, from the batch experiments in the 0.05 and 0.21 m diameter columns are shown in Figures 2.14a and 2.14b, respectively. At a gas velocity of 0.02 m/s, axial gas holdup profiles in both columns are nearly uniform; however, at a gas velocity of 0.04 m/s, there is a significant increase in the gas holdup between heights of 1.5 and 2.2 m above the distributor (i.e. in the small diameter column the gas holdup increases from 0.17 to 0.64 and in the large diameter column, the gas holdup increases from 0.16 to 0.28). This increase in gas holdup indicates the presence of a foam layer at the top of the dispersion. The

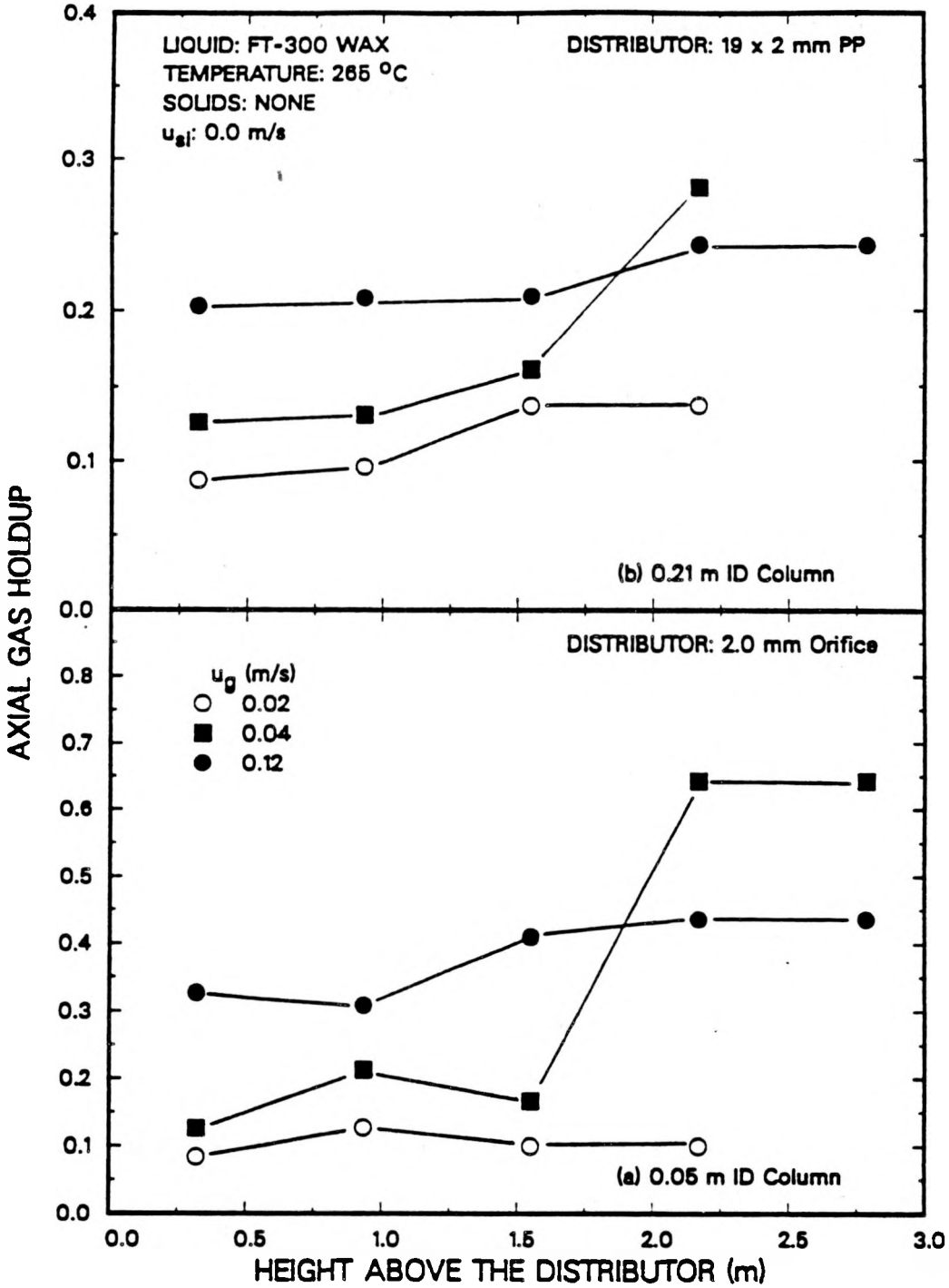

Figure 2.14. Effect of superficial gas velocity on axial gas holdup in the (a) small and (b) large diameter columns with FT-300 wax.

amount of foam present in the large diameter column at a gas velocity of 0.04 m/s was substantially less than the amount of foam present in the small diameter column at this gas velocity. The difference in the amount of foam produced in the two columns is due to differences in the flow patterns present in the two columns at this gas velocity. Liquid circulation patterns develop in the large diameter column at a gas velocity of 0.04 m/s which help break up the foam. At a gas velocity of 0.12 m/s, the gas holdup in the uppermost region of both columns was lower than that observed at a gas velocity of 0.04 m/s (see Figures 2.14a and 2.14b). Also, the gas holdup profile along the column height was fairly uniform in both columns. This indicates that the foam layer which was present in both columns at a gas velocity of 0.04 m/s had dissipated. Figure 2.15 compares axial gas holdup profiles at slurry velocities of 0.0, 0.005, and 0.02 m/s in the small diameter column. At a gas velocity of 0.02 m/s (Figure 2.15a) axial gas holdup profiles are similar for all slurry flow rates. At a gas velocity of 0.04 m/s there is a significant difference in the gas holdup profiles in the uppermost section of the column (i.e. at a height greater than 1.5 m above the distributor; see Figure 2.15b) between experiments conducted in the continuous mode of operation and the experiment conducted in the batch mode of operation. In the lower section of the column (i.e. <2.2 m above the distributor), the holdups from all three experiments are similar. This, shows that in the absence of foam, there is very little effect of liquid flow rate on gas holdup. Also, this substantiates the claim that a slight upward liquid flow rate is sufficient to dissipate the foam layer. At a gas velocity of 0.12 m/s (Figure 2.15c), we once again observe similar axial gas holdup profiles at all slurry flow rates. However, axial gas holdups are consistently lower at a slurry velocity of 0.02 m/s.

Experiments were conducted in both columns with FT–300 wax to study the effect of slurry flow rate on average gas holdup in three–phase systems. Results similar to those with FT–300 wax (no solids) were obtained (i.e. an increase in slurry flow rate

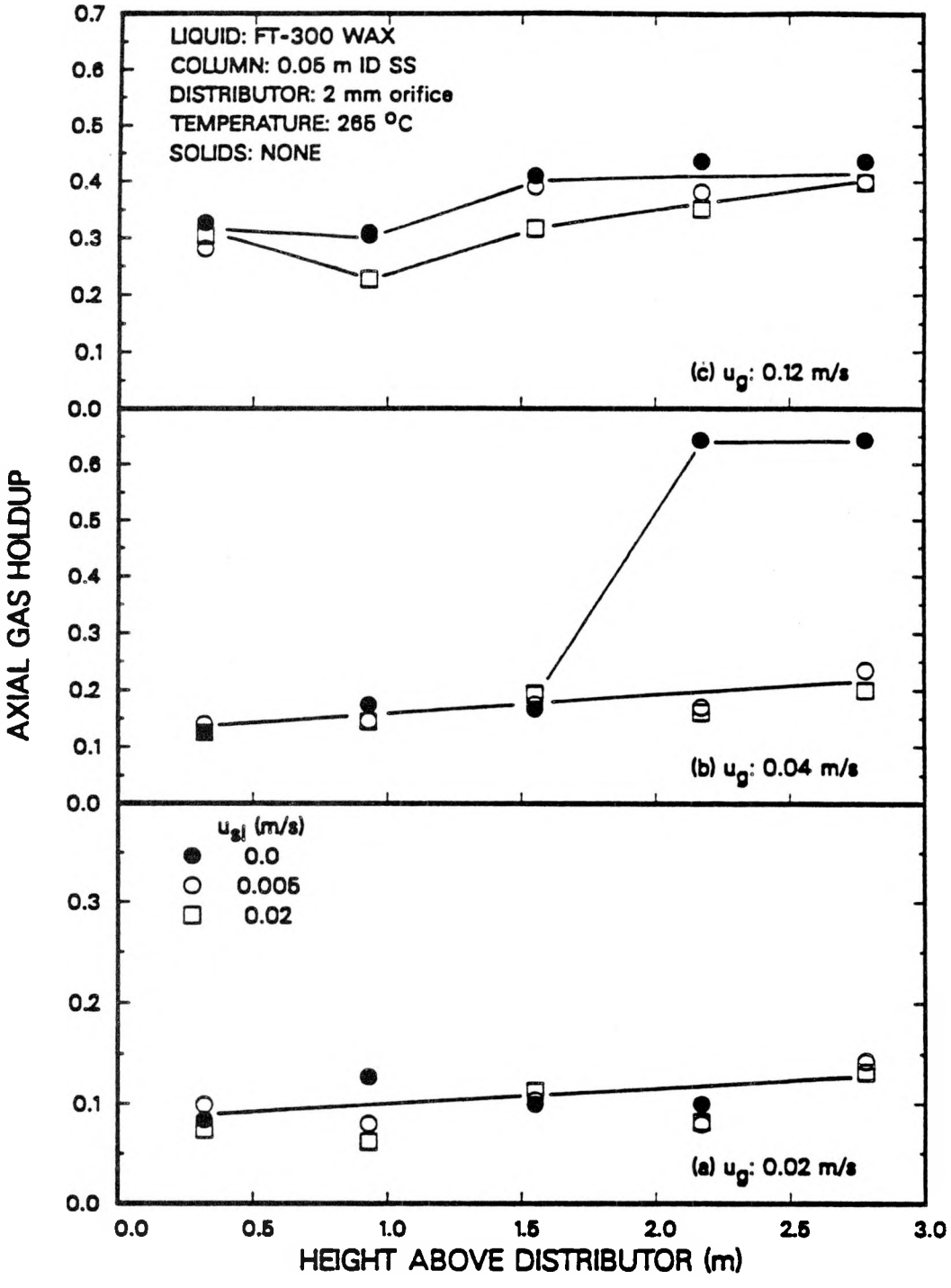

Figure 2.15. Effect of superficial slurry velocity on axial gas holdup in the small diameter column with FT-300 wax.

causes a decrease in gas holdup when foam is present). Figure 2.16 shows results for experiments in the 0.05 m ID column with 20 wt% slurries of 0 – 5 μm iron oxide (Figure 2.16a) and 0 – 5 μm silica particles (Figure 2.16b). For these systems, gas holdups from experiments conducted in the batch mode of operation were consistently higher than those obtained from experiments conducted in the continuous mode of operation. A substantial decrease in holdup was observed when the slurry velocity was increased from 0.0 to 0.005 m/s. This decrease in gas holdup with increasing slurry velocity is due to the dissipation of the foam present in batch experiments. Similar trends were observed for 10 and 30 wt% slurries of 0 – 5 μm iron oxide particles.

Results from experiments in the large diameter column, with 20 – 44 μm iron oxide particles are shown in Figure 2.17. During the batch experiment, foam was produced at a gas velocity of 0.04 m/s. Increasing the slurry velocity to 0.005 m/s decreased the gas holdup (i.e. $\epsilon_g = 0.28$ for $u_\ell = 0$ and 0.11 for u_ℓ=0.005) at a gas velocity of 0.04 m/s. In the absence of foam (i.e. $u_g = 0.08$ and 0.12 m/s), there is not a significant effect of slurry flow rate on gas holdup.

Thus, gas holdup decreases with increasing slurry velocity for experiments conducted with FT–300 wax (with and without solids) in the 0.05 and 0.21 m ID columns. The decrease in holdup with increasing slurry flow rate is most pronounced at gas velocities which favor the formation of foam. In the absence of foam, the effect of slurry flow rate on gas holdup is negligible.

Results from experiments with SASOL wax (no solids) in the 0.05 and 0.21 m ID columns are shown in Figures 2.18a and 2.18b, respectively. SASOL wax behaves quite differently from FT–300, i.e. it does not have a tendency to foam. An increase in slurry flow rate from 0.0 to 0.005 m/s caused a slight decrease in gas holdup in both columns (see Figures 2.18a and 2.18b). This behavior (i.e. negligible effect of $u_{s\ell}$ on ϵ_g) is consistent with that observed in experiments with FT–300 wax in the absence of foam.

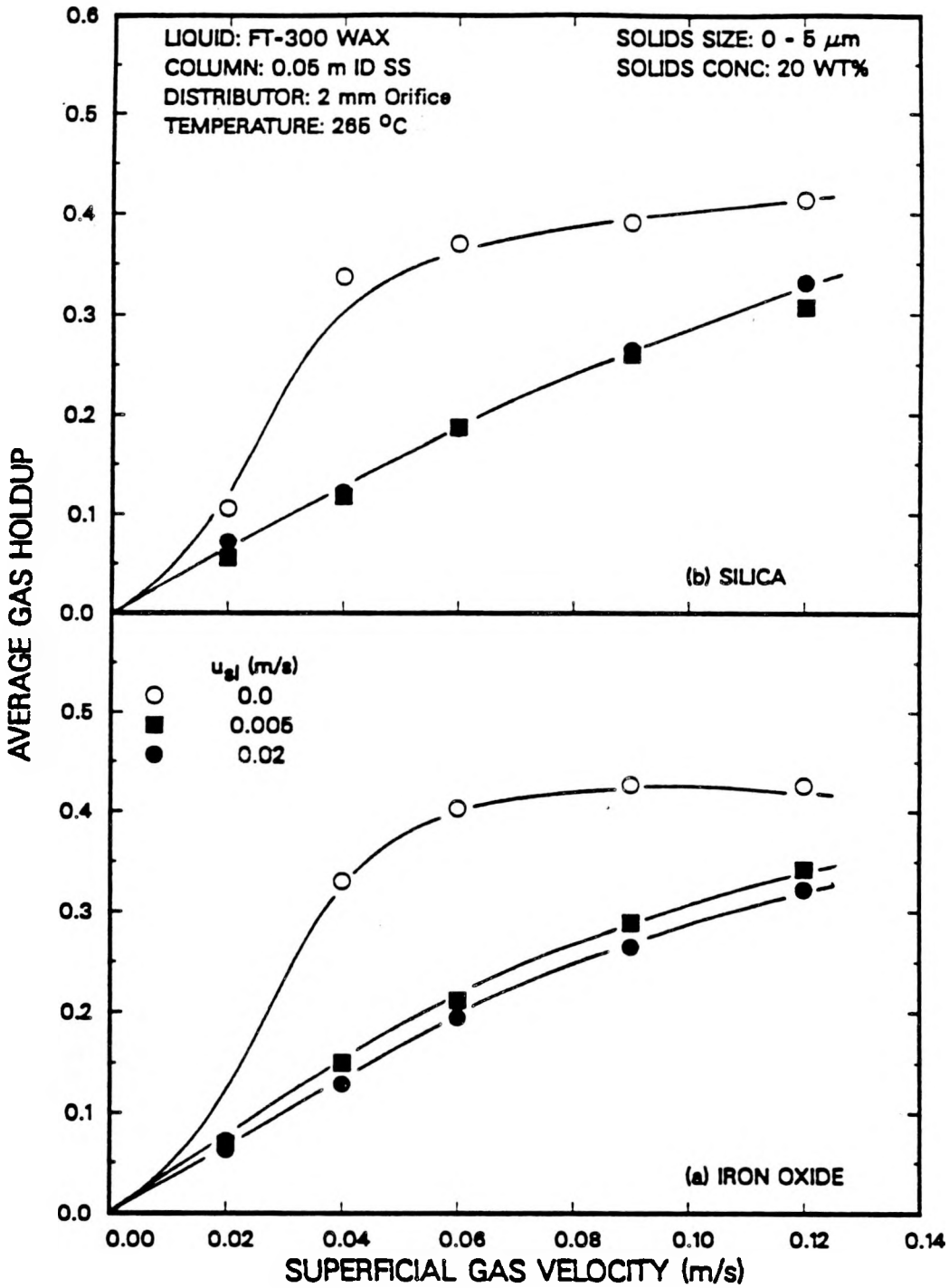

Figure 2.16. Effect of superficial slurry velocity on average gas holdup in the small diameter column with FT-300 wax in the presence of solids; (a) 0 - 5 μm iron oxide; (b) 0 - 5 μm silica.

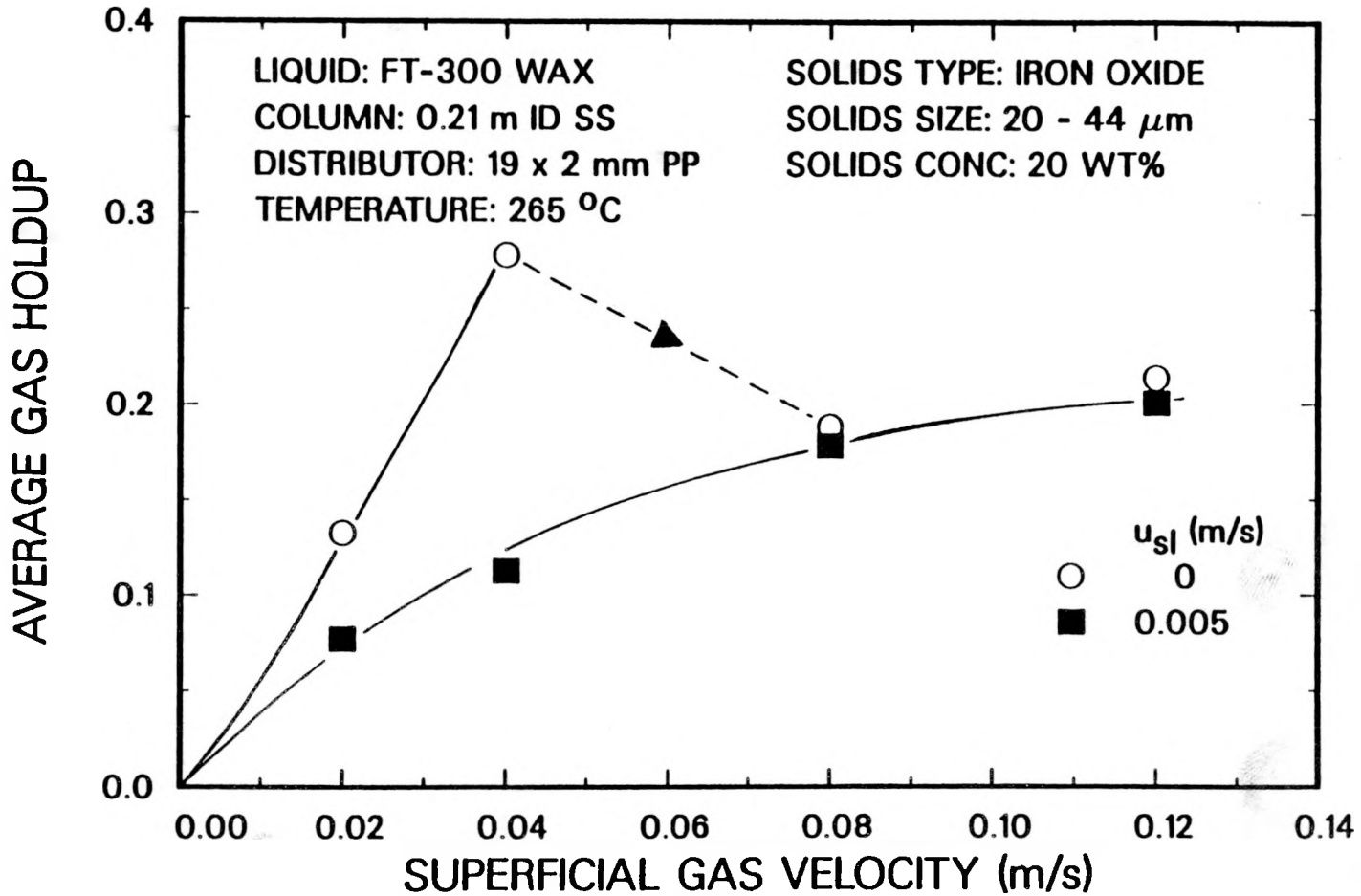

Figure 2.17. Effect of superficial slurry velocity on average gas holdup in the large diameter column with FT-300 wax (20 - 44 μm iron oxide).

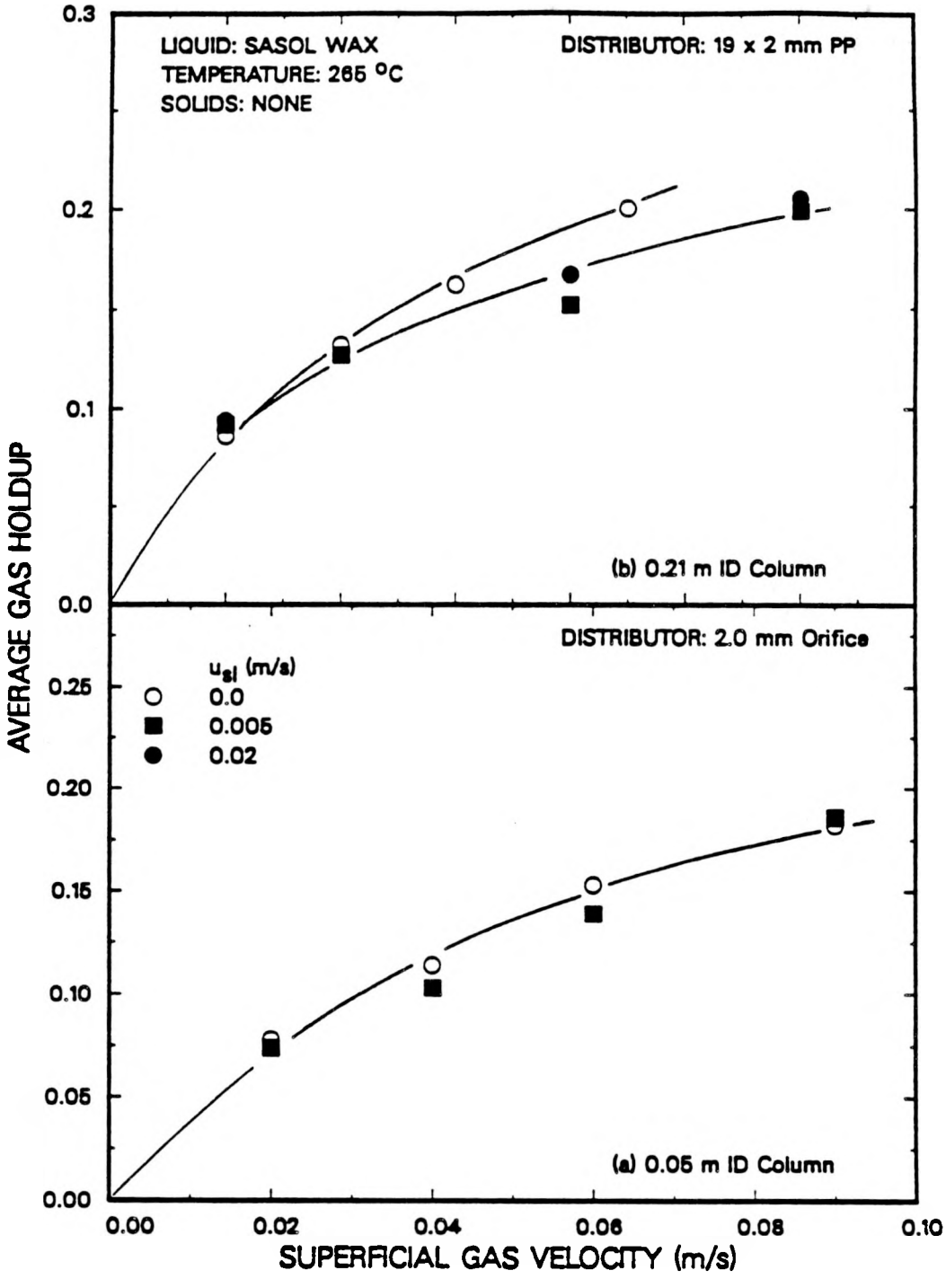

Figure 2.18. Effect of superficial slurry velocity on average gas holdup in the (a) small and (b) large diameter columns with SASOL wax.

Gas holdup results from three–phase experiments with SASOL reactor wax in the large diameter column are shown in Figure 2.19. There was no significant effect of slurry flow rate on average gas holdups for experiments with 0 – 5 μm and 20 – 44 μm iron particles (see Figures 2.19a and 2.19b, respectively). Results from the experiments conducted with 20 – 44 μm silica particles are shown in Figure 2.19c. During these experiments, the gas holdup decreased slightly with increasing slurry flow rate.

The trends observed in this study in the continuous mode of operation are in qualitative agreement with results from other studies. Studies with systems which do not foam (e.g., water – air) indicate that slurry (or liquid) velocity either has no effect on gas holdup (e.g., Akita and Yoshida, 1974; Shah et al., 1982), or decreases holdup only slightly (e.g., Kara et al., 1982; Buchholz et al., 1983; Kelkar et al., 1984; Ouyang and Tatterson, 1987). However, for systems which foam, gas holdup decreases markedly with increasing slurry velocity (e.g. Shah et al., 1985; Kelkar et al., 1983). For example, Shah et al. reported holdup values as high as 80 % with an aqueous ethanol solution at a superficial gas velocity of 0.20 m/s in the batch mode of operation; however, upon increasing the slurry flow rate to 0.0077 m/s, the gas holdup dropped to approximately 20 %.

Effect of Solids Concentration

The effect of solids concentration (iron oxide) on gas holdup in the 0.05 m (d_p = 0 – 5 μm) and 0.21 m ID (d_p = 20 – 44 μm) bubble columns with FT–300 wax as the liquid medium is shown in Figures 2.20a and 2.20b, respectively. Gas holdups in the small diameter column are highest for a solids concentration of 20 wt% at gas velocities greater than 0.02 m/s. At a solids concentration of 30 wt% the gas holdup values are lower than those for a 20 wt% slurry; however, the holdups are still higher than those with no solids present. In the large diameter column, gas holdups increased

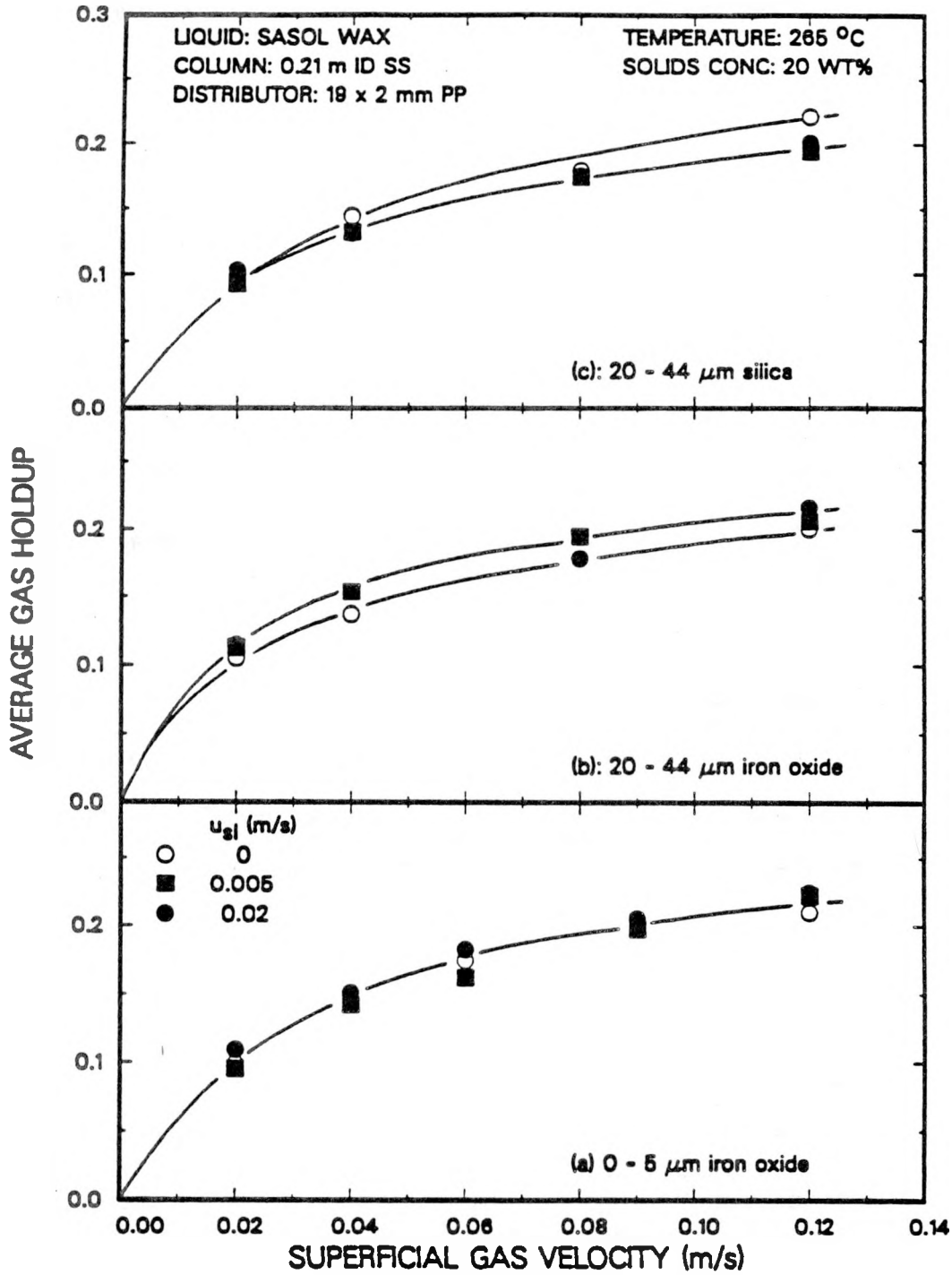

Figure 2.19. Effect of slurry velocity on average gas holdup in the large diameter column with SASOL wax ((a) 0 - 5 μm iron oxide, (b) 20 - 44 μm iron oxide, (c) 20 - 44 μm silica).

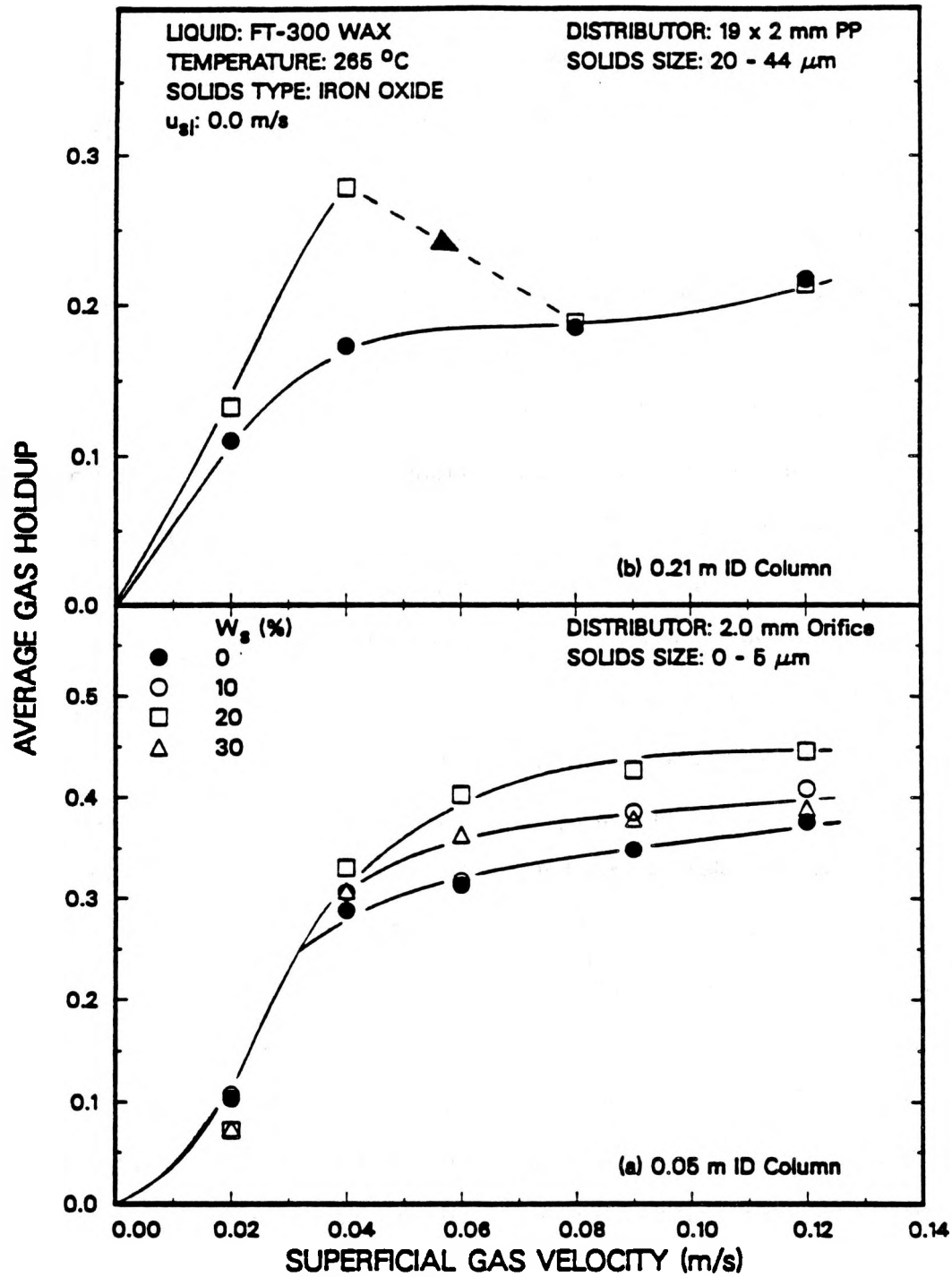

Figure 2.20. Effect of solids concentration on average gas holdup with FT-300 wax ((a) 0.05 m ID Column, 20 WT%, 0 - 5 μm iron oxide; (b) 0.21 m ID Column, 20 WT%, 20-44 μm iron oxide).

at gas velocities of 0.02 and 0.04 m/s with the addition of solids, but at gas velocities of 0.08 and 0.12 m/s, there was no effect of solids concentration on gas holdup.

Figure 2.21 shows axial gas holdup profiles at gas velocities of 0.02, 0.04, and 0.12 m/s for the four experiments conducted in the batch mode of operation with 0 – 5 μm iron oxide particles in the small diameter column. At a gas velocity of 0.02 m/s (Figure 2.21a), there was no consistent effect of solids concentration. However, at gas velocities of 0.04 and 0.12 m/s (Figures 2.21b and 2.21c, respectively), a definite trend exists in the uppermost sections of the column (i.e. above a height of 1.5 m above the distributor). The holdup in the presence of solids is consistently higher than that in the absence of solids. Also, the holdup increases with increasing concentration of solids up to a concentration of 20 wt %. Upon increasing the concentration of solids further (i.e. to 30 wt%), the holdup in the uppermost section of the column decreases.

Experiments were also conducted in the batch mode of operation with 20 wt% slurries of 20 – 44 μm iron oxide particles and 0 – 5 μm silica particles in the small diameter column. Average gas holdups from these experiments together with the experiment conducted without solids is shown in Figure 2.22. Once again, the gas holdup increased with the addition of both large iron oxide particles (Figure 2.22a) and small silica particles (Figure 2.22b).

As described below, the opposite trends were reported in the literature for the effect of solids concentration on gas holdup. In some studies, it was observed that gas holdup decreases with the addition of solids. This decrease in gas holdup was usually attributed to an increase in the slurry viscosity. Other investigators have found that when relatively small particles or low density particles are used, the addition of solids may cause the gas holdup to increase. In general, it was claimed that the increase in gas holdup is due to poor wettability of the solids.

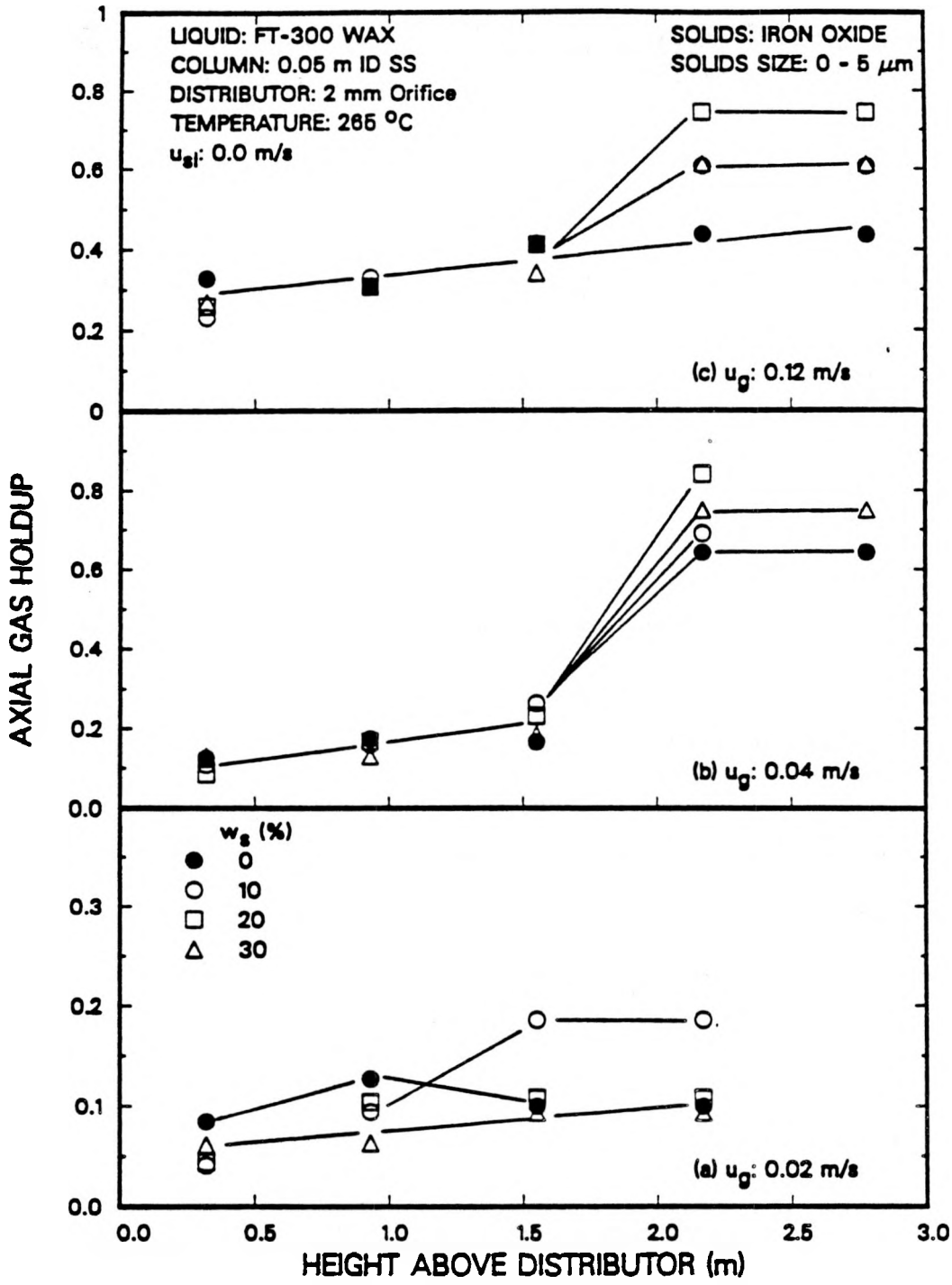

Figure 2.21. Effect of solids concentration and superficial gas velocity on axial gas holdup in the 0.05 m ID column with FT-300 wax (0 - 5 μm iron oxide particles; (a) u_g=0.02 m/s; (b) u_g=0.04 m/s; (c) u_g=0.12 m/s).

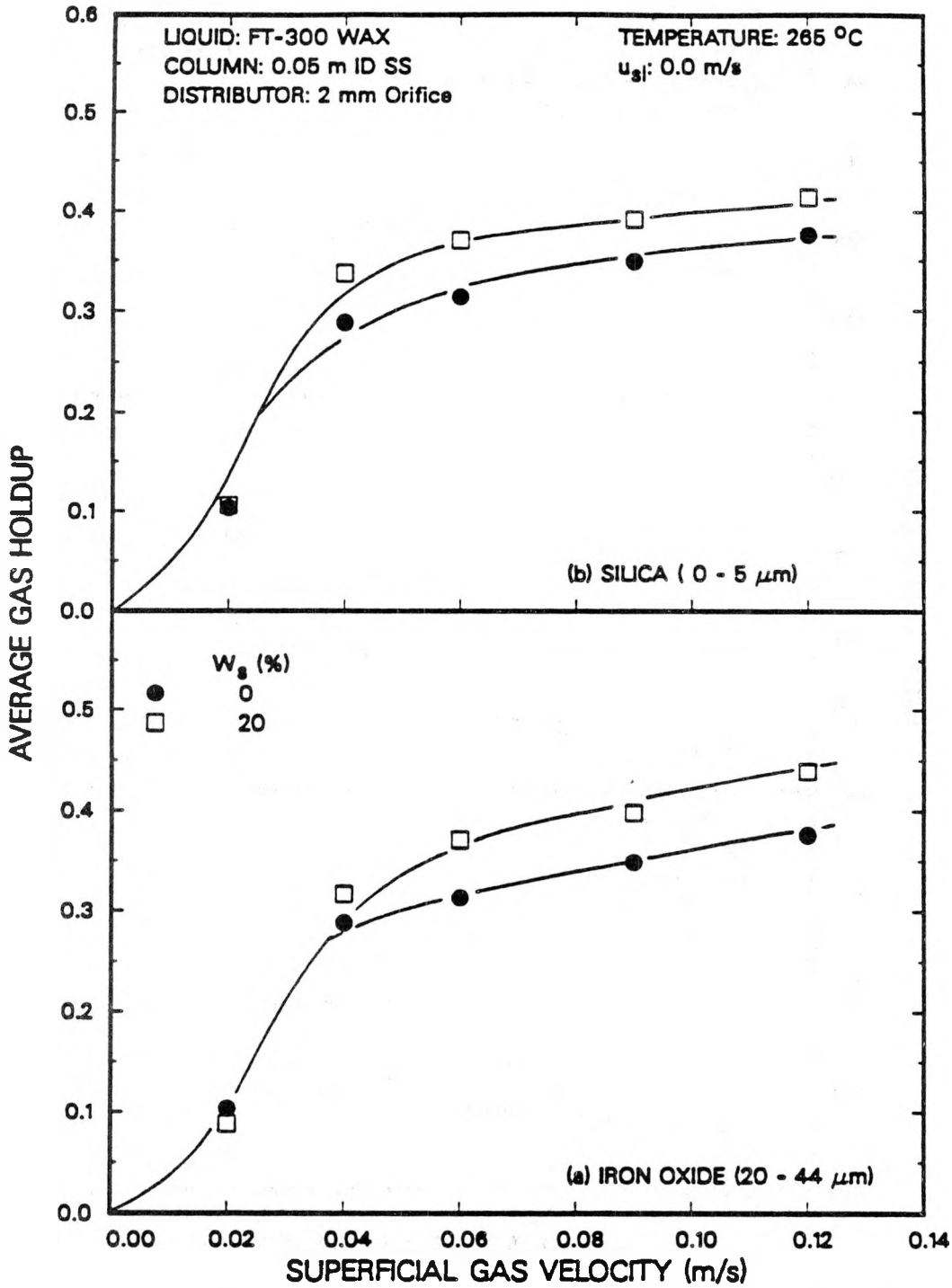

Figure 2.22. Effect of solids concentration on average gas holdup in the 0.05 m ID column with FT-300 wax ((a) 20 - 44 μm iron oxide; (b) 0 - 5 μm silica)

Deckwer et al. (1980) studied the effect of solids concentration (up to 16 wt%) in a paraffin wax/Al_2O_3/ nitrogen system. The solids were 0 – 5 μm in diameter. Their results, limited to low gas flow rates (u_g <0.04 m/s), showed that the addition of solids reduces gas holdup slightly ($\Delta\epsilon_g = 0.01$ to 0.02). However, they did not observe any specific trend in terms of the effect of solids concentration in the range 5.5 to 16 wt% on gas holdup. Ying et al. (1980) and Kato et al. (1972) also reported a decrease in gas holdup with increasing solids concentration. Kara et al. (1982) used various coal/water slurries with coal particles ranging from 10 to 70 μm in diameter, and solids loadings up to 44 wt%. In general, they observed a decrease in gas holdup with increasing solids concentration. However, with 10 μm particles, they observed a slight increase in gas holdup values relative to experiments conducted without solids. They postulated that the observed increase in gas holdup might be due to poor wettability. Results obtained from several other investigators show that the addition of solids increases gas holdup. Sada et al. (1986) examined the effect of fine particles (Al_2O_3 and $CaCO_3$) in both an electrolyte solution and in distilled water. Solids concentrations up to 1 wt% were used. Results from their study indicate that gas holdup decreases with the addition of solid particles ($d_p > 50$ μm). However, for particles less than 10 μm in diameter, in low concentrations, the gas holdup increases. They attributed this increase in gas holdup to the bubble coalescence hindering action of fine solids dispersed in the liquid film around the bubbles. They also observed, that the increase in gas holdup was more pronounced for systems which produce very fine bubbles. The effect of solids concentration and type was also studied by Sauer and Hempel (1987). They observed an increase in gas holdup with increasing solids concentrations (up to 13 wt%) for particles with densities less than 1300 kg/m^3 and superficial gas velocities in the range 0.01 to 0.04 m/s. They explained their results by using the qualitative model of Rabiger (1985). According to Rabiger, there exists an optimum ratio between the particle diameter

and microscale of turbulence which depends on density, particle shape and structure of liquid turbulence. Upon reaching the optimum ratio, the turbulence associated with the three–phase system is greater than that with the two–phase system, and as a result, smaller bubbles are produced and this gives rise to higher gas holdups. This increase in turbulence is only possible up to certain values of gas holdups and solids concentrations because the distances between bubbles and particles become very small in the swarm. Thus, on exceeding certain values, the turbulence subsides, resulting in larger bubbles and consequently lower holdups.

The increase in gas holdup with the addition of solids which we observed during experiments conducted in the batch mode of operation with FT–300 wax may be attributed to poor solids wettability in the region of high gas holdup (i.e. at heights greater than 1.5 m above the distributor). Bhatia et al. (1972) have shown that non-wettable particles cause an increase in bed expansion in a three–phase fluidized bed. They attributed the increase in bed expansion to solid particles adhering to the surface of the large fast rising gas bubbles and being carried upward through the column. In our case, we have relatively high density particles (ρ_s = 2650 and 5100 kg/m^3) and very small, slow rising gas bubbles (see Chapter V). Thus, when particles adhere to the surface of these small bubbles, they not only reduce coalescence, but they also reduce the effective rise velocity of the gas bubble, which results in a longer residence time. This in turn causes an increase in the gas holdup. In the lower portion of the column (i.e. below the foam layer), gas holdups are substantially lower than they are in upper portion of the column (see Figure 2.21). Figure 2.23 shows average gas holdups, excluding foam (i.e. neglecting axial gas holdups at heights of 2.2 and 2.8 m above the distributor when calculating the average gas holdup), for experiments conducted with small iron oxide particles in the 0.05 m ID column. As can be seen, there is a slight decrease in gas holdup with increasing solids concentration when the foam is neglected.

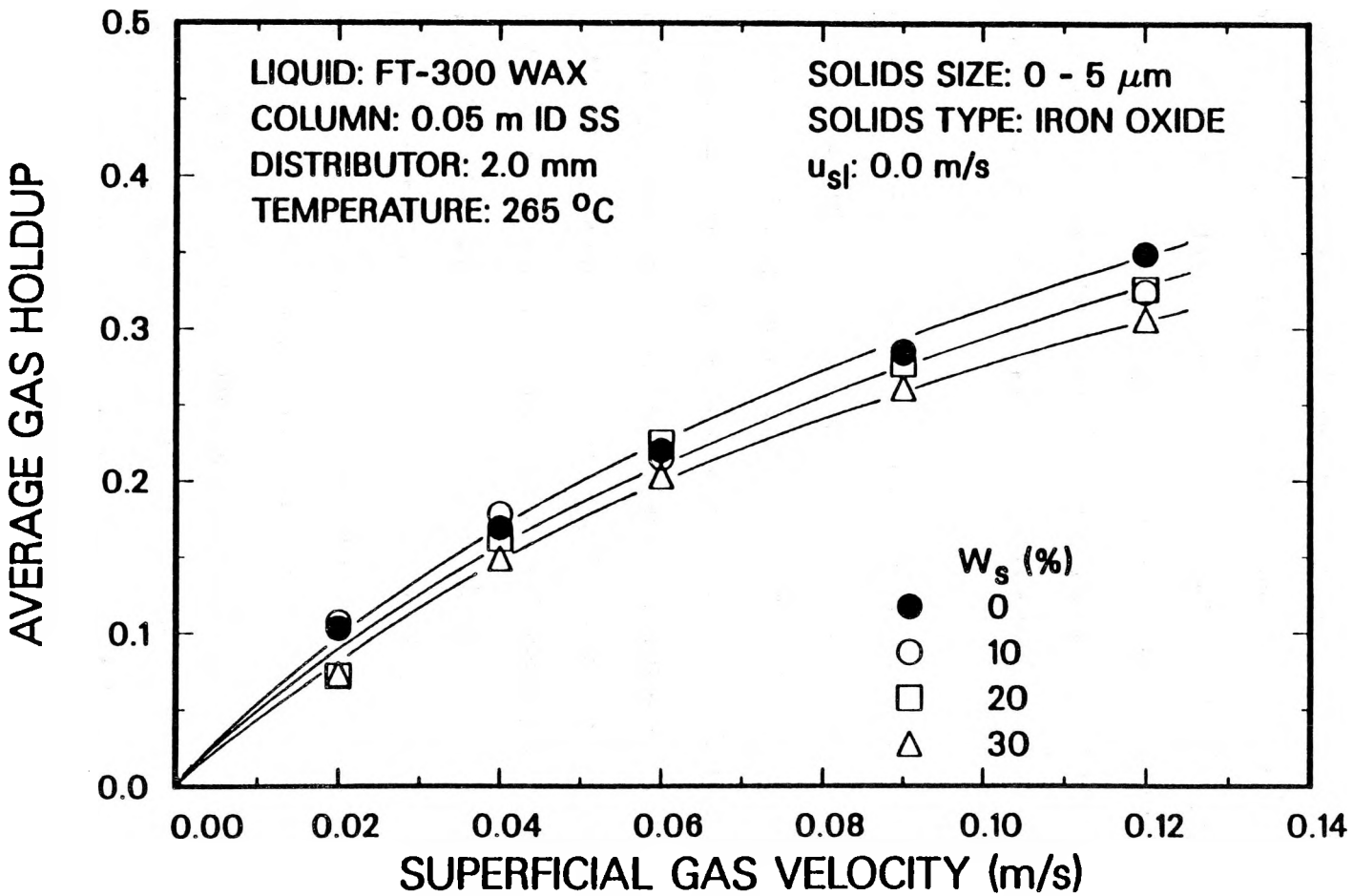

Figure 2.23. Effect of solids concentration on average gas holdup neglecting foam (0 - 5 μm iron oxide).

This decrease in gas holdup with increasing solids concentration may be attributed to an increase in the apparent viscosity of the slurry. It has been shown that an increase in slurry viscosity produces larger bubbles which in turn reduces the gas holdup (Bukur et al., 1987a). Thus, the variation in the effect of solids concentration on gas holdup may be due to: (1) poor wettability of solids, and (2) an increase in the slurry viscosity with the addition of solids. The former causes the gas holdup to increase, while the latter causes the gas holdup to decrease. These competing phenomena might be responsible for the maximum in gas holdup observed with the 20 wt% slurry of small iron oxide particles.

Some experiments were also conducted with FT–300 wax in the continuous mode of operation to determine the effect of solids concentration on average gas holdup. Figures 2.24a and 2.24b show results from experiments conducted with iron oxide particles (0 – 5 μm) in the small diameter column using slurry velocities of 0.005 and 0.02 m/s, respectively. The average gas holdup decreased with increasing solids concentration for experiments conducted in the continuous mode of operation. Thus, it appears that a small upward liquid flow is sufficient to disperse the fine bubbles at the top of the dispersion, and as a result, the adhesion of the solid particles to the liquid film of the bubbles comprising the foam no longer has a significant effect on the gas holdup. The decrease in gas holdup is due solely to the increase in slurry viscosity associated with the addition of solids. Similar results were observed for experiments with small silica silica particles in the 0.05 m ID column and with large iron oxide particles in the 0.21 m ID column at a slurry velocity of 0.005 m/s (see Figures 2.25a and 2.25b, respectively).

Gas holdups from batch experiments with SASOL reactor wax in the 0.05 m ID column with 20 – 44 μm iron oxide particles and in the 0.21 m ID column with both 20 – 44 and 0 – 5 μm iron oxide particles are shown in Figure 2.26. The trends were qualitatively similar to those observed in experiments with FT–300 wax in the presence

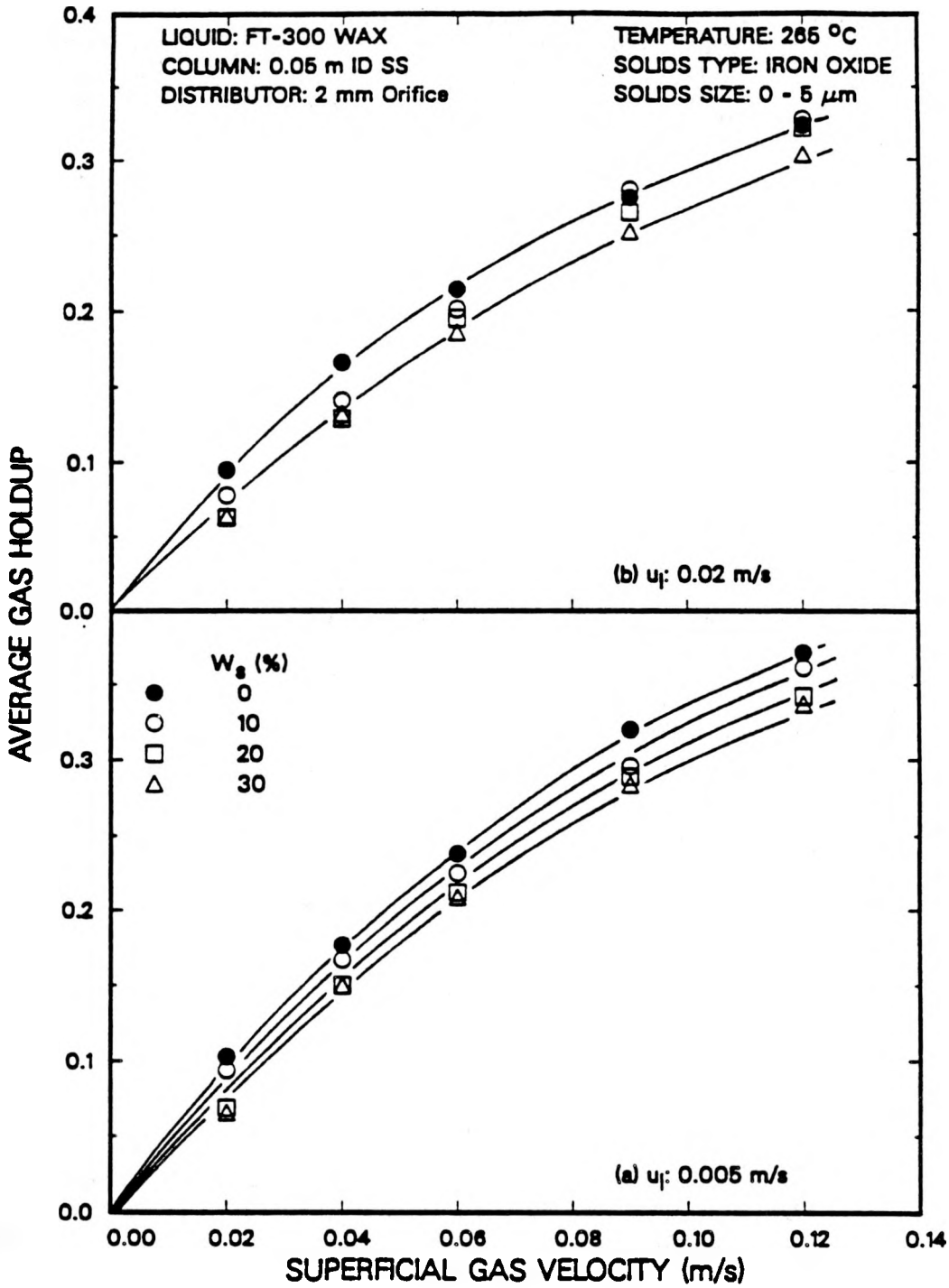

Figure 2.24. Effect of solids concentration on average gas holdup in the continuous mode of operation with FT-300 wax (0 - 5 μm iron oxide; (a) u_{sl} = 0.005 m/s; (b) u_{sl} = 0.02 m/s).

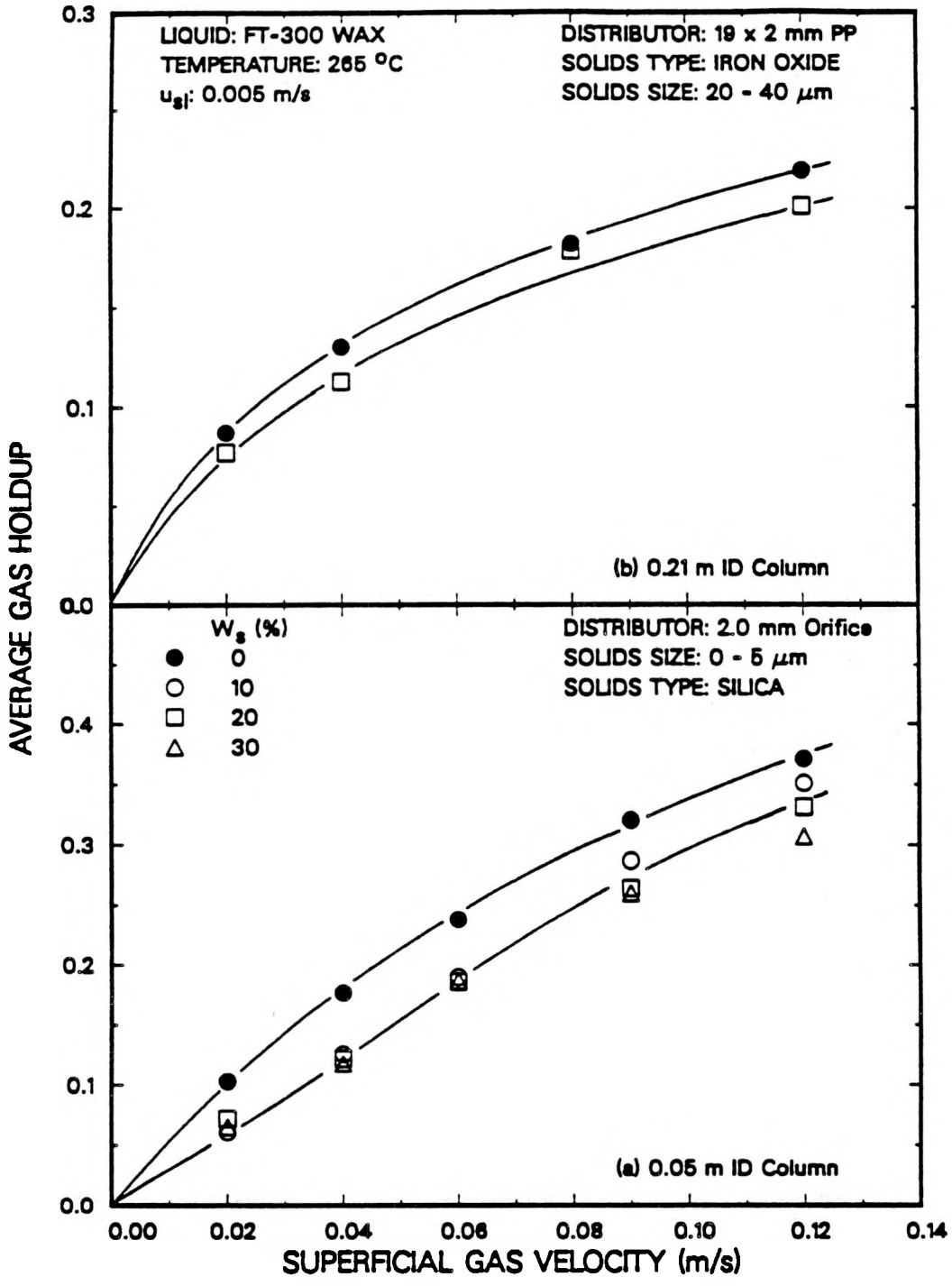

Figure 2.25. Effect of solids concentration on average gas holdup with FT-300 wax ((a) 0.05 m ID column, 0 - 5 μm silica; (b) 0.21 m ID column, 20 - 44 μm iron oxide).

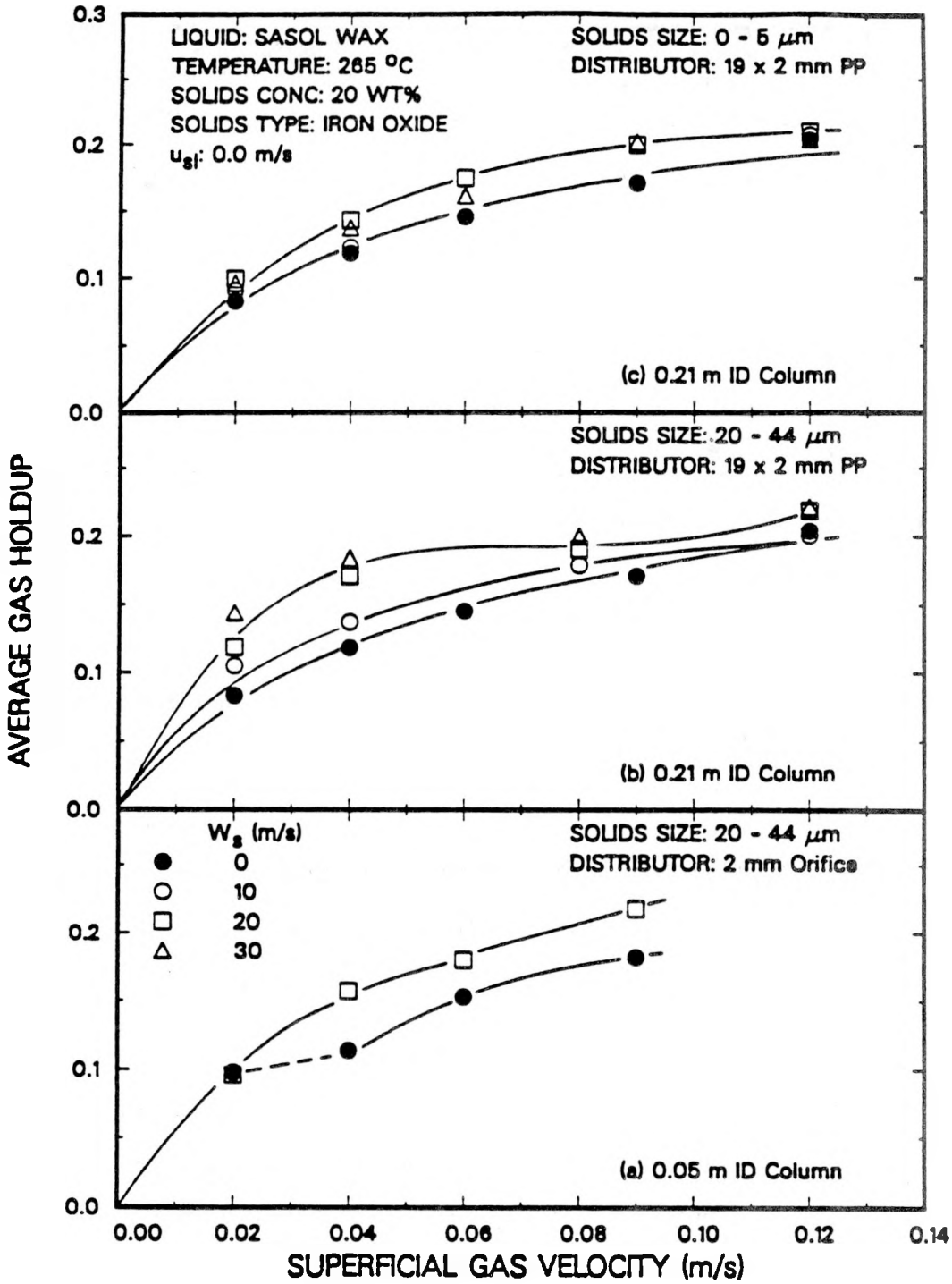

Figure 2.26. Effect of solids concentration on average gas holdup with SASOL wax ((a) 0.05 m ID column, 20 - 44 μm iron oxide, (b) 0.21 m ID column, 20 - 44 μm iron oxide, (c) 0.21 m ID column, 0 - 5 μm iron oxide).

of solids (i.e. the addition of solids caused an increase in gas holdup). These results were somewhat surprising since SASOL wax does not produce foam. Since we observed a decrease in gas holdup with the addition of solids in the absence of foam with FT–300 wax (see Figures 2.23 and 2.24), we expected gas holdups with SASOL reactor wax to decrease with increasing solids concentration. However, the solids used in this study may be less wettable in SASOL wax as compared to FT–300 wax, and as a result the holdups increased. One indication of this is the fact that the holdup in the uppermost section of the small diameter column increased by 50 to 70 % (relative) with the addition of large iron oxide particles for the experiment with SASOL wax, but increased only by 30 to 50 % (relative) for the experiment conducted with FT–300 wax.

Experiments were also conducted with SASOL wax in the continuous mode of operation. The addition of solids increased the gas holdup for experiments in both the small and large diameter columns. Figure 2.27a shows results from experiments conducted with small iron oxide particles in the 0.05 m ID column. Results from experiments conducted with various concentrations of large iron oxide particles and various concentrations of small iron oxide particles are shown in Figures 2.27b and 2.27c respectively. Gas holdups increased with increasing solids concentration. Holdup values from experiments in the large diameter column approached the same value at superficial gas velocities greater than 0.08 m/s. A similar trend was observed during batch experiments in the large diameter column (see Figures 2.26b and 2.26c).

Similar results were observed for experiments conducted with silica particles in the large diameter column; however, the increase in gas holdup with increasing solids concentration was less pronounced. The convergence of gas holdup values at high gas velocities for various slurry concentrations in the large diameter column is due to an increase in turbulence. Turbulence is greater in the large diameter column than the small diameter column (i.e. the flow patterns present in the large diameter column are

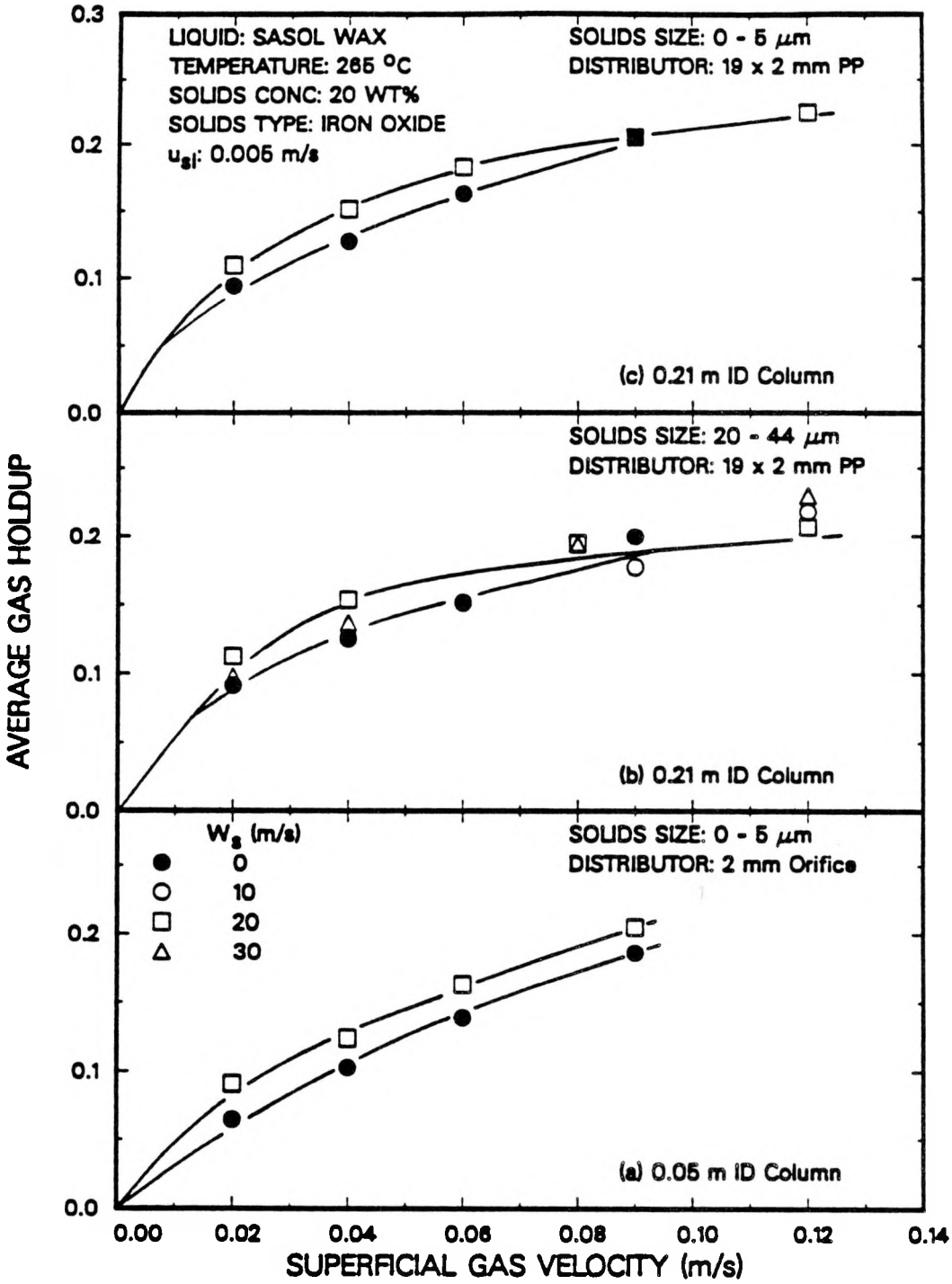

Figure 2.27. Effect of solids concentration on average gas holdup with SASOL wax in the continuous mode of operation ((a) 0.05 m ID column, 20 - 44 μm iron oxide, (b) 0.21 m ID column, 20 - 44 μm iron oxide, (c) 0.21 m ID column, 0 - 5 μm iron oxide).

much more chaotic). Therefore, at high superficial gas velocities, any particles which may adhere to the surface of gas bubbles are likely to be stripped away, and as a result, gas holdups in the presence of solids become similar to those in the absence of solids.

Thus, the addition of solids increases gas holdup for experiments conducted in the batch mode of operation with both FT–300 and SASOL reactor wax. However, in the continuous mode of operation, addition of solids to FT–300 wax causes a slight decrease in the gas holdup; whereas, addition of solids to SASOL wax causes a slight increase in the gas holdup. The differences in the behavior of the two waxes might be due to differences in the wettability of the particles with respect to each wax type.

Effect of Solids Type and Size

The effect of solids type and size for batch experiments with FT–300 wax in the small diameter column are shown in Figure 2.28. The highest holdups were obtained in experiments with small iron oxide particles. Gas holdups from experiments with large iron oxide particles and small silica particles were similar. An increase in gas holdup with increasing particle size has been observed in some earlier studies (Kim et al., 1977, Shah et al., 1982). A possible explanation for this is that the particles are breaking up the bubbles as they rise through the column, thus producing smaller bubbles and consequently higher gas holdups. Kim et al. showed that when solids have sufficient kinetic energy, they can cause bubble breakage which results in an increase in gas holdup. Using a balance between the surface tension forces of the bubble, and the force exerted by the particle, their proposed criterion for bubble breakage is:

$$We = \frac{\rho_p u_r^2 d_p}{\sigma_\ell} > 3 \qquad (2.28)$$

For the system in our study, the Weber number, We, has a maximum value of 1.5 and is obtained for large iron oxide particles suspended in FT–300 wax at u_g=0.12 m/s.

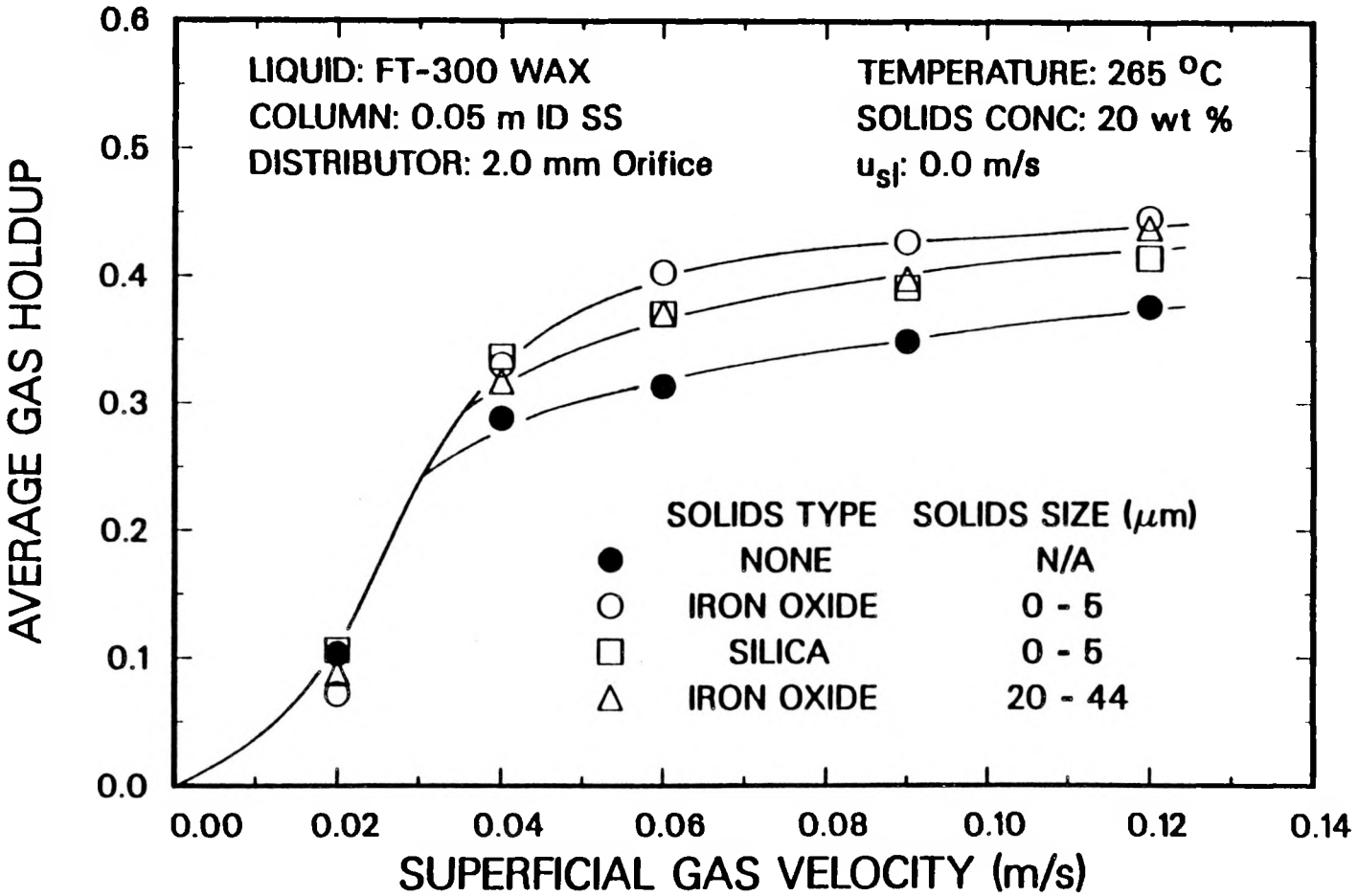

Figure 2.28. Effect of solids type and size on average gas holdup in the 0.05 m ID column with FT-300 wax.

Thus, we can assume that with our particles, no bubble breakage is occurring due to the presence of solids.

One possible explanation for the decrease in gas holdup with increasing particle size that was observed, might be due to the non–uniformity in the axial solids distribution of large particles. For the experiment conducted with small iron oxide particles, the solids concentration remains axially uniform ($\approx$ 20 wt%); however, in experiments with large iron oxide particles, the solids concentration at the bottom of the column ranged from 30 to 35 wt% (see the Figure on page 208). This increase in solids concentration at the bottom of the column results in a higher apparent slurry viscosity near the orifice plate. As a result, larger bubbles may be formed in the region near the distributor which results in lower gas holdups.

Figure 2.29 shows results for experiments conducted in the batch mode of operation with 30 wt % small iron oxide, 20 wt% small silica, and 20 wt% large iron oxide slurries. The gas holdups from all three runs are similar. All three experiments had similar volume concentrations of solids near the distributor (i.e. $\approx$ 0.045). These results indicate that the volume concentration of solids near the distributor may be important in determining the gas holdup. Similar results were observed for experiments conducted in the continuous mode of operation with small iron oxide and silica particles.

The effect of solids type and size for experiments with 20 wt% slurries (SASOL wax) in the large diameter column is shown in Figures 2.30a and 2.30b for experiments conducted in the batch and continuous modes of operation, respectively. Gas holdups were similar for batch experiments with small iron oxide particles and large iron oxide and silica particles. In the continuous mode of operation, there is no discernible effect of either solids type or size on gas holdup.

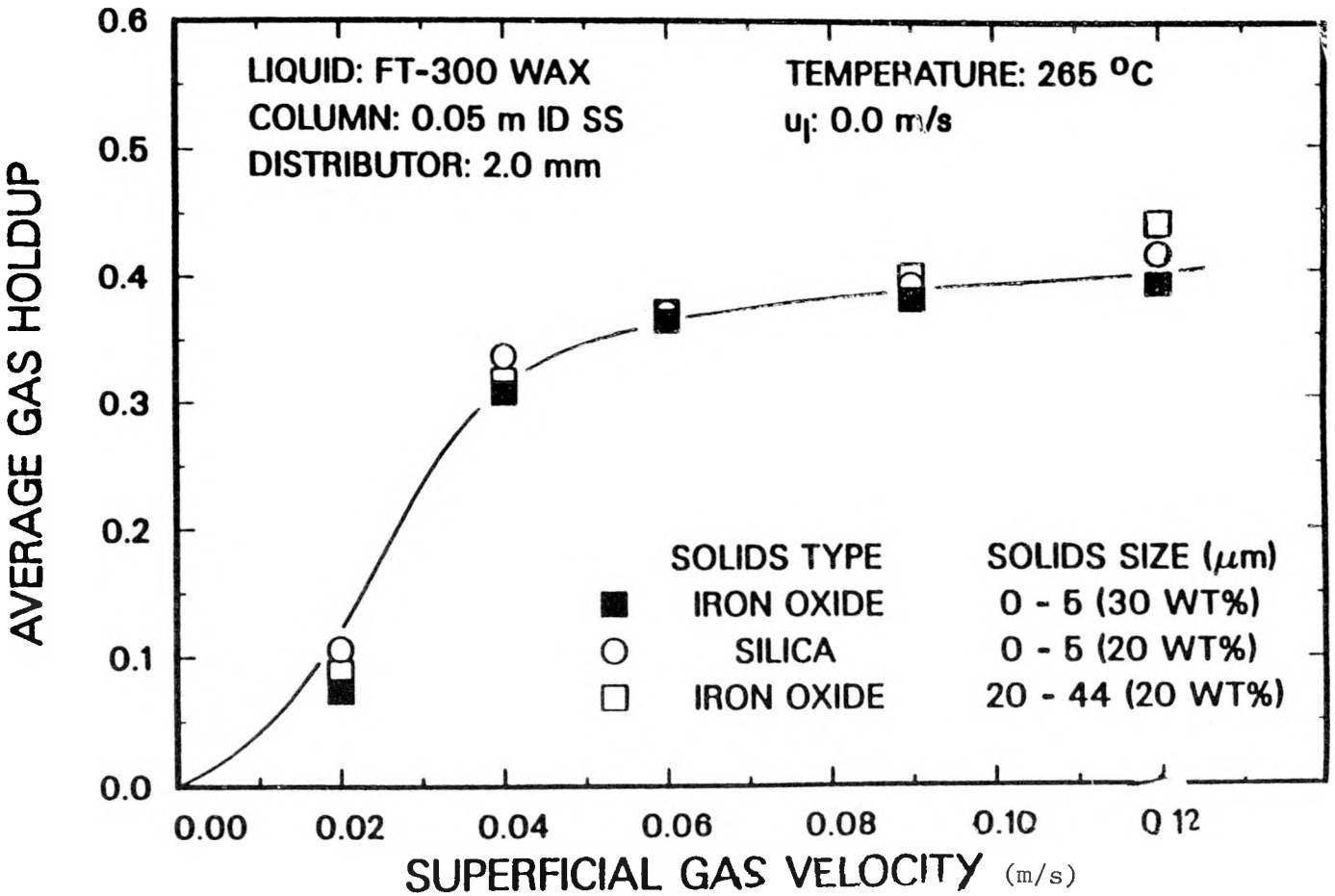

Fig. 2.29 Effect of solids type and size on average gas holdup in the 0.05 m ID column with FT-300 wax (volume fraction of solids at the distributor = 0.045).

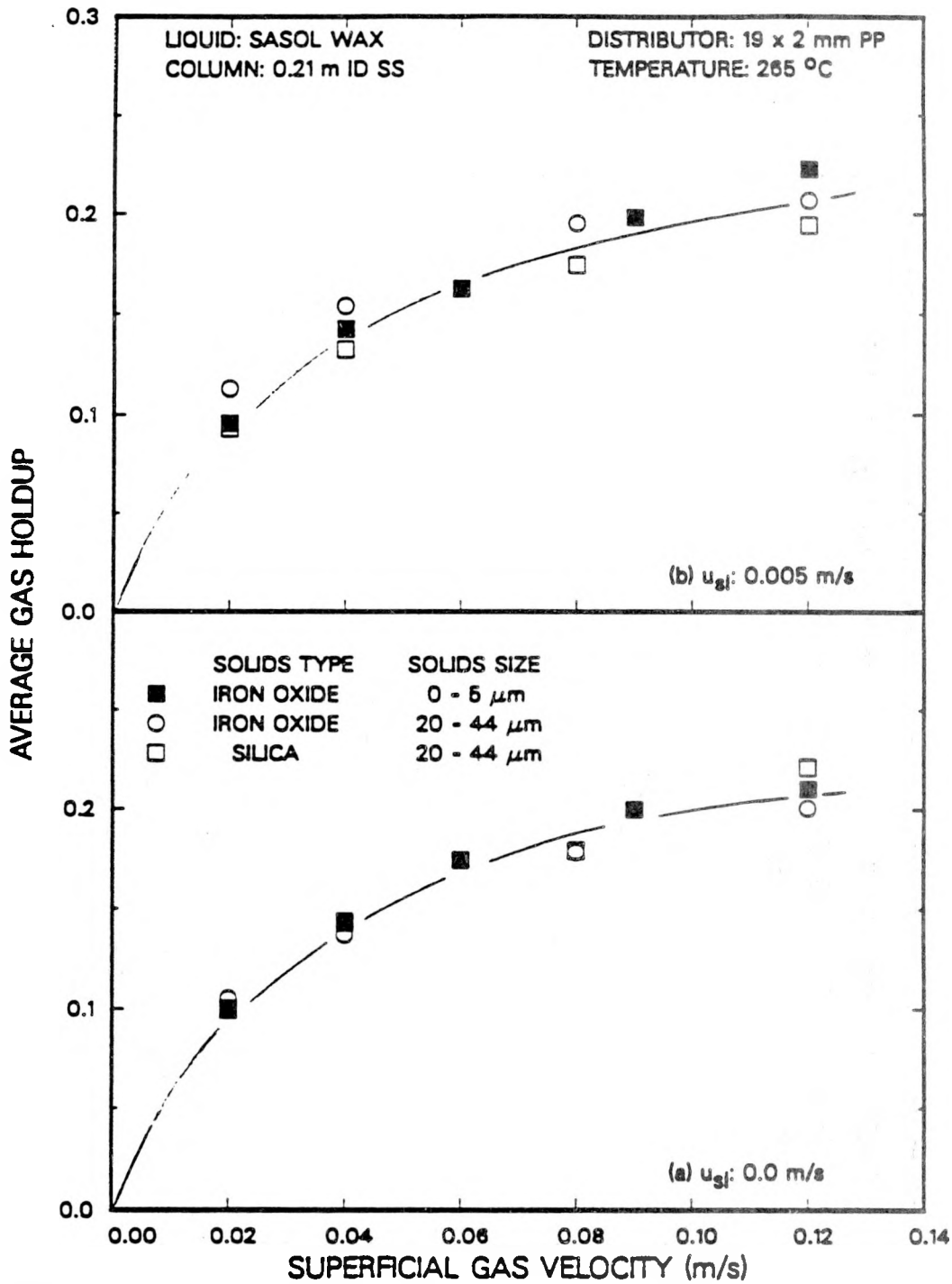

Figure 2.30. Effect of solids type and size on average gas holdup in the 0.21 m ID column with SASOL wax ((a) u_{sl} = 0.0 m/s; (b) u_{sl} = 0.005 m/s).

Effect of Liquid Medium

As mentioned previously, SASOL reactor wax and FT–300 wax behaved differently in the 0.05 m ID column. FT–300 wax has a tendency to foam, and as a result, gas holdups obtained with FT–300 wax were substantially higher than those obtained with SASOL reactor wax. Results from experiments with SASOL wax and FT–300 wax are shown in Figure 2.31. In particular, Figure 2.31a shows results from batch experiments conducted without solids and Figure 2.31b shows results for experiments conducted with 20 wt% 0 – 5 μm iron oxide particles at a superficial slurry velocity of 0.005 m/s. The results indicate that regardless of the presence of solids or liquid circulation, gas holdups are substantially higher with FT–300 wax. This increase in gas holdup is due to a higher concentration of fine bubbles present throughout the dispersion in FT–300 wax. Bubble sizes associated with FT–300 wax and SASOL reactor wax will be discussed in detail in Chapter V.

In the large diameter column, the foaming capacity of FT–300 wax is greatly reduced. This is primarily due to the increase in liquid mixing (or turbulence) with increasing column diameter (Kato et al., 1972; Heijnen and Van't Riet, 1984). This increase in liquid mixing hinders the production of a stable foam layer at the top of the dispersion and as a result, the nonfoamy or churn–turbulent regime dominates.

For experiments conducted in the batch mode of operation, gas holdups with FT–300 wax are significantly greater than those with SASOL wax at low gas velocities (see Figure 2.32a). In the fully developed churn–turbulent regime (i.e. at $u_g \geq 0.08$ m/s) gas holdups with FT–300 wax and SASOL wax are similar. The same trend was observed in experiments conducted in the batch mode of operation with 20 – 44 μm iron oxide particles (see Figure 2.32b). At a superficial gas velocity of 0.04 m/s the gas holdup with FT–300 was significantly greater than that of SASOL wax (28% for FT–300 and

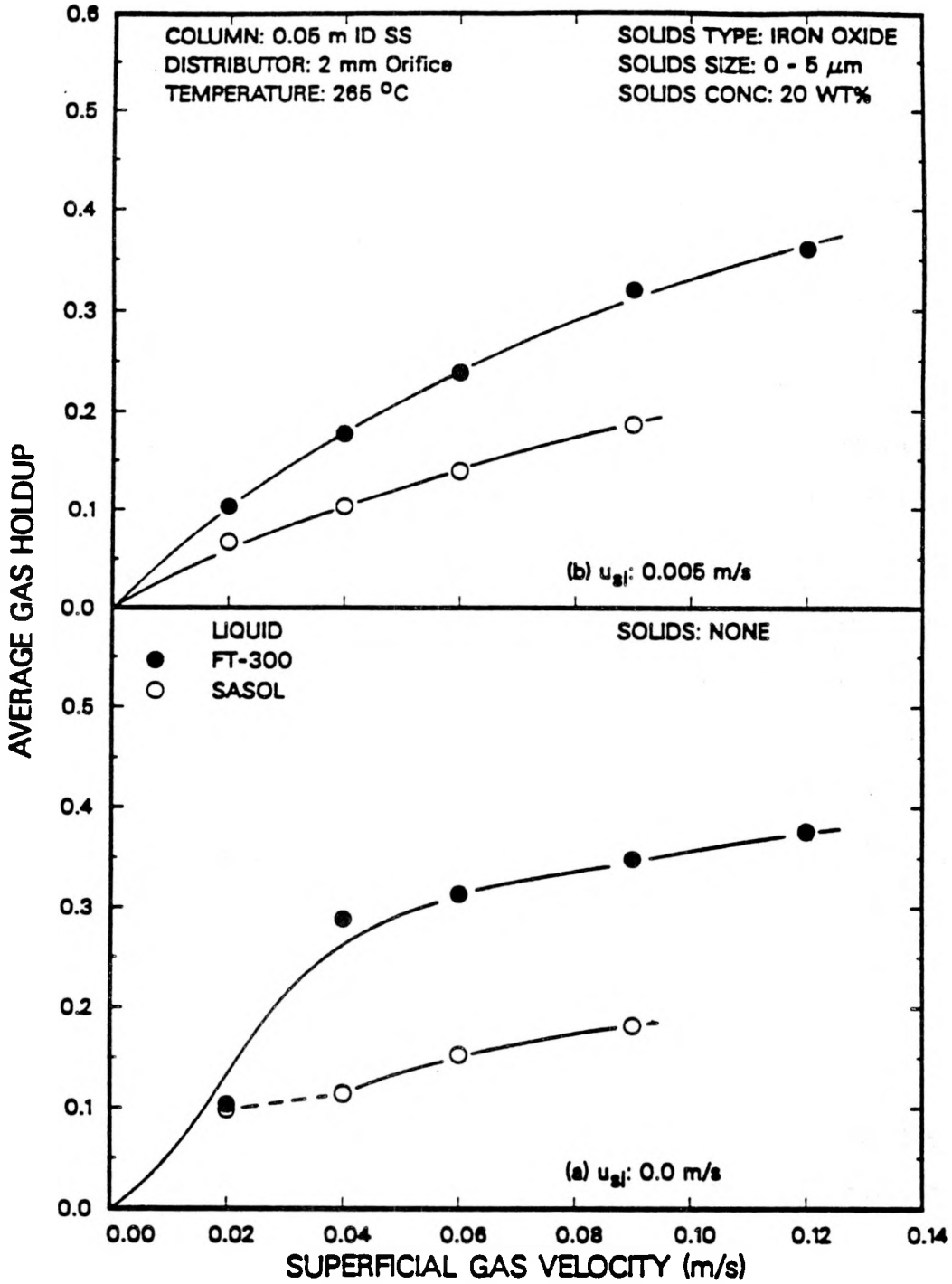

Figure 2.31. Effect of liquid medium on average gas holdup in the 0.05 m ID Column.

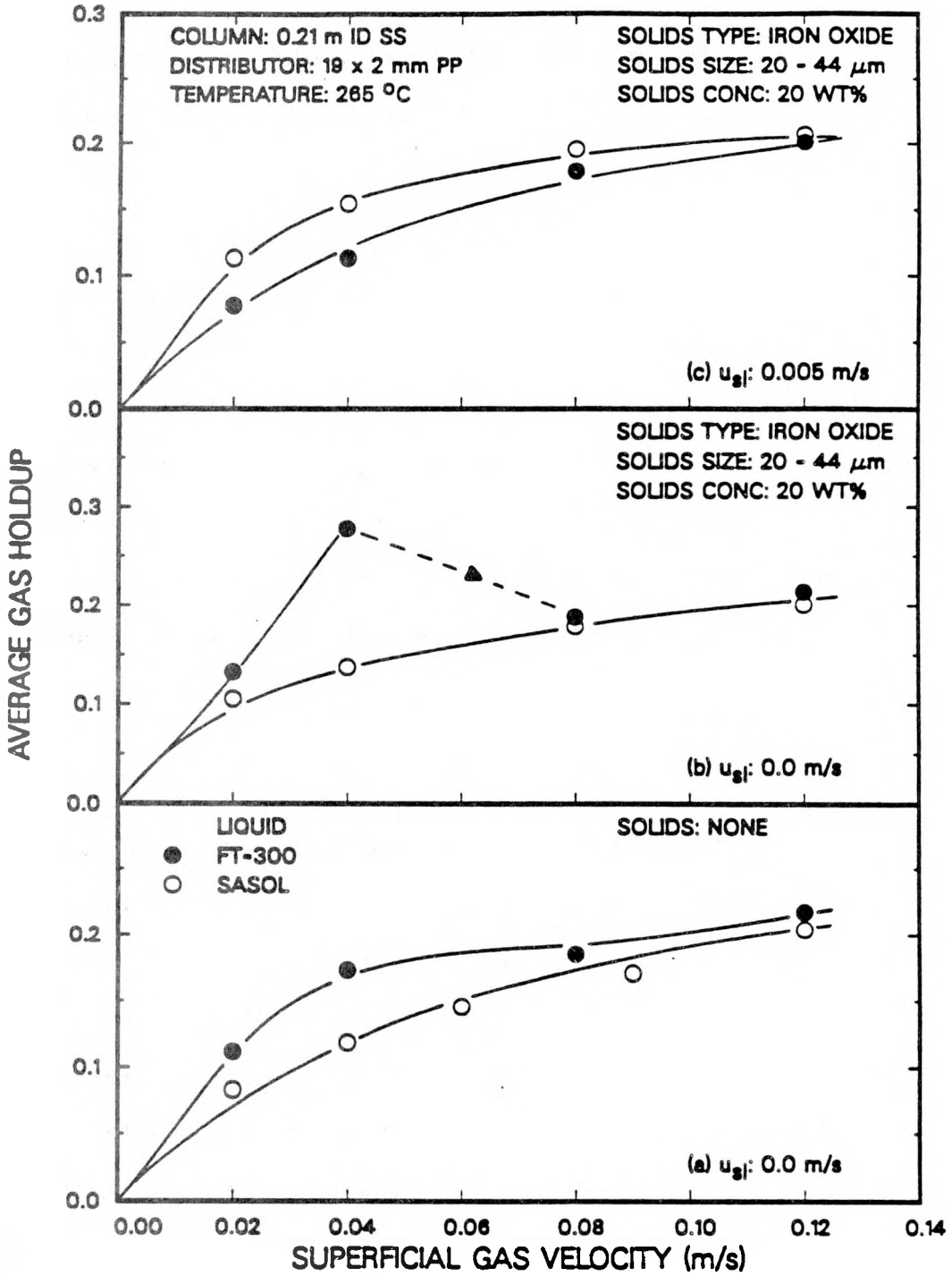

Figure 2.32. Effect of liquid medium on average gas holdup in th 0.21 m ID Column.

14% for SASOL). At higher gas velocities (i.e. $u_g = 0.08$ and 0.12 m/s) the foam layer collapses and gas holdups with FT–300 wax and SASOL wax approach the same value. Gas holdup values obtained with SASOL wax were greater than those with FT–300 wax for experiments conducted in the continuous mode of operation in the presence of large iron oxide particles (Figure 2.32c). As described previously, iron oxide particles appear to be partially nonwettable in SASOL wax, and as a result, when the slip velocity between the gas and liquid phases is reduced, the gas holdup increases. However, at sufficiently high gas velocities, the turbulence created in the large diameter column is sufficient to reduce the adhesion of solid particles to the surface of the tiny gas bubbles, which results in slightly lower holdups. Thus, at higher gas velocities ($u_g \geq 0.08$ m/s), holdup values obtained from the experiments with SASOL reactor wax and FT–300 wax approach the same value.

Effect of Distributor Type

A limited number of experiments were conducted with the bubble cap distributor in the large diameter column. Gas holdup values from experiments with the bubble cap distributor were consistently higher than those from experiments with the 19 x 2 mm perforated plate distributor. Figures 2.33a and 2.33b show results obtained with SASOL ($u_{s\ell} = 0$ m/s) and FT–300 wax ($u_{s\ell} = 0.005$ m/s), respectively. For both waxes, holdups associated with the bubble cap distributor were slightly higher than those with the perforated plate distributor. The jet velocity through both distributors is essentially the same (e.g. at $u_g = 0.12$ m/s, the jet velocity through the perforated plate is 69 m/s while, with the bubble cap it is 63 m/s). Based solely on jet velocities, one would expect the gas holdups to be essentially the same for both distributors. However, we believe that the way in which the gas flows through the two different distributors is the primary cause of the increase in holdup observed with the bubble cap distributor. The

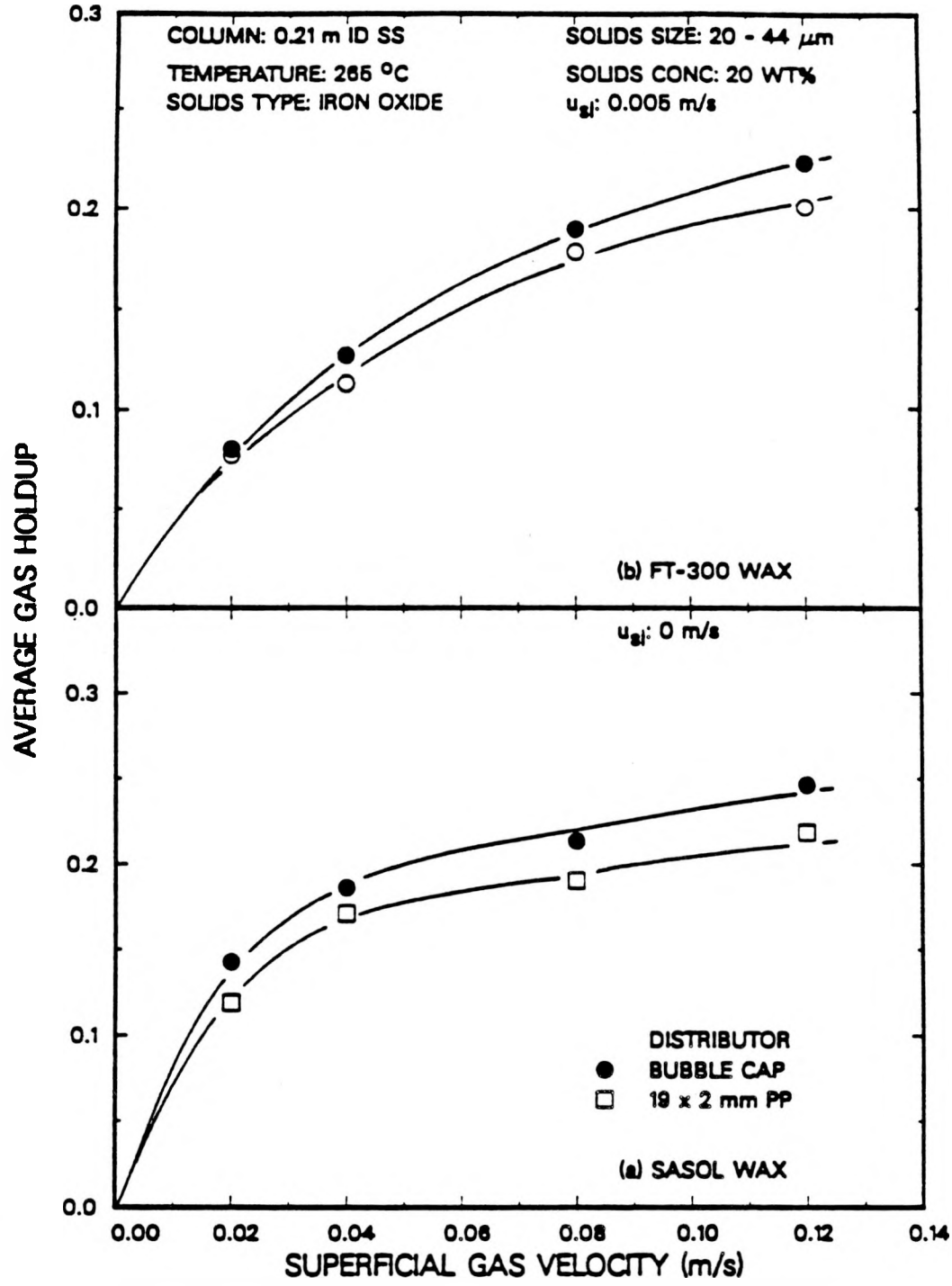

Figure 2.33. Effect of superficial gas velocity and distributor type on average gas holdup (20 – 44 μm iron oxide; (a) SASOL wax, $u_{s\ell} = 0.0$ m/s; (b) FT-300 wax, $u_{s\ell} = 0.005$ m/s).

bubble cap distributor is comprised of seven bubble caps, each with three 2 mm orifices. The flow of gas from each orifice is directed downward towards the distributor (see Figure 2.8). Thus, as the gas bubbles or gas jet exits the openings in the bubble caps, they are broken up by colliding with the distributor plate. On the other hand, as the gas exits the openings in the perforated plate distributor, it flows freely upward through the column; there are no obstacles in its path which may cause bubble breakup. Similar results were obtained for experiments conducted with small iron oxide particles in the batch and continuous modes of operation (see Figures 2.34a and 2.34b, respectively).

Effect of Column Diameter

Gas holdup values from experiments in the small diameter column with FT–300 wax were consistently higher than gas holdup values from experiments in the large diameter column (see Figure 2.35a). The main difference in gas holdups obtained in the two columns is that foam is produced more readily in the small diameter column and once produced, persists over a wider range of gas velocities. During one of the experiments in the small diameter column, the foam broke at a gas velocity of 0.09 m/s (see dashed line in Figure 2.35a) and the gas holdup value was similar to that obtained in the large diameter column. At a gas velocity of 0.02 m/s gas holdups in both columns are similar. This is expected, since at a velocity of 0.02 m/s, the homogeneous bubbling regime exists in both columns. Gas holdups from experiments conducted in the continuous mode of operation in the small diameter column (see Figures 2.35b and 2.35c) were higher than those observed in the large diameter column. It should be pointed out that experiments in the small diameter column were conducted in an increasing order of gas velocities; whereas, experiments in the large diameter column were conducted in a decreasing order of gas velocities. From our previous studies with FT-300 wax (Bukur et al. 1987a,b; Bukur and Daly,1987) it is known that the use of increasing gas

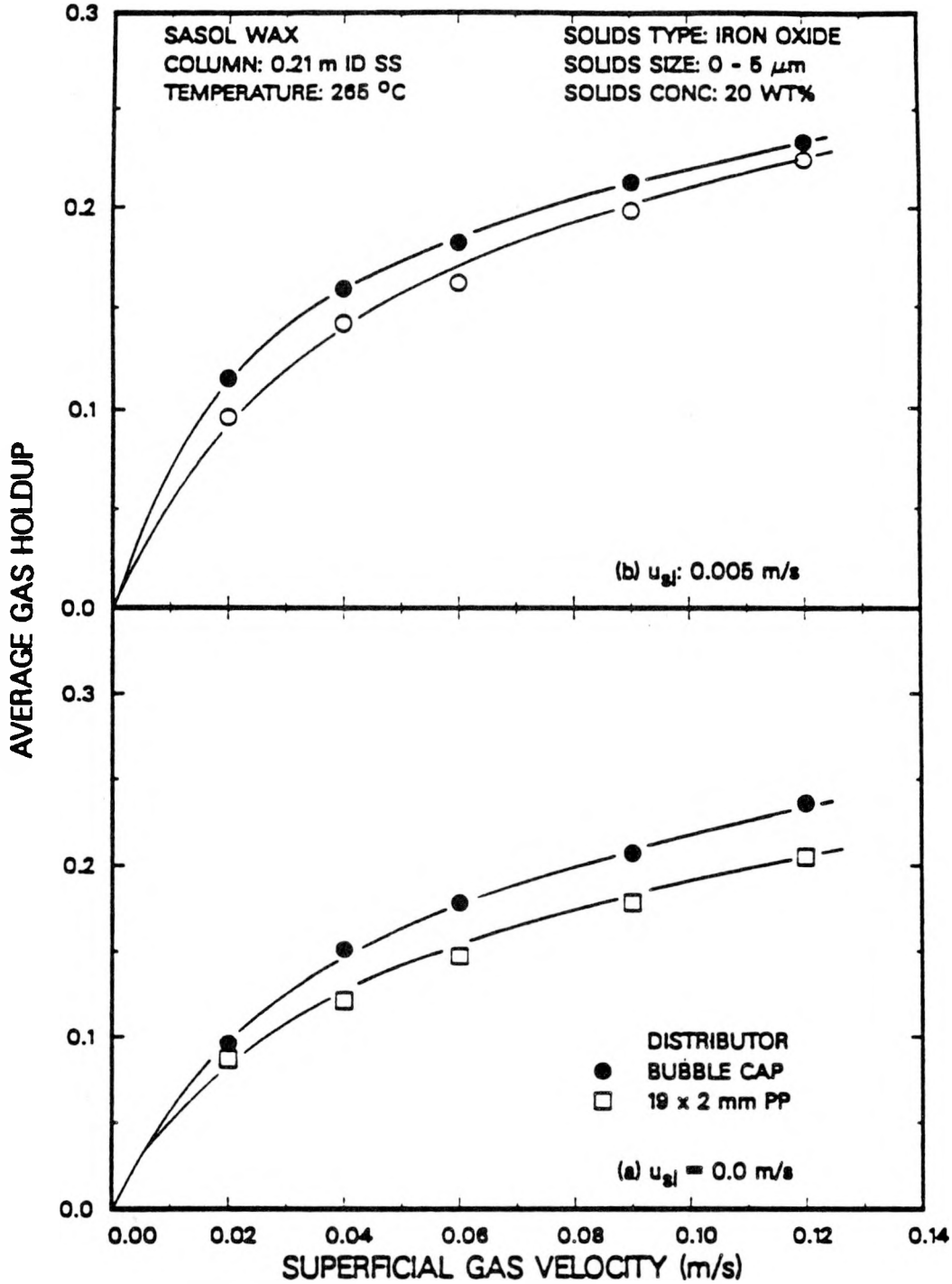

Figure 2.34. Effect of superficial gas velocity and distributor type on average gas holdup with SASOL wax (0 – 5 μm iron oxide; (a) $u_{s\ell} = 0.0$ m/s; (b) $u_{s\ell} = 0.005$ m/s).

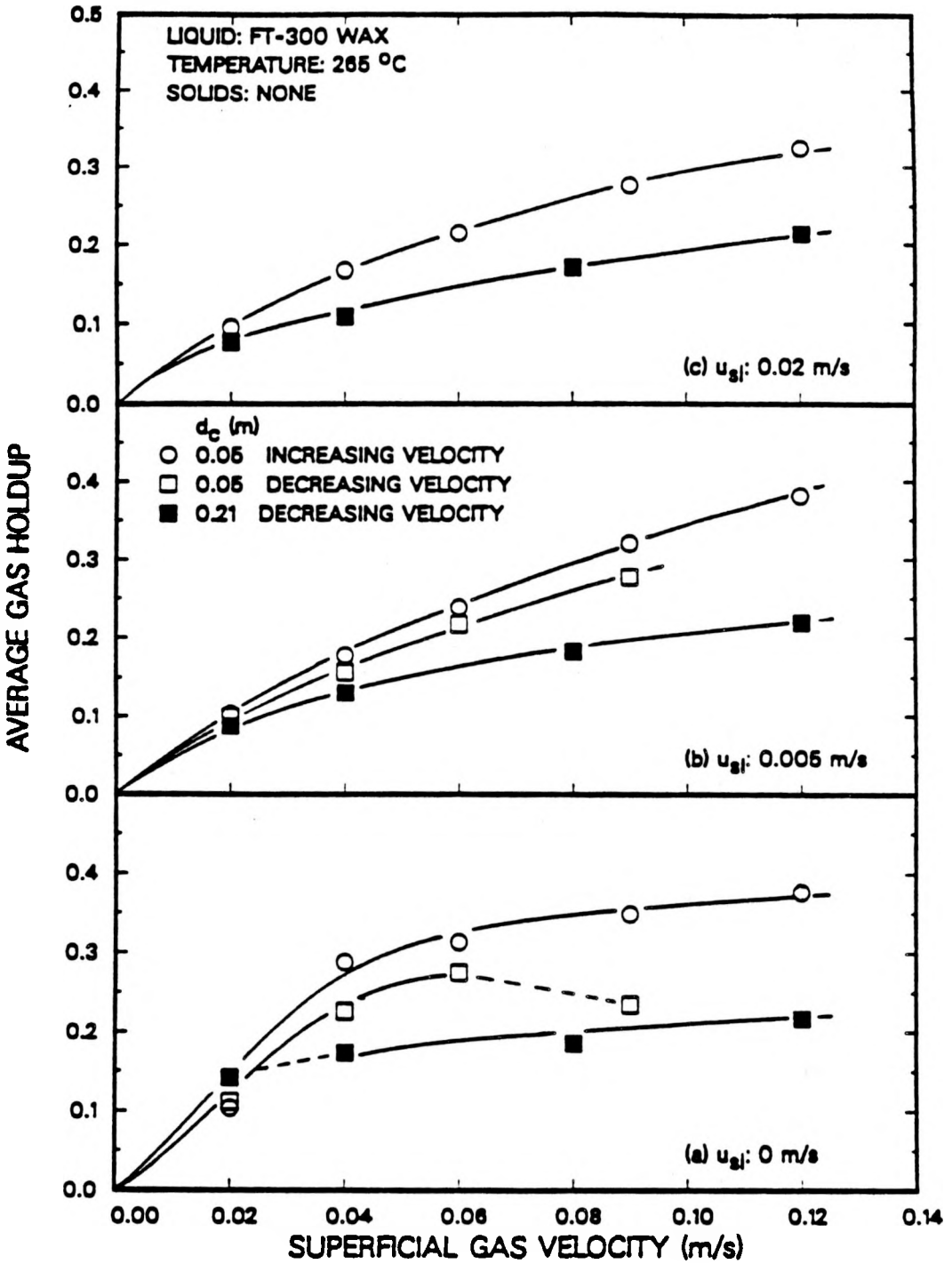

Figure 2.35. Effect of column diameter on average gas holdup with FT-300 wax.

velocities favors higher gas holdups. Thus results shown in Figure 2.35 do not illustrate the effect of column diameter onlybut the effect of operating procedure (increasing vs. decreasing order of gas velocities). The higher holdups observed in the small diameter column may be due to the use of increasing order of gas velocities.

SASOL wax, on the other hand, does not produce foam and gas hodups are not influenced markedly by the order of gas velocities employed. As a result, gas holdups obtained in the 0.05 and 0.21 m ID columns are similar regardless of operating procedures employed (see Figures 2.36a and 2.36b).

Very few experimental studies on the effect of column diameter have been conducted with molten waxes as the liquid medium. Only Mobil workers (Kuo, 1985) and Deckwer et al. (1980) have studied the effect of column diameter with molten waxes. Researchers at Mobil conducted experiments with FT–200 wax (MW = 640) in 0.03 and 0.05 m ID columns, each 2.2 m in height. Their results indicate that for similar jet velocities, column diameter did not have an effect on gas holdup. They also conducted similar studies in two tall columns (0.05 m ID and 0.10 m ID, 9.1 m tall) with FT–200 wax and reactor waxes produced in their bench scale bubble column slurry reactor. These studies showed no effect of column diameter of gas holdup for FT–200 wax; however, with experiments conducted with reactor waxes, slightly higher holdups were obtained in the 0.10 m ID column. Deckwer et al. conducted experiments in two different diameter columns (0.04 m and 0.10 m ID). For temperatures below 250 °C holdups in the smaller diameter column were consistently higher than holdups in the large diameter column for the range of velocities studied (0.005 – 0.03 m/s). Foam was present under these conditions. However, for experiments conducted at temperatures greater than 250 °C, holdup values from the two columns were similar. Reilly et al., 1986 summarized the findings of various researchers for holdups in different diameter columns. They reported that some discrepancy exists as to the effect of column diameter; however, they

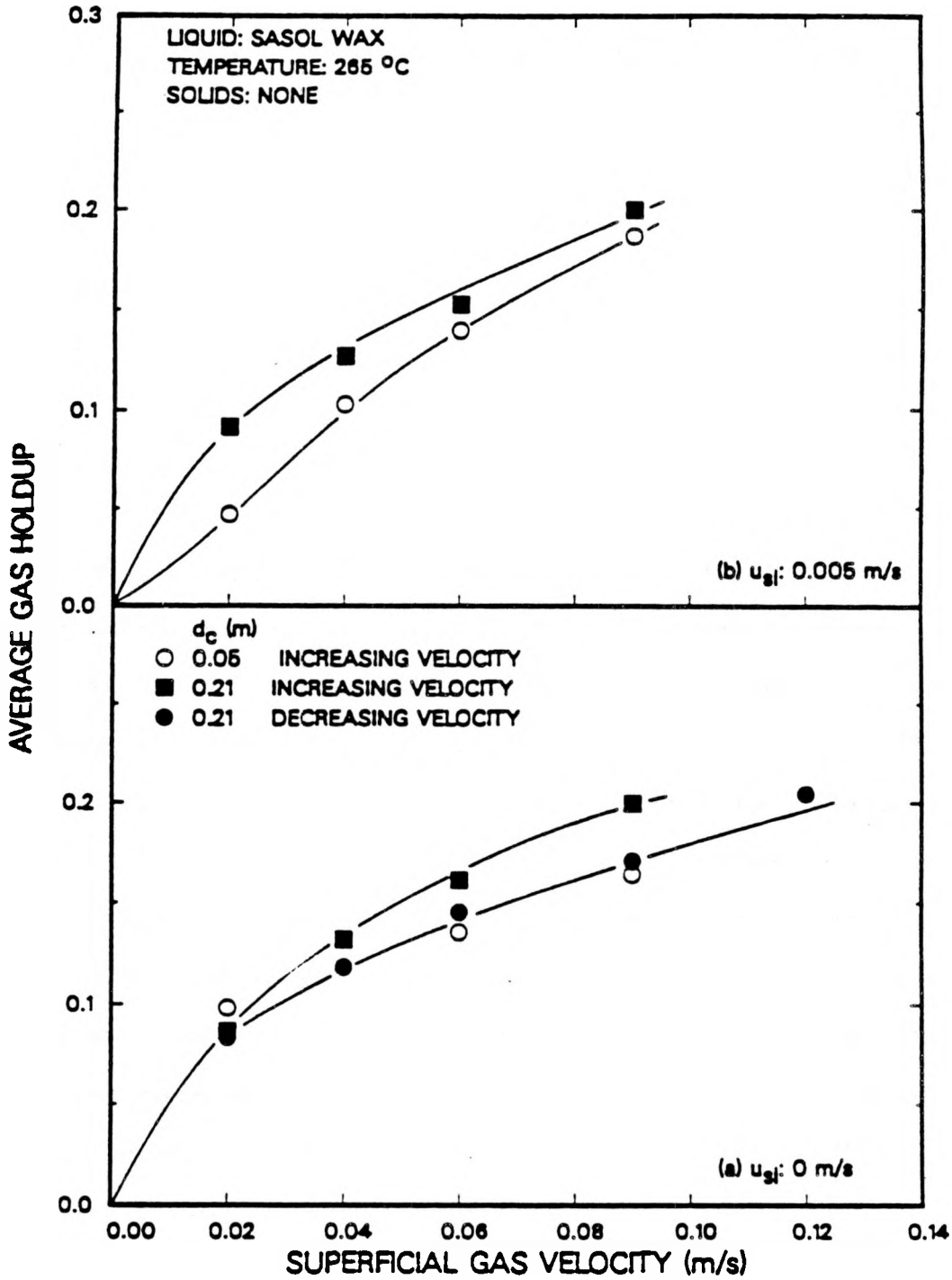

Figure 2.36. Effect of column diameter on average gas holdup with SASOL wax.

pointed out that for columns with diameters greater than 0.10 m, there is essentially no effect of column diameter. Shah et al. (1982) also summarized the findings of various researchers, from holdup measurements made in systems which did not produce foam (mostly air–water), which show that the effect of column diameter on the average gas holdup is minimal. In general, slightly lower holdups were observed in larger diameter columns compared to smaller diameter columns.

Physical Properties and Average Gas Holdup Correlations

Physical Property Measurements

The density and surface tension of FT–300 and SASOL wax were measured at different temperatures. The viscosity of both FT–300 wax and SASOL reactor wax was measured at 230 °C. The physical properties used in developing gas holdup correlations are presented in Table 2.6. The densities of iron oxide and silica particles are 5100 and 2650 kg/m^3, respectively.

Density Measurements

Densities of FT–300 and SASOL wax were measured using the pressure drop across known heights of liquid in the 0.05 m ID glass column. A differential pressure transducer was connected to the bottom of the glass column to measure the pressure drop across the column. The pressure transducer was calibrated with distilled water using the same procedure outlined earlier. The column was filled with the test liquid to a height of 2.5 m and brought to the desired temperature. Once at temperature, the pressure drop was recorded. A portion of the liquid was drained ($\approx$ 0.25 m) and the pressure drop was recorded again. This procedure was repeated until the liquid level in the column was approximately 1 m. The density of the wax at a given temperature was obtained from the slope of the pressure drop versus height plot, after appropriate corrections for the calibration factor.

Table 2.6. Physical Properties of FT-300 Wax and SASOL Wax

LIQUID	TEMPERATURE (°C)	DENSITY (kg/m^3)	VISCOSITY[a] FRESH WAX (kg/m-s)	VISCOSITY USED WAX (kg/m-s)	SURFACE TENSION FRESH WAX (N/m)	SURFACE TENSION[b] USED WAX (N/m)
FT-300	150	–	0.0064		0.024±0.0004	0.025
	200	722	0.0042		0.021±0.0006	0.02±0.001
	230	706	0.0036 (0.0023)[c]	0.0026–0.0041[d]	0.019±0.0005	0.019
	260	681	0.0028		0.017±0.001	0.017±0.0005
SASOL	150	–	0.0042		0.024	0.019±0.0005
	200	701	0.003		0.02±0.001	0.017±0.001
	230		0.0025		0.019	0.016±0.0009
	260	655	0.0022		0.016±0.0003	0.014±0.0008

[a] From Bukur et al., (1987c)

[b] Based on analysis of several samples – all contained solids

[c] Single measurement during this project

[d] Range of values (lowest for sample with no solids; highest for sample taken from slurry containing 30 wt% silica)

Viscosity Measurements

Viscosity measurements were made in a Brookfield viscometer (LV series, 2.5X) using a cylindrical spindle (SC4-18) operating at 60 RPM. A Brookfield Thermosel system allowed measurements up to temperatures of 250 °C. The system was first calibrated using fluids of known viscosities. Three fluids were used; water (0.01 kg/m-s), and two viscosity standards (.051 and .081 kg/m-s – supplied by Brookfield). The standards were used before and after viscosity measurements with wax to monitor errors due to device drift. Each measurement required an 8 ml sample of the test fluid.

Results from these measurements together with those presented by Bukur et al. (1987c) are presented in Table 2.6. The viscosity of the fresh FT–300 sample at 230 °C obtained in the current study was significantly lower than that previously obtained (i.e. 0.0023 kg/m–s vs 0.0035 kg/m–s). The reason for this discrepancy is not known. Several samples of used wax were also analyzed, one without any solids (0.0026 kg/m–s) and several samples from experiments conducted with solids (both iron oxide and silica). The samples from the experiments conducted with solids were prepared as follows. The solidified slurry sample was melted and the solids were allowed to settle. The liquid was decanted and the viscosity of the decanted liquid was measured. The viscosity of wax from experiments with solids was higher than that from experiments without solids. More than likely, the observed increase in viscosity was due to the presence of some solids in the samples. The viscosity was highest (0.0041 kg/m–s) for the sample from the experiment conducted with 30 wt% 0 – 5 μm silica particles.

Surface Tension Measurements

Surface tension measurements were made using a Fischer Model 215 Autotensiomat. The surface tension apparatus was modified for high temperature measurements, as suggested by the manufacturer. The surface tension was measured three times for each sample at a given temperature using both fresh and used FT–300 and SASOL wax. The average surface tension values from these measurements are given in Table 2.6. Some of the surface tension values presented in Table 2.6 are average values based on analysis of more than one sample. For these values, the standard deviation is also given.

Jasper (1972) presents surface tension data for normal paraffins (C5 – C20, C26 and C60). The values reported by Jasper for C5 – C20 paraffins were obtained at temperatures between 10 and 120 °C and for C26 and C60 paraffins, surface tension values were obtained for temperatures up to 180 °C. According to Jasper, surface tension is a linear function of temperature for reduced temperatures ($T/T_{critical}$) of 0.4 to 0.7. Thus, for the data he presented, he also gave values of the slopes and intercepts obtained from a plot of surface tension versus temperature. Figure 2.37 shows the effect of temperature on surface tension for data obtained in this study. Surface tension values for fresh FT–300 wax, used FT–300 wax, and fresh SASOL wax are similar and they vary linearly with temperature. The surface tensions of used SASOL wax were consistently lower than those of fresh SASOL wax (Table 2.6 and Figure 2.37).

The surface tension values for fresh FT–300 and fresh SASOL wax were fitted to the following equation using linear regression

$$\sigma = \text{int} - \text{slope} * T \tag{2.29}$$

where σ is the surface tension in dynes/cm and T is the temperature in °C. The following slopes and intercepts were obtained

FRESH FT–300: SLOPE = 0.0606, INT = 33.1

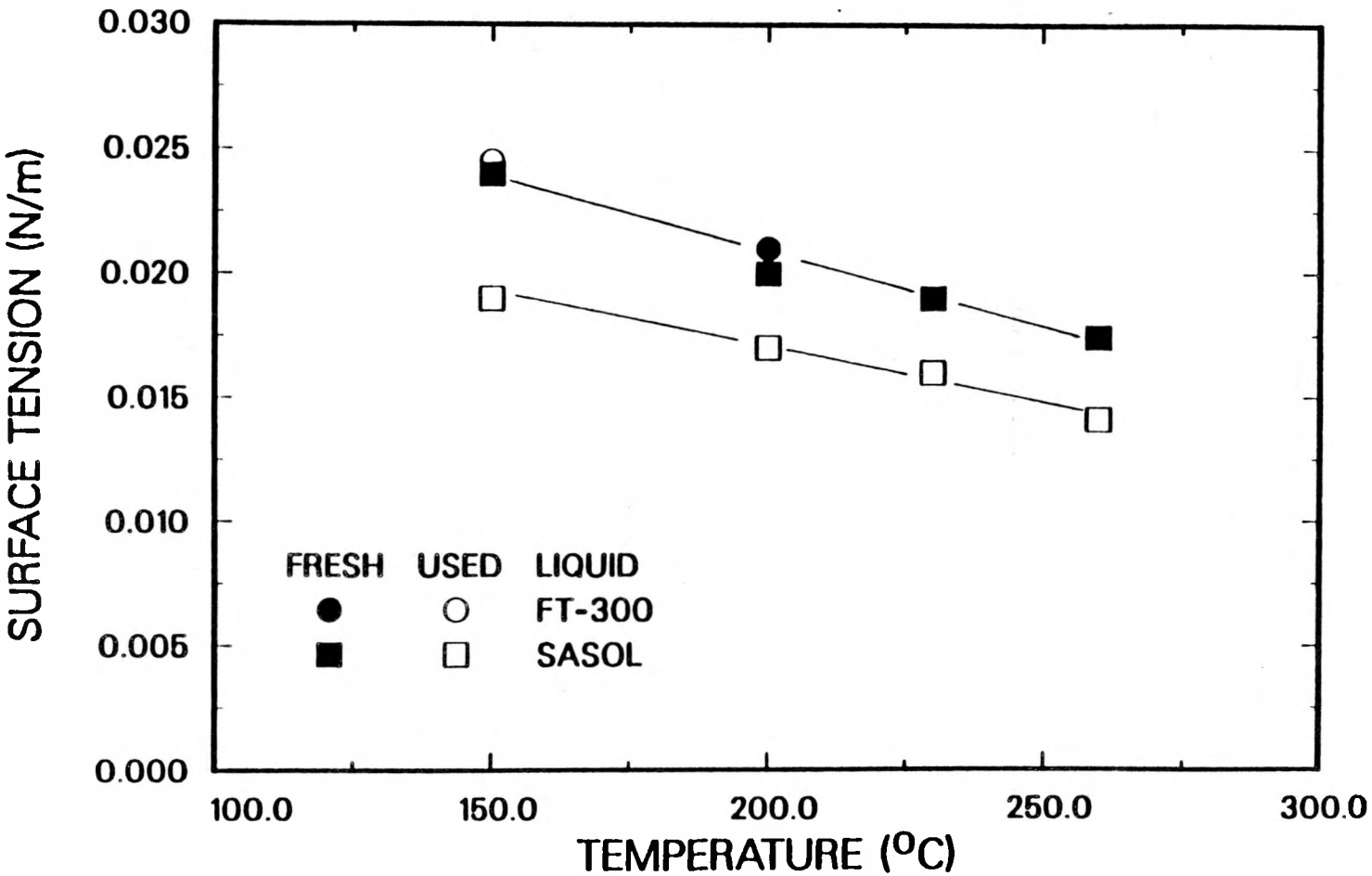

Figure 2.37. Effect of temperature on surface tension of fresh and used FT-300 and SASOL wax.

FRESH SASOL: SLOPE = 0.0659, INT = 33.7

FT–300 wax has a molecular weight of 730, which corresponds to a carbon number of 52. For a C26 paraffin, the slope and intercept values reported by Jasper were 0.07332 and 31.46, respectively and for a C60 paraffin the slope and intercept values were 0.05827 and 30.89, respectively. The results (i.e. slopes and intercepts) obtained in this study are in good agreement with the values reported by Jasper.

Gas Holdup Correlations

Numerous empirical correlations for predicting gas holdup in nonfoaming systems have been published (e.g. Hughmark, 1967; Akita and Yoshida, 1974; Bach and Pilhofer, 1978; Kara et al., 1982; Hatate et al., 1986, Badjugar et al., 1986, Zheng et al., 1988). The correlations evaluated in this study are presented in Table 2.7. Some researchers (e.g. Smith and Ruether, 1985; Fan, 1989) have found that in systems with low solids concentrations, correlations developed for two–phase systems can be applied to three–phase systems, if the physical properties (i.e density and viscosity) of the liquid are replaced by those of the slurry. The slurry density, $\rho_{s\ell}$ is obtained from:

$$\frac{1}{\rho_{s\ell}} = \frac{1}{\frac{\omega_s}{\rho_s} + \frac{1-\omega_s}{\rho_\ell}} \tag{2.30}$$

and the slurry viscosity may be estimated from

$$\mu_{s\ell} = \mu_\ell \frac{1 + 0.5\epsilon_s}{(1-\epsilon_s)^4} \tag{2.31}$$

Equation 2.31 is valid for $\epsilon_s < 0.4$ (Perry and Chilton, 1983), where ϵ_s is the volume fraction of solids in the liquid/solid slurry.

Average gas holdup results from our study can be divided into two groups: (1) results in which foam was observed and (2) results in which no foam was observed.

Table 2.7. Summary of Gas Holdup Correlations Presented in the Literature

CORRELATION	COLUMN ID	CONDITIONS	SYSTEM	REFERENCE
$\epsilon_g = aFr^b Ar^c Bo^d (1 + u_\ell / u_g)^e (1 - \epsilon_s)^f$ $Fr = \frac{u_g^2}{d_c g}$, $Ar = \frac{d_p^3 g(\rho_s - \rho_\ell)}{\rho_\ell \mu_\ell^2}$, $Bo = \frac{g d_p^2 \rho_\ell}{\sigma}$ where a, b, c, d, and e, are adjustable parameters which depend on flow regime	0.285 m	$0 < u_g < 0.16$ $0 \leq u_\ell \leq 0.04$ $\rho_\ell = 1000$ $d_p = 615$	gas: air liquid:water solids:glass spheres	Zheng et al., 1988
$\epsilon_g = 0.9(1 - \omega_s)^{0.7} u_g^{0.525}$	0.076 and 0.301 m	$0 < u_g \leq 0.14$ $0 \leq \omega_s \leq 0.20$ $751 \leq \rho_\ell \leq 1000$ $0.001 \leq \mu_\ell \leq 0.0013$ $49 \leq d_p \leq 107$	gas: air liquid: water, soltrol solids: glass spheres, ammonia synth. cat., Triple A cat., FCC	Badgujar et al., 1986
$\epsilon_g = \frac{u_g/(u_g + u_\ell)}{1.20 + 0.35/\sqrt{Fr_\ell}}$ $Fr_\ell = \frac{(u_g + u_\ell)^2}{g d_c}$	1.55 and 2.6 m	$0 \leq u_g < 5$ $u_\ell = 0.15$ and 0.6 $0 \leq \omega_s \leq 0.60$ $\rho_\ell = 1000$ $d_p = 30$, 63, and 100	gas: air liquid: tap water solids: glass spheres	Hatate et al., 1985

Table 2.7. (cont.)

CORRELATION	COLUMN ID	CONDITIONS	SYSTEM	REFERENCE
$\epsilon_g = \frac{Re_g}{A+BRe_g+CRe_{s\ell}+D\left(\frac{\epsilon_s}{\epsilon_s+\epsilon_\ell}\right)}$	0.152 m	$0 < u_g \leq 0.3$	gas: air	Kara et al., 1982
$Re_{s\ell} = \frac{d_c u_{s\ell} \rho_{s\ell}}{\mu_{s\ell}}$, $Re_g = \frac{d_c u_g \rho_g}{\mu_g}$		$0 \leq u_{s\ell} \leq 0.1$	liquid: water	
where A, B, C, D, and E are adjustable parameters		$0 \leq \frac{\epsilon_s}{\rho_{s\ell}} \leq 0.4$	solids: coal, dried mineral	
which depend on particle size		d_p = 0, 10, 30, 70		
$\epsilon_g = (2 + (0.35 / u_g)\{(\rho_\ell / 1000)(\sigma_\ell / 0.072)\}^{0.33})^{-1}$	< 0.1 m	$0.004 \leq u_g \leq 0.45$	gas: air	Hughmark, 1967
		$780 \leq \rho_\ell \leq 1700$	liquid: water, kerosene	
		$0.0009 \leq \mu_\ell \leq 0.152$	glycerol aqu. soln.,	
		$0.025 \leq \sigma \leq 0.076$	light oil, salt solns.	

u_i (m / s), ρ_i (kg / m^3), μ_i (kg / m − sec) where i = g, sℓ, ℓ

d_p (μm), σ_ℓ(N / m)

Deckwer et al. (1980) used the following empirical correlation to correlate holdup values obtained using molten paraffin wax in the foamy regime

$$\epsilon_g = 8.4 u_g^{1.1} \pm 0.015 \qquad u_g \leq 0.04 m/s \tag{2.32}$$

Researchers at Mobil (Kuo, 1985) used a similar correlation to predict gas holdups with FT–200 wax (MW=630) under foaming conditions.

$$\epsilon_g = 10.3 u_g^{1.1} \qquad u_g \leq 0.06 m/s \tag{2.33}$$

The correlations presented above were obtained from experiments conducted in the batch mode of operation. While the two correlations are similar, the difference in the constant (8.4 and 10.3) is probably due to differences in the foaming characteristics of the systems studied. Two correlations were developed by Bukur et al. (1987a) for data obtained in the foamy regime. One correlation was developed from gas holdup data obtained using orifice plate distributors

$$\epsilon_g = 0.94 u_g^{0.41} \qquad 0.01 \leq u_g \leq 0.07 m/s \tag{2.34}$$

and the other correlation was developed from gas holdup data obtained using a 40 μm sintered metal plate distributor

$$\epsilon_g = 1.06 u_g^{0.15} \qquad 0.01 \leq u_g \leq 0.12 m/s \tag{2.35}$$

The correlations proposed by Deckwer et al. and Kuo (Eqs. 2.32 and 2.33, respectively) show that holdup increases almost proportionally with superficial gas velocity, while results from the study by Bukur et al. show that holdup values tend to level off at higher gas velocities. A possible explanation for the discrepancy is the range of gas velocities employed in the three studies. The studies by Deckwer et al. and Kuo were limited to low gas velocities, where the holdup increases linearly with gas velocity.

However, at higher gas velocities, holdup values level off. Thus, it is evident, that a single correlation cannot be developed for predicting holdup values in the foamy regime. Therefore, the correlations developed in the present study are based on data obtained in the slug flow and churn–turbulent flow regimes. In particular, gas holdup data obtained in the 0.05 m ID stainless steel column in the batch mode of operation with FT–300 wax have been omitted.

Measured gas holdups values were compared with values predicted using the correlations presented in Table 2.7. The correlations developed by Hughmark (1967) and Hatate et al. (1986) were based on data obtained from two–phase systems. For Hughmark's correlation, the slurry density was used as opposed to the density of the liquid. Since constants in Zheng et al.'s correlation depend on the flow regime, it was assumed that at a gas velocity of 0.02 m/s the homogeneous bubbling regime prevails, at a gas velocity of 0.04 m/s the transition regime exists, and for gas velocities greater than 0.04 m/s the column was assumed to operate in either the churn–turbulent (0.21 m ID) or slug flow (0.05 m ID) regime. The correlation presented by Kara et al. (1982) has variable parameters as well. The constants change depending on the size of particles used. Thus, in applying Kara et al.'s correlation to our system, we used constants for 10 μm particles to estimate gas holdups for slurries containing 0 – 5 μm particles, and constants for 30 μm particles to estimate gas holdups for slurries containing 20 – 44 μm particles. The number of data points associated with a given set of conditions, which were used in the correlations are presented in Table 2.8. A total of 222 points were used. Mean square errors (MSE), defined as

$$\mathrm{MSE} = \frac{\sum_{i} (\epsilon_{\mathrm{meas}_i} - \epsilon_{\mathrm{pred}_i})^2}{n-1} \qquad i = 1 \text{ to } n \tag{2.36}$$

were first estimated using the original values of constants in the literature correlations. The MSE values were between 0.0015 to 0.017 (Table 2.9). The magnitude of the

Table 2.8. Summary of Number of Points at a Given Set of Conditions

LIQUID	COLUMN ID (m)	SOLIDS TYPE	SOLIDS SIZE μm	$u_{s\ell}$ (m/s)	No. Pts.
FT-300	0.05	None	–	0.005	4
FT-300	0.05	Iron oxide	0 – 5	0.005	12
FT-300	0.05	Iron oxide	0 – 5	0.02	12
FT-300	0.05	Silica	0 – 5	0.005	12
FT-300	0.05	Silica	0 – 5	0.02	4
FT-300	0.05	Iron oxide	20 – 44	0.005	7
FT-300	0.05	Iron oxide	20 – 44	0.02	3
FT-300	0.05	Silica	20 – 44	0	4
FT-300	0.21	None	–	0	4
FT-300	0.21	None	–	0.005	4
FT-300	0.21	None	–	0.02	4
FT-300	0.21	Iron oxide	20 – 44	0	3
FT-300	0.21	Iron oxide	20 – 44	0.005	8
SASOL	0.05	None	–	0	8
SASOL	0.05	Iron oxide	0 – 5	0.005	4
SASOL	0.05	Iron oxide	20 – 44	0	4
SASOL	0.21	None	–	0	9
SASOL	0.21	None	–	0.005	12
SASOL	0.21	None	–	0.02	4
SASOL	0.21	Iron oxide	0 – 5	0	24
SASOL	0.21	Iron oxide	0 – 5	0.005	15
SASOL	0.21	Iron oxide	0 – 5	0.02	5
SASOL	0.21	Iron oxide	20 – 44	0	16
SASOL	0.21	Iron oxide	20 – 44	0.005	12
SASOL	0.21	Iron oxide	20 – 44	0.02	12
SASOL	0.21	Silica	20 – 44	0	4
SASOL	0.21	Silica	20 – 44	0.005	8
SASOL	0.21	Silica	20 – 44	0.02	4

MSE is a measure of the goodness of fit, and a smaller value implies better agreement between the measured and predicted values. We then calculated new values of constants in these correlations by minimizing the MSE via non-linear regression (NLIN procedure in SAS). The MSE values obtained using new values for the constants in the existing correlations were slightly smaller than those obtained when the original constants were employed as shown in Table 2.9.

Figure 2.38 compares parity plots obtained using the original correlations proposed by Badjugar et al. (1986) and Hughmark (1967) (Figures 2.38a and 2.38c, respectively) with those for the same two correlations after the constants were recalculated (Figures 2.38b and 2.38d, respectively). The correlation proposed by Badjugar et al. is a three–phase correlation, and the correlation proposed by Hughmark is a two–phase correlation. For Hughmark's correlation, the liquid density was replaced by the slurry density (see Eq. 2.30). In Figures 2.38a and 2.38b (Badjugar et al. correlation) 85% of the measured gas holdup values are within ±30% of the predicted values using the original constants (Figure 2.38a) and 94 % of the measured holdup values were with ±30% of the predicted values using the new constants(Figure 2.38b). Similar results (i.e. better agreement between predicted and measured holdup values) were obtained with Hughmark's correlation (see Figures 2.38c and 2.38d). It is also evident from Figure 2.38 that a two–phase correlation may be used to predict gas holdups in three–phase Fischer–Tropsch slurry bubble columns in the slug flow and churn–turbulent flow regimes.

The lowest MSE (0.0007) was obtained using Zheng et al.'s correlation with re-calculated constants (see Table 2.9). This was expected since this correlation has the largest number of adjustable parameters. However, the difference in mean square errors between Zheng et al.'s correlation and Badjugar et al's correlation with recalculated constants was not that significant (0.0007 vs. 0.0010) even though there are twice as

2.9. Mean Square Errors for Literature Correlations

CORRELATION[a]	MSE[b]	MSE[c]	REFERENCE
$\epsilon_g = 0.46 Fr^{0.26} Ar^{-0.009} Bo^{0.06} (1 + u_{s\ell} / u_g)^{0.04} (1 - \epsilon_s)^{0.19}$	0.0018	0.0007	Zheng et al., 1988[d]
$\epsilon_g = 0.7 (1 - \omega_s)^{-0.08} u_g^{0.5}$	0.0015	0.0010	Badgujar et al., 1986
$\epsilon_g = \frac{u_g / (u_g + u_\ell)}{2.75 + 0.12 / \sqrt{Fr_t}}$	0.0017	0.0014	Hatate et al., 1986
$\epsilon_g = \frac{Re_g}{103.7 + 4.65 Re_g + 0.19 Re_{s\ell} - 573 \left(\frac{\epsilon_s}{\epsilon_s + \epsilon_\ell} \right)}$	0.0045	0.0032	Kara et al., 1982
$\epsilon_g = (2.74 + (0.29 / u_g) [(\rho_\ell / 1000)(\sigma_\ell / 0.072)]^{0.33})^{-1}$	0.0015	0.0012	Hughmark, 1967

[a] reevaluated constants

[b] based on original constants; 222 data points

[c] based on reevaluated constants; 222 data points

[d] Bond number is defined with respect to column diameter as opposed to particle diameter

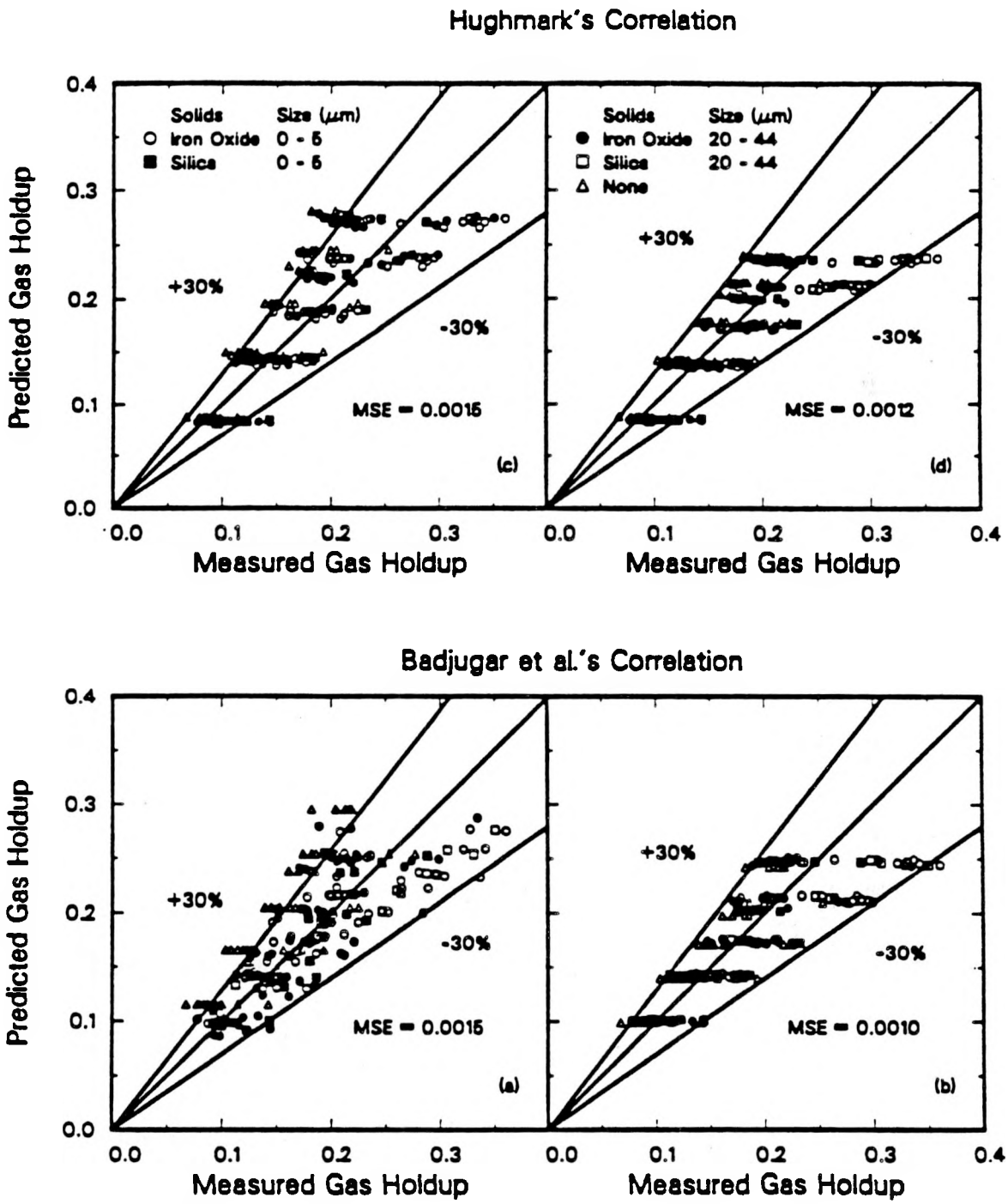

Figure 2.38. Parity plot of predicted versus measured gas holdup ((a and b) Badjugar et al., 1986; (c and d) Hughmark, 1967).

many adjustable parameters in the correlation proposed by Zheng et al. This is not surprising since we did not observe a significant effect of particle size, solids concentration, or slurry flow rate on gas holdup in the slug flow (0.05 m ID column) or churn–turbulent flow (0.21 m ID column) regimes. The following terms in the correlation proposed by Zheng et al., did not vary significantly over the range of conditions employed in this study

$$1.15 < Ar^{-0.009} < 1.21$$

$$1.0 < (1 - \epsilon_s)^{0.19} < 1.028$$

$$0.988 < (1 + u_{s\ell} / u_g) < 1.0$$

The correlation proposed by Badjugar et al. with recalculated constants also indicated that there was no significant effect of solids concentration on gas holdup, i.e.

$$1.0 < (1 - \omega_s)^{-0.08} < 1.03$$

Neglecting the terms presented above, the correlations proposed by Zheng et al., and Badjugar et al. are similar, with the exception of the fact that the former takes into account column diameter; whereas, the latter does not.

Since there was a negligible effect of solids size and concentration and slurry flow rate, the following dimensionless correlation was selected for further evaluation

$$\epsilon_g = a Fr_g^b Bo^c \tag{2.37}$$

We observed an effect of column diameter for gas holdups with FT–300 wax (see Figure 2.35). Eq. 2.35 was evaluated using either all data points (222) or omitting those associated with FT–300 wax in the small stainless steel column (165 points). Table 2.10 summarizes the parameters and MSE's associated with this analysis. Figures 2.39a and 2.39b are parity plots of the measured gas holdup values versus the predicted gas holdup

Table 2.10. Goodness of Fit and Parameters for Empirical Holdup Correlation.

CORRELATION:

$$\epsilon_g = a\ (Fr)^b\ (Bo)^c$$

where: $Fr = \frac{u_c^2}{g\ c_c}$; $Bo = \frac{d_c^2 \varrho_{sl}\ g}{\sigma_l}$

Number of Points	222	165
MSE	.0007	.0004
% Points within 30%	90	95
Parameters:		
a	0.51	0.24
b	0.26	0.22
c	0.05	0.11

Range of Variables:

$0 < u_g < 0.12$ m/s, u_l = 0, 0.005, 0.02 m/s , d_c = 0.05 and 0.21 m σ_l = 0.016 - 0.017 N/m, $0 < \epsilon_{sl} < 0.1$, ϱ_s = 5100 and 2650 kg/m^3, ϱ_l = 660 and 680 kg/m^3, d_p = 0-5 and 20-44 μm, μ_{sl} = 0.028 and 0.022 kg/(m-s)

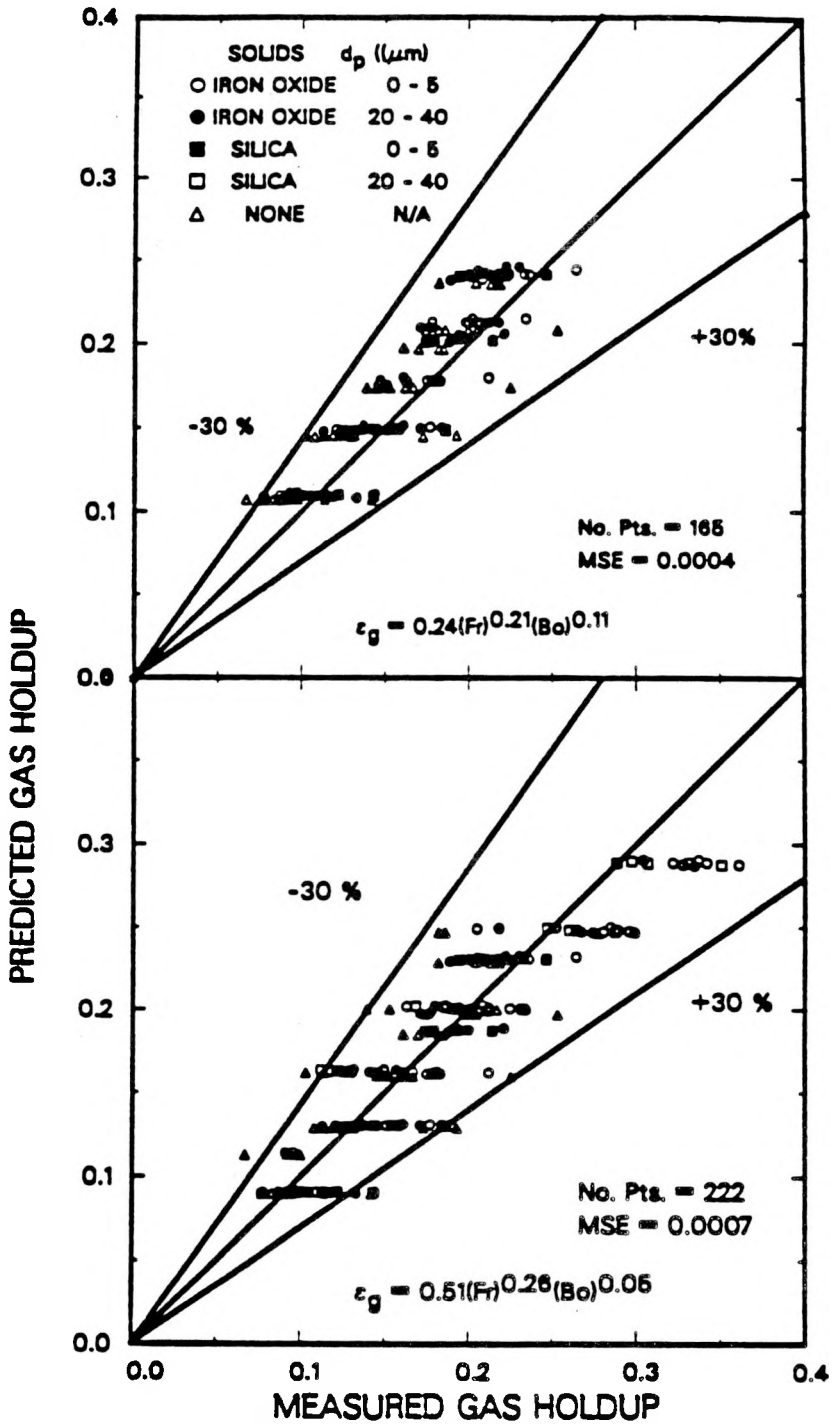

Figure 2.39. Parity plot of predicted versus measured gas holdups for the correlations developed in this study.

values when all data points (i.e. 222) were used and when data for FT–300 wax in the small diameter column were omitted (165 points), respectively. Approximately 90% of the predicted gas holdup values were within ± 30% of the measured values when all data points were used and 95% of the measured gas holdup values were within ±30% when data from the small diameter column for FT–300 wax were excluded.

Extensive two–phase studies were conducted by Bukur et al. (1987a,c) using FT–300 wax, FT–200 wax, Mobil reactor wax, and SASOL reactor wax in the glass columns. An empirical correlation was developed using 349 data points in the slug flow and churn–turbulent regimes. The correlation developed was similar to Eq. 2.37:

$$\epsilon_g = 0.247(Fr_g^{0.30}Bo^{0.15}) \tag{2.38}$$

Data from both our three–phase studies (excluding gas holdups in the small diameter column with FT–300 wax) and two–phase studies (Bukur et al.) were combined and the following general correlation was developed which may be used to predict gas holdups in Fischer–Tropsch slurry bubble column reactors operating in the slug flow or churn–turbulent regime:

$$\epsilon_g = 0.24(Fr_g^{0.28}Bo^{0.14}) \tag{2.39}$$

The MSE based on 514 data points was 0.0007. Figure 2.40 is a parity plot of the measured versus predicted gas holdups using Eq. 2.39. Approximately 94% of the experimental data were within ± 30% of the predicted values.

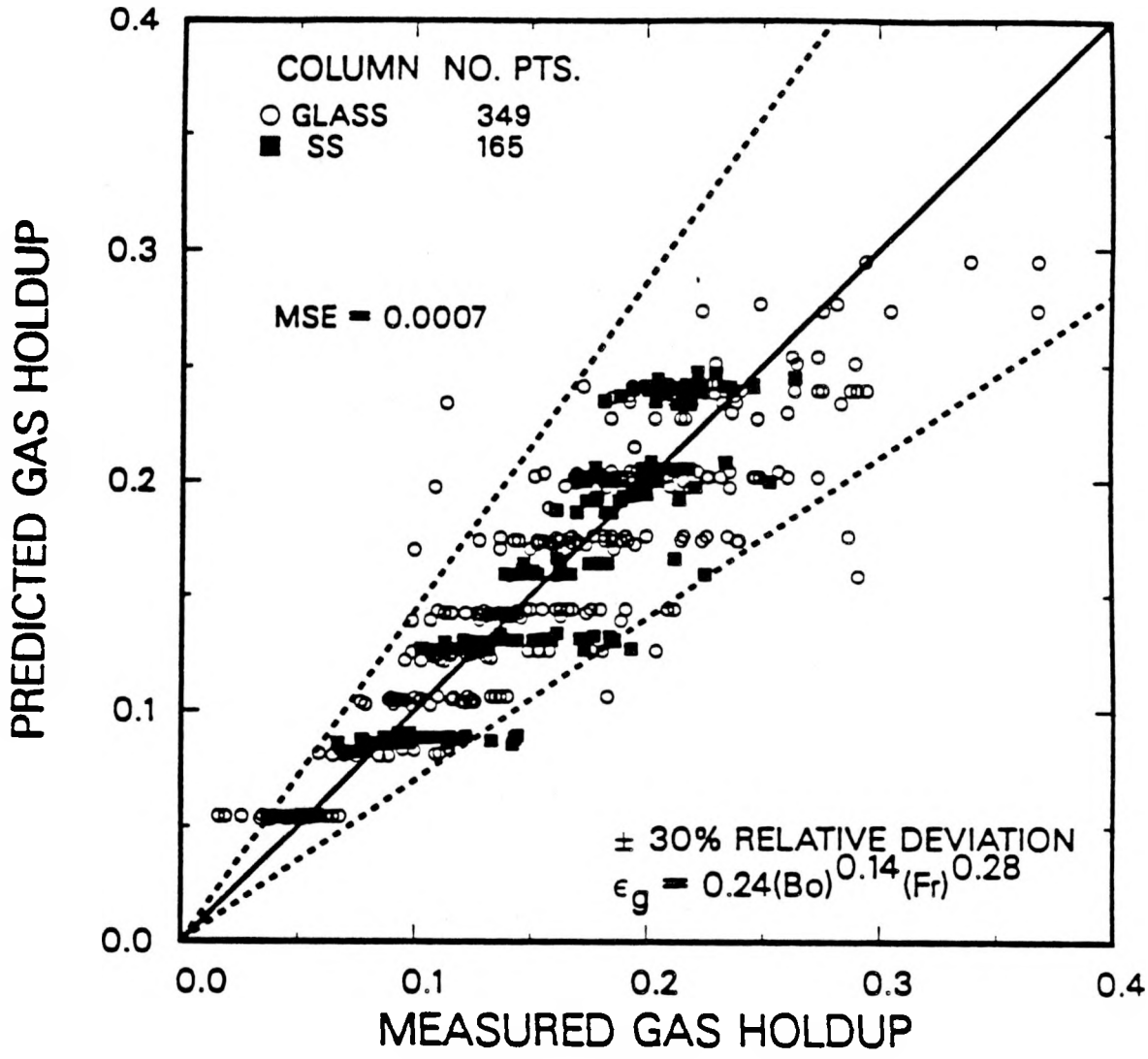

Figure 2.40. Parity plot of predicted versus measured gas holdup (wax type: SASOL, FT-300, Mobil; u_g = 0.01 to 0.15 m/s; $u_{s\ell}$= 0, 0.005, and 0.02 m/s; d_c = 0.05 and 0.21 m ID; solids: 0, 10, 20, and 30 wt% iron oxide and silica).

III. MEASUREMENT OF PHASE FRACTIONS BY GAMMA–RAY DENSITOMETRY

In many applications of industrial importance, systems operate at high temperatures and pressures. Under these conditions, experimental techniques commonly employed in hydrodynamic studies with systems that operate at low temperatures and pressures may not be applicable. Gamma–ray densitometry in a non–intrusive technique which may be used to measure various hydrodynamic parameters at high temperatures and pressures. The majority of previous investigations which have utilized this technique were limited to two–phase systems. Recently, several investigators (Seo and Gidaspow, 1987; Bernatowicz et al., 1987; and Abouelwafa and Kendall, 1980) have successfully used this technique to measure phase fractions in three–phase systems. However, the thickness of the absorbing media was less than 0.03 m. The objective of this work was to design and construct a dual energy gamma–ray densitometer which could be used to measure volume fractions (gas/liquid/solids) in a large diameter (0.21 m ID) bubble column.

Experiments were conducted using both two–phase and three–phase systems (see Table 2.5). Volume fractions were measured with a dual energy gamma–ray densitometer during most of these experiments. The theory associated with gamma–ray absorption, the selection of sources, the experimental apparatus and calibration techniques used, the applicability of this technique to large diameter three–phase systems and results from experiments conducted in both two–phase and three–phase systems will be discussed.

Theoretical Discussion

Gamma–ray absorption is based on the fact that the intensity of radiation decreases as it passes through a material. The change in intensity, ΔI, is proportional to the

thickness of the material, Δx, and the incident intensity, I_o. Therefore,

$$\Delta I = -\mu I_o \Delta x \tag{3.1}$$

where μ is a proportionality constant called the mass attenuation coefficient. If the radiation is homogeneous, Eq. 3.1 may be written as:

$$dI = -\mu I_o dx \tag{3.2}$$

which upon integration yields:

$$I = I_o \exp(-\mu x) \tag{3.3}$$

The intensity of radiation is given by:

$$I = h\nu B \tag{3.4}$$

where $h\nu$ is the energy/photon, B_o is the incident number (i.e. no absorber) of photons crossing a unit area per unit time, and B is the number of uncollided photons crossing a unit area per unit time. Thus, Eq. 3.3 may be written in terms of the number of photons or counts per second,

$$B = B_o \exp(-\mu x) \tag{3.5}$$

As discussed by Attix (1968), attenuation of the energy of an incident photon may occur through both scattering and absorption of the photon. Attenuation by some purely elastic process in which a photon does not give up any of its initial energy to the medium, but is merely deflected, is called scattering (e.g. Raleigh scattering). Whereas, in absorption, the entire energy of the incident photon is absorbed. One type of absorption process is called the photoelectric effect. During this process, the entire energy of an incident photon is absorbed by an atom of the medium and an electron is emitted. Pair–production, is another process by which total absorption may occur. During pair–production, a photon may be totally absorbed in either the atomic nucleus

or the field of an atomic electron, and a positron–negatron pair is emitted. The Compton effect is the intermediate case, in which some of the energy of the incident photon is absorbed and appears as a Compton recoil electron, and the remaining incident energy is present as a Compton scattered electron. The attenuation process includes both scattering and absorption of the incident photon. Thus, the attenuation coefficient, μ is the sum of the absorption coefficients, μ_a and the scattering coefficients, μ_s.

For energies in the range 0.01 to 10 MeV, attenuation is due primarily to photoelectric interactions, Compton scattering and absorption, and pair–production. Figure 3.1 (from Evans, 1955), shows the energy ranges over which these competing effects dominate for various atomic numbers, Z. For relatively large values of Z, the photoelectric effect dominates at low energies and pair–production dominates at high energies.

Attix (1968) present interpolation formulas which may be used to estimate attenuation coefficients for compounds given attenuation coefficients for the elements comprising the compounds. They also give formulas for estimating absorption and scattering coefficients for elements for which experimental data are not available. The following formula may be used to estimate the attenuation coefficient, μ_{mix}, for a compound

$$\frac{\mu_{mix}}{\rho_{mix}} = \sum_i \frac{\mu_i}{\rho_i}\omega_i \qquad i = 1 \text{ to no. of components} \tag{3.6}$$

where μ_i is in cm^{-1} and ω_i is the weight fraction of component i. The following interpolation formula may be used to estimate either Compton absorption or Compton scattering coefficients, σ_i

$$\frac{\sigma_1}{\rho_1} = \left(\frac{\sigma_2}{\rho_2}\right)\left(\frac{A_2}{A_1}\right)\left(\frac{Z_1}{Z_2}\right) \tag{3.7}$$

where Z is the atomic number, A is the atomic mass, and the subsripts 1 and 2 represent any two elements. For the photoelectric effect, the interpolation formula for the absorption coefficient , τ_i, is

$$\frac{\tau_1}{\rho_1} = \left(\frac{\tau_2}{\rho_2}\right)\left(\frac{A_2}{A_1}\right)\left(\frac{Z_1}{Z_2}\right)^n \tag{3.8}$$

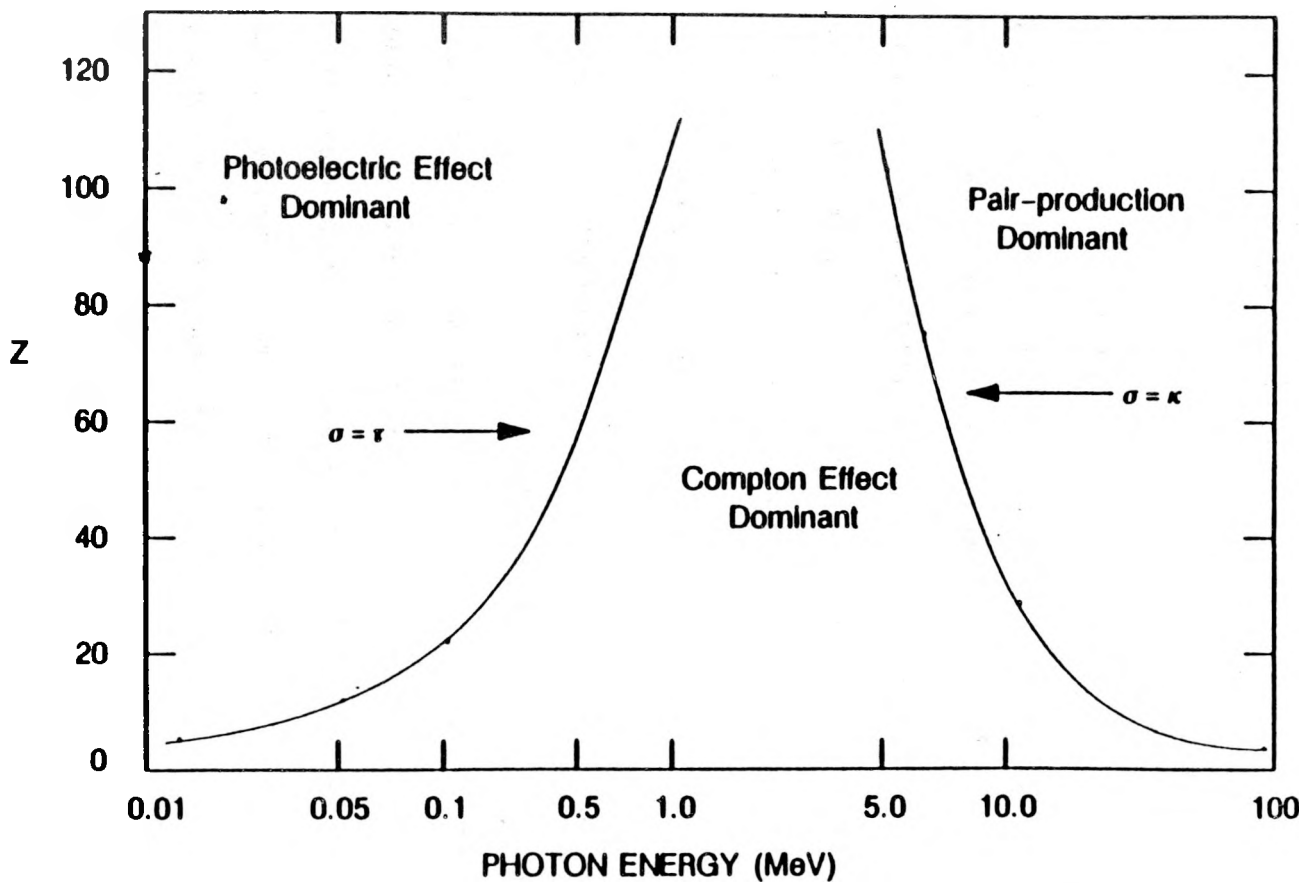

Figure 3.1. Relative importance of the three major types of gamma-ray attenuation.

where the exponent n is a function of the energy of the incident photon and ranges from 4 to 4.6. And, for pair–production,

$$\frac{\kappa_1}{\rho_1} = \left(\frac{\kappa_2}{\rho_2}\right)\left(\frac{A_2}{A_1}\right)\left(\frac{Z_1}{Z_2}\right)^2 \tag{3.9}$$

where κ_i is the absorption coefficient.

Models Used to Describe Three – Phase Systems

When the photons emitted from a radioactive source pass though a homogeneous material, a fraction of the energy associated with the photons is attenuated and Eq. 3.5 describes the absorption process. If multiple absorption mediums are aligned perpendicular to the incident beam of radiation (see Figure 3.2), the number of uncollided photons passing through the absorbing media per unit time is given by:

$$B = B_o \exp(-\sum_i \mu_i x_i) \qquad i = 1 \text{ to } n \tag{3.10}$$

where x_i is the thickness of absorber i; μ_i is the absorption coefficient for medium i; and n is the number of different absorbers.

In a three–phase bubble column, the gas, solid, and liquid phases are the absorbing media. The model used to describe the interaction between the beam of radiation and the three phases depends on the alignment of the three phases with respect to the beam of radiation. Two types of orientations were examined in this research. In one case, the three phases were assumed to be aligned perpendicular to the incident beam of radiation, and for the other case, all three phases were assumed to be aligned parallel to the beam of radiation. The two cases mentioned above represent the extremes of possible alignments.

Case I. Perpendicular Alignment

For the first case (i.e. perpendicular alignment), we assume that the beam of radiation may be represented by a cylinder, with the three phases occupying slices of

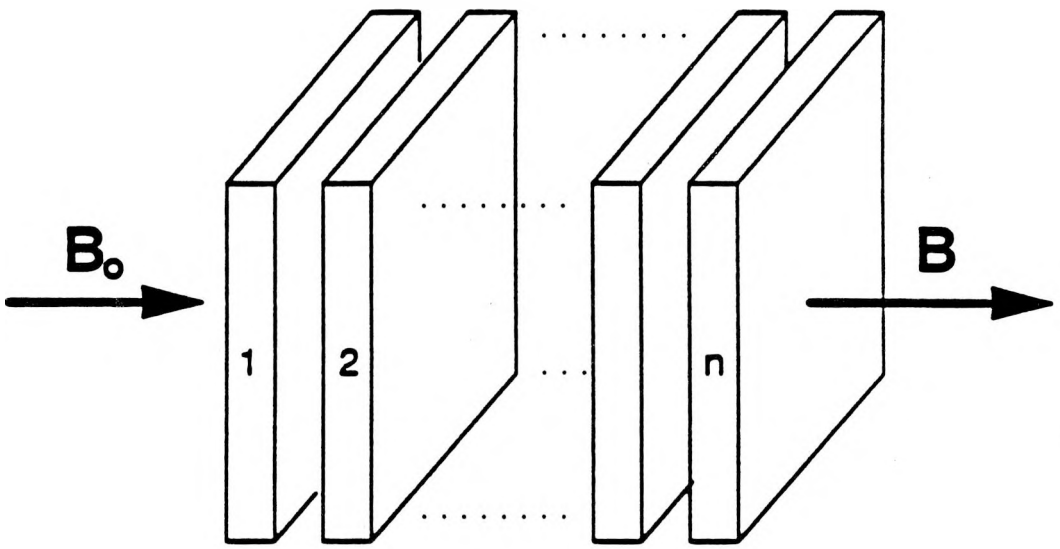

Figure 3.2. Schematic representation of multiple absorbers in series.

the cylinder (Figure 3.3). For this alignment, Eq. 3.10 may be used to describe the absorption process. The volume of phase i through which the beam of radiation passes is given by:

$$V_i = x_i A_x \qquad i = g, \ell, s \tag{3.11}$$

where A_x is the cross–sectional area of the absorbing media. The total volume of the absorbing media is

$$V_t = dA_x \tag{3.12}$$

The volume fraction of phase i, ϵ_i, is defined as the volume of phase i (Eq. 3.11) divided by the total volume (Eq. 3.12) and may be expressed as:

$$\epsilon_i = \frac{x_i A_x}{dA_x} \qquad i = g, \ell, s \tag{3.13}$$

or, the thickness of the absorbing media, x_i is

$$x_i = d\epsilon_i \qquad i = g, \ell, s \tag{3.14}$$

Substituting Eq. 3.14 into Eq. 3.10 for x_i yields the following expression for the amount of radiation transmitted through the column

$$B = B_o \exp[-d(\mu_g \epsilon_g + \mu_\ell \epsilon_\ell + \mu_s \epsilon_s)] \tag{3.15}$$

where the subscripts g, ℓ, and s refer to the gas, liquid, and solid phases, respectively. Equation 3.15 contains three unknowns, i.e. the volume fractions of the three phases. Thus, two additional equations are needed to characterize the system. Since attenuation coefficients are a function of radioactive source strength (i.e. energy), another equation arises from the use of an additional source. This equation is identical to Eq. 3.15 except that the values of the attenuation coefficients are different. These two equations along with a volume balance are used to obtain volume fractions of the individual phases.

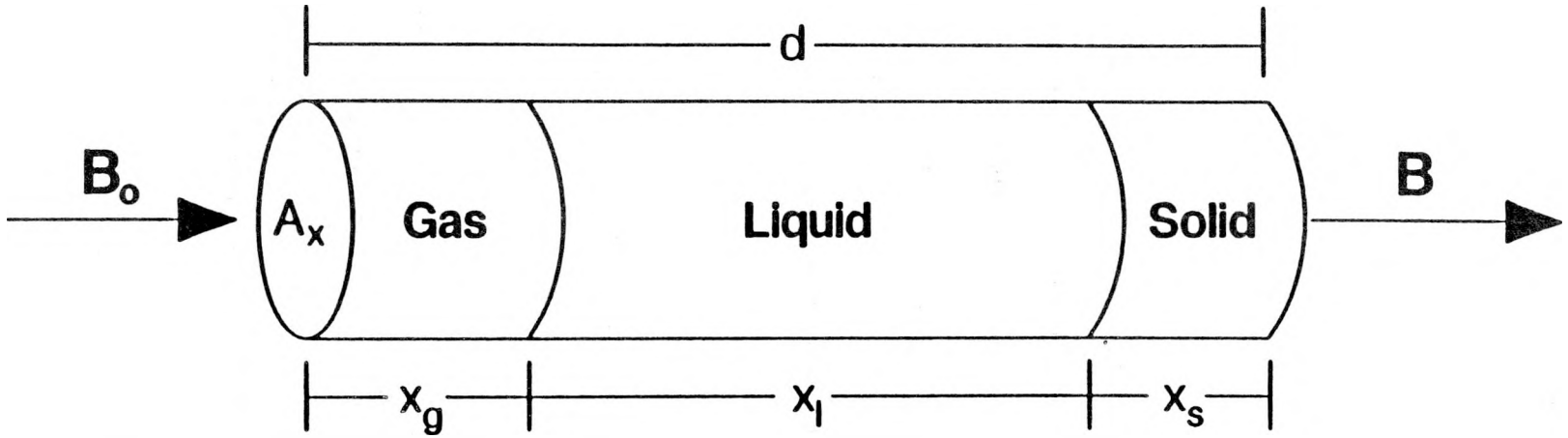

Figure 3.3. Schematic representation of Case I geometry (i.e. perpendicular alignment).

Thus, the set of equations used to determine volume fractions in a three–phase system is:

$$B_1 = B_{o1}\exp[-d(\mu_{g1}\epsilon_g + \mu_{\ell 1}\epsilon_\ell + \mu_{s1}\epsilon_s)] \tag{3.16}$$

$$B_2 = B_{o2}\exp[-d(\mu_{g2}\epsilon_g + \mu_{\ell 2}\epsilon_\ell + \mu_{s2}\epsilon_s)] \tag{3.17}$$

$$1 = \epsilon_g + \epsilon_\ell + \epsilon_s \tag{3.18}$$

where the subscripts 1 and 2 refer to the two different radioactive sources.

At atmospheric pressure, the attenuation of radiation due to the gas phase phase is negligible, and the quantity $\mu_{gi}\epsilon_{gi}$ may be omitted from equations 3.16 and 3.18. If the absorption by the gas phase is neglected, Eqs. 3.16 and 3.17 may be combined to yield a single expression for either the volume fraction of solids or the volume fraction of liquid. The volume fraction of the liquid phase is

$$\epsilon_\ell = \frac{\ln(B_1 / B_{o1})\mu_{s2} + \ln(B_2 / B_{o2})\mu_{s1}}{d(\mu_{\ell 2}\mu_{s1} - \mu_{\ell 1}\mu_{s2})} \tag{3.19}$$

Once the value of ϵ_ℓ is known, it is substituted into either Eq. 3.16 or Eq. 3.17 to obtain a value for ϵ_s. The gas holdup is then calculated from Eq. 3.18.

Case II. Parallel Alignment

Another possible geometric relationship between the incident beam of radiation and the absorbing media is when the three phases are aligned in parallel with respect to the beam of radiation (see Figure 3.4). A fraction of the incident beam of radiation passes through each phase separately. The fraction of the incident beam passing through a given phase is

$$f_{o_i} = \frac{A_i}{A_x} = \epsilon_i \qquad i = g, \ell, s \tag{3.20}$$

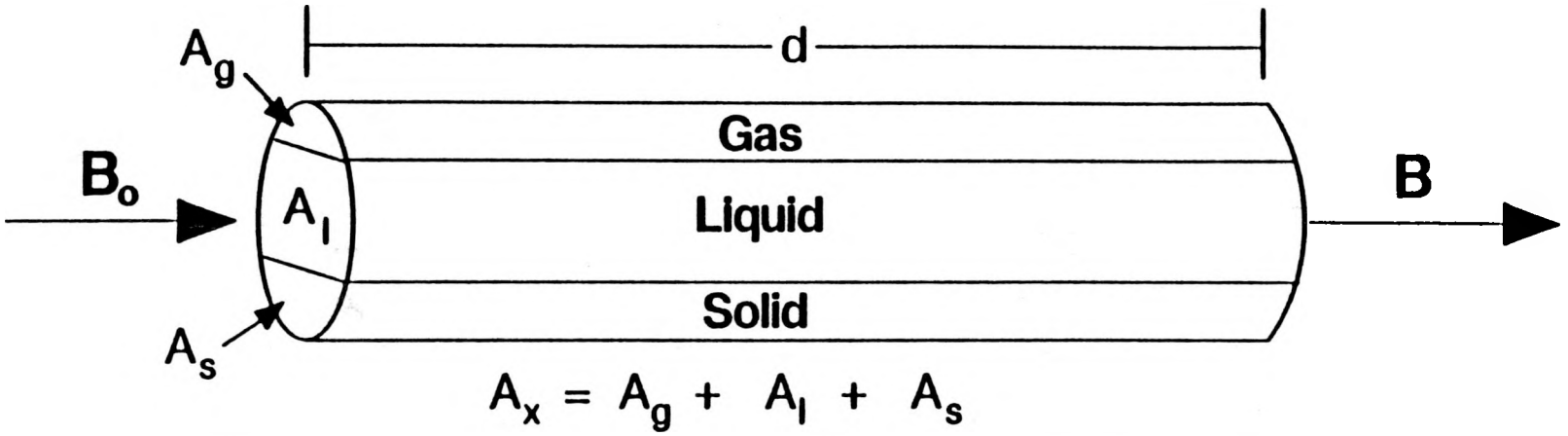

Figure 3.4. Schematic representation of Case II geometry (i.e. parallel alignment).

where A_i is the cross–sectional area of the cylinder occupied by the i^{th} phase. Thus, the amount of radiation passing through a given phase is

$$B_i = B_o \epsilon_i \exp(-\mu_i d) \qquad i = g, \ell, s \tag{3.21}$$

The total amount of radiation which passes through the absorbing media is the sum of the amounts of radiation which passes through the three phases,

$$B = B_o[\epsilon_g \exp(-d\mu_g) + \epsilon_\ell \exp(-d\mu_\ell) + \epsilon_s \exp(-d\mu_s)] \tag{3.22}$$

Once again, two different radioactive sources are needed and we may assume that attenuation due to the gas phase is negligible. The final set of equations used to describe this type of configuration is:

$$B_1 = B_{o1}[\epsilon_g + \epsilon_\ell \exp(-d\mu_{\ell 1}) + \epsilon_s \exp(-d\mu_{s1})] \tag{3.23}$$

$$B_2 = B_{o2}[\epsilon_g + \epsilon_\ell \exp(-d\mu_{\ell 2}) + \epsilon_s \exp(-d\mu_{s2})] \tag{3.24}$$

$$1 = \epsilon_g + \epsilon_\ell + \epsilon_s \tag{3.25}$$

Equations 3.23 to 3.25 may be solved to obtain the following expression for ϵ_ℓ,

$$\epsilon_\ell = \frac{(B_1 / B_{o1}) - 1 - \frac{((B_2/B_{o2})-1)(\exp(-d\mu_{s1})-1)}{(\exp(-d\mu_{s2})-1)}}{(\exp(-d\mu_{\ell 1}) - 1) - \frac{(\exp(-d\mu_{\ell 2})-1)(\exp(-d\mu_{s1})-1)}{\exp(-d\mu_{s2})-1}} \tag{3.26}$$

Equation 3.25 may be substituted into either Eq. 3.23 or Eq. 3.24 to obtain an expression for ϵ_s in terms of ϵ_ℓ. If Eq. 3.24 is used, the expression for ϵ_s is

$$\epsilon_s = \frac{(B / B_{o2}) - 1 - \epsilon_\ell(\exp(-d\mu_{\ell 2}) - 1)}{\exp(-d\mu_{s2}) - 1} \tag{3.27}$$

The value of ϵ_ℓ calculated from Eq. 3.26 is substituted into Eq. 3.27 to obtain a value for ϵ_s. Using these two values, the gas holdup, ϵ_g, is calculated directly from Eq. 3.25.

Comments on the Alignment of the Phases

Actual phase alignment with respect to the beam of radiation for two and three–phase flow will lie between the two cases described above. However, since there is a considerable amount of homogeneity in the flow patterns (except in the slug flow regime) in bubble columns, it may be assumed that the majority of the radiation will be attenuated according to Case I alignment.

Previous studies with three–phase systems (e.g. Bernatowicz et al., 1987; Seo and Gidaspow, 1987; Abouelwafa and Kendall, 1980) used Case I alignment (i.e. phases perpendicular to incident beam of radiation) to model the attenuation process. Petrick (1958) constructed several lucite models representative of different types of flow patterns in a two–phase system. There was excellent agreement between the predicted volume fractions and the actual volume fractions ($< 7\%$ relative error) assuming Case I alignment. In his experiments, he measured the volume fractions at various radial locations and used the average value. He also measured the volume fraction at a single location (i.e "one shot" method), and the error between the actual and predicted volume fractions was considerably higher ($< 36\%$ relative error) for models representative of non–homogeneous flow conditions. Under actual two–phase flow conditions in a vertical tube (air–water system), Petrick showed that when the width of the beam of radiation was equal to the width of the absorbing medium (i.e. the column diameter), there was no difference between volume fractions predicted using several measurements and averaging the results, and volume fractions obtained using the "one shot" method. However, when the column diameter was increased such that the width of the beam of radiation was less than the column diameter, he observed differences in the volume fraction calculated using the two techniques. He attributed the differences in results, to differences in the radial distribution of the volume fractions of air and water. Thus,

not only phase alignment, but also phase distributions (i.e. axial and radial variations in phase fractions) need to be taken into account when using the gamma–ray technique.

Figures 3.5a and 3.5b are schematic representations of two possible phase distributions (two–phases) in a square channel. Figure 3.5a represents annular flow, in which a gas fills the center of the duct, and Figure 3.5b, represents homogeneous flow (i.e. no radial variation in volume fractions). Based on the dimensionless distances given in Figure 3.5, the actual volume fraction of gas is 0.25 for both cases. For homogeneous flow conditions (Figure 3.5b), regardless of the radial location of the measurement, the volume fraction of gas (or liquid) may be accurately determined at any location assuming Case I alignment (i.e. using Eq. 3.10). However, for annular flow, if a single measurement is made in the center of the duct (see section A in Figure 3.5a), the measured volume fraction of gas obtained assuming Case I alignment would be 0.5 as opposed to the actual value of 0.25. Phase alignment becomes a problem, if measurements are made through section B in Figure 3.5a. In order to overcome these problems, measurements should be made at various locations across the duct and the volume fractions obtained from each measurement (via Eq. 3.10) should be averaged over the entire cross section of the duct to obtain an accurate estimate of the phase fractions.

Source Selection and Sensitivity Analysis

A gamma–ray densitometer system consists of three main parts: (1) radioactive sources, (2) detectors, and (3) associated electronic equipment. Of the three main components, the sources are the most important.

One must consider several factors, when selecting sources. These include transmission through the pipe walls and sensitivity to the slurry content. These two factors are competing. The lower the gamma–ray energy (i.e. higher attenuation) the more sensitive the system is to changes in the volume fractions of the slurry; however, with a

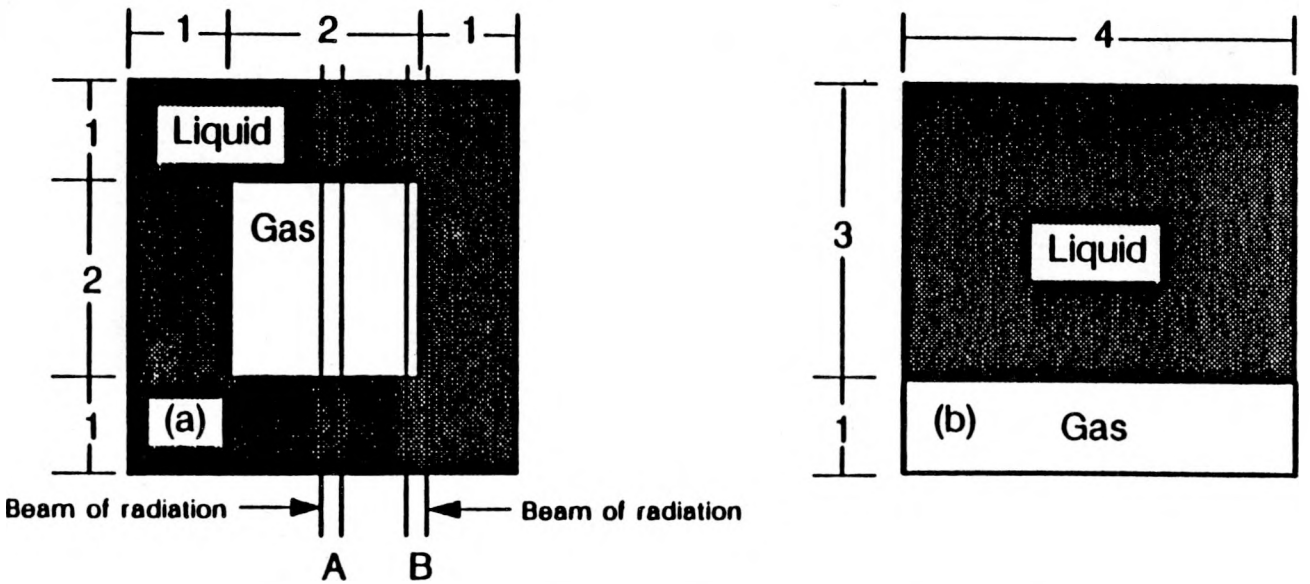

Figure 3.5. Schematic representations of (a) annular flow and (b) homogeneous flow in a square duct.

low energy source, more of the photons emitted from the source are attenuated by the vessel walls. This becomes a significant factor when the vessels (i.e. bubble column in this case) have thick metal walls. Other factors which need to be considered are the half–life of the source and the availability of the source. If a source with a very short half–life is used, then calibrations of the empty test section will have to be repeated frequently. This is to ensure that the initial count rate (or count rate through the empty pipe, B_o) is correct.

The factors described above need to be considered when selecting sources for both two–phase and three–phase applications. However, when two sources are required (i.e. three–phase measurements) one other criterion must be taken into account. Abouel-wafa and Kendall (1980) contend that the gamma–ray technique may be applied to multiphase systems provided the attenuation coefficients for the various phases are "different" for the sources selected. However, they never quantify what is meant by "different". It is obvious from Eqs. 3.16 and 3.17 that the attenuation coefficients for each phase must be "different" for the equations to be independent. However, it should be pointed out that while this is true, the following restriction must also be applied

$$\left(\frac{\mu_{\ell_1}}{\mu_{s_1}}\right)\left(\frac{\mu_{s_2}}{\mu_{\ell_2}}\right) \neq 1 \tag{3.28}$$

If the above criterion is not satisfied, the denominator in Eq. 3.19 is zero and volume fractions cannot be calculated. This poses a serious problem when the gamma–ray technique is applied to large diameter systems. As discussed previously, attenuation is due primarily to the photoelectric effect, Compton scattering and absorption, and pair production. Furthermore the various types of attenuations (i.e. photoelectric, Compton, and pair production) dominate at certain energy levels as shown in Figure 3.1. If two different sources are selected, with different attenuation coefficients; however, if attenuation is dominated by the same process for both sources, the denominator in

Eq. 3.19 approaches 0.0 making the calculated value of ϵ_ℓ very sensitive to slight errors in the measured quantities (i.e. count rates). It follows from Eqs. 3.6 to 3.9 that the best results would be obtained if a low energy source (i.e. one in which attenuation was dominated by the photoelectric effect) and a relatively high energy source (i.e. one in which attenuation was dominated by Compton scattering and absorption) were used.

However, in a large diameter system, it may not be possible to use a low energy source since the majority of the radiation will be attenuated by the absorbing medium. Thus, it is necessary to use a higher energy source. If this is the case, then the second source would have to be extremely powerful (i.e. energy $>$ 10 MeV) to satisfy the criterion presented in Eq. 3.28. However, these sources pose serious safety problems and may not be readily available.

Nevertheless, for a given set of two sources, the appropriate source activity must be chosen. The activity required will depend on several factors, including the counting period, collimation diameter, length of the collimator, detector efficiency, and emission ratio of the desired gamma–rays (Chan and Banerjee, 1981).

It is well known that the counting process is a Poisson process, where the probability of n counts occurring in the time interval Δt is given by:

$$P_n = \frac{(B\Delta t)^n}{n!}\exp(B\Delta t) \qquad (3.29)$$

The mean and variance of the Poisson process is B (i.e. the count rate). The standard deviation is $\sqrt{B}$. Thus, the actual count rate is the measured count rate $\pm \sqrt{B}$. Hence, the uncertainty in the count rate is $\frac{\sqrt{B}}{B}$. If B_o (i.e. empty column count rate) is measured over an extended period of time, the statistical error in B_o is assumed to be insignificantly small and the statistical error in void fractions may be calculated assuming only errors (or uncertainty) in the measured count rates (i.e. B).

Commercially available sources, with energies ranging from 0.0595 MeV (Americium – 241) to 1.17,1.33 MeV (Cobalt–60) were used to simulate the effect of uncertainty in the count rate on the predicted phase fractions. The two source combinations used to study the effect of errors in count rate on phase fractions were: (1) Americium – 241 – Cobalt–60 and (2) Cesium–137 (0.661 MeV) – Cobalt–60. For these simulations, the liquid phase was assumed to be a straight chain (C52) paraffin wax (MW = 730), and the solid phase was iron oxide. For the purpose of these calculations, Case 1 alignment was used, and the attenuation due to the gas phase was assumed negligible.

The attenuation coefficients for the solid and liquid phases for each source were estimated from data presented by Attix (1968). Attenuation coefficients are given by Attix for elements with atomic numbers up to 28 for energies ranging from 0.01 to 10 MeV. Equation 3.6 was used to estimate the attenuation coefficients for iron oxide and wax. Table 3.1 lists the attenuation coefficients used for sensitivity analysis. The criterion established in Eq. 3.28 is satisfied for both source combinations. For the Americium–Cobalt system, the quantity on the left hand side of Eq. 3.28 is 0.2, and for the Cesium–Cobalt system, the quantity on the left hand side of Eq. 3.28 is 0.98. Thus, one would expect that slight errors in measured quantities (i.e. count rates) would have less of an effect on the predicted volume fractions for the Americium–Cobalt system as compared to the Cesium–Cobalt system.

Tables 3.2a and 3.2b show results for the Americium–Cobalt system for errors in the count rate of Cobalt and errors in the count rate of Americium, respectively. An error of 1% in the Cobalt count rate corresponds to an error of approximately 10% in the predicted gas holdup. However, an error of 10 % in the Americium count rate would produce an error of only 4.5 % in the predicted gas holdup. Tables 3.3a and 3.3b show results for the Cesium–Cobalt system. For this system, an error of only 0.1 % in the count rates of Cesium or Cobalt produces an error of 19% and 26%, respectively, in the

Table 3.1. Attenuation Coefficients (cm^{-1}) Used for Error Analysis Calculations

ABSORBING MEDIUM	SOURCE		
	Am–241	Co–60	Cs–137
WAX ($C_{52}H_{106}$)	0.139	0.0423	0.0580
IRON OXIDE	4.575	0.2710	0.3820

Table 3.2a. Effect of Errors in the Count Rate of Co–60 on Volume Fractions Using the Am–241 and Co–60 System

% ERROR IN COUNT RATE	ϵ_g	% error	ϵ_s	% error
+0.1	0.152	1.3	0.0300	–
+0.5	0.157	4.7	0.0302	0.7
+1.0	0.165	10.0	0.0305	1.7
+5.0	0.223	48.7	0.0320	6.7
+10.0	0.294	96.0	0.0340	13.3

Table 3.2b. Effect of Errors in the Count Rate of Am–241 on Volume Fractions Using the Am–241 and Co–60 System

% ERROR IN COUNT RATE	ϵ_g	% error	ϵ_s	% error
+0.1	0.1500	–	0.0300	–
+0.5	0.1496	0.27	0.0299	0.3
+1.0	0.1492	0.5	0.0305	0.7
+5.0	0.1462	2.5	0.0320	2.3
+10.0	0.1426	4.9	0.0286	4.7

Base Conditions: $\epsilon_g = 0.15$, $\epsilon_\ell = 0.82$, and $\epsilon_s = 0.03$

Table 3.3a. Effect of Errors in the Count Rate of Co–60 on Volume Fractions Using the Cs–137 and Co–60 System

% ERROR IN COUNTRATE	ϵ_g	% error	ϵ_s	% error
+0.1	0.189	26	0.037	23
+0.5	0.344	129	0.065	117
+1.0	0.537	258	0.099	230
+5.0	2.050	1267	0.370	1133
+10.0	3.860	2473	0.694	2213

Table 3.3b. Effect of Errors in the Count Rate of Cs–137 on Volume Fractions Using the Cs–137 and Co–60 System

% ERROR IN COUNTRATE	ϵ_g	% error	ϵ_s	% error
+0.1	0.122	19	0.025	17
+0.5	0.013	91	0.0057	83
+1.0	-0.123	182	-0.021	170
+5.0	-1.170	893	-0.218	827
+10.0	-2.468	1745	-0.454	1613

Base Conditions: $\epsilon_g = 0.15$, $\epsilon_\ell = 0.82$, and $\epsilon_s = 0.03$

predicted gas holdup values. It is obvious from these results, that in order to accurately measure individual volume fractions in a three–phase system, one must use a relatively low energy source (e.g. Americium–241) and a high energy source (e.g. Cobalt–60).

If a suitable low energy gamma source is not available, then a three–phase system may be treated as a two–phase system (i.e. treat the solid phase and the liquid phase as a single phase), provided the weight fractions of the solid and liquid phases are known. These quantities are needed to calculate the attenuation coefficient for the slurry (see Eq. 3.6),

$$\frac{\mu_{s\ell}}{\rho_{s\ell}} = \sum_{i} \frac{\mu_i}{\rho_i} \omega_i \qquad i = 1 \text{ to no. of components} \tag{3.30}$$

The volume fraction of the slurry may be calculated using (see Eq. 3.10),

$$\epsilon_{s\ell} = \frac{-\ln(B \,/\, B_o)}{d\mu_{s\ell}} \tag{3.31}$$

where $\epsilon_{s\ell} = \epsilon_s + \epsilon_\ell$.

Experimental Apparatus and Operating Conditions

During some of the experiments in the 0.21 m ID column, the dual energy nuclear density gauge was used to determine gas holdups at various radial and axial locations. The density gauge system was composed of a movable assembly mechanism (MAM) which was used to transport the gauge both axially and radially along the column, two radioactive sources, two NaI detectors, and the associated electronics.

Movable Assembly Mechanism (MAM)

The MAM is used to transport the nuclear density gauges both axially and radially along the column. It is divided into two main parts, the axial movement mechanism (Figure 3.6) and the radial movement mechanism (Figure 3.7). Separate axial and radial movement mechanisms for the sources and detectors were constructed. Each axial movement mechanism consisted of a 6.35 cm diameter ball screw (Saginaw),

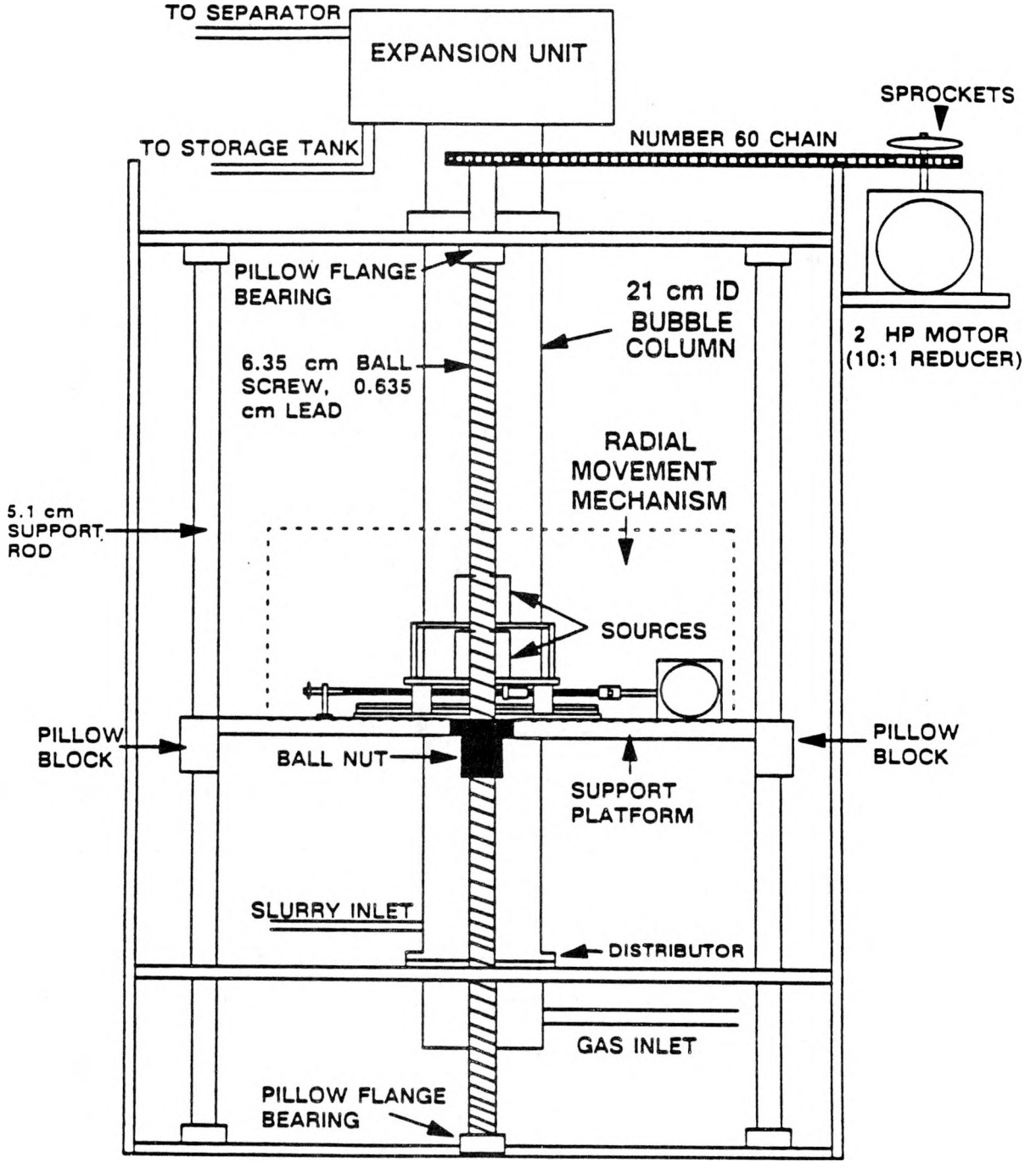

Figure 3.6. Schematic diagram of axial movement mechanism for the nuclear density gauge apparatus.

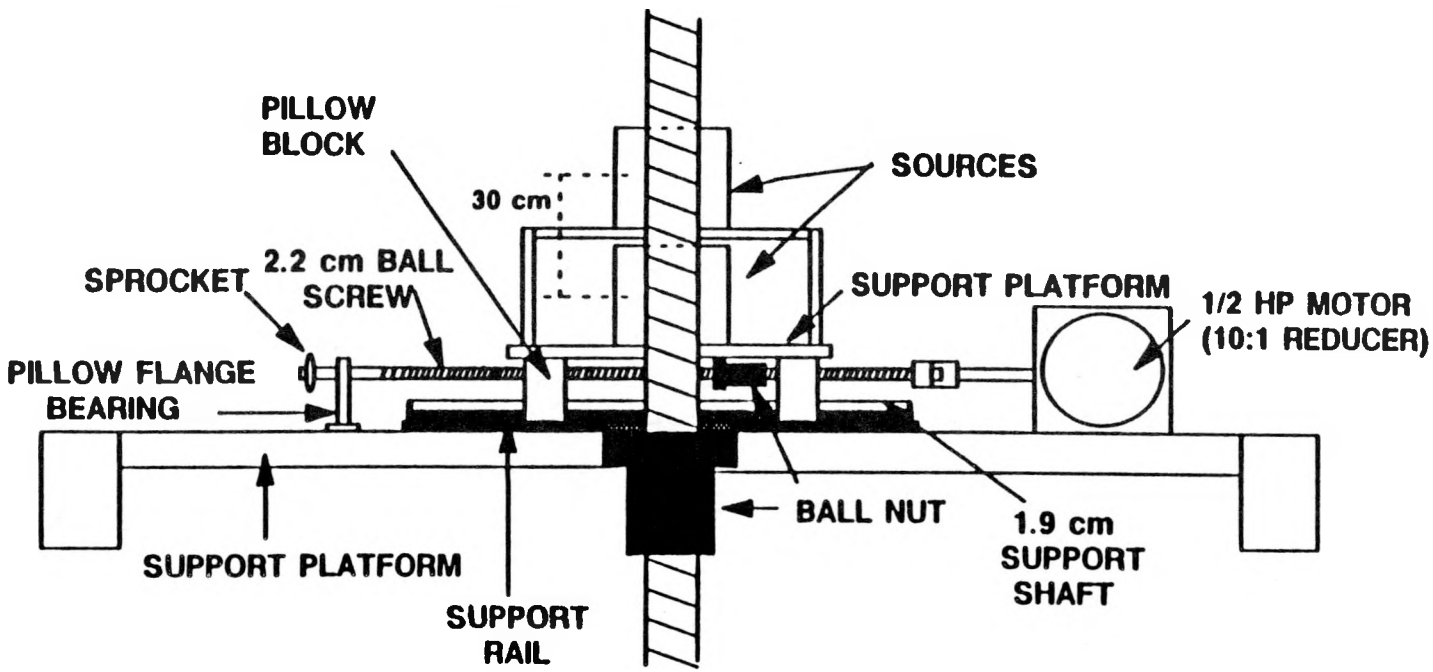

Figure 3.7. Schematic diagram of the radial movement mechanism for the nuclear density gauge apparatus.

3.3 m long, two support rods (5.1 cm diameter, 3.17 m long solids steel shafts), two 5.1 cm pillow blocks (Saginaw, SPB–32-ADJ), one non–preloaded ball nut (Saginaw, 5703263), two pillow flange bearings (Dodge, 059076), and one 1.27 cm thick aluminum plate on which the radial movement mechanism, was mounted. A 2 HP motor (Reliance, T16#3030) equipped with a 10:1 Tygear reducer (MR94667) and double single sprocket was mounted at the top of the apparatus and was used to transport the density gauge axially.

The radial movement mechanism was located on top of the aluminum plate described above (see Figure 3.7). Each radial movement mechanism consisted of two support shafts (1.9 cm diameter, 0.61 m long) which were mounted to two support rails (Saginaw, SR–12–PD), four pillow blocks (Saginaw, SPB–12–OPN), one ball screw 2.2 cm in diameter and 0.66 m long (Saginaw), one ball nut (Saginaw, 5708277), two pillow flange bearings (Dodge), and two 1.27 cm thick aluminum plates which supported the detectors or sources. A 1/4 HP motor (Reliance, T56H1019) equipped with a 10:1 Tygear reducer (MR94751) was mounted directly to the ball screw used to transport the sources radially. A chain and associated sprockets connected the radial movement mechanisms for the sources and detectors.

A series of magnetic switches were used to position the density gauge at predetermined locations (both axial and radial). The magnetic switches were connected to the motors and once activated, would turn–off the motor. Thus, measurements were made at the same location each time. This is extremely important for radial measurements, since the distance through the pipe varies with the radial position.

Sources and Detectors

A 35 mCi Cobalt–60 source, a 50 mCi Cesium–137 source, and a 300 mCi Americium – 241 source were used throughout our studies. The Cs–137 and Am–241 sources were donated by the Department of Energy and were previously used by Scientific

Applications Incorporated. The Cs–137 source was an encapsulated ceramic cylinder 3 mm in diameter and 3 mm long. The Co–60 source was an encapsulated metal cylinder of Cobalt–60, 1 mm by 1 mm. Am–241 was a disc source measuring approximately 12 mm in diameter. The Am–241 source was tested in our system by placing it in a source holder without any collimation and using a NaI (sodium iodide) detector (1.5" diameter crystal, 1 mm thick) with a beryllium window. The column was filled with water and air was bubbled through. The count rate measured at the detector was approximately 150 counts/sec. Once collimated, the count rate would be substantially lower. We consulted various manufacturers about low energy gamma sources; however, we were unable to locate a point source with sufficient activity for our application. The strongest low energy gamma source we were able to locate was a 5 Ci Am–241 disc source with an effective diameter of 40 mm. However, once collimated with a 2.54 cm long collimator, 0.63 cm in diameter, the estimated count rate would be approximately 30 counts/sec. One other alternative available was to have a low energy source manufactured which consisted of several disc or cylindrical sources aligned in series. Amersham makes a 25 Ci Am–241 source measuring 85 mm in length and 40 mm in diameter. If this source was used, we could expect a count rate of approximately 150 counts/sec, which is still extremely low. For dynamic systems, where the volume fraction of the individual phases at a given location fluctuate with time, higher count rates are required because the response time of the ratemeter is a function of the count rate. For a count rate of 150 counts/sec, it takes approximately 20 seconds (our system) for the count rate from the ratemeter to reach 99 % of its actual value. Thus, if count rates are measured over a short period of time, it is possible that they will not reflect the true (or average) count rate. Since, we were unable to obtain a low energy gamma source, we decided to use the Co–60 source and Cs–137 source as our two sources. We did not expect to obtain good results for three–phase measurements using this system (based on the discussion

presented in the section entitled Source Selection and Sensitivity Analysis); however, we felt we could always treat our three–phase system as a two–phase system using the measured weight fraction of solids (see Chapter II) to calculate a mean attenuation coefficient for the slurry.

The two source holders used to house the Co–60 and Cs–137 sources during measurements are shown in Figures 3.8 and 3.9, respectively. The Cobalt–60 source was collimated through a 76 mm long opening 5.1 mm in diameter and the Cesium source was collimated through a 50.8 mm long opening 6.35 mm in diameter. The source holders were designed such that the level of radiation detected at approximately 2 feet from the source (not including the open end) was less than 0.4 mrem/h.

NaI detectors (3.81 mm crystal diameter, 3.81 mm thick) manufactured by Bicron corporation were used with both the Co–60 source and Cs–137 source. The detectors were placed in an aluminum housings equipped with cooling coils (see Figure 3.10). A thermocouple was attached to the wall of the housing to monitor changes in the detector temperature. Collimators were also placed at the front of each detector and were approximately 38 mm long with a diameter of 6.35 mm.

Nuclear Electronics

A separate set of nuclear electronic components were used for each source–detector system so that data could be acquired simultaneously from both detectors. All nuclear electronics were manufactured by Tennelec and are listed in Table 3.4. Figure 3.11 is a schematic representation of the nuclear density gauge including the source, detector, electronics, and data acquisition system. The data acquisition system was the same as that used for acquiring data from the pressure transducers. The individual gamma pulses are amplified by the preamplifier, shaped and further amplified by an amplifier. Pulses from the amplifier pass through the single channel analyzer (SCA) which discriminates between different pulses so that only pulses corresponding to a given energy level are

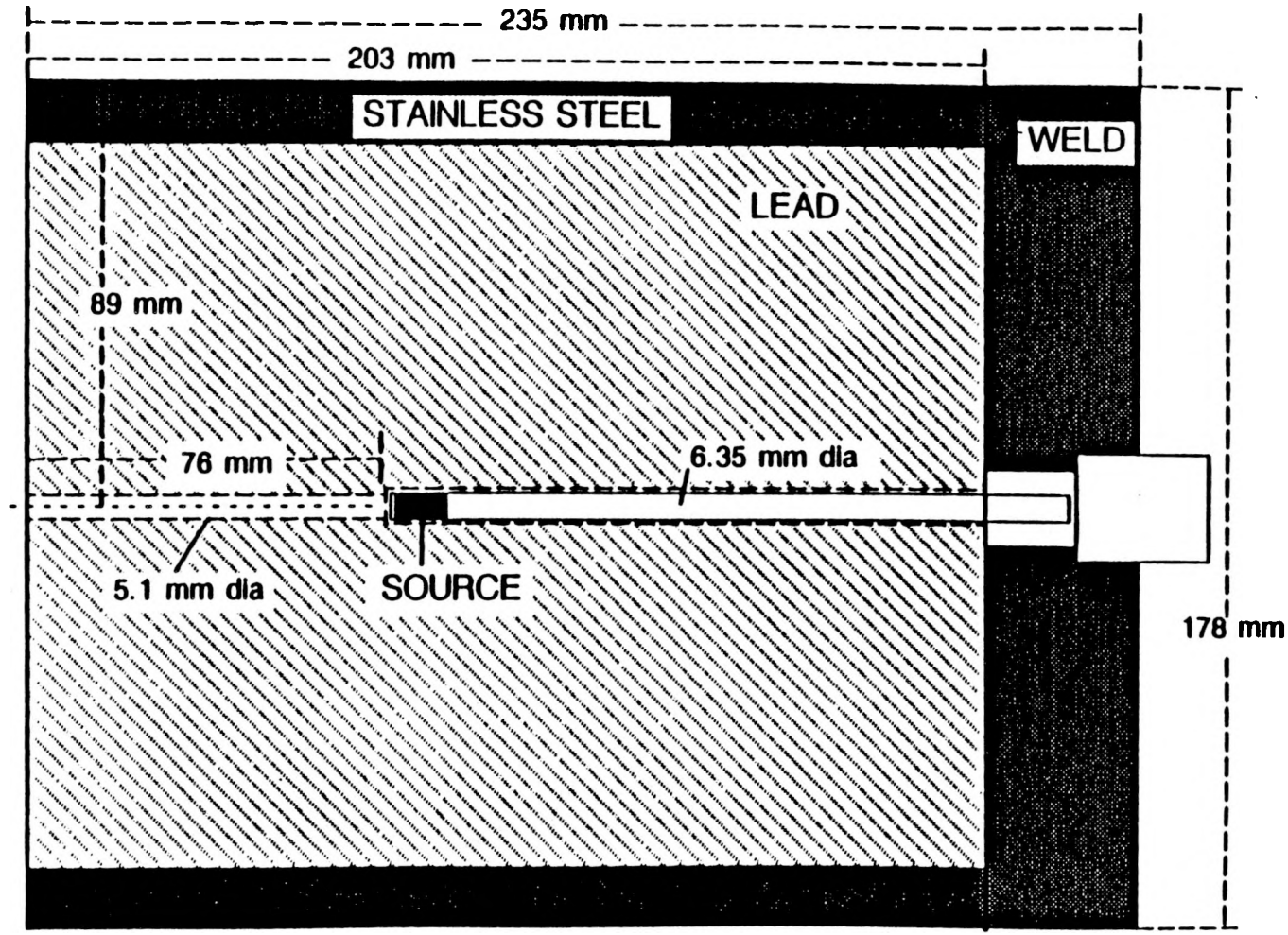

Figure 3.8. Schematic representation of the Cobalt-60 source holder.

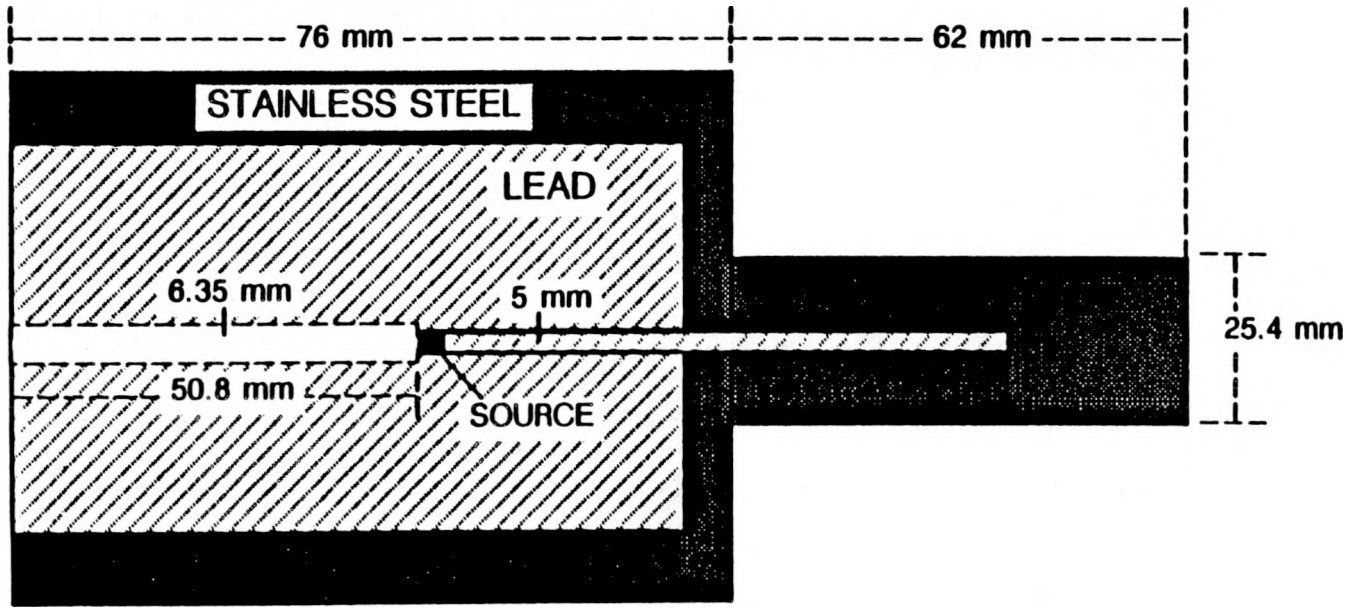

Figure 3.9. Schematic representation of the Ceslum-137 source holder.

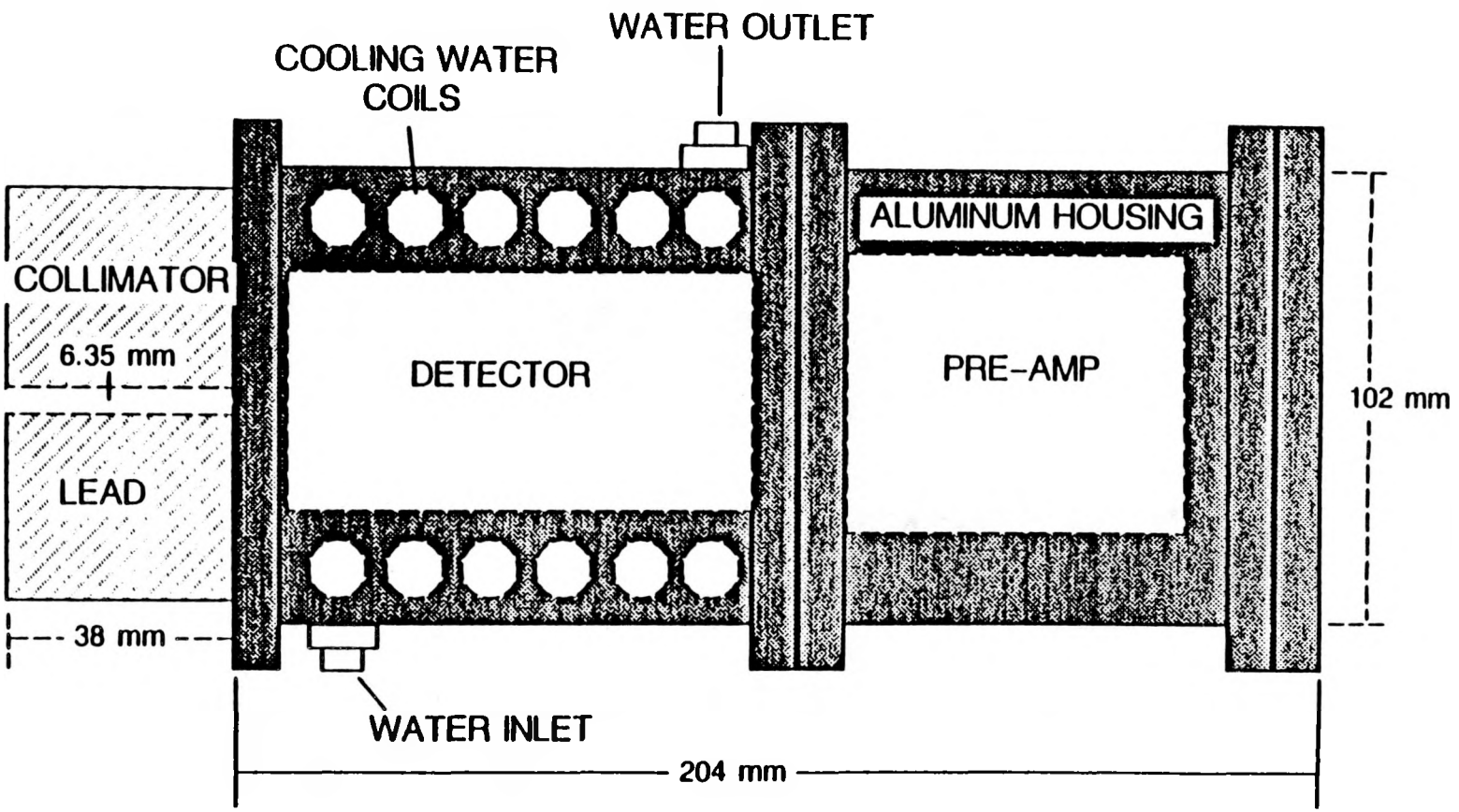

Figure 3.10. Schematic representation of the detector housing for the Cobalt-60 and Cesium-137 sources.

Table 3.4. Summary of Nuclear Density Gauge Electronics

EQUIPMENT	MANUFACTURER	MODEL #
DETECTOR	BICRON	1.5M1.5/1.5
HIGH VOLTAGE SUPPLY	TENNELEC	TC-948
PRE-AMPLIFIER	TENNELEC	TC-154A
AMPLIFIER	TENNELEC	TC-248
SCA[a]	TENNELEC	TC-450
RATEMETER	TENNELEC	TC-526

[a] SCA: Single channel analyzer

Table 3.5. Summary of Settings for the High Voltage Supply (HVS), Amplifier (AMP), and Single Channel Analyzer (SCA)

INSTRUMENT	DIAL	Co-60	Cs-137
HV	OUTPUT VOLTAGE	681	585
AMP	COARSE GAIN	100	50
	FINE GAIN	1.17	0.57
	TIMING AMP GAIN	50	50
SCA	UPPER LEVEL	9.5	5.0
	LOWER LEVEL	5.1	4.5

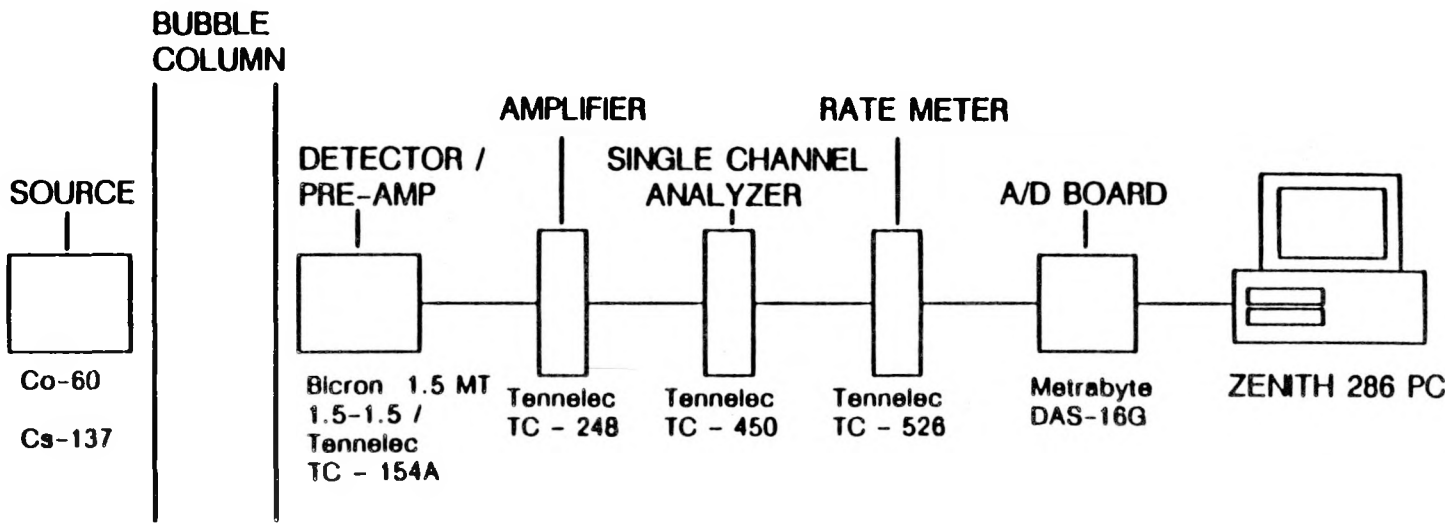

Figure 3.11. Schematic diagram of the nuclear density gauge electronic and data acquisition system.

counted. The output pulses from the SCA are then fed into the ratemeter and a voltage corresponding to the count rate is sent to the computer for data acquisition.

The single channel analyzers were operated in the normal mode of operation. Since we did not have access to a multichannel analyzer, the windows (i.e. lower level thresholds and upper level thresholds) were set experimentally using the procedure outlined in the SCA manual provided by Tennelec. The settings of the SCA as well as the other instrumentation is given in Table 3.5.

Calibration Procedures

Once the electronics were adjusted, calibration procedures were initiated to obtain attenuation coefficients for SASOL wax, FT–300 wax, iron oxide, and silica. A 0.1524 m wide x .1524 m deep x 0.61 m tall stainless steel chamber was constructed for conducting calibrations (see Figure 3.12). Attenuation coefficients were determined for wax at 265 ° C. In order to obtain the attenuation coefficient for pure wax (i.e. no solids), two measurements were made: (1) empty chamber, B_o and (2) full chamber, B. Knowing B, Bo and the thickness of the absorbing medium, d (i.e. 0.1524 m) the attenuation coefficient for the liquid phase was calculated using:

$$\mu_\ell = \frac{\ln(B / B_o)}{-d} \tag{3.32}$$

The attenuation coefficients for the solids (i.e. iron oxide and silica) could not be measured using the same procedure (i.e. filling the calibration chamber with pure solids) since voids exist between the individual solid particles. Due to the presence of the voids, the exact width of the absorbing medium is not known. To overcome this problem, a slurry composed of wax and solids was used to acquire the attenuation coefficients of the solids. First, an empty chamber count rate, B_o was obtained. Then, a known amount of wax was added to the calibration chamber and heated to 265 °C. Once at temperature, solids were added to form a 10 wt % slurry. A stirrer was used to

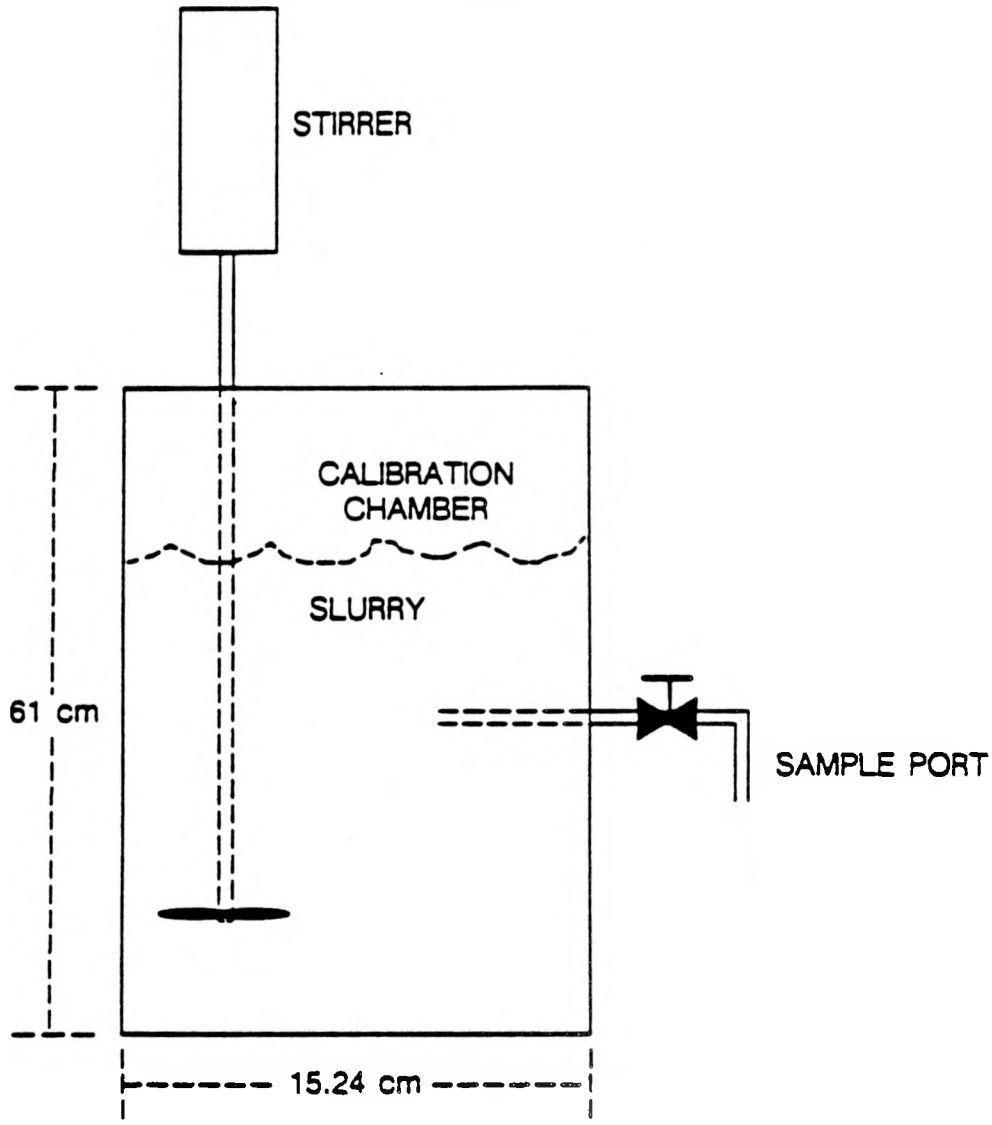

Figure 3.12. Schematic diagram of the calibration chamber.

suspend the solid particles. Once the system stabilized (approximately 30 minutes) a full chamber count rate, B was obtained, and a sample of the slurry was withdrawn at the same height at which the measurement was made and analyzed (using the procedure described in Chapter II) to determine the solids concentration in the slurry. The solids concentrations from the samples were within 3% (relative) of the solids concentrations calculated based on the amount of wax and solids added to the chamber. B, B_o, μ_ℓ, and the measured solids weight fraction were then used to calculate the attenuation coefficient for the solid phase (i.e. iron oxide or silica) using:

$$\mu_s = \frac{\frac{\ln(B/B_o)}{-d} - \frac{(1-\omega_s)\rho_{s\ell}\mu_\ell}{\rho_\ell}}{\frac{\omega_s \rho_{s\ell}}{\rho_s}} \qquad (3.33)$$

This procedure was repeated with solids concentrations of 20 and 30 wt% for each solid type, and the average attenuation coefficient from the three measurements was used in subsequent calculations. Table 3.6 lists the measured attenuation coefficients for SASOL wax and FT–300 wax. Also shown in Table 3.6 is the measured attenuation coefficients for iron oxide and silica using 10, 20, and 30 wt% slurries, as well as the average values of the attenuation coefficient for each solid. There was very good agreement between attenuation coefficients obtained using different slurry concentrations.

Table 3.7 compares the measured attenuation coefficients to those calculated based on the data presented by Attix (1968) (see Table 3.1). Their is very good agreement between the measured and predicted attenuation coefficients.

Data Acquisition and Reduction Procedures

Nuclear density gauge measurements were made during the majority of experiments in the 0.21 m ID stainless steel column. As mentioned previously (see Chapter II), during experiments the system was allowed to remain at a given set of conditions (i.e. constant gas flow rate) for a period of one and a half hours. Measurements with the

Table 3.6. Measured Attenuation Coefficients (cm^{-1}) for FT–300 Wax, SASOL Wax, Iron Oxide, and Silica

ABSORBING MEDIUM	WT% SOLIDS	SOURCE	
		Co–60	Cs–137
FT–300 WAX	–	0.0421	0.0555
SASOL WAX	–	0.0415	0.0519
IRON OXIDE	10	0.2718	0.3910
	20	0.2690	0.3891
	30	0.2750	0.3920
SILICA	10	0.1411	0.2039
	20	0.1409	0.2072
	30	0.1380	0.2110
IRON OXIDE	AVERAGE	0.272	0.391
SILICA	AVERAGE	0.140	0.207

Table 3.7. Comparison of Measured and Theoretical Attenuation Coefficients (cm^{-1})

ABSORBING MEDIUM	Co–60		Cs–137	
	Measured	Theoretical	Measured	Theoretical
FT–300 WAX	0.0421	0.0423	0.0555	0.0580
IRON OXIDE	0.272	0.271	0.391	0.382
SILICA	0.140	0.148	0.207	0.205

nuclear density gauge were initiated after approximately one hour. The output voltage from the ratemeter is related to the count rate through a scaling factor, S_C. For all measurements, S_C was 500. The count rate at time i is calculated from the output voltage using the following expression

$$B_i = (\text{OutputVoltage})_i(S_C) \tag{3.34}$$

Count rates were determined from output voltage data recorded over a period of 2 to 3 minutes at a sampling frequency of 50 Hz using the data acquisition system described in Chapter II. The output voltages at each time, were converted to count rates via Eq. 3.34, and the average count rate, B, which was used in all calculations is

$$B = \frac{\sum_i^n B_i}{n} \tag{3.35}$$

where n is the total number of data points (e.g. if one samples at 50 Hz for 60 seconds, n would be 3000). The average count rate was used to determine the phase fractions in the system. Figure 3.13 is a schematic representation of the locations at which measurements were made. In some experiments, measurements were limited to heights of 0.91 and 1.52 m above the distributor. The distance through the column, which represents the thickness of the absorbing media, at each measurement location was measured experimentally by obtaining count rates for the empty column at each position and count rates with a full column of wax (i.e. no gas) at each position. These values, together with the attenuation coefficient for wax were used to calculate the distance through the column at each location using,

$$d_i = \frac{\ln(B_i / B_{o_i})}{-\mu_\ell} \tag{3.36}$$

where i represents the location of the density gauge (see Figure 3.13). Values of d_i were obtained at the beginning of each set (or batch) of experiments. These values

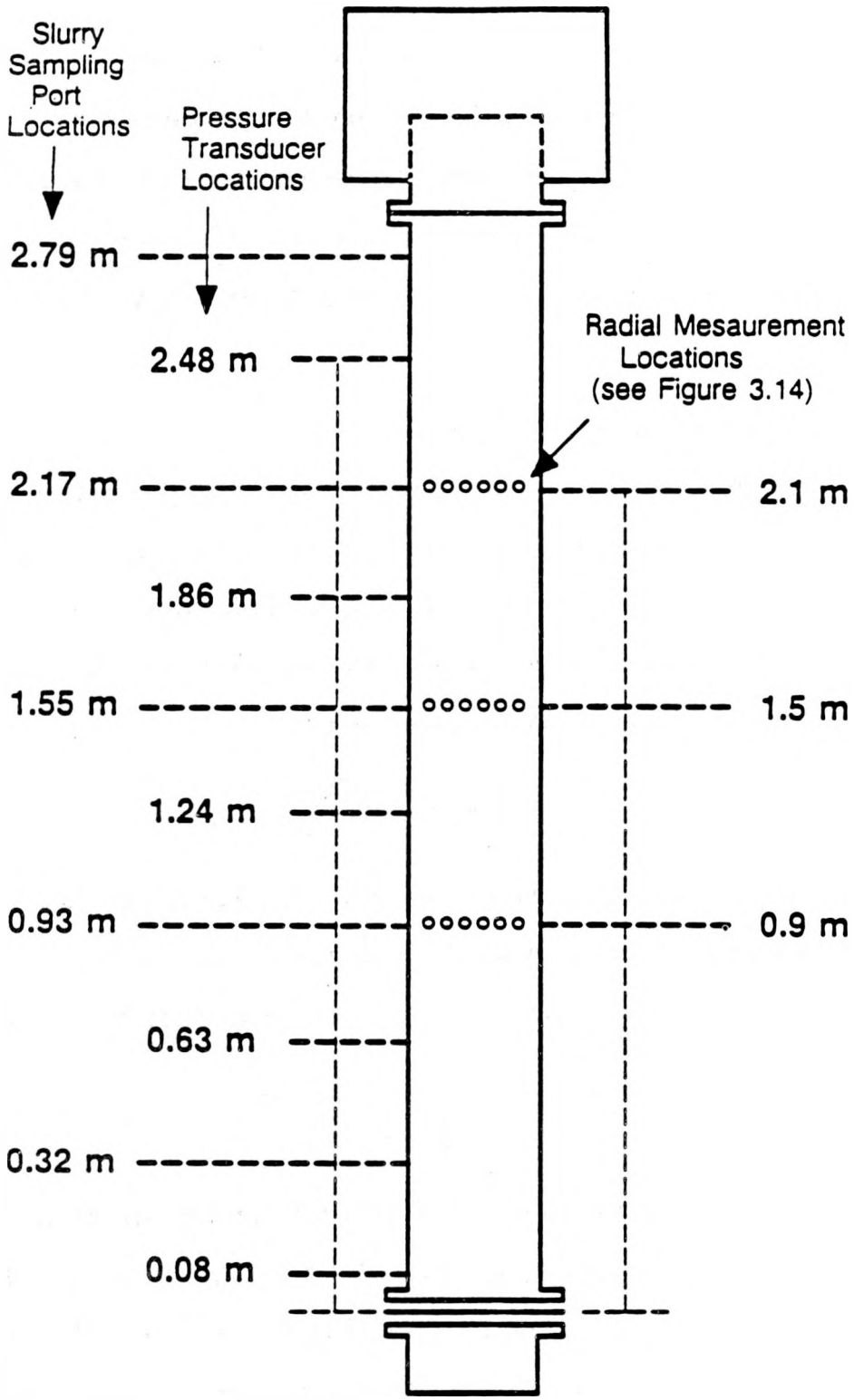

Figure 3.13. Schematic diagram of the nuclear density gauge measurement locations.

did not change by more than 1.5% throughout these studies, for either source. The distances through the column obtained prior to the experiments with FT–300 wax in the large column are given in Table 3.8. The distances are similar to the left and right of the center of the column for each source. The differences in the distance through the column for the two sources may be due to slightly different radial locations and/or axial locations.

Gas Holdups in Two – Phase Systems

Experiments were conducted using both two–phase (gas/liquid) and three–phase (gas/liquid/solid) systems. For two–phase experiments, gas holdups were obtained using each density gauge and the values compared. As described above, measurements were made at various radial and axial locations. The gas holdup at a given radial position, for both sources was calculated using:

$$\epsilon_{r_i} = 1 - \frac{\ln(B_i / B_{o_i})}{-d_i \mu_\ell} \tag{3.37}$$

Axial gas holdups were obtained from a volumetric weighted average of the radial gas holdups at a given axial location. Knowing the distance through the column at each radial position, d_i, and the column diameter, d_c, the radial position (measured from the center), r_{pos_i}, is

$$r_{pos_i} = \frac{\sqrt{d_c^2 - d_i^2}}{2} \tag{3.38}$$

Since the distances through the column did not vary significantly with axial position or column side (i.e. left or right of center), average values for r_{pos_i} and d_i were used to obtain the volumetric weights, w_i, needed to calculate the gas holdup at each axial location (see Eq. 3.40). The average values for r_{pos_i} and d_i that were used to calculate the weights are shown in Figure 3.14.

Table 3.8. Distance Through the Column for Both Sources at All Locations for the Experiments with FT–300 Wax

HEIGHT (m)	SOURCE	DISTANCE THROUGH THE COLUMN[a], d_i (m)					
		1	2	3	4	5	6
0.9	Co–60	16.10	18.62	20.23	20.11	18.42	16.30
	Cs–137	16.31	18.69	19.87	19.90	18.51	16.41
1.5	Co–60	15.81	18.77	20.07	20.06	18.76	16.49
	Cs–137	15.79	18.17	19.85	20.26	18.83	16.96
2.1	Co–60	16.33	18.97	20.31	20.45	18.87	16.63
	Cs–137	15.60	18.64	19.91	20.04	18.74	16.59

[a] Radial positions corresponding to numbers (1 to 6) are shown in Figures 3.13 and 3.14

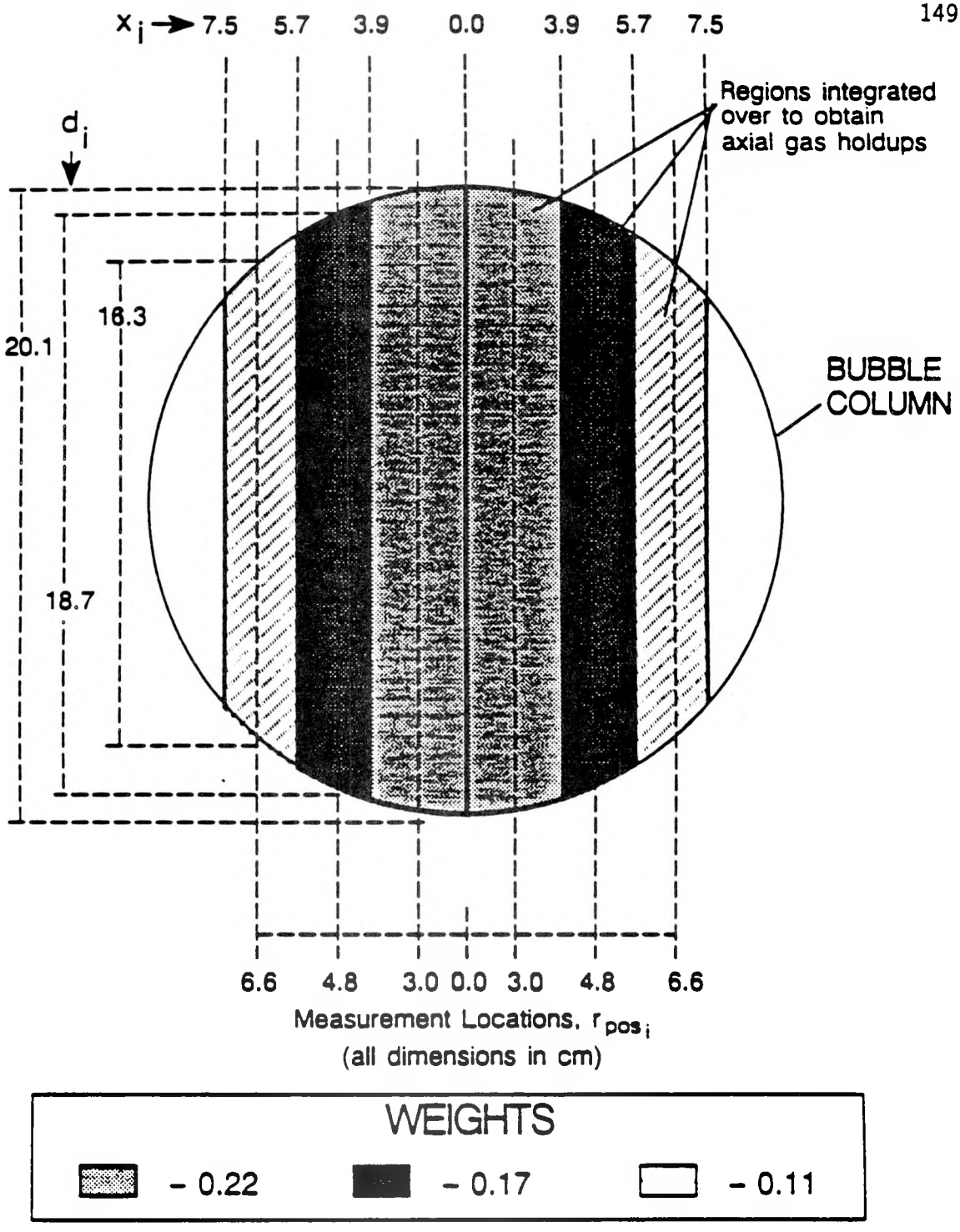

Figure 3.14. Schematic representation of the locations for radial measurements with the nuclear density gauge apparatus.

The column was divided into six sections (shaded regions in Figure 3.14) surrounding each measurement location. The cross–sectional area in a given shaded region, divided by the total area of the shaded regions was used as the weighting factor for measurements made in that region. The area of region i, A_{s_i} is given by:

$$A_{s_i} = [x_{i+1}\sqrt{r_c^2 - x_{i+1}^2} + r_c^2 \sin^{-1}(x_{i+1} / r_c)] - [x_i\sqrt{r_c^2 - x_i^2} + r_c^2 \sin^{-1}(x_i / r_c)] \qquad (3.39)$$

where r_c is the radius of the column and x_i and x_{i+1} are the distances (measured from the center of the column) bounding the region to be evaluated. In particular, the values of x_i and x_{i+1} that were used are (0,3.9), (3.9,5.7), and (5.7,7.5). The area of each section was divided by the total area integrated over (i.e. sum of the area of each section) to obtain the appropriate weighting factor, w_i

$$w_i = \frac{A_{s_i}}{\sum_{i=1}^{6} A_{s_i}} \qquad (3.40)$$

The weights obtained are given in Figure 3.14. The gas holdup at a given axial position was then calculated from:

$$\epsilon_{g_{ax}} = \sum_i \epsilon_{r_i} w_i \qquad i = 1 \text{ to } 6 \qquad (3.41)$$

where $\epsilon_{g_{ax}}$ is the axial gas holdup and ϵ_{r_i} (see Eq. 3.37) is the radial gas holdup at location i.

Once axial gas holdups have been calculated, average gas holdups may be calculated. Recall that the average gas holdup is defined as

$$\epsilon_g = \frac{\text{volume of gas in the dispersion}}{\text{volume of the dispersion}} \qquad (3.42)$$

Assuming the column can be divided into i sections, Eq. 3.42 may be rewritten as

$$\epsilon_g = \sum_i \frac{V_{g_i}}{V_{sect_i}} \frac{V_{sect_i}}{V_{exp}} = \sum_i \epsilon_{g_{ax_i}} \frac{h_i}{h_{exp}} \qquad (3.43)$$

where V_{g_i} is the volume of gas in section i, V_{sect_i} is the total volume of section i, V_{exp} is the total volume of the dispersion, ϵ_{gax_i} is the gas holdup in section i, h_i is the length of section i, and h_{exp} is the expanded height of the slurry. Assuming h_i approaches 0, Eq. 3.43 may be rewritten in integral form as

$$\epsilon_g = \frac{1}{h_{exp}} \int_0^{h_{exp}} \epsilon_{gax} dh \qquad (3.44)$$

Since measurements were made at three axial locations only, one may estimate the average gas holdup using various techniques. Three different approaches were examined in this study. First, the axial gas holdup data may be fitted to a curve. The equation for the curve may then be substituted into Eq. 3.44 for ϵ_{gax_i} to obtain an estimate for the average gas holdup. The second approach, uses the discretized form of Eq. 3.44 (i.e. Eq. 3.43) to obtain an estimate for the average gas holdup. Since measurements are made at three locations, the column may be divided into three sections. The sections used were (1) 0 to 1.2 m above the distributor, (2) 1.2 to 1.8 m above the distributor, and (3) 1.8 m above the distributor to the top of the dispersion (maximum of 3 m for continuous slurry flow). Thus, the values of h_i are 1.2 m, 0.6 m, and <1.2 m (see Figure 3.15). The third, and simplest approach would be to weight each axial gas holdup evenly. Using this approach, the average gas holdup is

$$\epsilon_g = \sum_i \frac{\epsilon_{gax_i}}{n} \qquad i = 1 \text{ to } 3 \qquad (3.45)$$

Since axial gas holdups did not vary significantly, there were no significant differences in the values of gas holdup estimated using the three different approaches. Table 3.9 compares average gas holdups obtained using the three techniques described above for data obtained at gas velocities of 0.02 and 0.09 m/s, during experiment number 4 in Table 2.5. This experiment was conducted in the continuous mode of operation. As shown in Table 3.9a there is very little difference in gas holdups obtained using

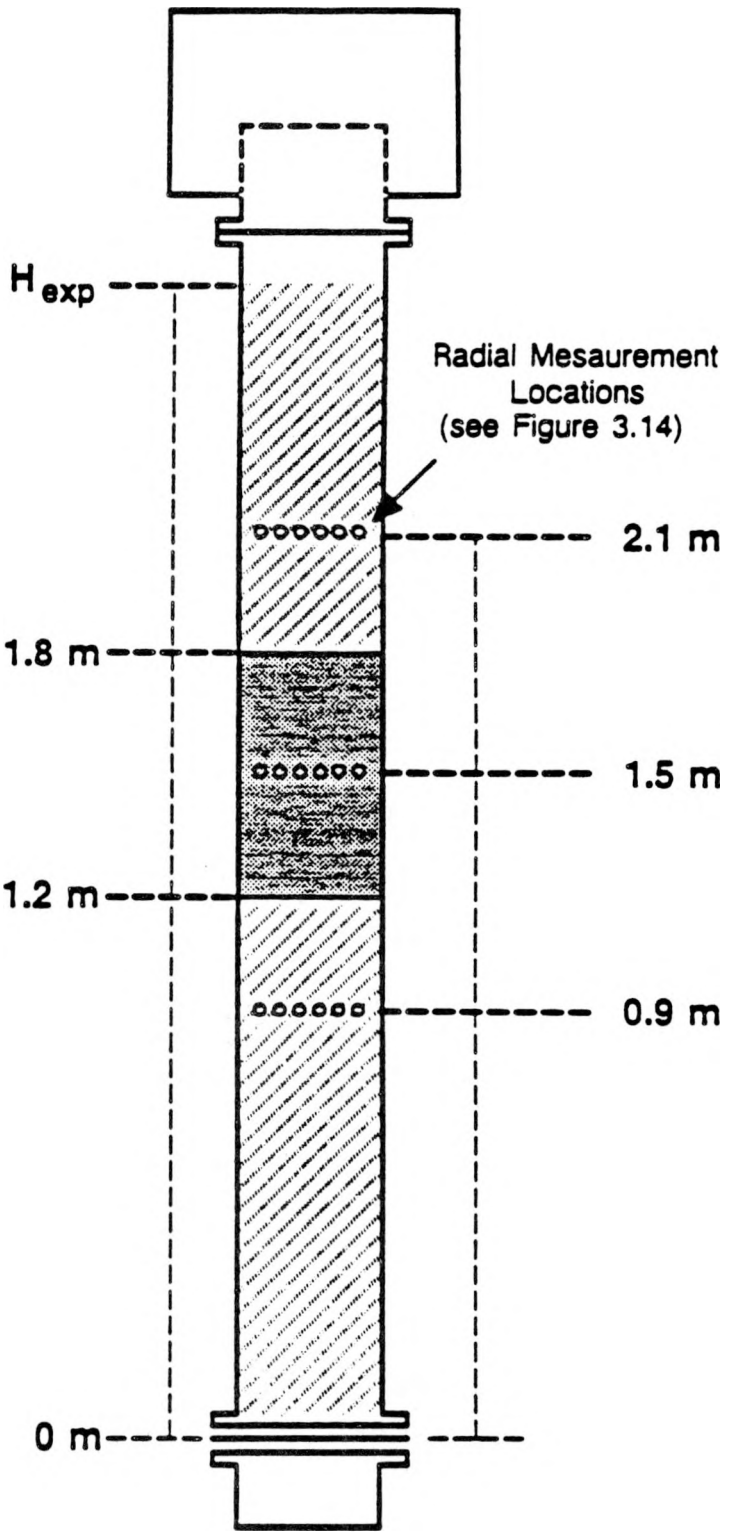

Figure 3.15. Schematic diagram of the regions used to obtain average gas holdups.

Table 3.9a. Effect of Technique Used to Obtain Average Gas Holdups from Axial Gas Holdups (Data from Experiment 4 in Table 2.5, u_g = 0.02 m/s)

EXP. HEIGHT (m)	HEIGHT (m)			ϵ_g^a	ϵ_g^b	ϵ_g^c
	0.9	1.5	2.1			
2.6[d]	0.0947	0.1083	0.1323	0.106	0.109	0.112
3.0[e]	0.0947	0.1083	0.1323	0.114	0.116	0.112

[a] Obtained from Eq. 3.44
[b] Obtained from Eq. 3.43
[c] Obtained from Eq. 3.45
[d] Representative of a batch mode experiment
[e] Representative of a continuous mode experiment, column height is 3.0 m

Table 3.9b. Effect of Technique Used to Obtain Average Gas Holdups from Axial Gas Holdups (Data from Experiment 4 in Table 2.5, u_g = 0.09 m/s)

EXP. HEIGHT (m)	HEIGHT (m)			ϵ_g^a	ϵ_g^b	ϵ_g^c
	0.9	1.5	2.1			
2.6[d]	0.2342	0.2446	0.2637	0.245	0.246	0.247
3.0[e]	0.2342	0.2446	0.2637	0.252	0.249	0.247

[a] Obtained from Eq. 3.44
[b] Obtained from Eq. 3.43
[c] Obtained from Eq. 3.45
[d] Representative of a batch mode experiment
[e] Representative of a continuous mode experiment, column height is 3.0 m

the various approaches. The data from this experiment were also analyzed assuming an expanded height of only 2.6 m (i.e. simulate a batch experiment). For this case (see Table 3.9b), the differences in the calculated gas holdups were slightly greater than those for the continuous case; however, they were still relatively small ($< 6\%$ difference). Thus, for simplicity, Eq. 3.45 was used to estimate the average gas holdup for all experiments.

Gas Holdups in Three – Phase Systems

Gas holdups for three–phase systems were calculated by treating all three phases independently, as well as, by treating the three–phase system as a two–phase system (i.e. grouping the liquid and solid phases together). When treating the three–phase system as a two–phase system, Eq. 3.37 is used to calculate radial gas holdups by replacing the liquid phase attenuation coefficient, μ_ℓ with the slurry phase attenuation coefficient, $\mu_{s\ell}$ (see Eq.3.30). If all three phases are treated separately, then Eqs. 3.16, 3.17, and 3.18 may be used to calculate radial gas holdups. Once radial gas holdups are obtained, axial and average gas holdups are calculated using Eqs. 3.41 and 3.45, respectively.

Discussion of Results

Radial, axial and average gas holdups were measured with the nuclear density gauge during two–phase and three–phase experiments in the 0.21 m ID column. Data collected during all experiments were analyzed assuming Case I alignment. Furthermore, data from three–phase experiments were analyzed by two different methods: (1) treat all three phases independently and (2) group liquid and solids together to form a pseudo two–phase system.

Independent Treatment of all Three – Phases

Gas holdup values obtained from nuclear density gauge measurements, treating all three phases independently, were not good. However, this was not surprising, since sensitivity analysis revealed that very small errors in the count rate could produce substantial errors in volume fractions for the Co–60/Cs–137 system (see Table 3.3).

Data acquired from the density gauges during several experiments were analyzed to obtain radial gas holdups. Table 3.10a shows radial gas holdup values obtained from the batch experiment with 20 wt%, 20 – 44μm iron oxide particles in FT–300 wax. Radial gas holdups varied significantly for each gas velocity. In order to see what effect slight errors in the path length through the column, d, had on the gas holdups, it was varied. These results are shown in Table 3.10b for the experiment with FT–300 wax. We assumed that the volume fraction of solids did not vary with radial position and adjusted the value of d, until the volume fraction of solids, ϵ_s, was similar to that obtained from analysis of the slurry sample withdrawn at the same height of the density gauge measurement (see Figure 3.13). Once similar values of ϵ_s were obtained, axial gas holdups were calculated from the radial gas holdups using Eq. 3.41, and these values were compared to those values obtained at the same location (for this case, the axial gas holdups were compared to the measured gas holdups between pressure transducers 3 and 4; see Figure 3.13) using conventional techniques (see Chapter II). As shown in Table 3.10b, there was excellent agreement between axial gas holdups obtained using the different techniques. Also shown in Tables 3.10a and 3.10b is the distance through the column, d, for the high and low energy source, before and after altering its value, respectively. A range of values is presented in Table 3.10b, since different values of d were used at each gas velocity. For all experiments, the maximum percent difference between the measured value of d for each source and the altered value of d for each source at each radial location was less than 4%, and usually less than 2%. Thus

Table 3.10a. Gas holdups from Measurements with the Nuclear Density Gauge at a Height of 1.5 m Above the Distributor (FT-300 Wax, 20 wt% 20 – 44 μm Iron Oxide)

u_g	Radial Position[a]					
(m/s)	6.6	4.8	3.0	3.0	4.8	6.6
0.02	0.06	0.24	0.04	0.21	0.37	0.24
0.04	-0.09	0.27	0.03	0.23	0.07	0.16
0.08	-0.03	0.19	0.12	0.31	0.45	0.14
0.12	0.13	0.18	0.12	0.35	0.48	0.13
d_L^b	16.96	18.17	20.26	19.85	18.83	15.79
d_H^c	16.49	18.76	20.06	20.07	18.77	15.81

[a] – Measured from the center of the column (cm)
[b] – Distance through the column for the Cs–137 source (cm)
[c] – Distance through the column for the Co–60 source (cm)

Table 3.10b. Gas and Solids Holdups from Measurements with the Nuclear Density Gauge at a Height of 1.5 m Above the Distributor After Modifying the Thickness (d) of the Absorbing Media (FT-300 Wax, 20 wt% 20 – 44 μm Iron Oxide)

u_g	RADIAL POSITION[a]						ϵ_g^b	ϵ_g^c	ϵ_s^b	ϵ_s^c
(m/s)	6.6	4.8	3.0	3.0	4.8	6.6				
0.02	0.117	0.124	0.128	0.129	0.124	0.105	0.122	0.128	0.015	0.016
0.04	0.159	0.164	0.194	0.183	0.166	0.150	0.172	0.189	0.024	0.024
0.08	0.161	0.210	0.213	0.221	0.198	0.194	0.202	0.172	0.026	0.024
0.12	0.189	0.197	0.223	0.222	0.215	0.185	0.210	0.216	0.021	0.025
d_L^d	16.86-16.98	18.15-18.19	20.10-20.28	19.75-19.95	18.79-18.87	15.69-15.79				
d_H^e	16.6-16.8	18.9	20.25	19.9	18.8	15.6-15.9				

[a] – Measured from the center of the column (cm)
[b] – Axial holdups from nuclear density gauge measurements
[c] – Axial holdups from conventional measurements (Chapter II)
[d] – Range of values for the distance through the column for the Cs–137 source (cm)
[e] – Range of values for the distance through the column for the Co–60 source (cm)

indicating once again, that slight errors in the measured quantities (i.e. count rate, distance through the column, etc.) have a significant effect on the calculated holdups, when two "high" energy sources are employed. Data obtained from other experiments were also analyzed treating all three–phases independently. The results from these experiments are shown in Tables 3.11 to 3.14. Tables 3.11a and 3.11b show results obtained from the batch mode experiment with 20 wt% large silica particles in SASOL wax at a height of 1.5 m above the distributor. Results from this experiment were similar to those obtained during the experiment with large iron oxide particles suspended in FT–300 wax (Table 3.10). Namely, there was a significant variation in radial gas holdup profiles when the measured distances were used; however, upon slightly adjusting the distance through the column, more uniform radial holdup values were obtained. Axial holdups calculated from the modified radial profiles were comparable to those using conventional techniques (see Chapter II) were obtained. Similar results were also obtained at different heights and with small iron oxide particles. Radial gas holdup profiles for the experiment conducted with 20 – 44 μm iron oxide particles in FT–300 wax at a height of 2.1 m above the distributor are shown in Table 3.12. Results from the experiment with large silica particles in SASOL wax, at a height of 0.9 m above the distributor are shown in Table 3.13, and results from the experiment with small iron oxide particles at a slurry velocity of 0.005 m/s at a height of 1.5 m above the distributor are shown in Table 3.14.

Two – Phase and Pseudo Two – Phase Results

Figures 3.16 to 3.19 show radial gas holdup profiles at a height of 1.5 m above the distributor obtained from different experiments in two–phase (Figure 3.16) and three–phase systems (Figures 3.17, 3.18, and 3.19). The results shown for the three–phase system were obtained by treating it as a pseudo two–phase system (i.e. the liquid and solid phases were grouped together). Radial gas holdups for three–phase experiments

Table 3.11a. Gas Holdups from Measurements with the Nuclear Density at a Height of 1.5 m Above the Distributor (SASOL Wax, 20 wt% 20 – 44 μm Silica)

u_g	Radial Position[a]			
(m/s)	6.6	3.0	3.0	6.6
0.02	0.34	0.12	0.15	0.21
0.04	0.23	0.17	0.16	0.24
0.08	0.32	0.30	0.26	0.42
0.12	0.30	0.33	0.34	0.46
d_L^b	16.65	20.44	20.49	15.99
d_H^c	16.55	20.31	20.41	15.9

[a] – Measured from the center of the column (cm)
[b] – Distance through the column for the Cs–137 source (cm)
[c] – Distance through the column for the Co–60 source (cm)

Table 3.11b. Gas and Solids Holdups from Measurements with the Nuclear Density Gauge at a Height of 1.5 m Above the Distributor After Modifying the Thickness (d) of the Absorbing Media (SASOL Wax, 20 wt% 20 – 44 μm Silica)

u_g	RADIAL POSITION[a]				ϵ_g^b	ϵ_g^c	ϵ_s^b	ϵ_s^c
(m/s)	6.6	3.0	3.0	6.6				
0.02	0.104	0.116	0.120	0.115	0.117	0.115	0.067	0.066
0.04	0.146	0.168	0.162	0.143	0.157	0.150	0.066	0.066
0.08	0.206	0.224	0.230	0.207	0.218	0.191	0.070	0.065
0.12	0.205	0.262	0.266	0.225	0.244	0.253	0.067	0.066
d_L^d	16.5-16.95	20.45-20.49	20.49-20.59	16.3-16.4				
d_H^e	16.2	20.3	20.4	15.9				

[a] – Measured from the center of the column (cm)
[b] – Axial holdups from nuclear density gauge measurements
[c] – Axial holdups from conventional measurements (Chapter II)
[d] – Range of values for the distance through the column for the Cs–137 source (cm)
[e] – Range of values for the distance through the column for the Co–60 source (cm)

Table 3.12a. Gas Holdups from Measurements with the Nuclear Density Gauge at a Height of 2.1 m Above the Distributor (FT-300 Wax, 20 wt% 20 – 44 μm Iron Oxide)

u_g	Radial Position[a]					
(m/s)	6.6	4.8	3.0	3.0	4.8	6.6
0.02	0.03	0.02	0.07	0.13	0.08	-0.04
0.04	0.30	0.39	0.34	0.61	0.41	0.38
0.08	0.04	0.06	0.08	0.47	0.11	-0.01
0.12	0.02	-0.02	0.06	0.27	0.18	0.12
d_L^b	16.60	18.64	19.91	20.04	18.91	16.59
d_H^c	16.33	18.97	20.31	20.45	18.87	16.63

[a] – Measured from the center of the column (cm)
[b] – Distance through the column for the Cs–137 source (cm)
[c] – Distance through the column for the Co–60 source (cm)

Table 3.12b. Gas and Solids Holdups from Measurements with the Nuclear Density Gauge at a Height of 2.1 m Above the Distributor After Modifying the Thickness (d) of the Absorbing Media (FT-300 Wax, 20 wt% 20 – 44 μm Iron Oxide)

u_g	RADIAL POSITION[a]						ϵ_g^b	ϵ_g^c	ϵ_s^b	ϵ_s^c
(m/s)	6.6	4.8	3.0	3.0	4.8	6.6				
0.02	0.131	0.152	0.171	0.169	0.149	0.140	0.151	0.137	0.014	0.014
0.04	0.220	0.279	0.282	0.301	0.280	0.259	0.271	0.274	0.023	0.021
0.08	0.161	0.230	0.233	0.260	0.211	0.187	0.221	0.232	0.023	0.023
0.12	0.170	0.247	0.261	0.272	0.251	0.219	0.224	0.240	0.023	0.024
d_L^d	16.4-16.5	18.1-18.4	19.5-20.0	20.0-20.5	18.6-19.0	16.1-16.4				
d_H^e	16.33	18.97	20.31	20.45	18.87	16.63				

[a] – Measured from the center of the column (cm)
[b] – Axial holdups from nuclear density gauge measurements
[c] – Axial holdups from conventional measurements (Chapter II)
[d] – Range of values for the distance through the column for the Cs–137 source (cm)
[e] – Range of values for the distance through the column for the Co–60 source (cm)

Table 3.13a. Gas Holdups from Measurements with the Nuclear Density Gauge at a Height of 0.9 m Above the Distributor (SASOL Wax, 20 wt% 20 – 44 μm Silica)

u_g	Radial Position[a]			
(m/s)	6.6	3.0	3.0	6.6
0.02	0.11	0.10	0.18	0.01
0.04	0.19	0.11	0.14	0.11
0.08	0.36	0.29	0.25	0.29
0.12	0.22	0.25	0.21	0.32
d_L^b	16.32	19.84	19.92	16.39
d_H^c	16.41	20.19	20.09	16.52

[a] – Measured from the center of the column (cm)
[b] – Distance through the column for the Cs–137 source (cm)
[c] – Distance through the column for the Co–60 source (cm)

Table 3.13b. Gas and Solids Holdups from Measurements with the Nuclear Density Gauge at a Height of 0.9 m Above the Distributor After Modifying the Thickness (d) of the Absorbing Media (SASOL Wax, 20 wt% 20 – 44 μm Silica)

u_g	RADIAL POSITION[a]				ϵ_g^b	ϵ_g^c	ϵ_s^b	ϵ_s^c
(m/s)	6.6	3.0	3.0	6.6				
0.02	0.08	0.11	0.12	0.08	0.10	0.10	0.08	0.07
0.04	0.10	0.13	0.13	0.09	0.12	0.14	0.07	0.07
0.08	0.17	0.20	0.20	0.16	0.18	0.14	0.07	0.07
0.12	0.18	0.22	0.21	0.18	0.20	0.20	0.07	0.06
d_L^d	16.4-16.9	19.8-20.2	19.95-20.1	16.2-16.6				
d_H^e	16.4	20.2	20.1	16.5				

[a] – Measured from the center of the column (cm)
[b] – Axial holdups from nuclear density gauge measurements
[c] – Axial holdups from conventional measurements (Chapter II)
[d] – Range of values for the distance through the column for the Cs–137 source (cm)
[e] – Range of values for the distance through the column for the Co–60 source (cm)

Table 3.14a. Gas Holdups from Measurements with the Nuclear Density Gauge at a Height of 1.5 m Above the Distributor (SASOL Wax, 20 wt% 0 – 5 μm Iron Oxide)

u_g	Radial Position[a]					
(m/s)	6.6	4.8	3.0	3.0	4.8	6.6
0.02	-0.016	0.055	0.005	0.037	0.035	0.047
0.04	0.337	0.382	0.289	0.314	0.172	0.071
0.06	0.238	0.300	0.297	0.226	0.210	0.081
0.09	0.203		0.313	0.189		-0.001
0.12	0.351	0.389	0.277	0.282	0.091	0.025
d_L^b	16.57	19.20	20.70	20.59	18.99	16.76
d_H^c	16.48	19.17	20.42	20.47	18.97	16.86

[a] – Measured from the center of the column (cm)
[b] – Distance through the column for the Cs–137 source (cm)
[c] – Distance through the column for the Co–60 source (cm)

Table 3.14b. Gas and Solids Holdups from Measurements with the Nuclear Density Gauge at a Height of 1.5 m Above the Distributor After Modifying the Thickness (d) of the Absorbing Media (SASOL Wax, 20 wt% 0 – 5 μm Iron Oxide)

u_g	RADIAL POSITION[a]						ϵ_g^b	ϵ_g^c	ϵ_s^b	ϵ_s^c
(m/s)	6.6	4.8	3.0	3.0	4.8	6.6				
0.02	0.105	0.134	0.125	0.123	0.129	0.108	0.121	0.107	0.029	0.029
0.04	0.152	0.175	0.180	0.189	0.165	0.147	0.169	0.157	0.029	0.028
0.06	0.140	0.170	0.188	0.193	0.169	0.145	0.171	0.175	0.027	0.027
0.09	0.159		0.226	0.223		0.164	0.200	0.211	0.026	0.026
0.12	0.186	0.219	0.238	0.245	0.216	0.188	0.219	0.208	0.025	0.025
d_L^d	15.9-16.2	18.6-19.0	20.0-20.3	20.3-20.7	18.5-19.0	16.5-16.8				
d_H^e	16.48	19.17	20.42	20.47	18.97	16.86				

[a] – Measured from the center of the column (cm)
[b] – Axial holdups from nuclear density gauge measurements
[c] – Axial holdups from conventional measurements (Chapter II)
[d] – Range of values for the distance through the column for the Cs–137 source (cm)
[e] – Range of values for the distance through the column for the Co–60 source (cm)

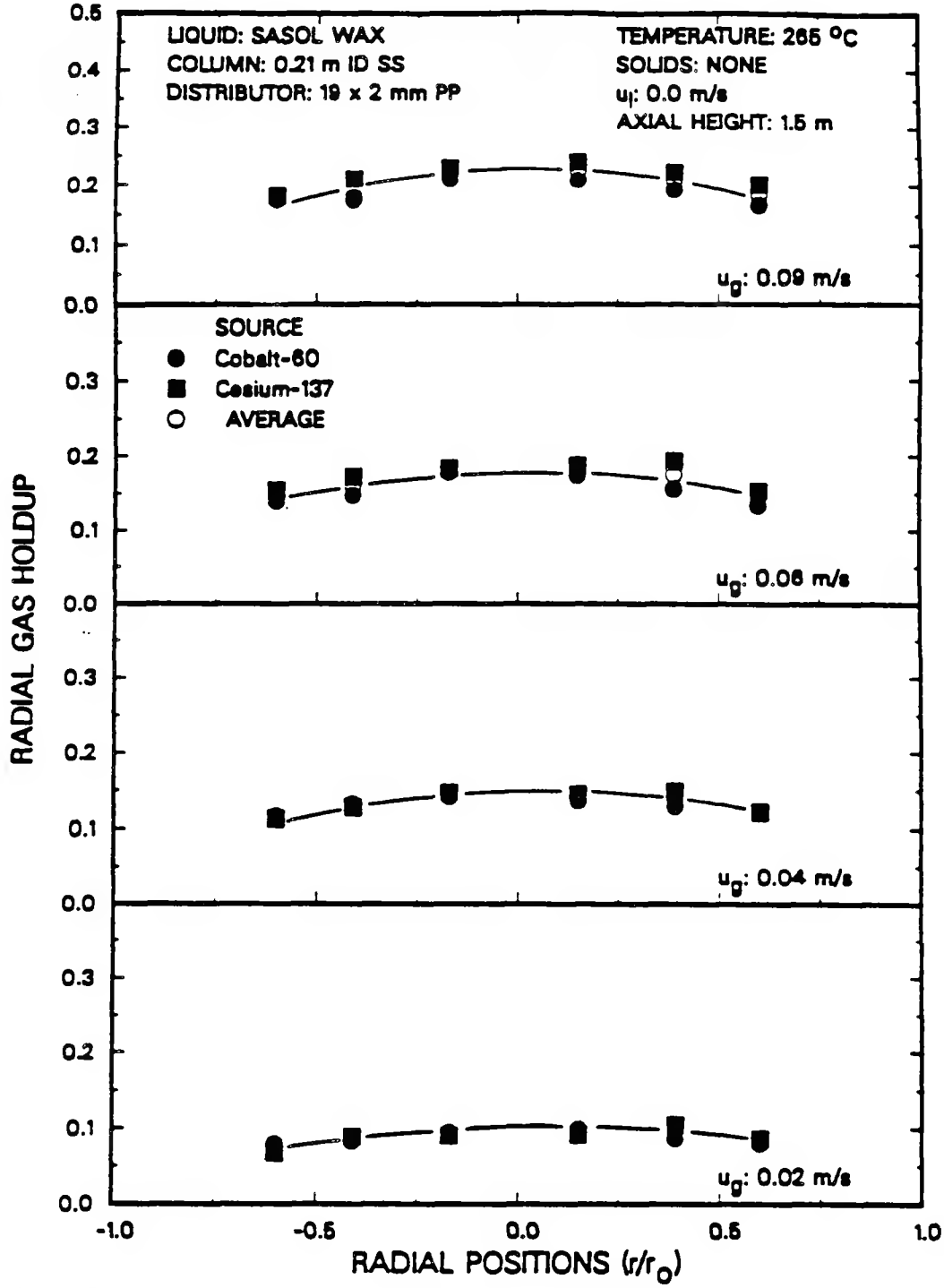

Figure 3.16. Effect of superficial gas velocity on radial gas holdup (SASOL wax, no solids, u_l = 0.0 m/s).

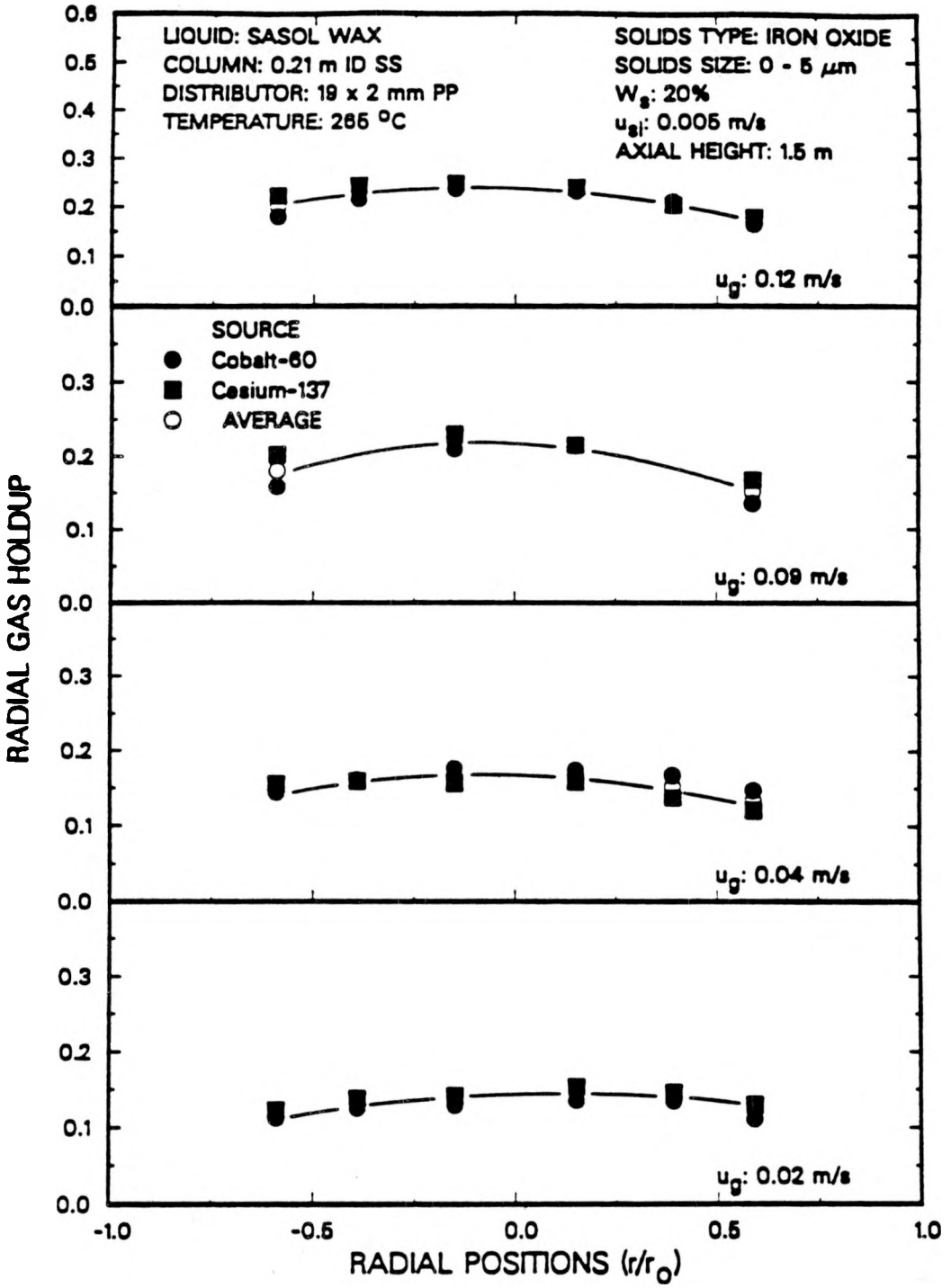

Figure 3.17. Effect of superficial gas velocity on radial gas holdup (SASOL wax, 20 wt% 0 - 5 μm iron oxide, u_{sl} = 0.005 m/s).

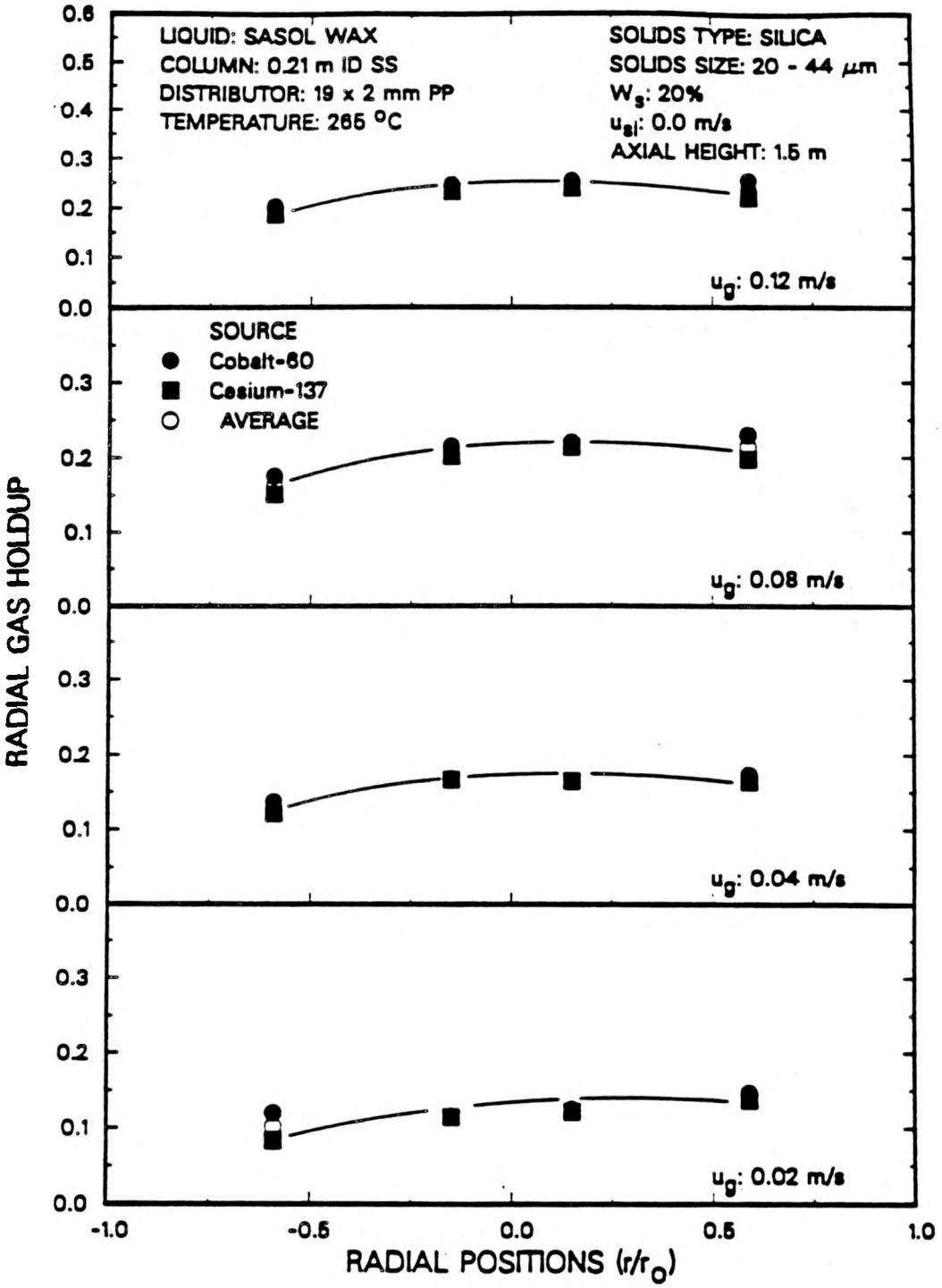

Figure 3.18. Effect of superficial gas velocity on radial gas holdup (SASOL wax, 20 wt% 20 - 44 μm silica, u_{sl} = 0.0 m/s).

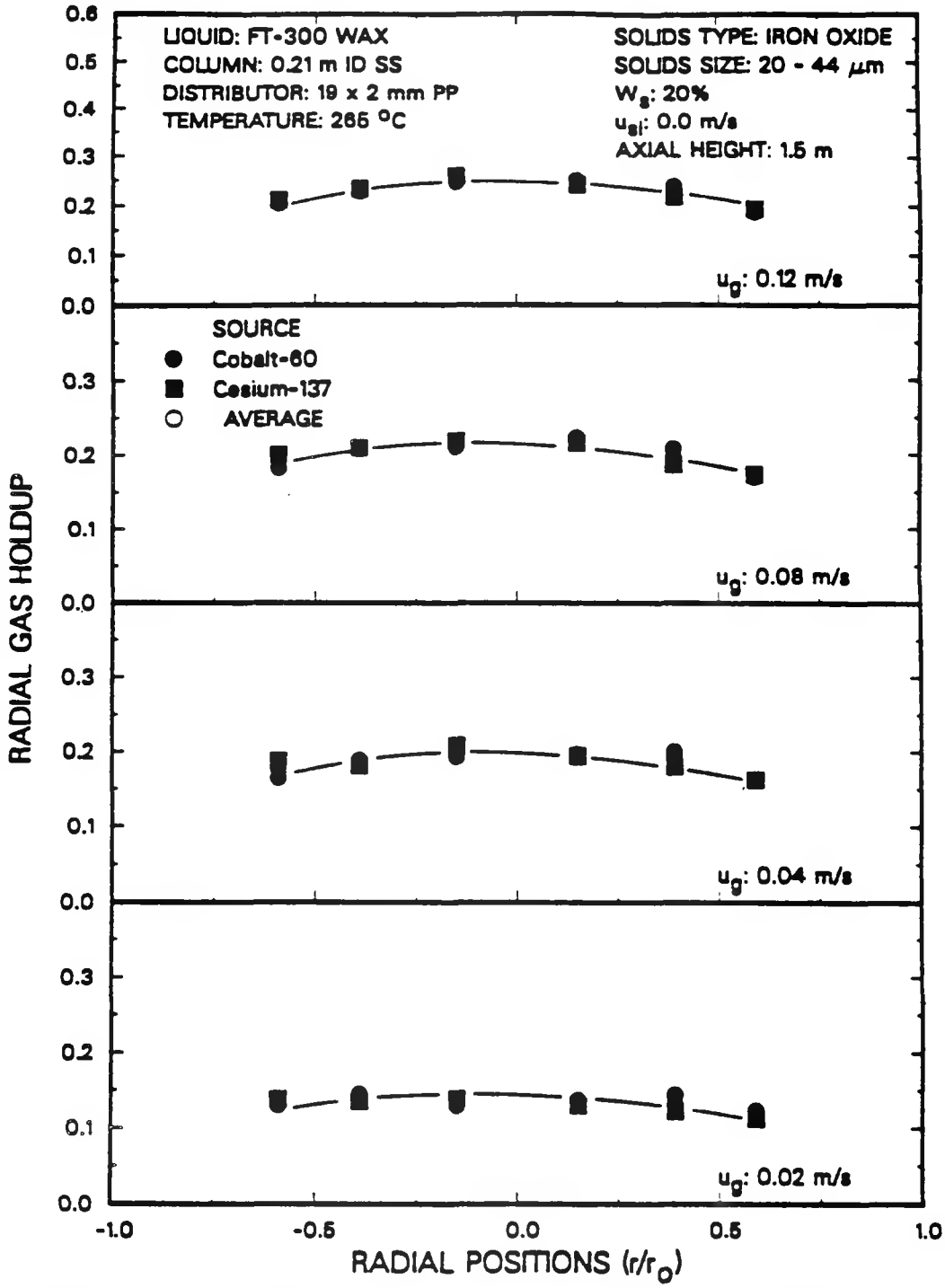

Figure 3.19. Effect of superficial gas velocity on radial gas holdup (FT-300 wax, 20 wt% 20 - 44 μm iron oxide, u_{sl} = 0.0 m/s).

were obtained using Eq. 3.37, and replacing the attenuation coefficient of the liquid, μ_ℓ, by the attenuation coefficient of the liquid/solid mixture – see Eq. 3.6). Since a pseudo two–phase system was assumed (three–phase systems), independent results could be obtained from each density gauge. For each case, independent results from the two density gauges are presented along with with average values of the radial gas holdup. The average values are simply an arithmetic average of the holdup values obtained from the two sources. In general, radial gas holdup profiles were fairly uniform at a gas velocity of 0.02 m/s, which was expected since flow is in the homogeneous bubbling regime at this velocity. However, as the gas velocity increases, the flow becomes slightly non–uniform with higher holdups in the center of the column. At higher gas velocities, larger gas bubbles are produced which tend to move upward through the center of the column and this in turn results in higher gas holdups in the center of the column. The trends observed at the other two heights (0.9 and 2.1 m) were similar to those shown at a height of 1.5 m above the distributor.

The radial holdups shown in Figures 3.16 to 3.19 are also presented in tabular form (see Tables 3.15 to 3.18, respectively). Also shown in these tables are the values of the attenuation coefficients and the initial (or empty column) count rates that were used. Empty column count rates at a given radial position did not vary by more than 2% between experiments. The empty column count rate decreases with increasing distance from the center of the column. This decrease in the count rate with increasing distance from the center of the column is because the thickness of the column changes due to its curvature (see Figure 3.20).

For all of the results shown in Figures 3.17 to 3.19 (three–phase systems), the attenuation coefficient was assumed to be constant at all gas velocities, since the solids concentration did not vary significantly with gas velocity in the large column (see Chapter IV), with the exception of the experiments conducted with large iron oxide particles.

Table 3.15a. Radial Gas Holdups Obtained Using the Co–60 Source
(SASOL Wax, No Solids, u_ℓ = 0 m/s)

u_g	$\mu_{s\ell}$	Radial Position[a]					
(m/s)	(cm^{-1})	6.6	4.8	3.0	3.0	4.8	6.6
0.02	0.0415	0.102	0.113	0.145	0.115	0.111	0.101
0.04	0.0415	0.132	0.143	0.154	0.146	0.135	0.136
0.06	0.0415	0.151	0.178	0.178	0.183	0.180	0.156
0.09	0.0415	0.171	0.209	0.219	0.223	0.212	0.181
B_o[b]		3582	3805	3926	3957	3852	3742
d[c]		16.10	17.70	19.18	19.43	18.16	16.40

[a] – Measured from the center of the column (cm)
[b] – Empty column count rate (counts/sec)
[c] – Distance through the column (cm)

Table 3.15b. Radial Gas Holdups Obtained Using the Cs–137 Source
(SASOL Wax, No Solids, u_ℓ = 0 m/s)

u_g	$\mu_{s\ell}$	Radial Position[a]					
(m/s)	(cm^{-1})	6.6	4.8	3.0	3.0	4.8	6.6
0.02	0.0519	0.106	0.109	0.117	0.118	0.095	0.099
0.04	0.0519	0.141	0.155	0.167	0.158	0.137	0.136
0.06	0.0519	0.171	0.190	0.199	0.204	0.170	0.175
0.09	0.0519	0.205	0.229	0.245	0.246	0.212	0.202
B_o[b]		1958	2082	2149	2164	2120	2011
d[c]		16.20	18.78	20.60	20.70	19.23	17.38

[a] – Measured from the center of the column (cm)
[b] – Empty column count rate (counts/sec)
[c] – Distance through the column (cm)

Table 3.16a. Radial Gas Holdups Obtained Using the Co–60 Source
(SASOL Wax, 20 wt% 0 – 5 μm Iron Oxide, u_{sl} = 0.005 m/s)

u_g	μ_{sl}	Radial Position[a]					
(m/s)	(cm^{-1})	6.6	4.8	3.0	3.0	4.8	6.6
0.02	0.0494	0.111	0.134	0.135	0.128	0.126	0.113
0.04	0.0494	0.147	0.149	0.174	0.176	0.161	0.145
0.06	0.0494	0.149	0.177	0.192	0.191	0.173	0.157
0.09	0.0494	0.171		0.214	0.209		0.177
0.12	0.0494	0.199	0.209	0.231	0.235	0.215	0.197
B_o[b]		3618	3828	3903	3901	3815	3677
d[c]		16.48	19.17	20.42	20.47	18.97	16.86

[a] – Measured from the center of the column (cm)
[b] – Empty column count rate (counts/sec)
[c] – Distance through the column (cm)

Table 3.16b. Radial Gas Holdups Obtained Using the Cs–137 Source
(SASOL Wax, 20 wt% 0 – 5 μm Iron Oxide, u_{sl} = 0.005 m/s)

u_g	μ_{sl}	Radial Position[a]					
(m/s)	(cm^{-1})	6.6	4.8	3.0	3.0	4.8	6.6
0.02	0.0635	0.129	0.146	0.154	0.142	0.138	0.122
0.04	0.0635	0.121	0.137	0.181	0.157	0.160	0.145
0.06	0.0635	0.157	0.159	0.176	0.187	0.168	0.158
0.09	0.0635	0.167		0.215	0.230		0.192
0.12	0.0635	0.210	0.203	0.239	0.246	0.242	0.211
B_o[b]		2007	2116	2174	2185	2108	1997
d[c]		16.57	19.20	20.70	20.59	18.99	16.76

[a] – Measured from the center of the column (cm)
[b] – Empty column count rate (counts/sec)
[c] – Distance through the column (cm)

Table 3.17a. Radial Gas Holdups Obtained Using the Co–60 Source
(SASOL Wax, 20 wt% 20 – 44 μm Silica, u_{sl} = 0 m/s)

u_g	μ_{sl}	Radial Position[a]			
(m/s)	(cm^{-1})	6.6	3.0	3.0	6.6
0.02	0.0478	0.131	0.125	0.115	0.111
0.04	0.0478	0.157	0.164	0.167	0.128
0.08	0.0478	0.214	0.219	0.214	0.167
0.12	0.0478	0.235	0.254	0.246	0.196
B_o[b]		3619	3953	3970	3675
d[c]		16.55	20.31	20.41	15.9

[a] – Measured from the center of the column (cm)
[b] – Empty column count rate (counts/sec)
[c] – Distance through the column (cm)

Table 3.17b. Radial Gas Holdups Obtained Using the Cs–137 Source
(SASOL Wax, 20 wt% 20 – 44 μm Silica, u_{sl} = 0 m/s)

u_g	μ_{sl}	Radial Position[a]			
(m/s)	(cm^{-1})	6.6	3.0	3.0	6.6
0.02	0.0642	0.137	0.121	0.114	0.084
0.04	0.0642	0.163	0.164	0.166	0.121
0.06	0.0642	0.198	0.213	0.201	0.151
0.12	0.0642	0.219	0.239	0.232	0.186
B_o[b]		2049	2226	2230	2050
d[c]		16.65	20.44	20.49	16.0

[a] – Measured from the center of the column (cm)
[b] – Empty column count rate (counts/sec)
[c] – Distance through the column (cm)

Table 3.18a. Radial Gas Holdups Obtained Using the Co-60 Source
(FT-300 Wax, 20 wt% 20 – 44 μm Iron Oxide, $u_{sl} = 0$ m/s)

u_g	μ_{sl}	Radial Position[a]					
(m/s)	(cm^{-1})	6.6	4.8	3.0	3.0	4.8	6.6
0.02	0.0466	0.123	0.144	0.137	0.131	0.144	0.131
0.04	0.0495	0.163	0.199	0.197	0.193	0.188	0.165
0.08	0.0495	0.170	0.208	0.223	0.211	0.208	0.183
0.12	0.0495	0.188	0.238	0.250	0.248	0.228	0.204
B_o[b]		3603	3821	3941	3981	3837	3691
d[c]		16.49	18.76	20.06	20.07	18.77	15.81

[a] – Measured from the center of the column (cm)
[b] – Empty column count rate (counts/sec)
[c] – Distance through the column (cm)

Table 3.18b. Radial Gas Holdups Obtained Using the Cs-137 Source
(FT-300 Wax, 20 wt% 20 – 44 μm Iron Oxide, $u_{sl} = 0$ m/s)

u_g	μ_{sl}	Radial Position[a]					
(m/s)	(cm^{-1})	6.6	4.8	3.0	3.0	4.8	6.6
0.02	0.0619	0.112	0.122	0.130	0.139	0.136	0.138
0.04	0.0662	0.163	0.181	0.194	0.208	0.181	0.187
0.08	0.0662	0.173	0.189	0.216	0.219	0.210	0.200
0.12	0.0662	0.194	0.228	0.242	0.259	0.236	0.210
B_o[b]		2065	2197	2252	2273	2216	2102
d[c]		16.96	18.17	20.26	19.85	18.83	15.79

[a] – Measured from the center of the column (cm)
[b] – Empty column count rate (counts/sec)
[c] – Distance through the column (cm)

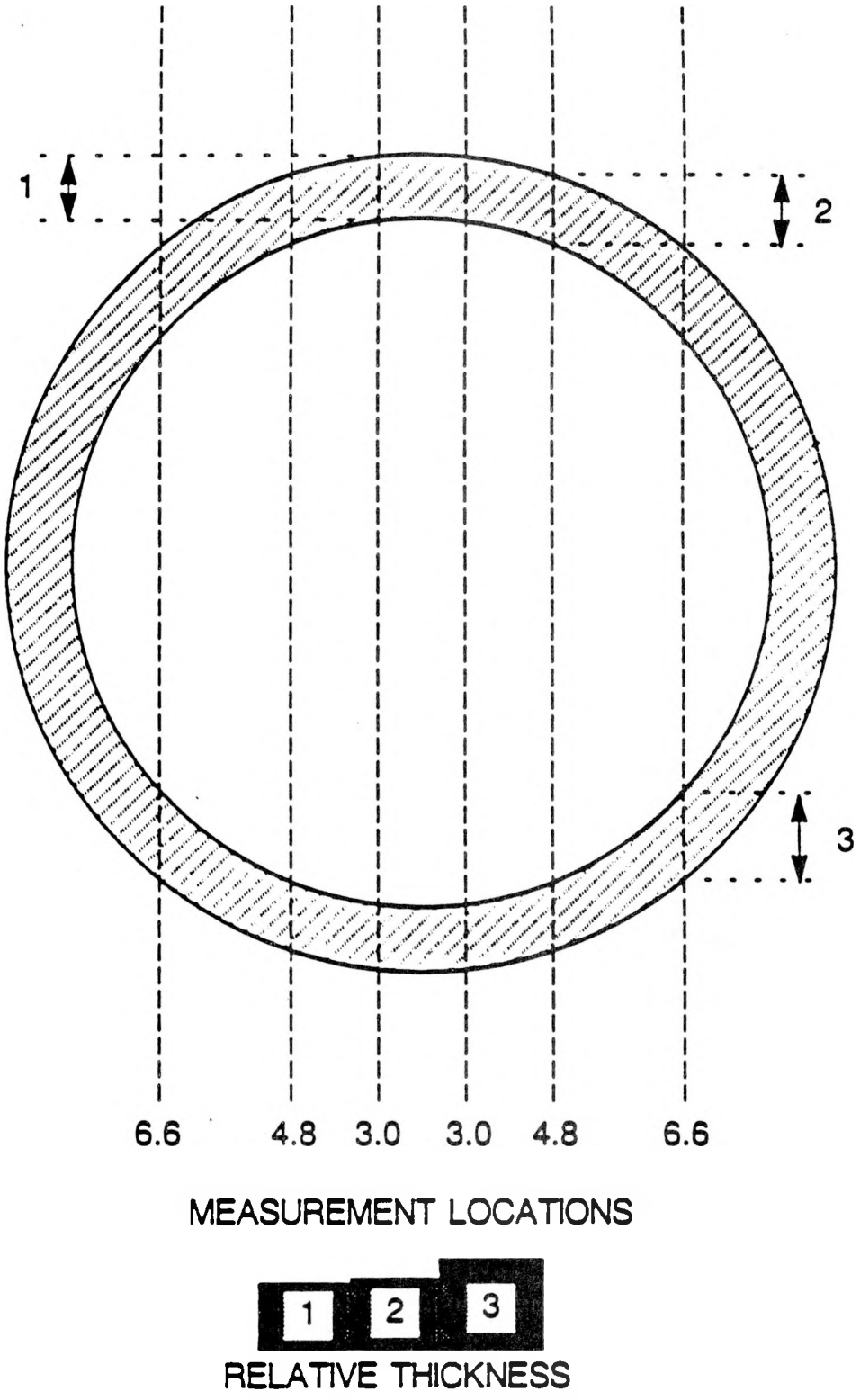

Figure 3.20. Schematic representation of bubble column wall.

During these experiments, the solids concentration in the column was lower at a gas velocity of 0.02 m/s than at higher gas velocities and thus, the attenuation coefficient of the slurry at this gas velocity was different than those at other velocities (see Table 3.18).

Figures 3.21a and 3.21b compare average gas holdup values obtained using pressure measurements to those obtained with the nuclear density gauges for experiments with SASOL wax (no solids) at liquid velocities of 0 m/s and 0.005 m/s, respectively. There is very good agreement between different sets of values for both runs. For the batch experiment (Figure 3.20a), gas holdup values obtained using pressure measurements were somewhat lower than those from the density gauge using the Cs–137 source and comparable to those obtained with the density gauge using the Co–60 source.

Figures 3.22a, 3.22b, and 3.22c compare average gas holdups from pressure measurements with those obtained using the nuclear density gauges for experiments with SASOL wax (20 wt% 0 – 5 μm iron oxide particles) at slurry velocities of 0 m/s, 0.005 m/s, and 0.02 m/s, respectively. There is excellent agreement in results obtained in the continuous mode of operation (Figures 3.22a and 3.22b) using the different methods. However, for the batch experiment, gas holdup values obtained using pressure measurements were consistently lower than those obtained using either of the density gauges. As mentioned previously, average gas holdups for the NDG technique were calculated by simply using an arithmetic average of the axial gas holdups (see Eq. 3.45). In order to determine if this method for calculating the average gas holdups caused the differences, average holdups were also calculated by fitting the data to a curve and integrating across the expanded height (see Eq. 3.44). While average holdups were slightly lower using this technique (between 0.4% and 2.0% - relative), they were still higher than the values obtained using the pressure transducers. Axial gas holdups measured using the density gauges for this experiment at gas velocities of 0.04 and 0.09 m/s are compared

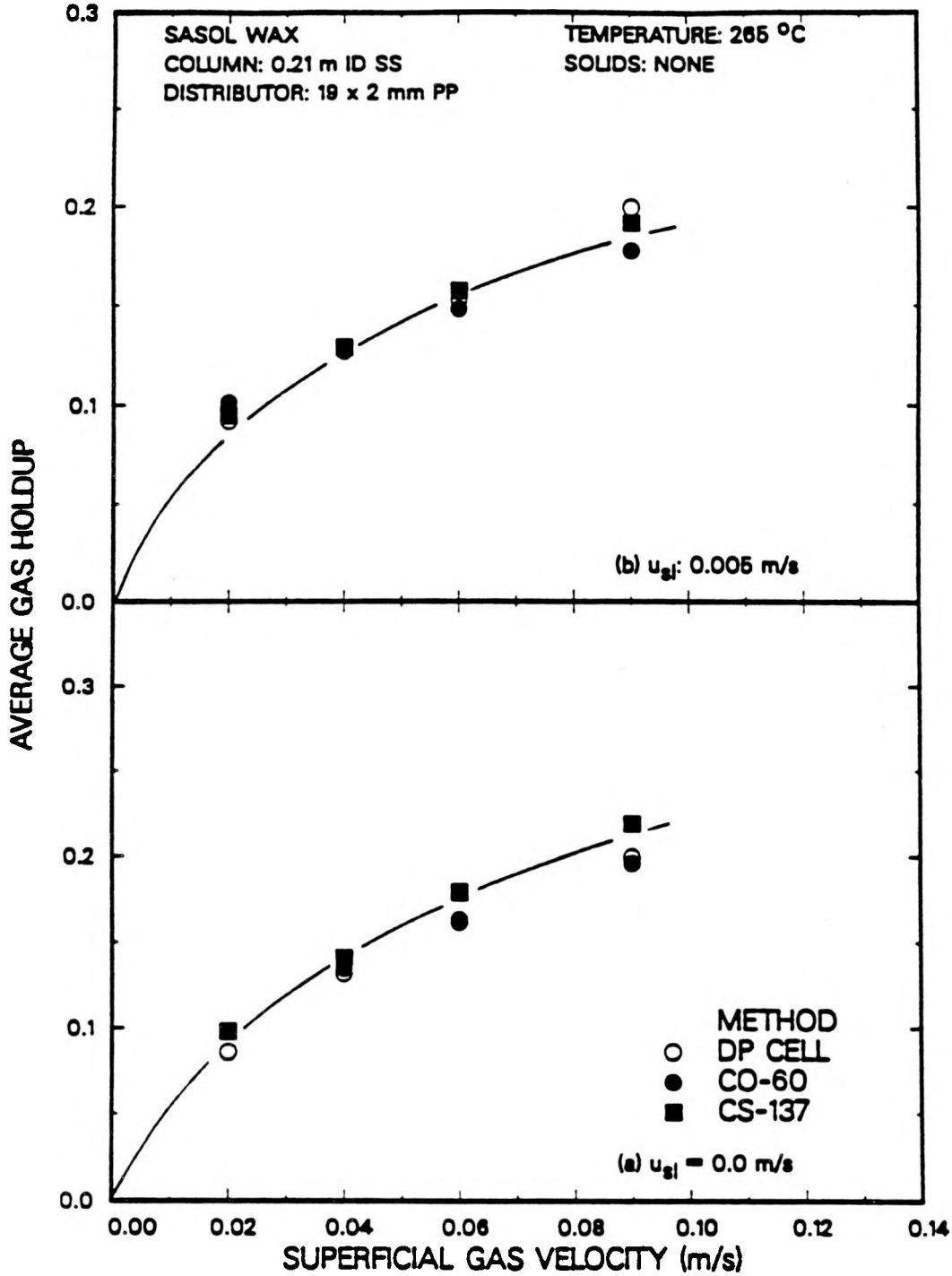

Figure 3.21. Comparison of average gas holdups from the DP cells and nuclear density gauges (SASOL wax, no solids; (a) u_l = 0.0 m/s; (b) u_l = 0.005 m/s).

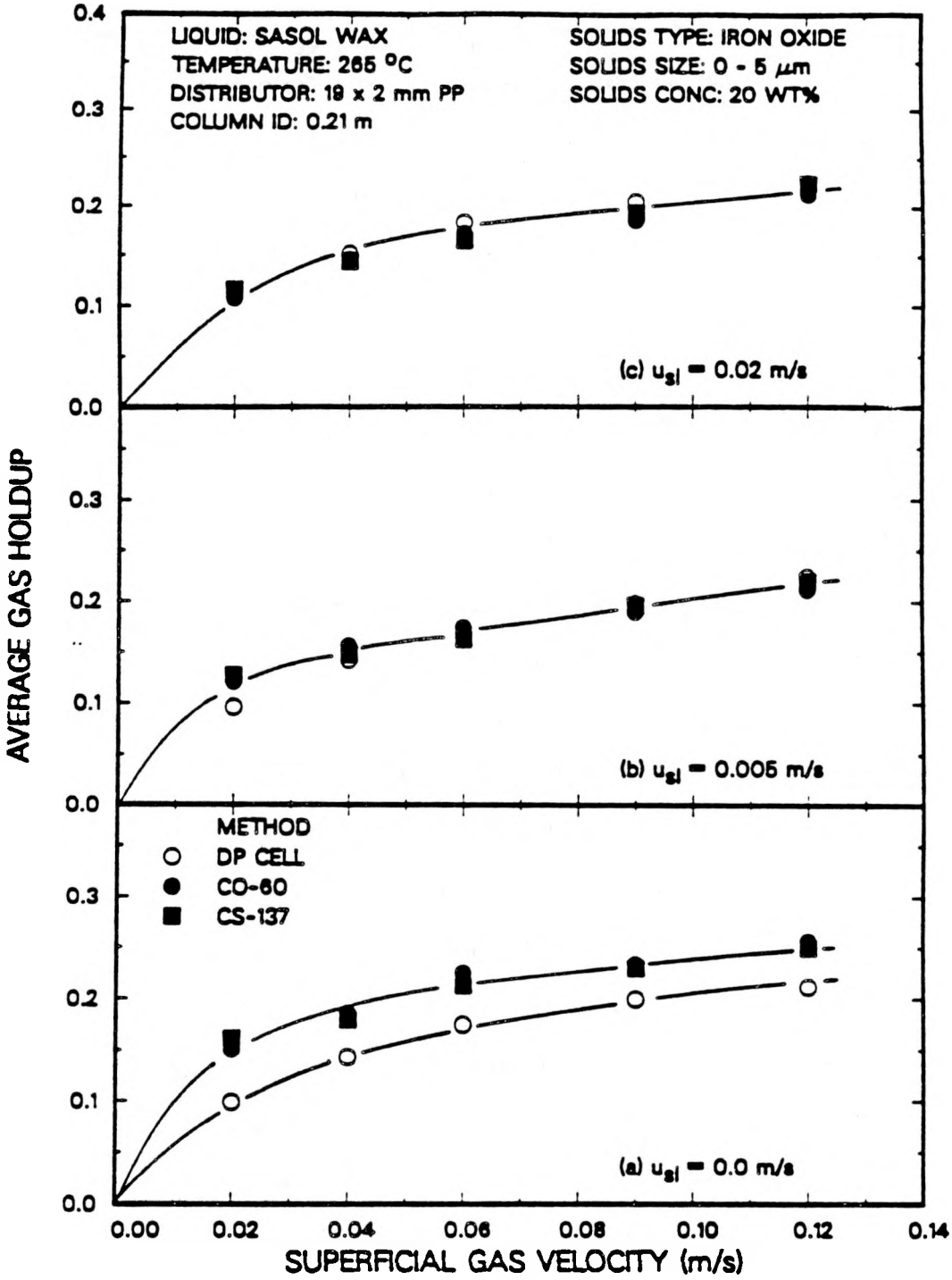

Figure 3.22. Comparison of average gas holdups from the DP cells and nuclear density gauges (SASOL wax, 20 wt% 0 - 5 μm iron oxide; (a) u_{sl} = 0.0 m/s, (b) u_{sl} = 0.005 m/s, (c) u_{sl} = 0.02 m/s).

to axial gas holdups obtained using pressure measurements in Figure 3.23a and 3.23b, respectively. At a gas velocity of 0.04 m/s, the axial gas holdups obtained from pressure measurements were somewhat lower than those obtained using the density gauge. At the present time, we do not know what caused this difference (i.e. if it was due to errors in pressure readings, solids concentrations, or density gauge measurements). At a gas velocity of 0.09 m/s, axial gas holdups obtained from pressure measurements and density gauge measurements were comparable. However, in the bottom most section of the column (0.31 m), the axial gas holdup (pressure measurements) is considerably lower. As a result, the average gas holdup obtained from the density gauges is higher than that obtained from the pressure measurements. This implies, that if axial gas holdups vary considerably over the height of the dispersion, more measurements with the density gauge are needed to obtain an accurate estimate for the average gas holdup. As shown in Figure 2.15, axial gas holdups from continuous experiments varied almost linearly with height. Thus, it is not surprising that average gas holdups obtained with the density gauge were comparable to those obtained with the pressure transducers.

Average gas holdup results from batch experiments with 20 wt% large iron oxide and silica particles are shown in Figures 3.24a and 3.24b, respectively. Once again, gas holdups from the two density gauges were comparable. However, gas holdup values obtained by conventional techniques (pressure measurements) were lower, especially for the experiment with large iron oxide particles. During this experiment, axial gas holdups in the bottom section of the column (i.e. 0.31 m above the distributor) were substantially lower than those at heights of 0.9, 1.5 and 2.1 m as shown in Figure 3.25a and 3.25b. Axial gas holdups from pressure measurements and density gauge measurements were comparable at heights of 0.9, 1.5, and 2.1 m above the distributor, once again indicating that a better estimate for the average gas holdup would be obtained if measurements were made at additional axial positions. During the experiment with large

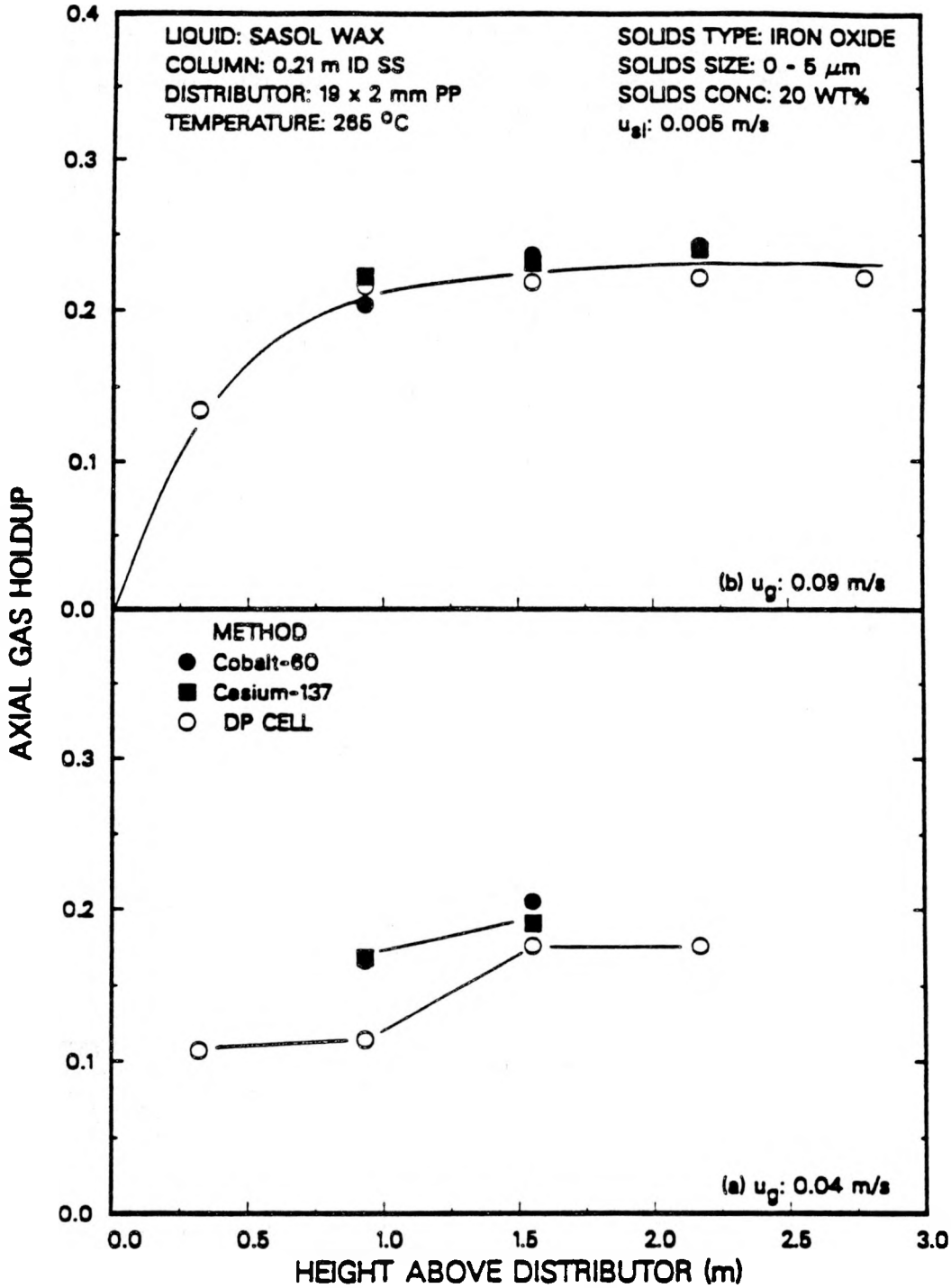

Figure 3.23. Comparison of axial gas holdups from the DP cells and nuclear density gauges (SASOL wax, no solids: (a) u_g = 0.04 m/s; (b) u_g = 0.09 m/s).

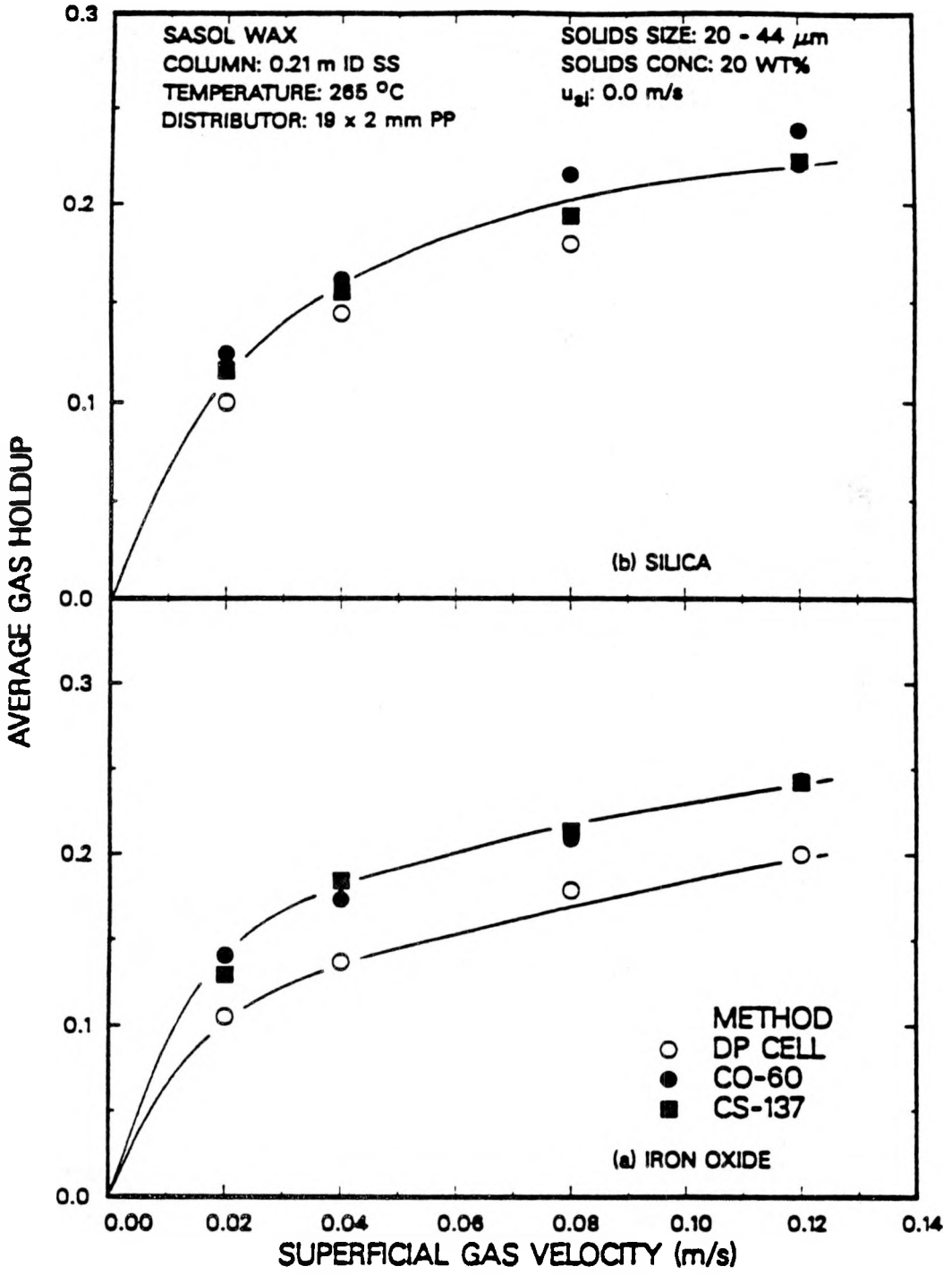

Figure 3.24. Comparison of average gas holdups from the DP cells and nuclear density gauges (SASOL wax; u_{gl} = 0.0 m/s; (a) 20 wt% 20 - 44 μm iron oxide; (b) 20 wt% 20 - 44 μm silica).

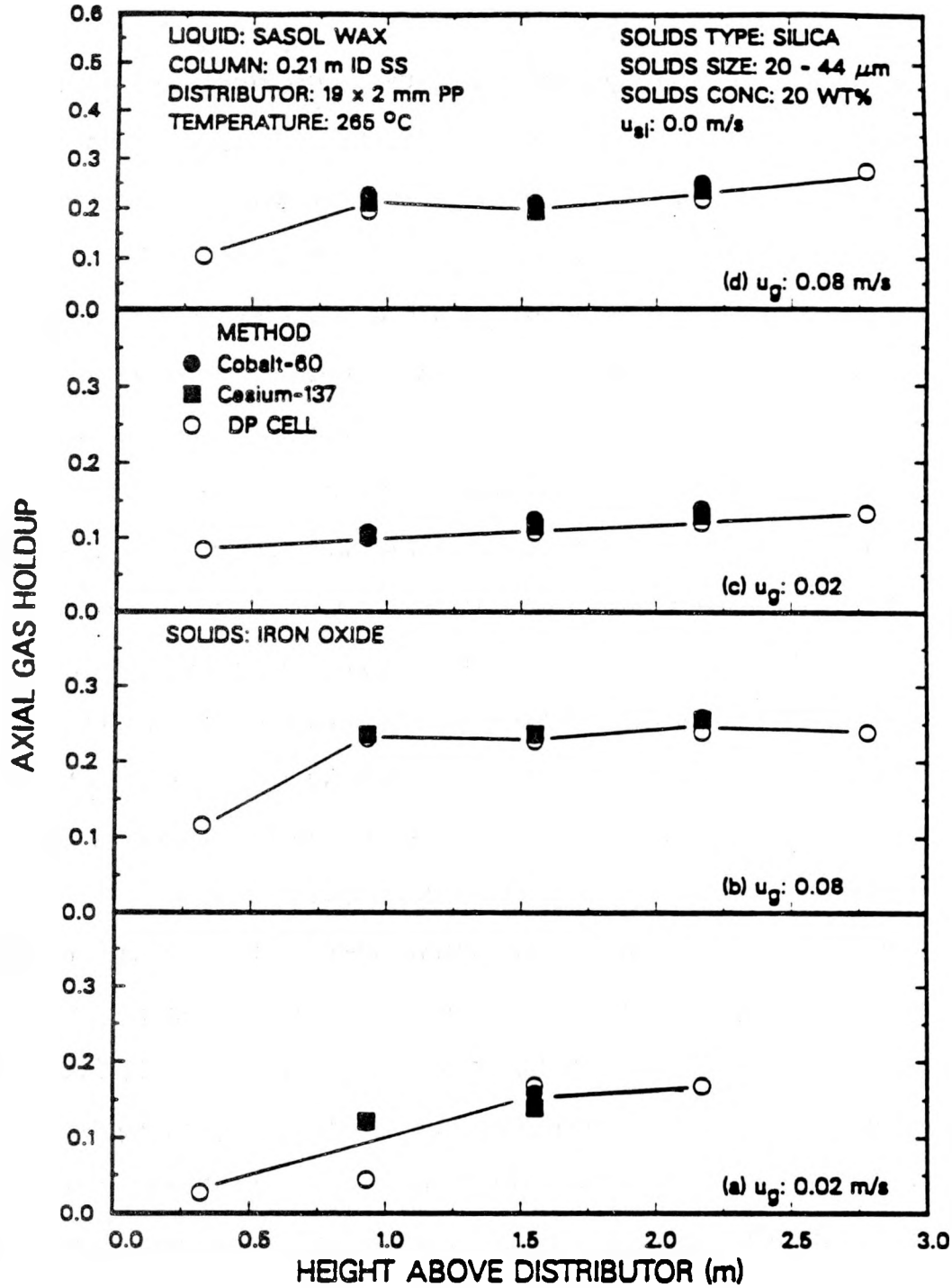

Figure 3.25. Comparison of axial gas holdups from the DP cells and nuclear density gauges (SASOL wax, 20 wt% 20 - 44 μm iron oxide - (a) u_g = 0.02 m/s; (b) u_g = 0.08 m/s; SASOL wax, 20 wt% 20 - 44 μm silica - (c) u_g = 0.02 m/s; (d) u_g = 0.08 m/s).

silica particles, we did not observe as significant difference in axial gas holdups between heights of 0.3 and 0.9 m above the distributor (see Figure 3.25c and 3.25d), consequently, the average gas holdup values obtained using the density gauges compared favorable with those obtained using the pressure transducers.

Figure 3.26 compares average gas holdup values from pressure measurements with those obtained from density gauge measurements for experiments with FT–300 wax. In particular, Figures 3.26a and 3.26b show results from two–phase experiments at slurry velocities of 0.0 and 0.005 m/s, respectively. There is excellent agreement in gas holdups obtained using both pressure measurements and density gauge measurements. For the batch mode experiment with large iron oxide particles, average gas holdups from pressure measurements and density gauge measurements were comparable at all gas velocities except at a velocity of 0.04 m/s (see Figure 3.26c). At this gas velocity, the average gas holdup obtained from pressure measurements was substantially larger than that obtained from density gauge measurements. Once again, this difference is due to the fact that measurements with the density gauges were made at only three positions (i.e. 0.9, 1.5, and 2.1 m); whereas, measurements with the pressure transducers were made at five positions. For this experiment, foam the uppermost region of the column (i.e. above 2.1 m), and the axial gas holdup in this region was 0.68. Since density gauge measurements were limited to heights below this, the average gas holdup estimated from analysis of density gauge data (for both sources) was less than the actual gas holdup.

Axial gas holdups at velocities of 0.04 and 0.12 m/s for the two experiments with no solids are presented in Figure 3.27. The axial gas holdup profile obtained from pressure measurements did not vary significantly with axial position during either of these experiments. Axial gas holdups obtained from density gauge measurements were similar to those obtained from pressure measurements. Axial gas holdups did not vary significantly over the length of the column, and since axial gas holdups from conventional

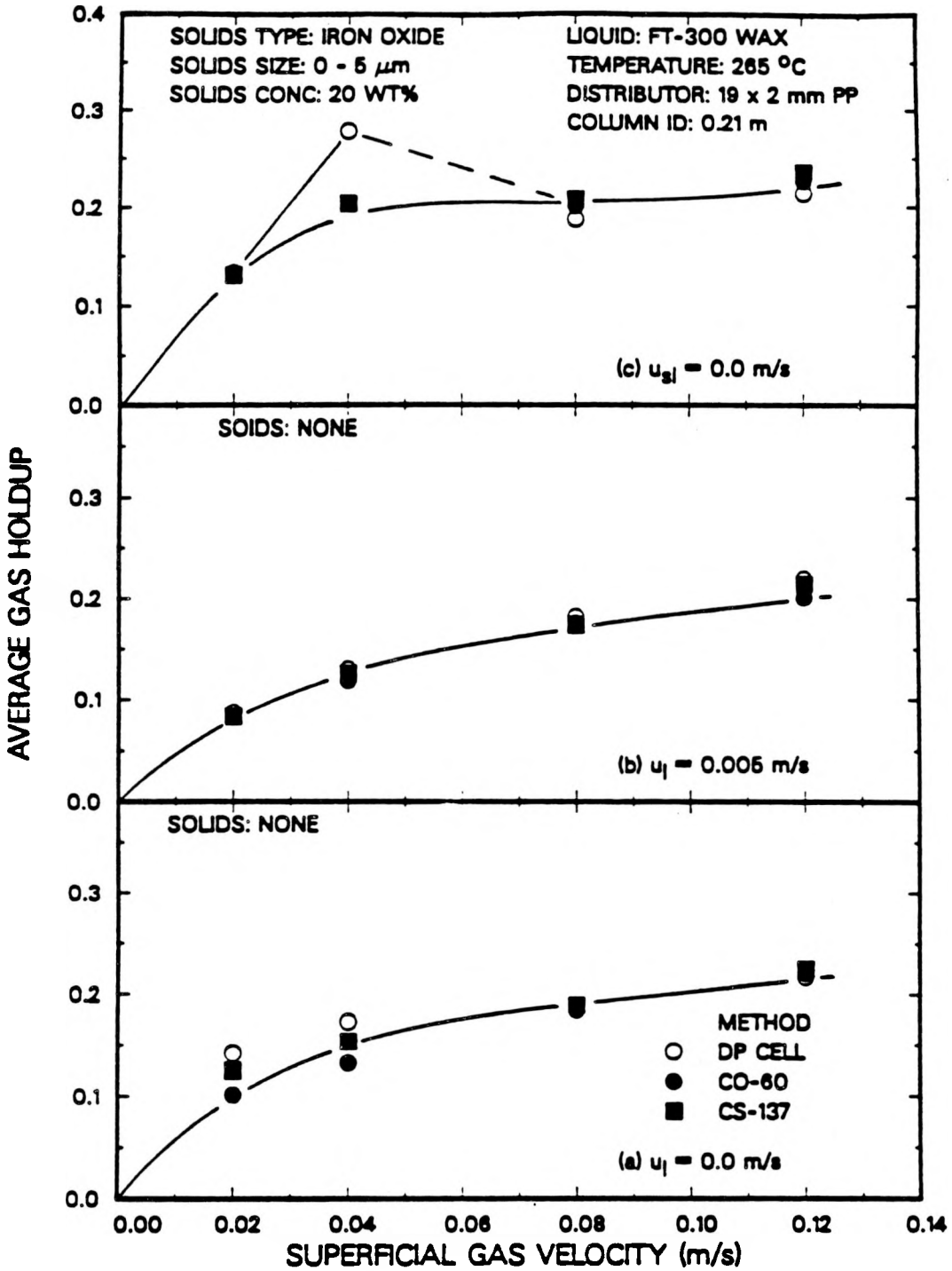

Figure 3.26. Comparison of average gas holdups from the DP cells and nuclear density gauges (FT-300 wax; (a) u_l = 0.0 m/s, no solids; (b) u_l = 0.005 m/s, no solids; (c) u_{sl} = 0.0 m/s, 20 wt% 20 - 44 μm iron oxide).

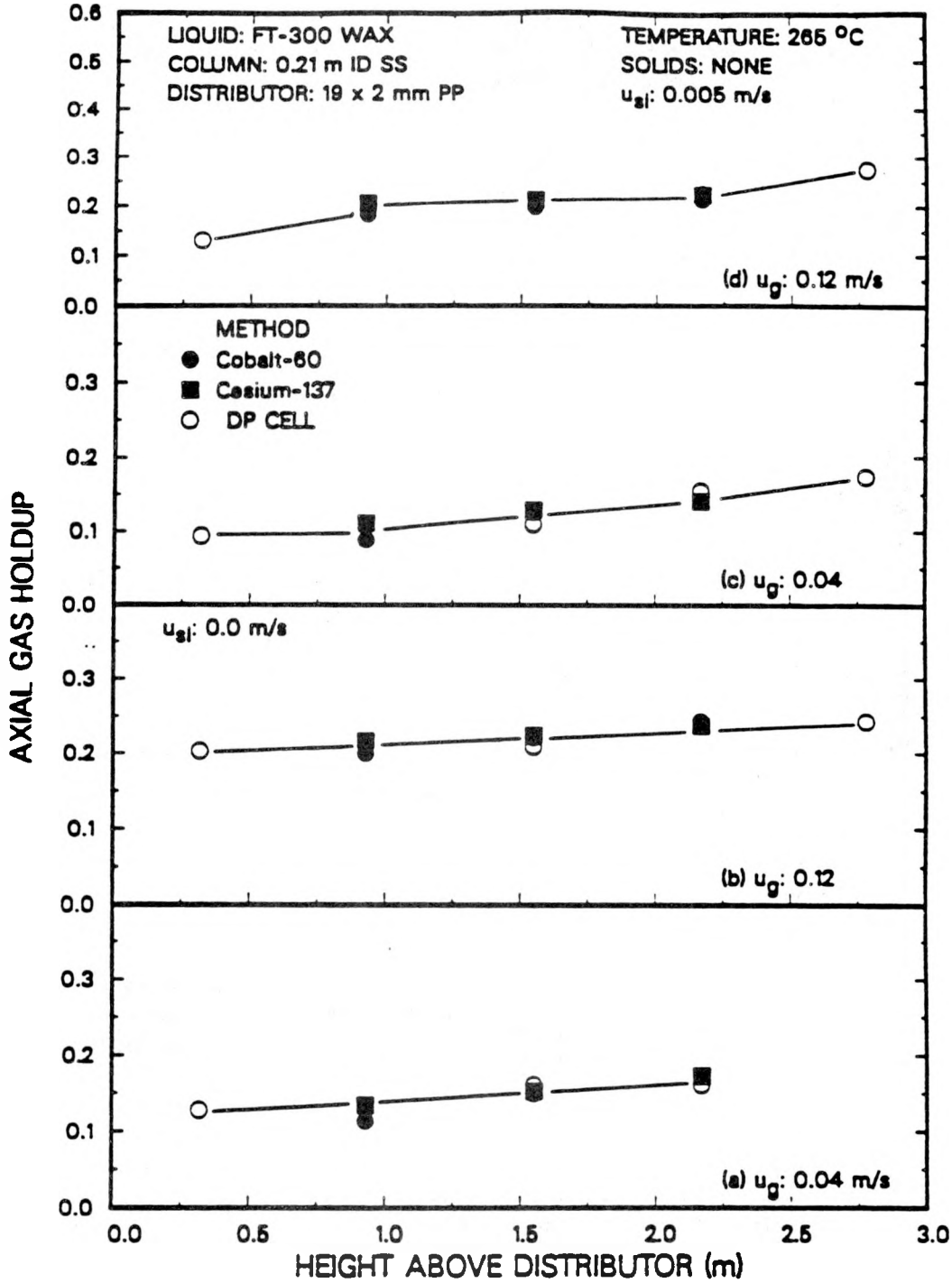

Figure 3.27. Comparison of axial gas holdups from the DP cells and nuclear density gauges with FT-300 wax and no solids (u_l = 0.0 m/s - (a) u_g = 0.04 m/s; (b) u_g = 0.12 m/s; u_l = 0.005 m/s - (c) u_g = 0.04 m/s; (d) u_g = 0.12 m/s).

measurements and density gauge measurements were comparable at heights of 0.9, 1.5 and 2.1 m above the distributor, it is not surprising that there was excellent agreement in average gas holdups obtained from the different techniques. Figure 3.28 shows axial gas holdups obtained from the batch experiment with large iron oxide particles (see Figure 3.26c) at gas velocities of 0.02, 0.04, and 0.08 m/s. During this experiment axial gas holdups almost varied linearly with height above the distributor, with the exception of the axial gas holdup in the uppermost section of the column at a gas velocity of 0.04 m/s. Thus, average gas holdups obtained from the pressure measurements are higher than those obtained from the density gauge measurements at this gas velocity.

Overall, axial gas holdups obtained from the nuclear density gauges compared favorably with those obtained using pressure measurements. For experiments in which either there was not a significant gradient in axial gas holdups, or where axial gas holdup increased linearly with height the average gas holdup values from the different methods were similar. Based on our results from pressure measurements, it appears that axial gas holdups are essentially uniform (or vary only slightly) in the central portion of the column; however, in the uppermost region of the column, or at the bottom of the column, axial gas holdups can be substantially different. Thus, a better estimate of the average gas holdup could be obtained if density gauge measurements were made in the top and bottom regions of the column.

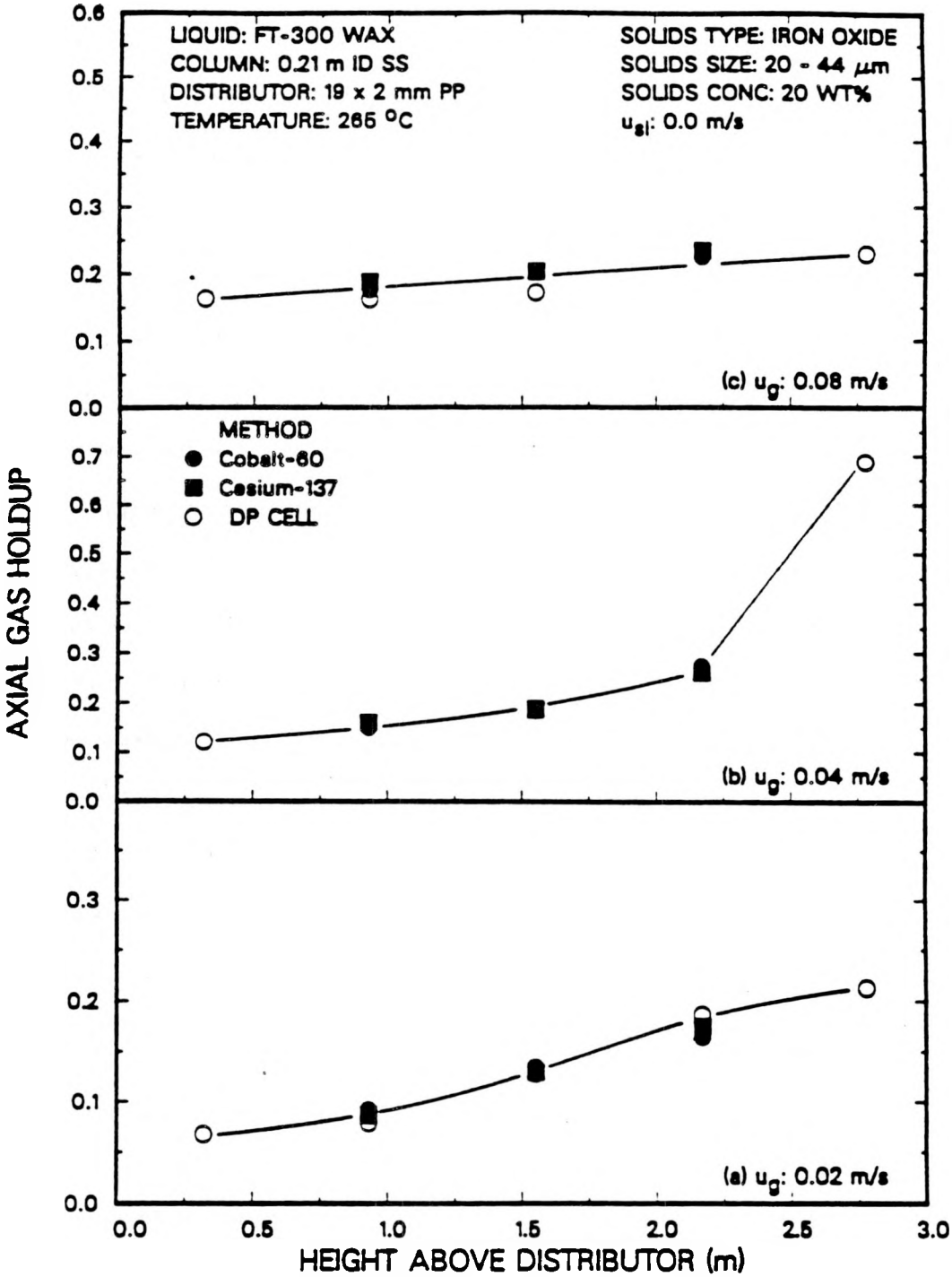

Figure 3.28. Comparison of axial gas holdups from the DP cells and nuclear density gauges (FT-300 wax, 20 wt% 20 - 44 μm iron oxide - (a) u_g = 0.02 m/s; (b) u_g = 0.04 m/s; (c) u_g = 0.08 m/s).

IV. AXIAL SOLIDS DISTRIBUTION

Knowledge of axial solids distribution is essential to properly design a slurry bubble column reactor. The distribution of solid particles in a bubble column reactor has an effect on reactant conversion and may affect product selectivity (Bukur and Kumar, 1986; Smith and Ruether, 1985). Operating conditions (i.e. gas and slurry velocity), physical properties of the liquid medium, particle size and density, and column diameter influence the axial distribution of solid particles in a slurry bubble column reactor.

In this study, the effect of particle size and type, column diameter, slurry velocity and gas velocity on axial solids distribution was examined. The semi–infinite dispersion model presented by Smith and Ruether (1985) was used to analyze our results. The theory (semi–infinite dispersion model), a summary of the average solids concentrations in the bubble column and storage tank during each run, and results (i.e. axial solids distributions and axial solids dispersion coefficients) from our studies are discussed.

Semi–Infinite Dispersion Model

Several variations of the one–dimensional sedimentation dispersion model, based on different frames of reference, are available in the literature. The model presented by Parulekar and Shah (1980) is based on the cross–sectional area of the column; whereas, the models by Cova (1966), Kato et al. (1972), Smith and Ruether (1985), and O'Dowd et al. (1987), are based on the cross–sectional area occupied by the slurry phase alone (i.e. the area associated with the gas phase is not included). More recently, Murray and Fan (1989) developed a mechanistic model to describe the solids distribution in slurry bubble columns. In the present analysis, the model presented by Smith and Ruether (1985) was used to analyze our experimental data. Their one–dimensional dispersion

model is given by

$$\frac{\delta}{\delta x}\left[\frac{-E_s}{h_{exp}}\frac{\delta C_s}{\delta x}\right]+\frac{\delta}{\delta x}\left[\left[\frac{u_{s\ell}}{(1-\epsilon_g)}-\Phi_\ell u_p\right]C_s\right]=h_{exp}\frac{\delta c_s}{\delta t} \tag{4.1}$$

where x is the dimensionless height above the distributor (based on the expanded height, h_{exp}), E_s is the axial solids dispersion coefficient, C_s is the solids concentration in the slurry, $u_{s\ell}$ is the average slurry flow rate, u_p is the hindered settling velocity of the solid particles, Φ_ℓ is the volume fraction of liquid in the slurry, and t is the time. The solids concentration in the slurry, C_s is defined as

$$C_s=\omega_s\rho_{s\ell} \tag{4.2}$$

where ω_s is the weight fraction of solids and $\rho_{s\ell}$ is the density of the slurry.

Since the volume fraction of liquid in the slurry, Φ_ℓ, does not vary significantly with axial position (less than 3% for our experiments), an average value may be used and is defined as:

$$\overline{\Phi_\ell}=(1-\frac{\overline{C_s}}{\rho_s}) \tag{4.3}$$

where ρ_s is the density of the solids and $\overline{C_s}$ is the average solids concentration in the slurry and is given by

$$\overline{C_s}=\frac{\sum_i C_{s_{ij}}V_{ij}}{V_T} \qquad i=1 \text{ to } 5 \text{ and } j=i+1 \tag{4.4}$$

where V_T is the total volume of slurry, V_{ij} is the volume of slurry between pressure ports i and j (see Figure 2.9) and $C_{s_{ij}}$ is the solids concentration in the slurry between pressure ports i and j. Note, j = 6 corresponds to the top of the column. The total volume of slurry is

$$V_T=h_{exp}(1-\epsilon_g) \tag{4.5}$$

where h_{exp} is the expanded height of the dispersion and ϵ_g is the average gas holdup in the column. The volume of slurry between pressure ports i and j is

$$V_{ij} = \Delta h_{ij}(1 - \epsilon_{g_{ij}}) \qquad i = 1 \text{ to } 5 \text{ and } j = i + 1 \tag{4.6}$$

where Δh_{ij} is the distance between pressure ports i and j and $\epsilon_{g_{ij}}$ is the axial gas holdup in the i,j section of the column.

For batch experiments (i.e. $u_{s\ell} = 0$) at steady state (no time derivatives), and assuming no dependency of Φ_ℓ on height, Eq. 4.1 reduces to

$$\frac{\delta}{\delta x}\left[\frac{-E_s}{h_{exp}}\frac{\delta C_s}{\delta x}\right] - \frac{\delta}{\delta x}\left[\overline{\Phi_\ell} u_p C_s\right] = 0 \tag{4.7}$$

Equation 4.7 may be integrated twice to yield:

$$C_s = C_1 + C_2 \exp\left[-h_{exp}\overline{\Phi_\ell}\frac{u_p}{E_s}x\right] \tag{4.8}$$

For the semi–infinite dispersion model, the boundary conditions are given by: $C_s = 0$ as x approaches infinity and $C_s = C_s^B$ for x=0, where C_s^B is the concentration of solids at the bottom of the dispersion. Application of these boundary conditions to Eq. 4.8 yields:

$$C_s = C_s^B \exp\left[-h_{exp}\overline{\Phi_\ell}\frac{u_p}{E_s}x\right] \tag{4.9}$$

Solids concentration vs. axial position data can now be used to obtain estimates of $\frac{u_p}{E_s}$ and the concentration of solids at the bottom of the column, C_s^B, using regression analysis.

For continuous slurry flow, the solution to Eq. 4.1 is:

$$C_s = (C_s^B + a)\exp\left[-(u_p\overline{\Phi_\ell} - u'_{s\ell})\frac{h_{exp}}{E_s}x\right] - a \tag{4.10}$$

where $a = \frac{u'_{s\ell} C_s^f}{\Phi_\ell u_p - u_{s\ell}}$ and $u'_{s\ell} = \frac{u_{s\ell}}{(1-\epsilon_g)}$. The quantity C_s^f is the concentration of solids in the feed (or storage tank). It is assumed that no settling occurs in the feed stream (i.e.,

at $x<0$, $u_p = 0.0$ and $\frac{\delta C_s}{\delta x} = 0.0$). In developing Eqs. 4.9 and 4.10, it was assumed that the gas holdup did not vary with axial position. The assumption of an axially uniform gas holdup holdup profile leads to the assumptions of a constant (i.e. no axial variation) dispersion coefficient and a constant hindered settling velocity. With the exception of experiments in which foam was produced, axial gas holdup profiles were fairly uniform (see Figures 2.14 and 2.15). The model also assumes a uniform particle size.

A variety of approaches may be used to obtain values for u_p, E_s, and C_s^B (see Eq. 4.10). Kato et al. (1972) assumed that E_s and u_p were not affected by slurry velocity, $u_{s\ell}$. They used the quantity $\frac{u_p h_{exp}}{E_s}$ obtained from batch experiments (see Eq. 4.9) together with two points taken from a smoothed plot of concentration versus axial position (continuous experiment) to obtain a value for $\frac{u'_{s\ell} h_{exp}}{E_s}$, from which E_s was calculated. Then substituting the values of E_s and h_{exp} into $\frac{u_p h_{exp}}{E_s}$, a value for u_p was obtained. On the other hand, Smith and Ruether (1985), used non–linear regression analysis of Eq. 4.10 to obtain E_s, u_p, and C_s^B.

For batch experiments, u_p and E_s are not separable, and in order to obtain axial dispersion coefficients, one must assume values for the hindered settling velocity of the solids, u_p. There are various correlations available in the literature for estimating the hindered settling velocity (e.g. Kato et al., 1972; Smith and Ruether, 1985; Zigrand and Sylvester, 1980; and O'Dowd et al., 1987). The correlations proposed by Kato et al., Smith and Ruether, and O'Dowd et al. are all of the form

$$u_p = a u_t^b u_g^c \overline{\Phi_\ell}^d \tag{4.11}$$

where u_t is the terminal rise velocity of a single particle in an infinite medium. The numerical values of constants (a, b, c, and d) in Eq. 4.10 are (1.33, 0.75, 0.25, 2.5) for Kato et al., (1.91, 0.8, 0.26, 3.5) for Smith and Ruether, and (1.69, 0.8, 0.23, 1.28) for O'Dowd et al. correlation.

Several correlations have been presented in the literature for predicting axial dispersion coefficients. The correlation proposed by Kato et al. is:

$$Pe_p = \frac{13Fr_g(1 + 0.009Re_pFr_g^{-0.8})}{1 + 8Fr_g^{0.85}} \tag{4.12}$$

The equation presented by Smith and Ruether is:

$$Pe_p = 9.6\left[\frac{Fr_g^6}{Re_g}\right]^{0.114} + 0.019Re_p^{1.1} \tag{4.13}$$

and the equation presented by O'Dowd et al. for an unbaffled bubble column is:

$$Pe_p = 7.7\left[\frac{Fr_g^6}{Re_g}\right]^{0.098} + 0.019Re_p^{1.1} \tag{4.14}$$

where $Pe_p = \frac{u_g d_{col}}{E_s}$, $Re_g = \frac{u_g d_{col}\rho_\ell}{\mu_\ell}$, $Fr_g = \frac{u_g}{\sqrt{g d_{col}}}$, and $Re_p = \frac{d_p \rho_\ell u_t}{\mu_\ell}$. The terms containing Re_p in Eqs. 4.12 to 4.14 are correction factors which take into account particle size. Due to insufficient data with different size particles, O'Dowd et al., used the correction factor presented by Smith and Ruether. Murray and Fan (1989) also presented an empirical correlation for predicting axial solids dispersion coefficients, E_s; however, their correlation does not take into account the effect of column diameter.

Summary of Solids Concentrations in the Column and Storage Tank

As mentioned in Chapter II, slurry samples were withdrawn from the storage tank and column during three–phase experiments. Table 4.1 contains the nominal solids concentration for each run, as well as the range of average solids concentration in the column and in the storage tank during each run. Also shown in Table 4.1 is the total amount of solids charged in the storage tank and the total amount of solids accounted for during each experiment. The experiment numbers given in the first column of Tables

4.1a (0.05 m ID column) and 4.1b (0.21 m ID column) correspond to the experiment numbers given in Tables 2.4 and 2.5, respectively.

For experiments conducted with small particles, the solids concentrations measured in both the storage tank and column were usually within 3 % (absolute) of the desired (or nominal) concentration. However, very low solids concentrations were observed in both the storage tank and bubble column during our initial continuous experiments with large iron oxide particles (experiments 19 and 20 in Table 4.1a) in the 0.05 m ID column. Following these experiments, the entire system was inspected and approximately 50% of the initial amount of solids charged in the storage tank was recovered in the expansion unit. The expansion unit was modified to reduce the amount of settling (see Figure 4.1). Partitions were added inside the expansion unit to minimize the surface area available for the deposition of solids. Experiments 26 and 27 were conducted with large iron oxide particles at superficial slurry velocities of 0.02 and 0.005 m/s following the modification of the expansion unit. There was some settling of solids during these experiments; however, the amount of settling was substantially less than that previously observed (i.e. the solids concentration in the column was 18 – 19 %). During experiment 27 ($u_{s\ell}$ = 0.005 m/s), the overflow line from the expansion unit to the calibration chamber (see Figure 4.1) plugged during the last gas velocity (i.e. u_g = 0.02 m/s), and the solids concentration in column dropped considerably (i.e. ω_s (column) = 19.2% at u_g = 0.04 m/s and 9.3 % at u_g = 0.02 m/s). Also, during this same experiment solids concentrations in the storage tank were very low (i.e. 6.9 – 8.4 wt%). Similar results were obtained during the experiment with SASOL wax and large iron oxide particles at a slurry flow rate of 0.005 m/s (see results for experiment 33 in Table 4.1a).

Solids accountability (large particles) was substantially better for experiments conducted in the large diameter column, with the exception of experiments 15 and 16 (see Table 4.1b). The solids concentration in these two experiments (both in the column and

Table 4.1a. Summary of Solids Concentrations for Experiments in the 0.05 m ID Bubble Column

EXP. No.	u_ℓ (m/s)	SOLIDS[a]	NOMINAL CONC (WT %)	AVG CONC IN COLUMN (WT %)	AVG CONC IN TANK (WT %)	AMOUNT CHARGED (g)	AMOUNT ACCOUNTED TANK+COLUMN (g)
4	0.005	1	10	9.5–10.0	N/A	1900	N/A
5	0.02	1	10	8.9–9.5	N/A	1900	N/A
6	0.0	1	10	9.5–10.2	N/A	1900	N/A
7	0.005	1	20	16.4–17.4	15.8–17.4	3910	3000–3100
8	0.02	1	20	17.3–17.7	16.9–18.3	3910	3400–3600
9	0.0	1	20	18.5–19.1	19.4	3910	3200
10	0.005	1	30	28.4–28.9	27.9–29.3	7282	6220–6300
11	0.02	1	30	28.5–29.3	27.6–28.6	7282	6300–6500
12	0.0	1	30	29.2–29.6	28.5–29.1	7282	6325–6370
13[e]	0.005	2	10	3.0–5.0	3.0–5.0	1765	200–650
14	0.005	3	10	9.2–10.5	8.6–9.4	1766	1410–1580
15	0.005	3	20	18.9–20.0	18.8–19.2	4284	3600–3800
16	0.02	3	20	17.2–18.6	18.1–19.1	4284	3400–3700
17	0.0	3	20	18.0–20.0	17.68	4284	3300–3400
18	0.005	3	30	26.3–28.1	25.1–27.1	7926	5100–5500
19	0.005	2	10	2.5–3.6	1.2–1.7	1816	230–370
20	0.02	2	10	5.3–6.5	4.2–5.2	1816	680–840
21	0.0	2	20	21.4–24.0	21.2	4103	3871–3960
22	0.0	4	20	7.5–8.2,20.2[b]	18.3	2800	2741
25	0.0	2	20	10.16–17[c]	19.3	4540	4120
26	0.02	2	20	17.8–19.5	15.6–17.0	4540	3600–3730
27	0.005	2	20	9.21–22.6[d]	6.9–8.4	4540	1790–2710
28	0.0	4	20	17.8–18.7	19.4	3280	3050
31	0.005	1	20	17.0–21.3	17.2–18.2	3936	3180–3540
32	0.0	2	20	18.3–22.6	18.5	3973	3820
33	0.005	2	20	14.6–18.3	9.9–10.8	3973	2032–2086
34[e]	0.005	2	20	N/A	N/A	3973	N/A

[a] 1: 0 – 5 μm iron oxide
2: 20 – 44 μm iron oxide
3: 0 – 5 μm silica
4: 20 – 44 μm silica

[b] 20 wt% at u_g = 0.12 m/s

[c] 10 wt% at u_g = 0.02 m/s

[d] 9 wt% at u_g = 0.02 m/s

[e] Pump shut down during the experiment

Table 4.1b. Summary of Solids Concentration for Experiments in the 0.21 m ID Bubble Column

EXP. No.	u_ℓ (m/s)	SOLIDS[a]	NOMINAL CONC (WT %)	AVG CONC IN COLUMN (WT %)	AVG CONC IN TANK (WT %)	AMOUNT CHARGED (g)	AMOUNT ACCOUNTED TANK+COLUMN (g)
6	0.0	1	10	9.7–10.1	9.2	13620	13260
7	0.0	1	20	18.0–19.9	20.6	30418	30640
8	0.005	1	20	20.2–20.7	20.4–20.9	30418	28550–29940
9	0.02	1	20	20.2–21.2	20.9–21.2	30418	28400–30300
10	0.0	1	20	19.0–21.2	20.3	30418	29680
11	0.005	1	20	20.3–21.0	19.7–21.1	30418	28500–29140
12	0.0	1	20	20.4–22.1	19.5	30418	27310
13	0.0	1	30	29.0–30.7	28.7–29.9	47216	45800–44970
14	0.005	30	29.3–30.3	29.5–30.0	47216	39400–43400	
15[b]	0.005	2	10	6.4–8.5	7.1–7.5	14272	8210–10120
16[b]	0.02	2	10	0.6–7.7	2.2–8.6	14272	1900–5160
17	0.0	2	20	17.2–22.2	21.1	41016	41467
18	0.005	2	20	20.9–24.9	18.0–20.9	41016	34310–39770
19	0.02	2	20	22.7–23.7	20.7–22.4	41016	40410–41100
20	0.0	2	20	18.5–22.9	N/A	41016	N/A
21	0.0	2	20	14.9,23.0–24.6[c]	N/A	41016	N/A
22	0.0	2	30	36.5–37.4	29.4	68710	63823
23	0.005	2	30	34.1–35.1	30.5–32.1	68710	59750–69240
24	0.02	2	30	33.1–36.6	32.4–34.9	68710	59750–69240
26	0.0	4	20	23.7–26.7	23.8	37355	39400
27	0.005	4	20	19.0–20.1	19.9–21.6	37355	31900–34100
28	0.02	4	20	18.5–23.0	19.5–21.8	37355	31970–34400
29	0.005	4	30	33.6–35.4	33.4–34.0	60764	60890–62470
33	0.0	2	20	13.0[c],20.4–21.2	N/A	30645	N/A
34	0.005	2	20	17.2–20.7	13.7–17.4	30645	21550–27704
35	0.005	2	20	15.8[c],19.9–21.5	14.4,18.0–19.7	33709	25320–35650

[a] 1: 0 – 5 μm iron oxide
2: 20 – 44 μm iron oxide
4: 20 – 44 μm silica

[b] Poor solids suspension in the storage tank

[c] Low solids concentrations at u_g = 0.02 m/s was due to settling in the bottom of the column

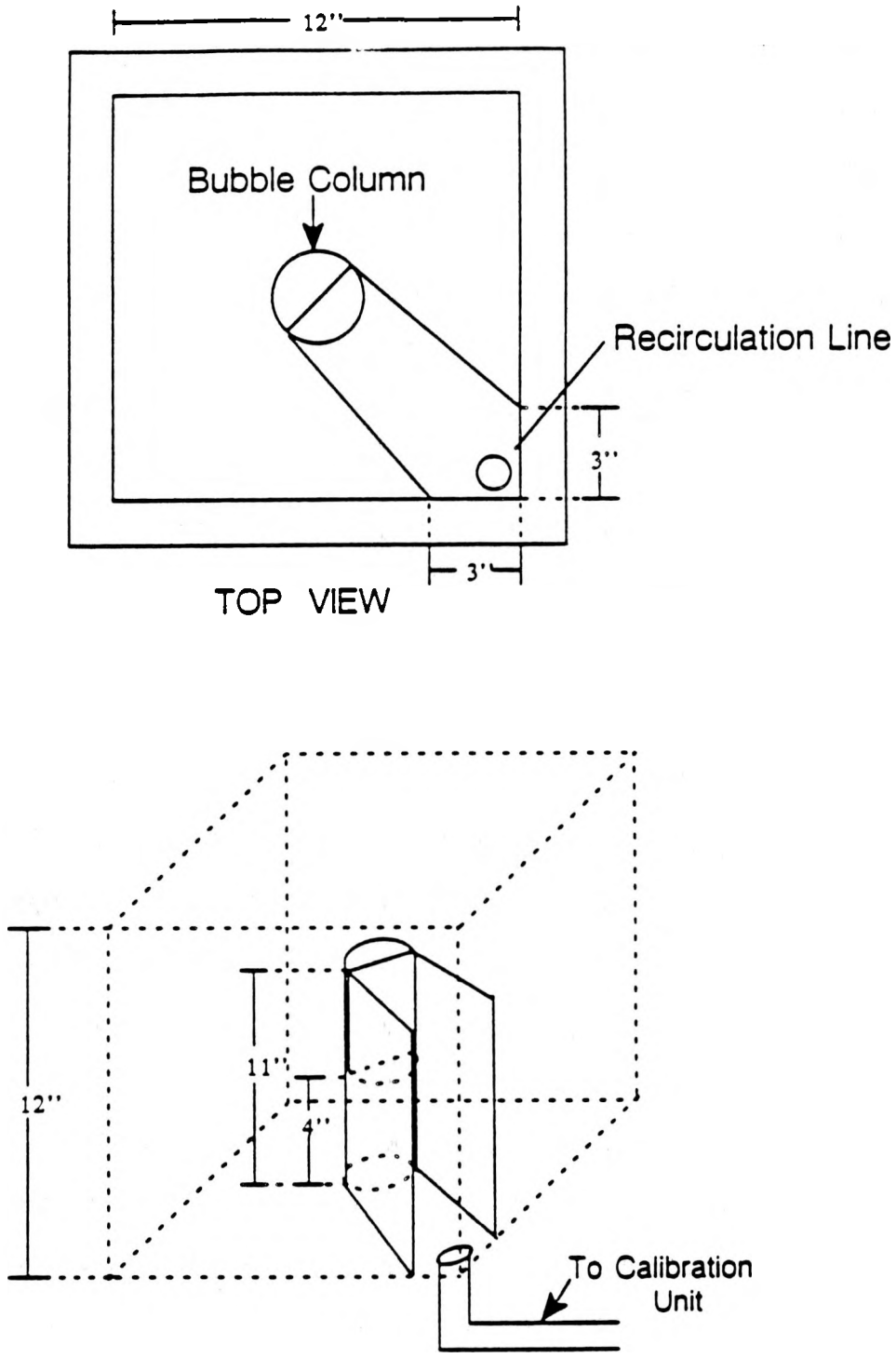

FIGURE 4.1. Schematic diagram of modified expansion unit.

storage tank) was considerably lower than the nominal wt% solids. After these runs, the system was shut down and inspected. It was found that the majority of solids had settled at the bottom of the storage tank. In order to improve mixing in the storage tank, a new propeller was installed. Following this modification, solids concentrations in the storage tank and bubble column were similar to the desired (or nominal) concentration. During three of the experiments with large particles (i.e. experiments 21, 33, and 35 in Table 4.1b), solids settled in the bottom of the column at a gas velocity of 0.02 m/s. Since we were unable to account for these solids, the measured solids concentrations in both the bubble column and storage tank were low at this gas velocity.

Following each batch of experiments, the slurry (wax + solids) was removed from the system and weighed. For experiments in the small column, approximately 90 – 95% of the slurry charged was recovered. And, for experiments in the large column, approximately 95 – 99% of the slurry charged was recovered.

Results and Discussion

Solids concentration profiles obtained from batch experiments in the 0.05 m ID column with large (i.e. 20 – 44 μm) iron oxide and silica particles were analyzed using the one–dimensional sedimentation dispersion model to obtain axial solids dispersion coefficients, E_s. Due to operational problems with both the pump (i.e. inability to maintain a constant flow rate) and settling of solids in the expansion unit, solids concentration data from experiments conducted in the continuous mode of operation in the small column were not analyzed. Data from both batch and continuous (one) experiments in the 0.21 m ID column with large particles were analyzed to obtain axial solids dispersion coefficients.

Regardless of the slurry flow rate, particle type, or column diameter, axial solids distributions were fairly uniform at all gas velocities for experiments conducted with

small (i.e. 0 – 5 μm) particles. Figures 4.2a and 4.2b show axial solids concentrations (wt%) from batch experiments conducted with slurries containing 20 wt% small iron oxide and small silica particles, respectively, in the 0.05 m ID column. The decrease in axial solids concentration at a height of 2.2 m is due to the inability of the foam to suspend the solids. Solids concentrations from a batch experiment with 0 – 5 μm iron oxide particles (20 wt%) in the 0.21 m ID column are shown in Figure 4.2c. Axial solids concentrations for experiments with small particles varied by less than 2 wt% (actual) across the entire column during all continuous experiments.

Solids concentration profiles from batch experiments with 20 wt% 20 – 44 μm iron oxide and silica particles in the 0.05 m ID column are shown in Figures 4.3a and 4.3b, respectively. During these experiments, significant gradients in the axial solids distribution were observed. Our results from the continuous experiments with large iron oxide particles show that a slight upward slurry velocity (0.02 m/s) significantly improves the suspension of solids (see Figure 4.3c). During this experiment, there were some problems with the pump, and the actual slurry velocity ranged from approximately 0.01 to 0.03 m/s. However, these results indicate that solids suspension, which does not show any noticeable improvement when gas velocity is increased (see Figures 4.3a and 4.3b) improves significantly with the introduction of a small upward slurry flow. This is expected since the terminal settling velocity for large iron oxide particles is about 0.001 m/s and that for silica particles is 0.0004 m/s. Both of these values are well below the slurry circulation velocity (0.01 – 0.03 m/s).

Figures 4.4a and 4.4b show solid concentration profiles for batch experiments conducted with large iron oxide particles in the 0.21 m ID bubble column with the perforated plate (PP) and bubble cap (BC) distributors, respectively. Axial solids concentration profiles from experiments with the PP and BC distributors were similar. Solids concentration gradients in the small column for batch experiments with large particles (see

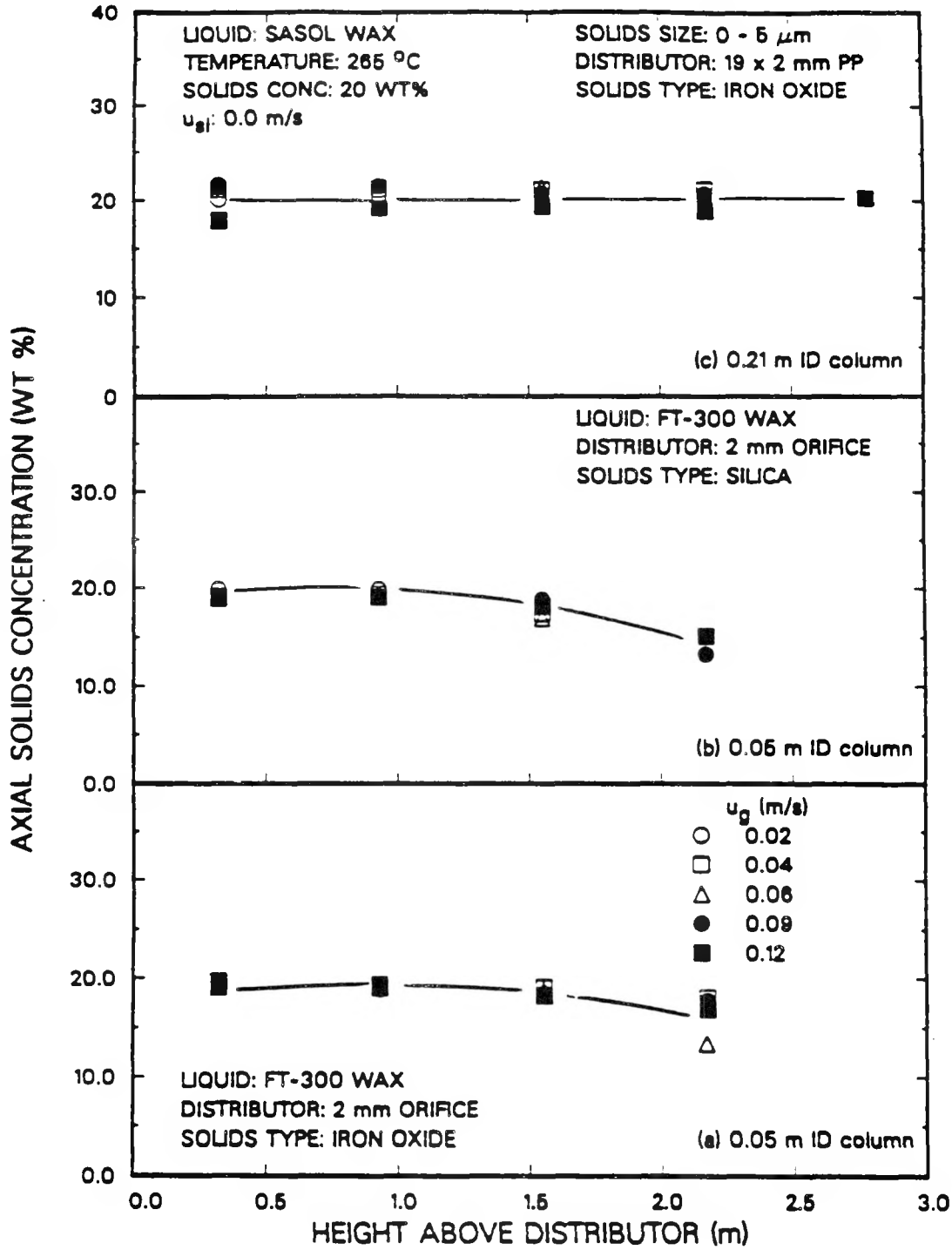

Figure 4.2. Effect of axial position and superficial gas velocity on solids concentrations (20 wt%, 0 - 5 μm particles, u_{sl} = 0.0 m/s; (a) iron oxide, 0.05 m ID column; (b) silica, 0.05 m ID column; (c) iron oxide, 0.21 m ID column).

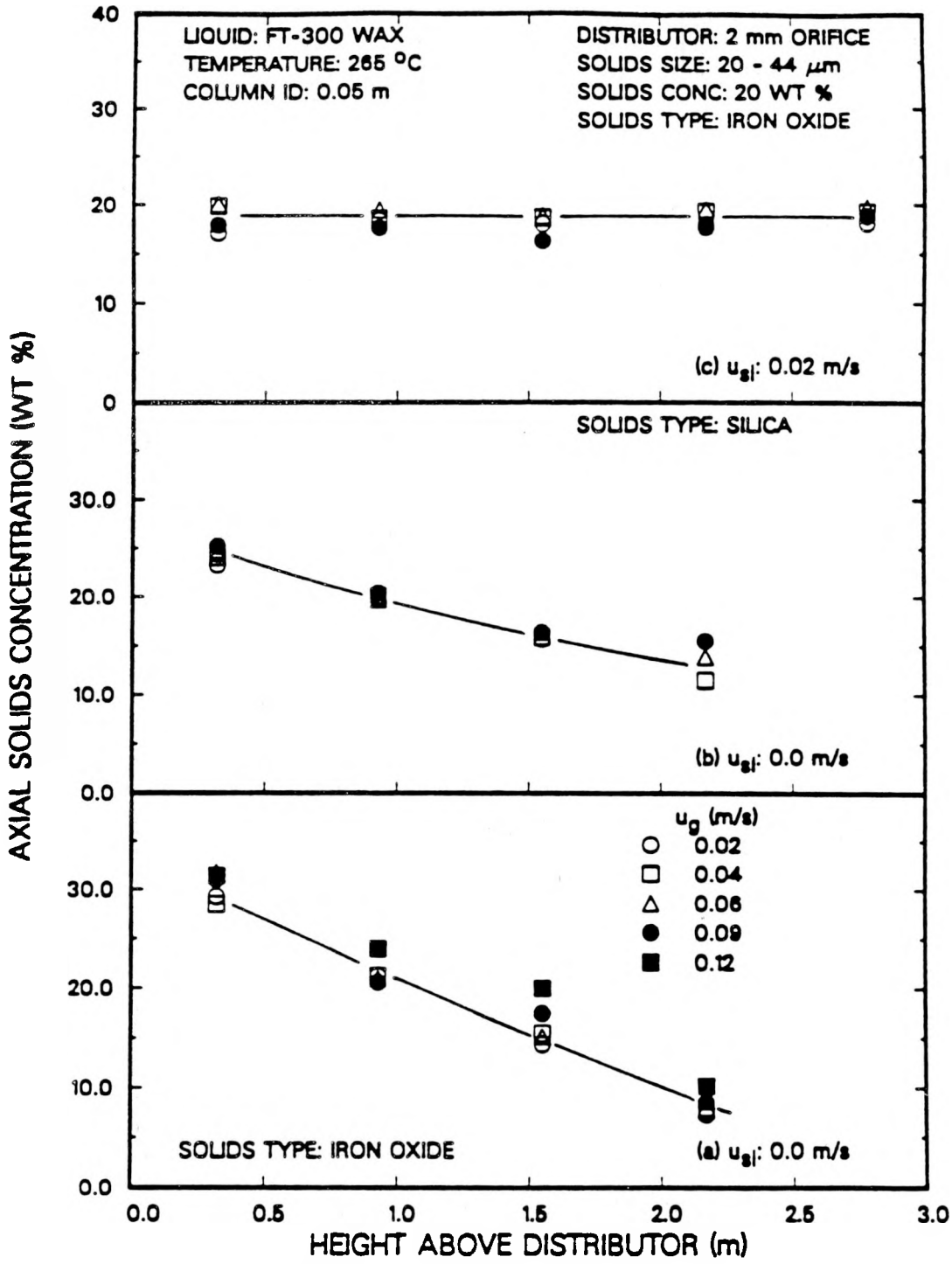

Figure 4.3. Effect of axial position and superficial gas velocity on solids concentrations (20 - 44 μm particles, 0.05 m ID bubble column; (a) iron oxide, u_{sl}=0 m/s; (b) silica, u_{sl}=0 m/s; (c) iron oxide, u_{sl}=0.02 m/s).

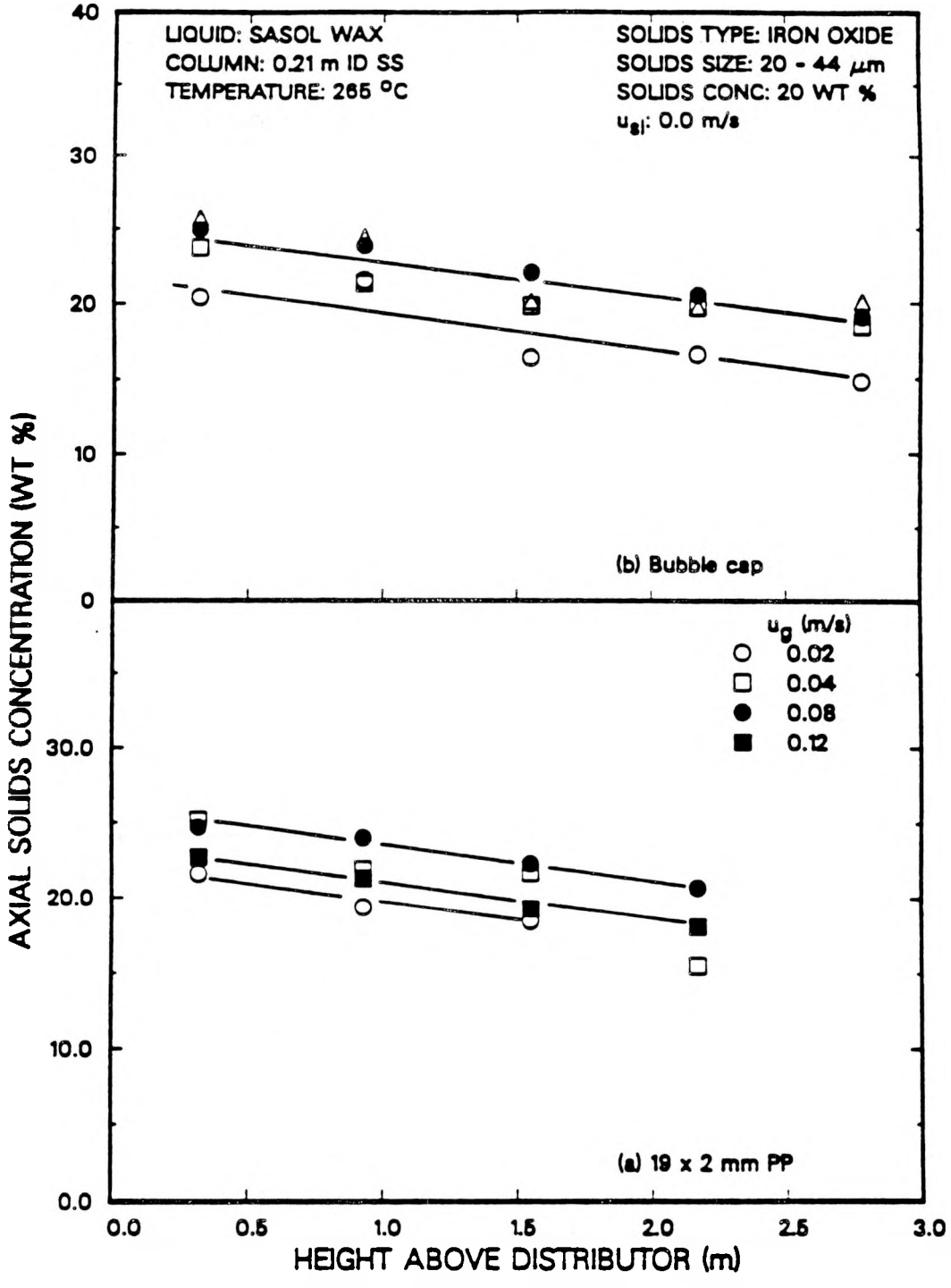

Figure 4.4. Effect of axial position and superficial gas velocity on solids concentrations (20 wt% 20 - 44 μm iron oxide particles, 0.21 m ID bubble column, u_{sl}=0 m/s; (a) 19 x 2 mm PP distributor; (b) bubble cap distributor).

Figures 4.3a and 4.3b) were steeper than those observed in the large column for experiments conducted in the batch mode of operation with large particles (see Figures 4.4a and 4.4b). This trend is expected since intense circulation patterns develop in the large diameter column which help to suspend the solid particles. A similar trend was observed with large silica particles in the 0.05 and 0.21 m ID columns.

Solids concentration profiles were fairly uniform for experiments conducted with both large iron oxide and large silica particles in the continuous mode of operation in the 0.21 m ID column. For experiments conducted with a slurry velocity of 0.02 m/s, the solids concentration profiles were essentially uniform (i.e. ω_s varied by less than 2 wt% (actual) across the entire column). During the experiment conducted with 30 wt% large iron oxide particles at a slurry velocity of 0.005 m/s, a slight solids concentration gradient was observed (see Figure 4.5a). Results from other experiments with large iron oxide particles at a superficial slurry velocity of 0.005 m/s also indicated a slight decrease in solids concentration with increase in height above the distributor; however, during these runs, the solids concentration profiles in the column below a height of 2.2 m fluctuated with axial position (see Figure 4.5b). Thus, the only data (i.e. axial solids concentrations) from a continuous experiment that were analyzed, were from the experiment conducted with 30 wt% large iron oxide particles at a slurry velocity of 0.005 m/s.

Axial solids dispersion coefficients for iron oxide and silica were estimated using solids distribution profiles from batch mode experiments in both the 0.05 m and 0.21 m ID bubble columns via Eq. 4.9. A total of three batch experiments with large iron oxide particles were conducted in the 0.05 m ID bubble column, two with FT–300 wax as the liquid medium and the other with SASOL wax as the liquid medium. Two batch mode experiments were also conducted in the small diameter column with large silica particles suspended in FT–300 wax. A total of four batch mode experiments with large

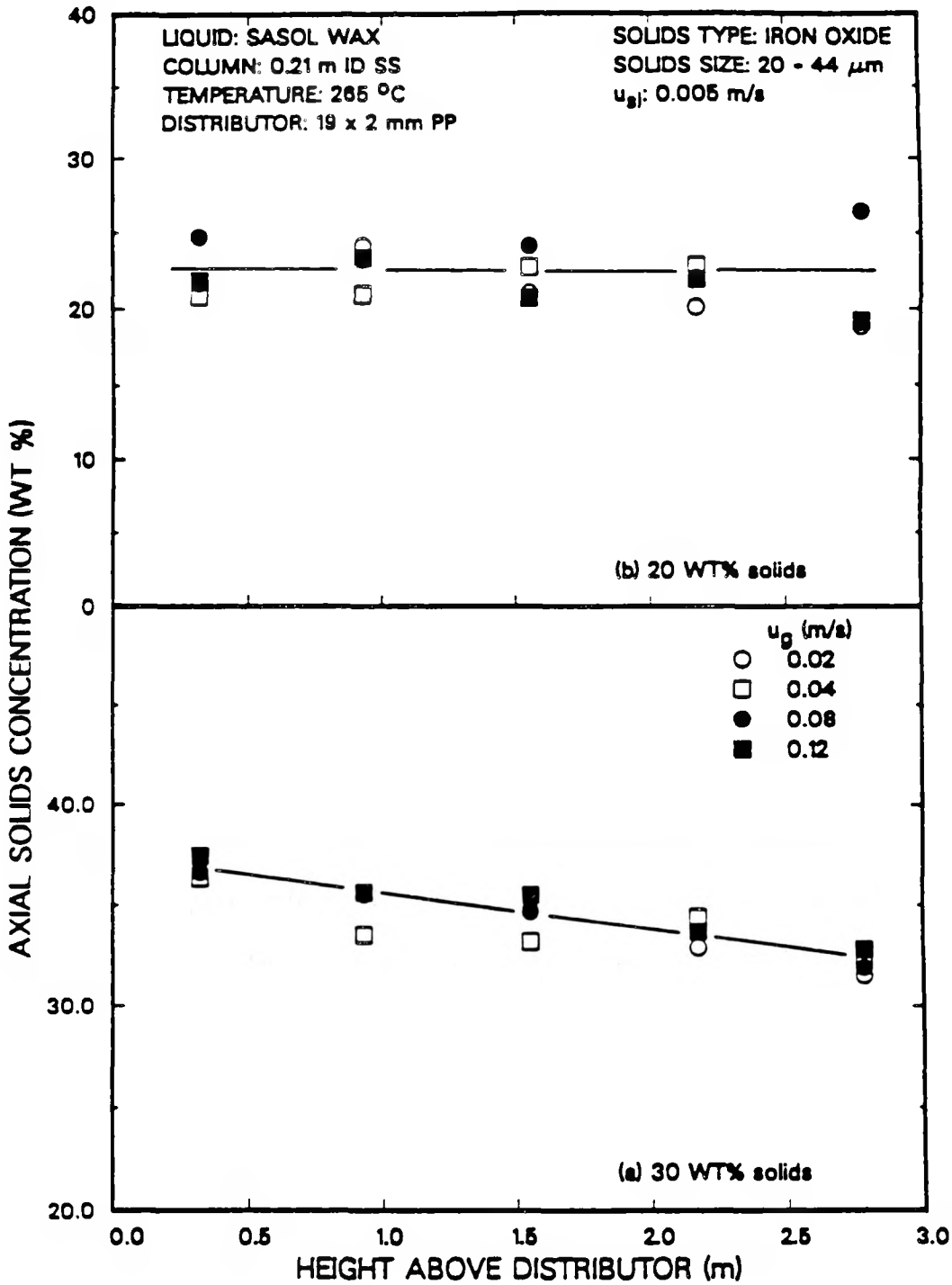

Figure 4.5. Effect of axial position and superficial gas velocity on solids concentrations (20 - 44 μm iron oxide particles, 0.21 m ID bubble column, u_{sl}=0.005 m/s; (a) 30 wt %; (b) 20 wt %).

iron oxide particles were conducted in the large diameter column, three with SASOL wax and the other with FT–300 wax as the liquid medium.

Figure 4.6 shows the effect of superficial gas velocity on the quotient $\frac{u_p}{E_s}$, which was estimated by fitting solids concentration (g/cc) vs. normalized axial height data to Eq. 4.9. Figures 4.6a and 4.6b correspond to values of $\frac{u_p}{E_s}$ obtained from batch experiments in the small diameter column with large iron oxide and large silica particles, respectively. Figure 4.6c shows results from batch experiments with large iron oxide particles in the 0.21 m ID column. Values of $\frac{u_p}{E_s}$ obtained from different experiments with large silica particles in the 0.05 m ID column were similar (Figure 4.6b); whereas, there was some variation in the values of $\frac{u_p}{E_s}$ obtained from different experiments with large iron oxide particles in the small column, particularly at a gas velocity of 0.02 m/s (Figure 4.6a). u_p / E_s values obtained from different experiments with large iron oxide particles in the large column were comparable (see Figure 4.6c).

As noted earlier, for batch mode experiments, the terms u_p and E_s are not separable, and hindered settling velocities must be assumed in order to estimate the dispersion coefficients. Hindered settling velocities and axial solids dispersion coefficients were obtained from the experiment conducted at a superficial slurry velocity of 0.005 m/s with 30 wt%, 20 – 44 μm iron oxide particles in the large diameter column using non–linear regression analysis (NLIN on SAS) of the experimental data (i.e. fit data (solids concentration vs. normalized height) to Eq. 4.10). The solids concentration of the feed, C_s^f, was assumed to be equal to the average solids concentration in the storage tank. The values of u_p from this experiment agreed with the values predicted using the correlation presented by Kato et al. (1972); whereas, the correlations presented by Smith and Ruether (1985) and O'Dowd et al. (1987) overestimated the hindered settling velocities (see Figure 4.7). Thus, the correlation presented by Kato et al. (Eq.

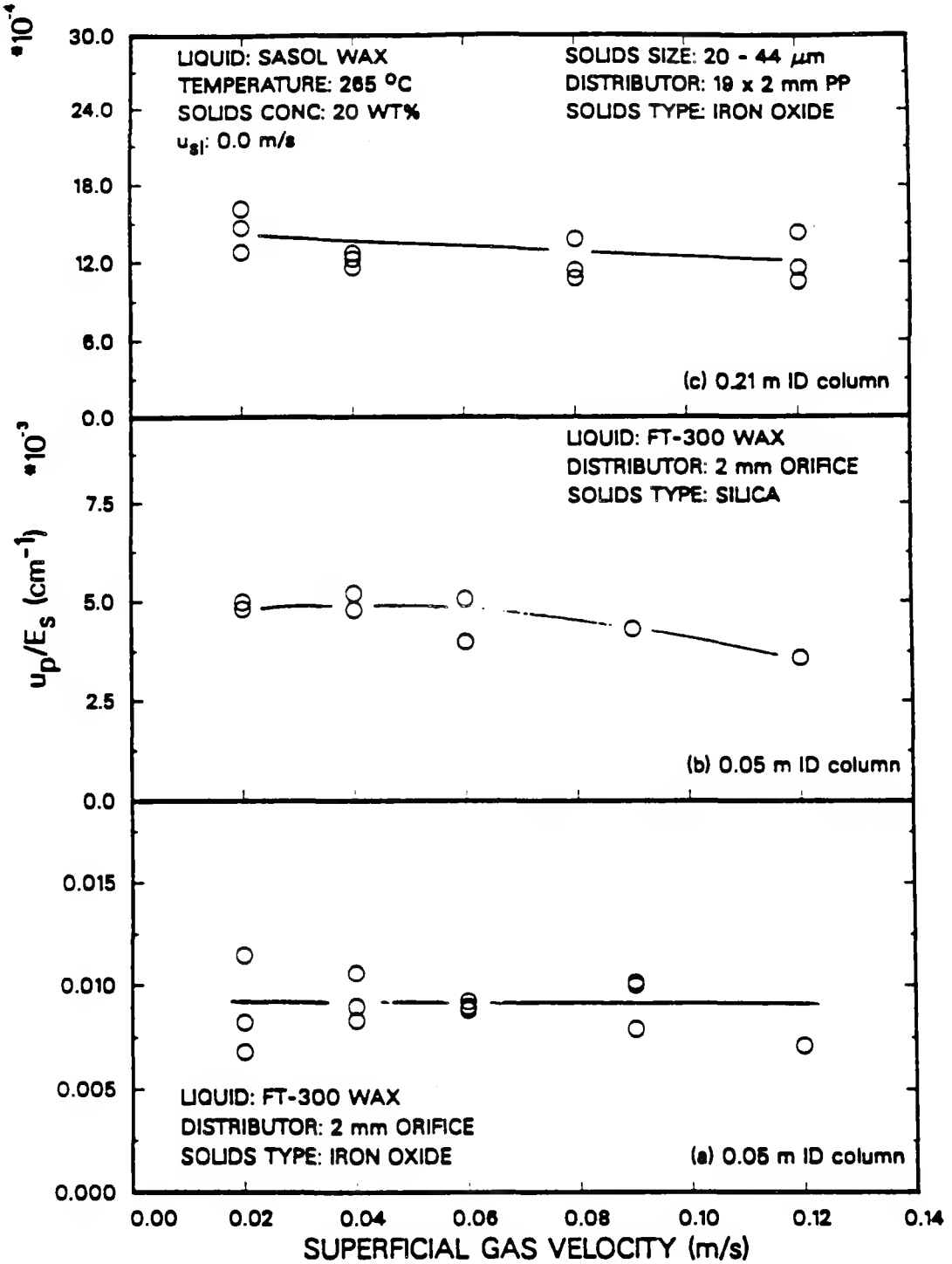

Figure 4.6. Effect of superficial gas velocity on u_p/E_s (20 - 44 μm particles, u_{sl} = 0.0 m/s; (a) iron oxide, 0.05 m ID column; (b) silica, 0.05 m ID column; (c) iron oxide, 0.21 m ID column).

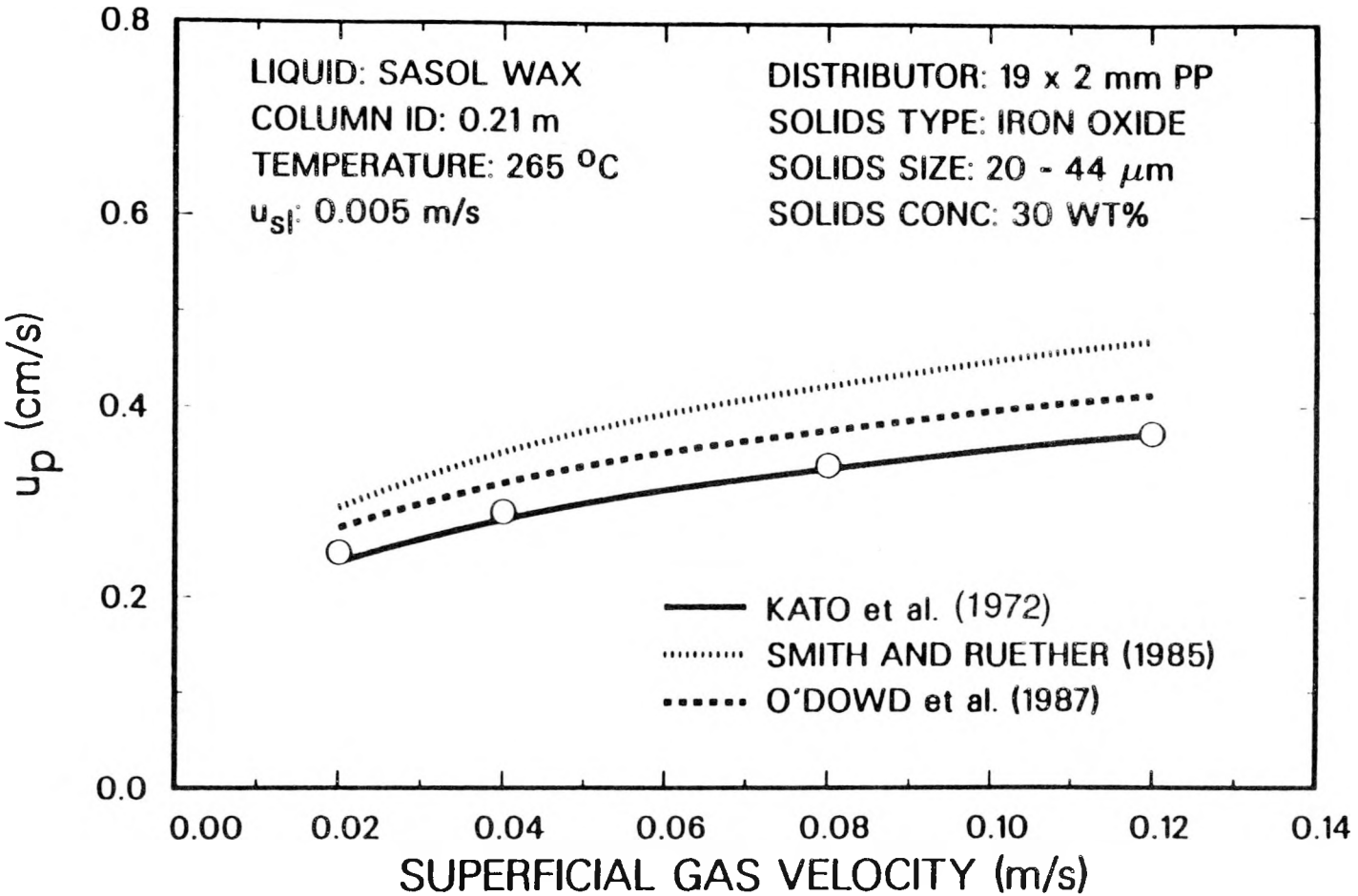

Figure 4.7. Effect of superficial gas velocity on hindered particle settling velocity for 20 - 44 μm iron oxide particles in SASOL reactor wax.

4.11) was used to calculate the hindered settling velocities needed to obtain the axial solids dispersion coefficients for experiments conducted in the batch mode of operation.

Axial solids dispersion coefficients, E_s, for batch experiments in both columns were calculated using $\frac{u_p}{E_s}$ (from least square fit of experimental data) and u_p (from Kato et al.'s correlation). The following correlation for the particle Pectlet number, Pe_p, which is similar to the ones presented by Smith and Ruether (1985) (Eq. 4.13) and O'Dowd et al. (1987) (Eq. 4.14) was developed

$$Pe_p = 8.4\left[\frac{Fr_g^6}{Re_g}\right]^{0.107} = \frac{u_g d_{col}}{E_s} \qquad (4.15)$$

for $0.014 < Fr_g < 0.271$ and $283 < Re_g < 7140$. The estimated parameters (i.e. 8.4 and 0.107) in Eq. 4.15 are comparable to those given by Smith and Ruether (9.6 and 0.114) and O'Dowd et al. (7.7 and 0.098).

Figures 4.8a and 4.8b show results for axial dispersion coefficients from experiments conducted with large particles in both the 0.05 m and 0.21 m ID columns, respectively, together with the predicted dispersion coefficients obtained using Eq. 4.15. The correlation overestimates the measured axial solids dispersion coefficients at gas velocities greater than 0.06 m/s in the large diameter column and underestimates the axial dispersion solids coefficients in the small diameter column at gas velocities less than 0.06 m/s. Axial solids dispersion coefficients obtained from the experiment in the large diameter column with the bubble cap distributor were consistently lower than those obtained from experiments with the perforated plate distributor at high gas velocities.

Figure 4.9 compares predicted and measured axial solids concentrations (g/cc). The predicted solids concentrations were obtained using Eq. 4.15 to predict the axial solids dispersion coefficient, E_s, and Kato et al.'s (1972) correlation to predict the hindered settling velocity, u_p. These quantities were then used in Eq. 4.9 to obtain the solids concentration at a given axial location for batch mode experiments. The solids

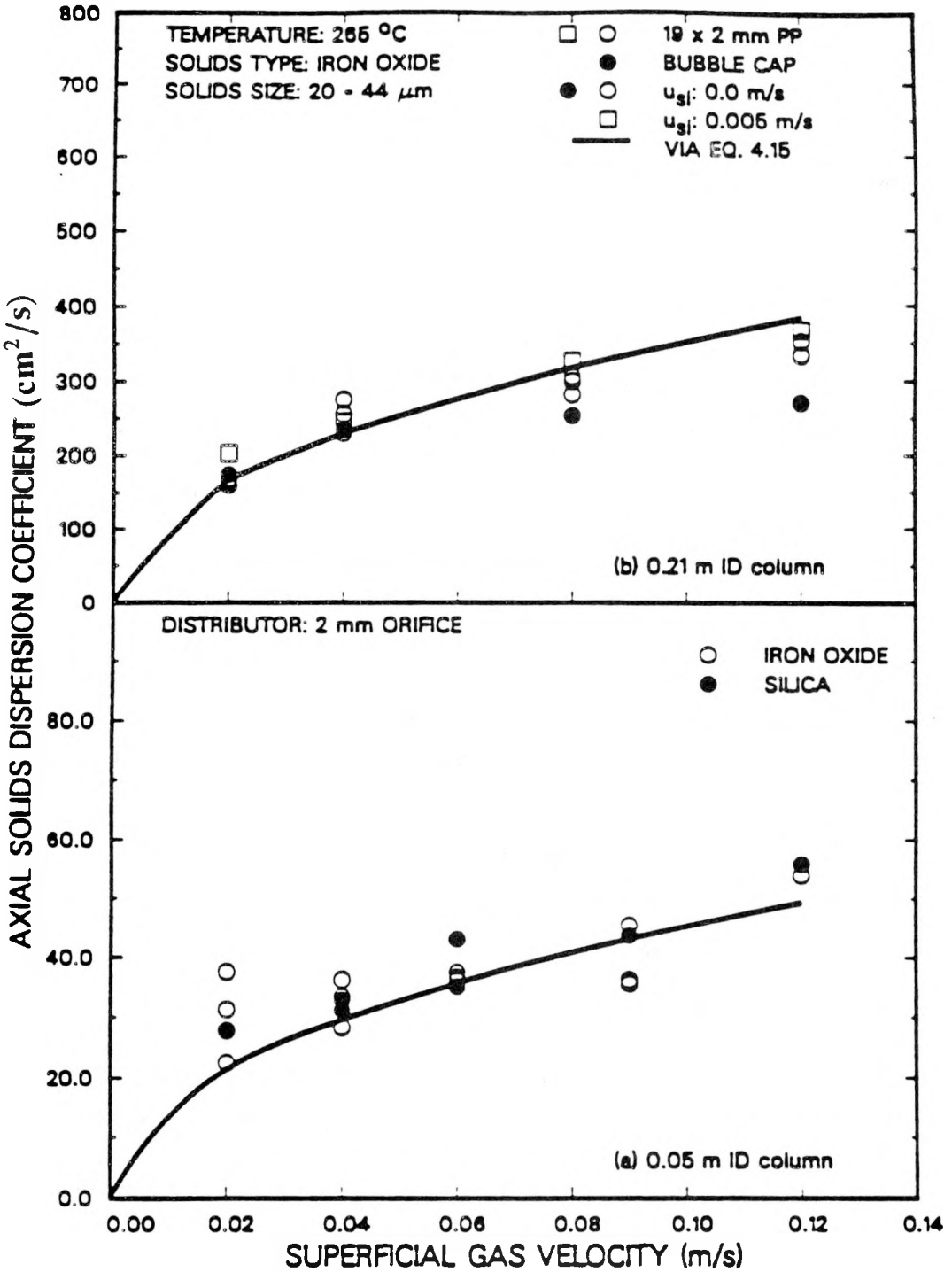

Figure 4.8. Effect of superficial gas velocity on axial solids dispersion coefficients ((a) 0.05 m ID column, (b) 0.21 m ID column).

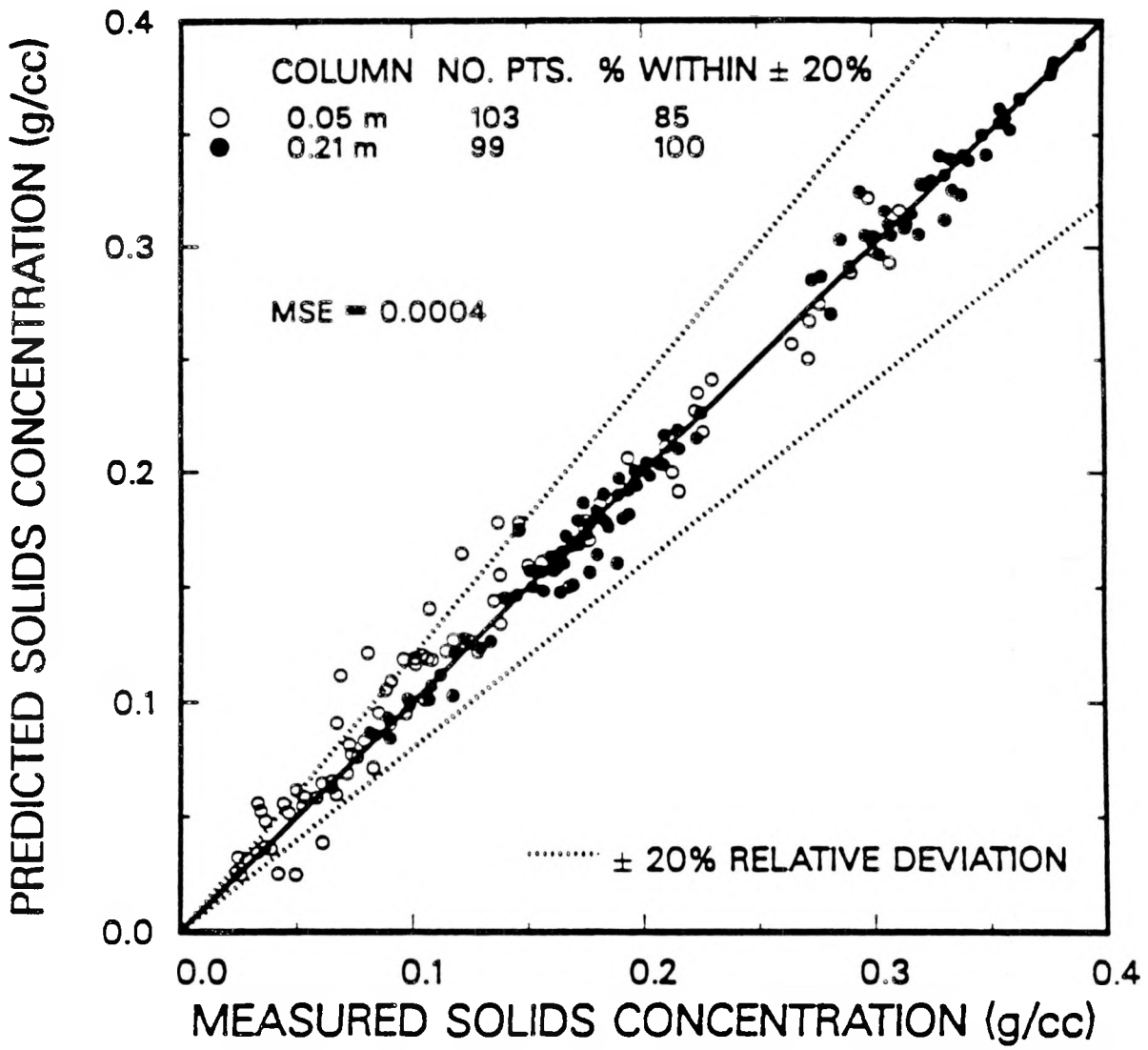

Figure 4.9. Parity plot of measured versus predicted solids concentrations; (20 - 44 μm iron oxide and silica particles; u_{sl} = 0.0 m/s and 0.005 m/s - 0.21 m ID column only).

concentration at the bottom of the column, C_s^B, was assumed to be the same as that obtained in the original analysis. For the experiment conducted in the continuous mode, the solids concentration profile was obtained using Eq. 4.10 with C_s^B and C_s^f being the same as determined in the original analysis. As shown in Figure 4.9 there is excellent agreement between the predicted and measured solids concentrations in both the small and large diameter columns.

As mentioned previously, no attempt was made to obtain axial solids dispersion coefficients for experiments conducted in the batch mode of operation with small particles because of the uniform solids concentration profiles. Theoretical solids concentration profiles for iron oxide and silica at gas velocities of 0.01, 0.12, and 0.30 m/s (Figures 4.10a and 4.10b, respectively) were determined. These profiles were obtained using the normalized (with respect to the solids concentration at the bottom of the column, C_s^B) form of Eq. 4.9. The axial solids dispersion coefficients were obtained from Eq. 4.15 and the hindered settling velocity were calculated from Eq. 4.11 using the constants given by Kato et al. (1972). The expanded height, h_{exp} was assumed to be 3 m. As shown in Figure 4.10, the solids concentration profiles for both iron oxide and silica are fairly uniform, and show very little effect of gas velocity. Similar trends were observed with our experimental data (see Figures 4.2a and 4.2b).

The effect of particle size (iron oxide) on the theoretical solids concentration distribution at gas velocities of 0.01, 0.12, and 0.30 m/s is shown in Figures 4.11a, 4.11b, and 4.11c, respectively. Particle sizes of 3 and 30 μm are representative of the average size of the particles used in the present study. The predicted trends (i.e. increasing solids concentration gradient with increasing particle size) are in agreement with those obtained from our experiments (symbols in Figure 4.11b). An increase in gas velocity decreases the concentration gradient along the height of the bubble column. However,

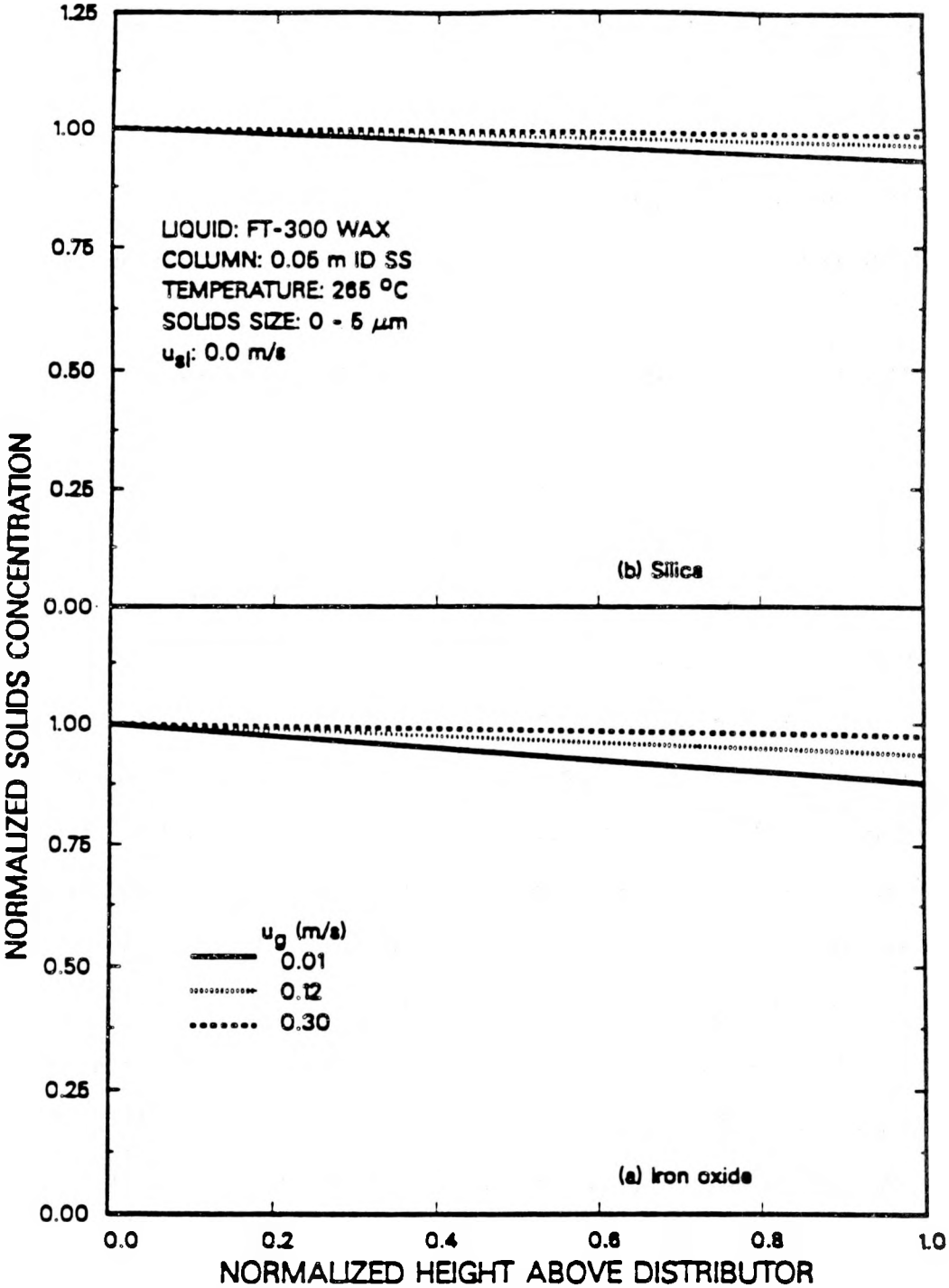

Figure 4.10. Effect of superficial gas velocity on axial solids concentrations (0 - 5 μm particles; 0.05 m ID bubble column; u_{sl}=0 m/s; (a) iron oxide (b) silica).

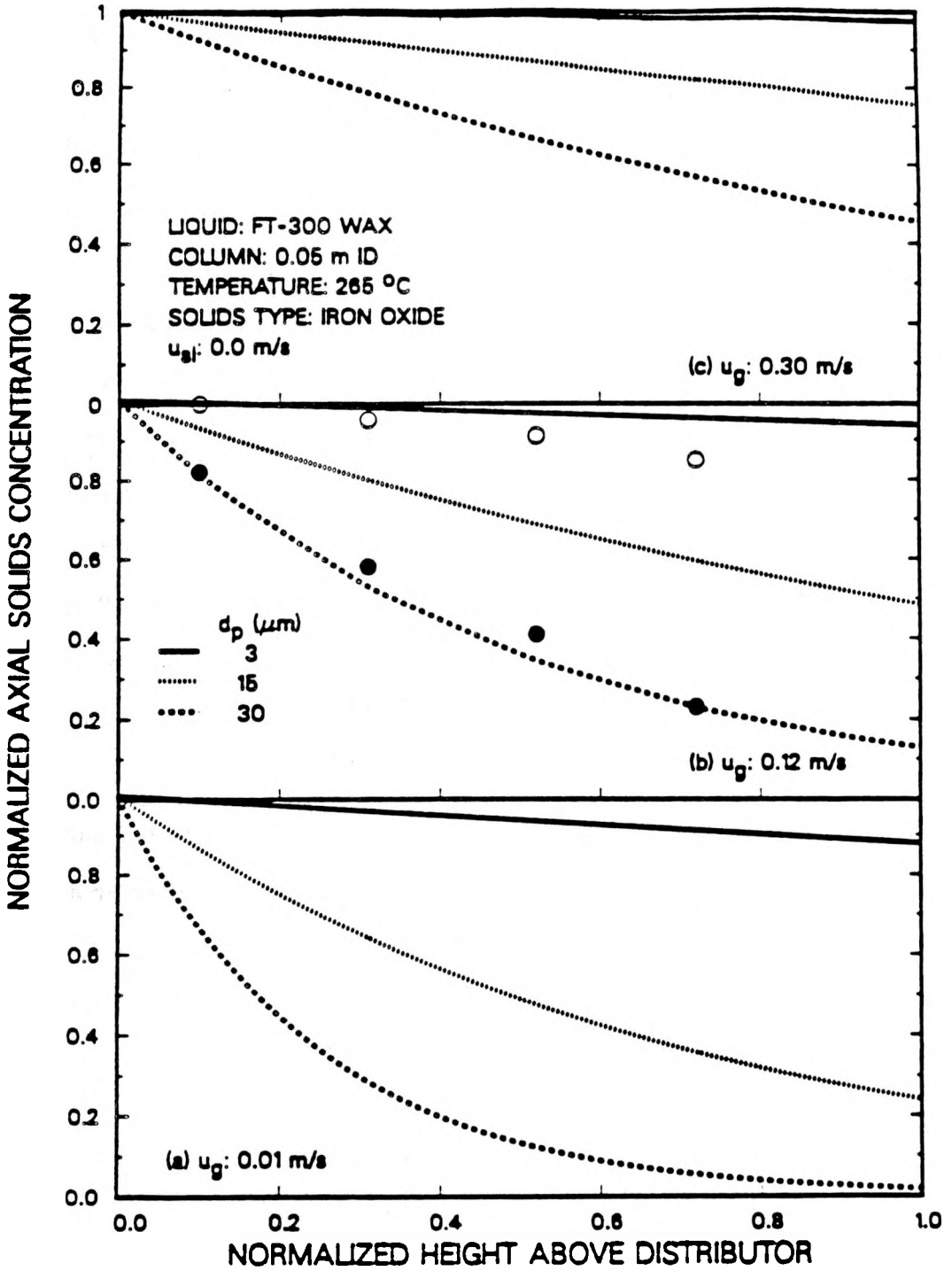

Figure 4.11. Effect of particle size and superficial gas velocity on axial solids concentrations.

(● - Experimental data with 20–44 μm particles;

○ - Experimental data with 0–5 μm particles)

even for a gas velocity of 0.30 m/s, there is still approximately a 58 % decrease in the solids concentration along the height of the reactor for 30 μm particles.

Figures 4.12a and 4.12b show the effect of slurry flow rate on solids (20 – 44 μm iron oxide particles) suspension in both the 0.05 and 0.21 m ID bubble columns, respectively. Also shown in Figure 4.12 are data obtained from batch experiments in the small and large diameter columns. The results presented in Figure 4.12 were obtained from Eq. 4.10, using Eq. 4.15 to estimate E_s and Eq. 4.11 to estimate u_p (Kato et al.'s constants). The solids concentrations were normalized with respect to the concentration at the bottom of the column, C_s^B. There is excellent agreement in the solids concentration obtained from the theory and those measured experimentally in both columns ($u_{s\ell} = 0$ m/s). At a slurry velocity of 0.02 m/s in the small column, the solids concentration profile is essentially uniform, which agrees with the results from our study (see Figure 4.3c). The theory predicts that a concentration gradient will exist in the small diameter column at a slurry velocity of 0.005 m/s with large iron oxide particles (see Figure 4.12a). However, due to operational problems with our pump, we were not able to obtain data at this slurry velocity. In the large diameter column, there is very little effect of slurry flow rate on axial solids distribution; whereas, in the small diameter column, there is a significant effect. At a slurry velocity of 0.02 m/s, the solids concentration profile in both columns is essentially uniform.

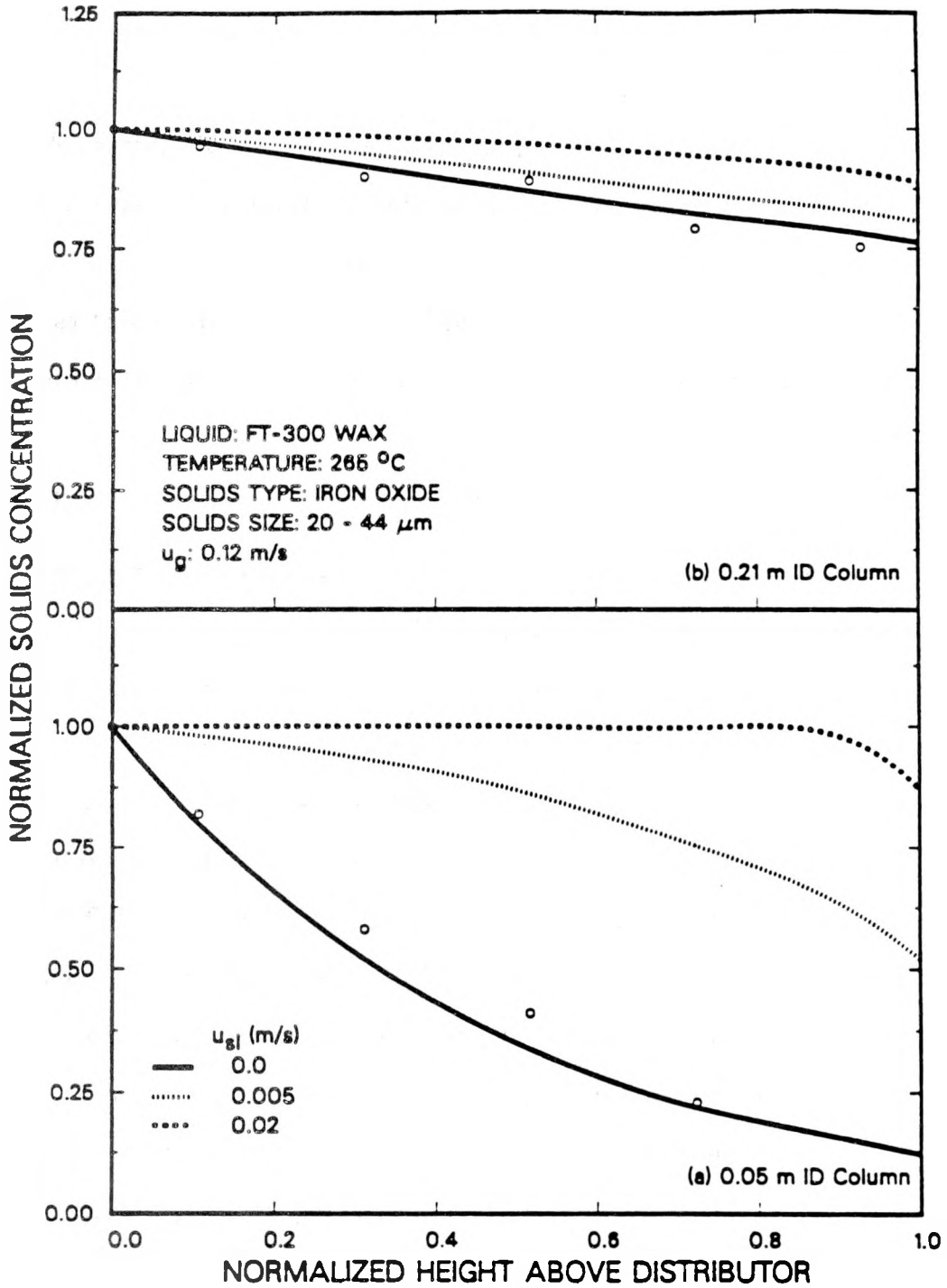

Figure 4.12. Effect of column diameter and superficial slurry velocity on axial solids concentrations.

(○ - Experimental data from batch mode experiments)

V. BUBBLE SIZE DISTRIBUTIONS

The overall mass transfer rate per unit volume of the dispersion in a bubble column is governed by the liquid–side mass transfer coefficient ($k_\ell a$), assuming that the gas–side resistance is negligible. In a bubble column reactor, the variation in $k_\ell a$ is primarily due to variations in the interfacial area (Fan, 1989). Assuming spherical bubbles, the specific gas–liquid interfacial area is related to the gas holdup, ϵ_g and the Sauter mean bubble diameter, d_s, by

$$a_s = \frac{6\epsilon_g}{d_s} \tag{5.1}$$

Thus, a precise knowledge of the gas holdup and bubble size distribution is needed to determine the specific gas–liquid interfacial area.

Extensive work on bubble size measurements in two–phase systems has been reported in the literature, and has been reviewed by several authors (e.g. Buchholz and Schugerl, 1979; Shah et al., 1982; Saxena et al., 1988); however, the majority of these studies pertain to air–water systems. Bubble size measurements with molten wax as the liquid medium are rather limited (e.g. Calderbank et al., 1963; Quicker and Deckwer, 1981; O'Dowd et al., 1987; Bukur et al., 1987a,c; Patel et al., 1990) and there is some disagreement between bubble size data reported in these studies. The general consensus is that some molten wax systems depict an unique behavior, namely, an abundance of very small bubbles is present and high gas holdups are obtained in comparison to pure hydrocarbons having similar physical properties. The resulting specific gas–liquid interfacial areas could be an order of magnitude greater than those of pure hydrocarbons (Quicker and Deckwer, 1981). The findings from bubble size measurement studies with molten waxes are summarized below.

Calderbank et al. (1963) used a light transmission technique to measure interfacial areas of Krupp wax at 265 °C for gas velocities less than 0.06 m/s in a 0.05 m ID column equipped with a ball and cone type sparger. When these data, together with the average gas holdup values reported by them, are used in Eq. 5.1, Sauter mean bubble diameters in the range 2 – 3 mm are obtained. Zaidi et al. (1979) and Deckwer et al. (1980) reported a much lower d_s value, 0.7 mm, for paraffin wax using photography in 0.041 and 0.1 m ID columns equipped with 75 μm porous plate spargers (T = 250 – 270 °C, $u_g \leq 0.03$ m / s). Quicker and Deckwer (1981) measured d_s values for FT–300 wax in a 0.095 m ID column equipped with a 0.9 mm nozzle. Sauter mean bubble diameters, determined by the photographic method, at 170 °C ranged from 1.3 mm (u_g = 0.01 m/s) to 0.6 mm (u_g = 0.035 m/s). More recently, O'Dowd et al. (1987) obtained d_s values for a P–22 wax, and for reactor wax from run 7 in Mobil's pilot plant slurry reactor (Unit CT–256) using the hot wire anemometer technique at 250 °C and 1.48 MPa. Their d_s values, from a 0.022 m ID column equipped with a 1 mm orifice plate, for the two waxes were in the range 2.7 to 3.9 mm for $u_g \leq 0.02$ m/s, and are comparable to values reported by Calderbank et al. (1963).

The lower d_s values from the studies conducted by Zaidi et al., Deckwer et al., and Quicker and Deckwer, cannot be attributed to the limitation of the photographic technique (i.e. its bias towards small bubbles in the vicinity of the wall). This is because all of these studies were conducted in the homogeneous bubbling regime ($u_g \leq 0.035$ m/s) where the dispersion is expected to be radially uniform. Discrepancies in results might be due to use of different waxes in these studies. We have shown in our laboratory (Bukur et al., 1987a,c) that hydrodynamic parameters obtained in experiments with different waxes could differ significantly, despite similarites in physical properties of different waxes.

Numerous techniques have been used to measure bubble size distributions. Some of the techniques which are commonly employed are photography, hot wire anemometry, electrical conductivity, and light transmission. More recently, the dynamic gas disengagement (DGD) technique, originally developed by Sriram and Mann, 1977, has been employed (e.g. Vermeer and Krishna, 1981; Kuo, 1985; Bukur et al., 1987a,c; Patel et al., 1989). This technique was used in the present study.

The approach presented by Sriram and Mann has been used by several researchers to determine the holdup structure of the dispersion. In most cases, the dispersion was assumed to consist of one or two dominant bubble sizes. Vermeer and Krishna (1981) applied this approach to the nitrogen–turpentine 5 system. They assumed a bimodal distribution with large bubbles forming the transport portion of the holdup and small, slow rising, bubbles forming the entrained portion. Based on this assumption, they considered the initial part of the disengagement profile to be dictated solely by the large bubbles, with the small bubbles disengaging only after all of the large bubbles have left the system. They used the resulting disengagement profiles to estimate the contribution to the gas holdup by the two bubble classes. Schumpe and Deckwer (1982), and Godbole et al. (1982, 1984) conducted experiments with highly coalescing CMC (carboxymethyl cellulose) systems and used bimodal bubble size distributions to determine the holdup structure of the dispersion by dynamic gas disengagement. For such systems, they showed that the contribution of small bubbles to the overall gas holdup is negligible. In similar experiments with different concentrations of surfactants added to the CMC solution, Godbole et al. (1984) showed that the contribution of small bubbles to the overall gas holdup increased with increasing surfactant concentration (i.e. decreasing coalescence rates), while the contribution due to large bubbles remained virtually unchanged. In experiments conducted with alcohol solutions (noncoalescing media) by Kelkar et al. (1983), similar results were obtained when the holdup structure

was determined using the dynamic gas disengagement technique assuming a bimodal bubble size distribution. For these solutions, the contribution to overall gas holdup by small bubbles was even greater than that due to large bubbles.

More recently, Schumpe and Grund (1986) have presented results for the air–water system, with an emphasis on some of the problems associated with the DGD technique and have proposed corrective measures which to some extent can alleviate these problems. The problems analyzed by the authors include the subjectivity involved in obtaining an accurate disengagement profile during large bubble disengagement, the "waterfall" effect or downward flow of liquid during bubble disengagement and its impact on the rise velocity of small bubbles, and errors introduced by bubbles entering the dispersion as the pressure in the plenum chamber equilibrates with the hydrostatic pressure of the dispersion, following the interruption of the gas supply. The authors assumed a bimodal bubble size distribution in their analysis and presented the gas holdup structure as well as bubble rise velocities for the two bubble classes. The problems associated with obtaining accurate disengagement profiles were also discussed by Lee et al. (1985), who developed a digital sensor with a computer interface that greatly improved accuracy and reproducibility of the measured disengagement profile.

Researchers at Mobil (Kuo, 1985) were the first to discretize Sriram and Mann's original equation without introducing any new assumptions other than a noncontinuous distribution. They applied the resulting equations to disengagement profiles obtained from experiments using molten wax as the liquid medium at low gas velocities and assumed either unimodal or bimodal bubble size distributions. The quantities estimated in their study included the gas holdup structure, bubble rise velocities, and bubble sizes.

The dynamic gas disengagement technique offers several advantages over the previously mentioned techniques. Bubble size distributions obtained from DGD are based

on the entire dispersion; whereas, all other techniques mentioned above are local measurement techniques. We have shown previously (Bukur et al., 1987a,c and Patel et al., 1990) that the bubble size distribution is a function of radial position (i.e. larger bubbles rise through the center of the column). Thus, when employing any of the "probe" techniques or even photography, measurements must be made at numerous radial positions to obtain an accurate estimate of the Sauter mean bubble diameter. The major drawback with DGD is the fact that bubble sizes are not measured directly.

The purpose of this study was to determine bubble size distributions, and consequently specific gas–liquid interfacial areas for FT–300 wax and SASOL reactor wax in both the 0.05 and 0.21 m ID bubble columns. A description of the DGD technique, the theory associated with DGD, and results from experiments conducted with waxes (FT–300 and SASOL) are presented.

Experimental Techniques for Measurement of the Disengagement Profile

The DGD technique requires an accurate measurement of the rate at which the gas–liquid dispersion drops once the gas flow to the bubble column is shut off. As mentioned previously, one of the problems associated with this technique is determination of the rate at which the liquid level drops during the initial period of disengagement. The majority of previous studies (transparent systems) utilized a video camera/VCR system to measure the rate at which the dispersion dropped once the gas flow was shut off. During large bubble disengagement, the top of the dispersion is not well defined because of splashing caused by the disengagement of large bubbles. In the current study, a video camera/VCR system could not be used since measurements were made in stainless steel columns. Thus, pressure transducers were used to measure the rate at which the liquid level dropped during the disengagement process. The use of pressure transducers not only enables one to use this technique in opaque systems, but also reduces the

subjectivity involved in estimating the rate at which the liquid level drops during large bubble disengagement. In our previous studies (Bukur et al., 1987a,c; Patel et al., 1990), DGD was used to obtain bubble size distributions for a variety of waxes in the 0.05 and 0.23 m ID glass bubble columns. During these studies, the rate at which the liquid level dropped, once the gas flow had been interrupted, was recorded with a video camera/VCR system.

The primary difference in the analysis of data obtained from different forms of data acquisition (i.e. video system vs. pressure transducers) is the frame of reference. Analysis of data obtained from visual observations (i.e. video system) is based on the cross–sectional area of the liquid in the gas/liquid dispersion; whereas, analysis of data obtained from pressure transducers is based on the cross–sectional area of the dispersion. For the former, the volume of liquid in the dispersion remains constant, but the total volume of the dispersion changes (Patel et al., 1989); whereas, for the latter, the total volume of the dispersion below the pressure transducer remains constant but the volume of the liquid varies.

Theory

In the following analysis, we will assume that the dispersion is axially homogeneous and no bubble–bubble interactions occur once the gas flow is interrupted. These are the same assumptions as those used by Sriram and Mann (1977). Deviations from these assumptions may occur in strongly coalescing systems (e.g. air–water system) at high gas flow rates. The assumption of axial homogeneity may also be violated with noncoalescing systems in which there is a high concentration of fine bubbles at the top of the dispersion.

For simplicity, we have assumed a bimodal distribution; however, equations are also presented for multimodal distributions. The dispersion for a bimodal distribution may

be partitioned into three fractions representing the liquid volume, total volume of large bubbles, and total volume of small bubbles. Under the assumption of axial homogeneity, the dispersion, just before gas flow is cut off, may be represented by Figure 5.1. Since information is not obtained for the dispersion above the pressure transducer, no distinction is made between large and small bubbles in this region. The volumes of the three components are proportional to the respective holdup fractions. The disengagement process may be envisioned as either a constant rate process, case I, where the small and large bubbles disengage independent of one another, or as an interactive process, case II, where the disengagement of large bubbles retards the disengagement rate of small bubbles. Even though the latter case is interactive, it does not account for bubble–bubble interaction (i.e. coalescence and breakup). A third, although less likely possibility, is the case where the disengagement rate of small bubbles is enhanced by the disengagement of large bubbles. This could occur if small bubbles adhere to the surface of large bubbles and disengage along with them. The actual disengagement process is expected to lie between the two extremes described above (i.e. case I and case II).

Case I. Constant Rate Disengagement Process

Before analyzing this case, it is important to define the constant rate disengagement process. Under this condition, the volumes representing the large and small bubbles (Figure 5.1) move away from the bottom of the column (disengage) at constant rise velocities. Furthermore, if we assume each volume to be a column of gas with a constant cross sectional area, then this constancy is preserved during the time it takes that column of gas to disengage. At any time during the first period of disengagement (Figure 5.2), the volume of liquid passing below the pressure transducer (V_ℓ) must be the same as the volume of gas associated with the small (V_s) and large (V_L) bubbles which rise above the pressure transducer. Thus, at any time t, a volume balance between the

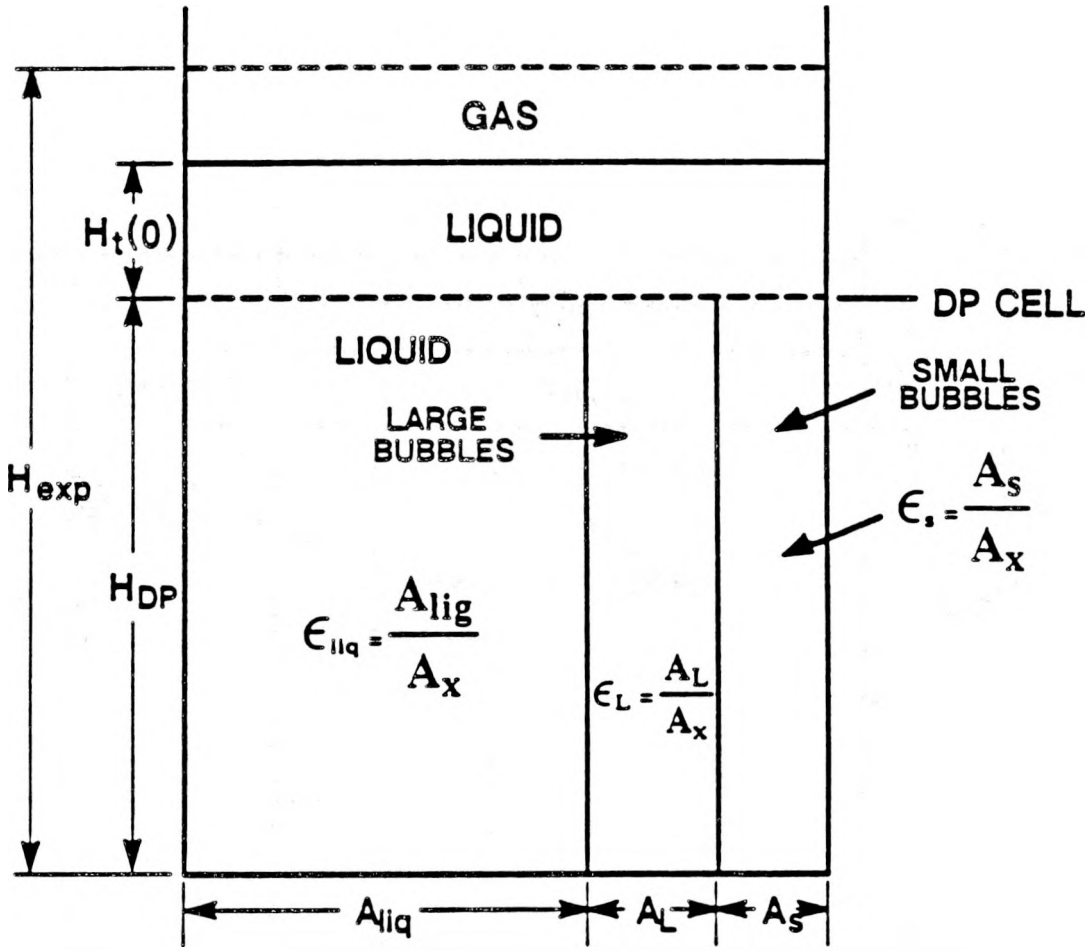

Figure 5.1. Dispersion prior to disengagement (t = 0).

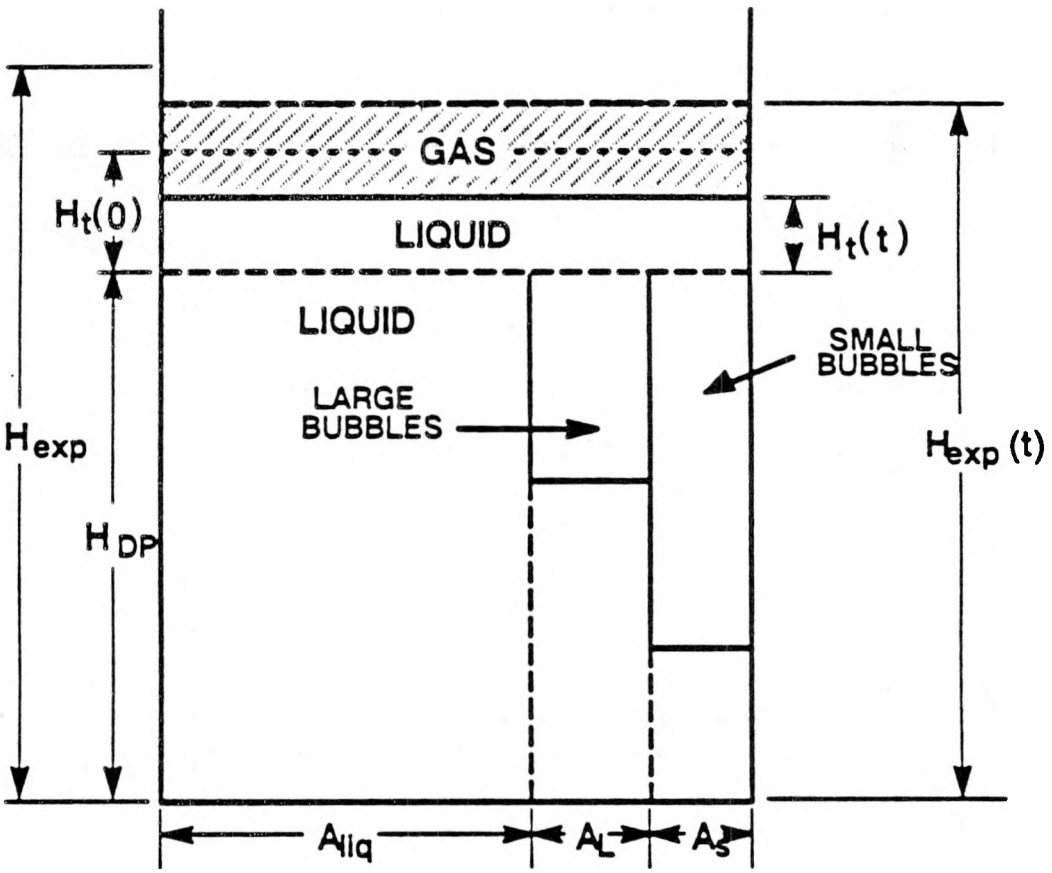

Figure 5.2. Dispersion during the constant rate disengagement process (Period 1).

liquid entering and gas exiting is

$$V_\ell(t) = V_s(t) + V_L(t) \tag{5.2}$$

Furthermore, by the definition of the constant rate disengagement process, the distance between the rear of the small or large bubble swarm would simply be the product of the respective rise velocity and the time elapsed since the initiation of the disengagement process.

The volume of liquid passing below the pressure transducer at any time t may be expressed as

$$V_\ell(t) = V_o - V(t) \tag{5.3}$$

where V_o is the volume of liquid above the pressure transducer immediately prior to interruption of the gas flow and V(t) is the volume of liquid above the pressure transducer during the disengagement process at time t. Substituting Eq. 5.3 into Eq. 5.2 and expressing volumes in terms of heights yields upon rearrangement

$$H_t(t)A_x = H_t(0)A_x - t[u_{bs}A_s + u_{bL}A_L] \tag{5.4}$$

where $H_t(t)$ is the height of liquid above the pressure transducer at time t, $H_t(0)$ is the initial (i.e. at steady state) height of liquid above the pressure transducer, A_x is the cross–sectional area of the column, u_{bs} is the rise velocity of small bubbles, A_s is the cross–sectional area of the column of small bubbles (see Figure 5.1), u_{bL} is the rise velocity of large bubbles, A_L is the cross–sectional area of the column of large bubbles, and t is the time. The cross–sectional area of bubbles of size i (i = s or L) divided by the cross–sectional area of the column represents the volume fraction of gas corresponding to bubbles of size i. Thus, dividing Eq. 5.4 by A_x yields

$$H_t(t) = H_t(0) - t[u_{bs}\epsilon_{gos} + u_{bL}\epsilon_{goL}] \tag{5.5}$$

where ϵ_{gos} is the volume fraction of small bubbles at steady state conditions and ϵ_{goL} is the volume fraction of large bubbles at steady state conditions. The above equation is valid as long as large bubbles are present below the pressure transducer (i.e. for $t < H_{DP}/u_{bL}$, where H_{DP} is the height of the pressure transducer above the distributor).

Similarly, a balance equation for the liquid entering the section of the column below the pressure transducer during the second period of disengagement (Figure 5.3) may be written as

$$V_\ell(t) = H_t(t_1)A_x - H_t(t)A_x = u_{bs}A_s(t - t_1) \qquad t \geq H_{DP}/u_{bL} \tag{5.6}$$

where t_1 corresponds to the time at which all large bubbles passed by the pressure transducer (i.e. $t_1 = H_{DP}/u_{bL}$), $H_t(t)$ is the height of liquid above the pressure transducer at time t and $H_t(t_1)$ is the height of liquid above the pressure transducer at the beginning of period 2 (i.e. small bubble disengagement). Dividing Eq. 5.6 by the cross–sectional area of the column, A_x yields upon rearrangement

$$H_t(t) = H_t(t_1) - u_{bs}\epsilon_{gs}(t - t_1) \qquad t \geq H_{DP}/u_{bL} \tag{5.7}$$

For a multimodal distribution, the following expression is used to describe the rate at which the level drops during the disengagement of bubbles of size j

$$H_t(t) = H_t(t_k) - \sum_{i=j}^{n} u_{bi}\epsilon_{gi}(t - t_k) \qquad k = j - 1, \quad t_k < t < H_{DP}/u_{bj} \tag{5.8}$$

where n is the total number of bubble classes. Note $j = 1$ corresponds to the first period of disengagement and $j = n$ corresponds to the last period of disengagement (i.e. disengagement of the smallest bubbles). Also, for $k = 0$ (i.e. $j = 1$), $t = 0$.

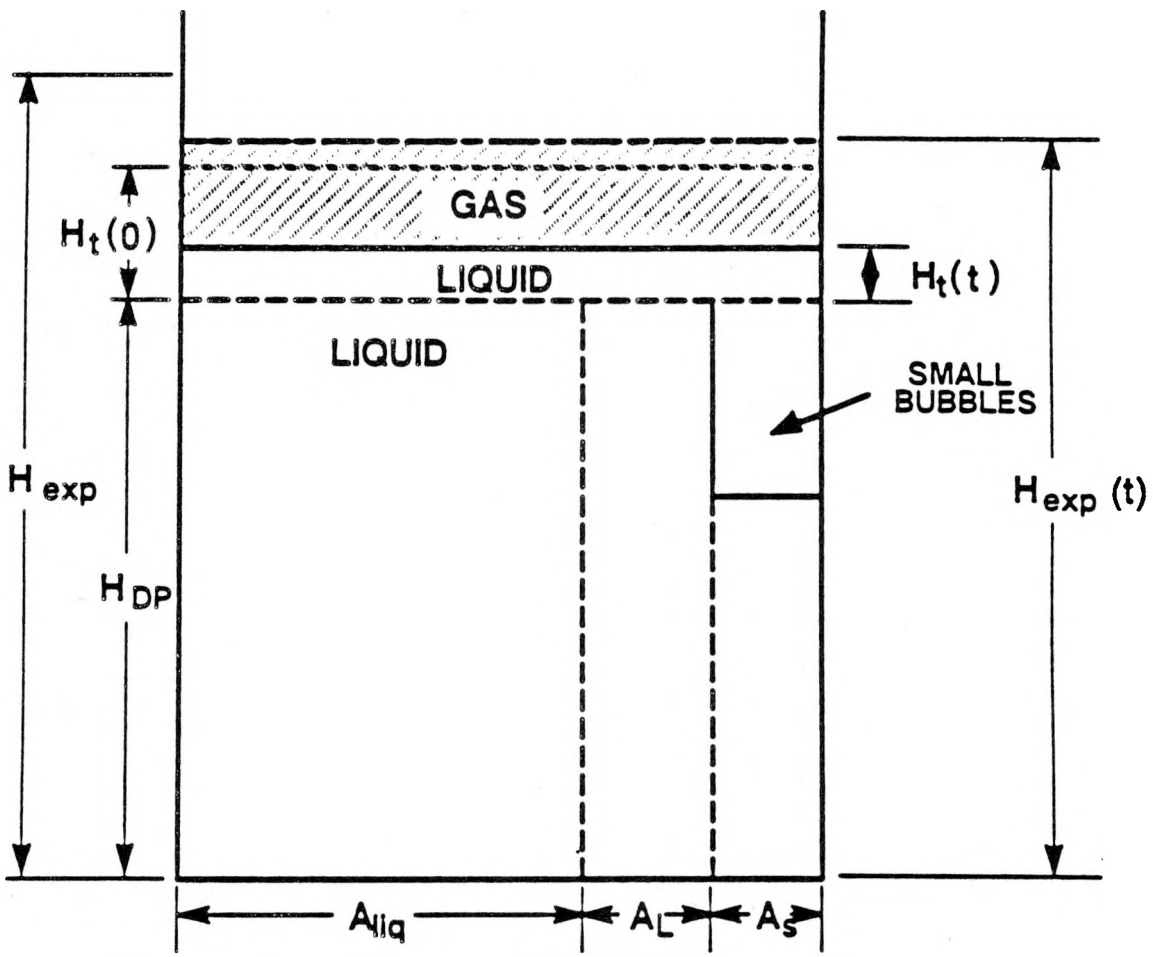

Figure 5.3. Dispersion during the constant rate disengagement process (Period 2).

Estimating Bubble Rise Velocities and Gas Holdups During Constant Rate Disengagement

Equation 5.8 implies that a plot of height of liquid above the pressure transducer, $H_t(t)$, versus time, t, should yield a series of straight lines (Figure 5.4) which may be used to determine the rise velocities and volume fractions of bubbles in the dispersion. Since we assumed that the bubbles disengaged from the bottom of the column at a constant rate, the rise velocity associated with bubbles of size j is simply

$$u_{bj} = \frac{H_{DP}}{t_j} \tag{5.9}$$

where t_j is the time at which the last bubble of size j, passed above the pressure transducer. Once the rise velocities of the bubbles are determined, the gas holdup corresponding to bubbles of size j can be obtained from Eq. 5.8, and is expressed as follows

$$\epsilon_{goj} = \frac{-S_j - \sum_{i=j+1}^{n} u_{bi}\epsilon_{goi}}{u_{bj}} \tag{5.10}$$

where S_j is the slope of the disengagement curve corresponding to the disengagement of bubbles in period j (see Figure 5.4). Eq. 5.10 is solved recursively beginning with j = n (i.e. last period of disengagement). Note, for j=n, $\epsilon_{gon} = -S_n/u_{bn}$.

Estimating Bubble Diameters and the Specific Gas-Liquid Interfacial Area

Bubble rise velocities are estimated from the analysis presented above. However, this analysis does not take into account any radial variations in the rise velocities due to the presence of circulation patterns. This limitation of the DGD technique has been acknowledged in previous studies (e.g. Sriram and Mann, 1977; Schumpe and Grund, 1986), although no effort has been made to introduce any corrective measures. Based on our visual observations using DGD in the glass columns, the dispersion is fairly uniform once all the large bubbles have disengaged. However, during large bubble

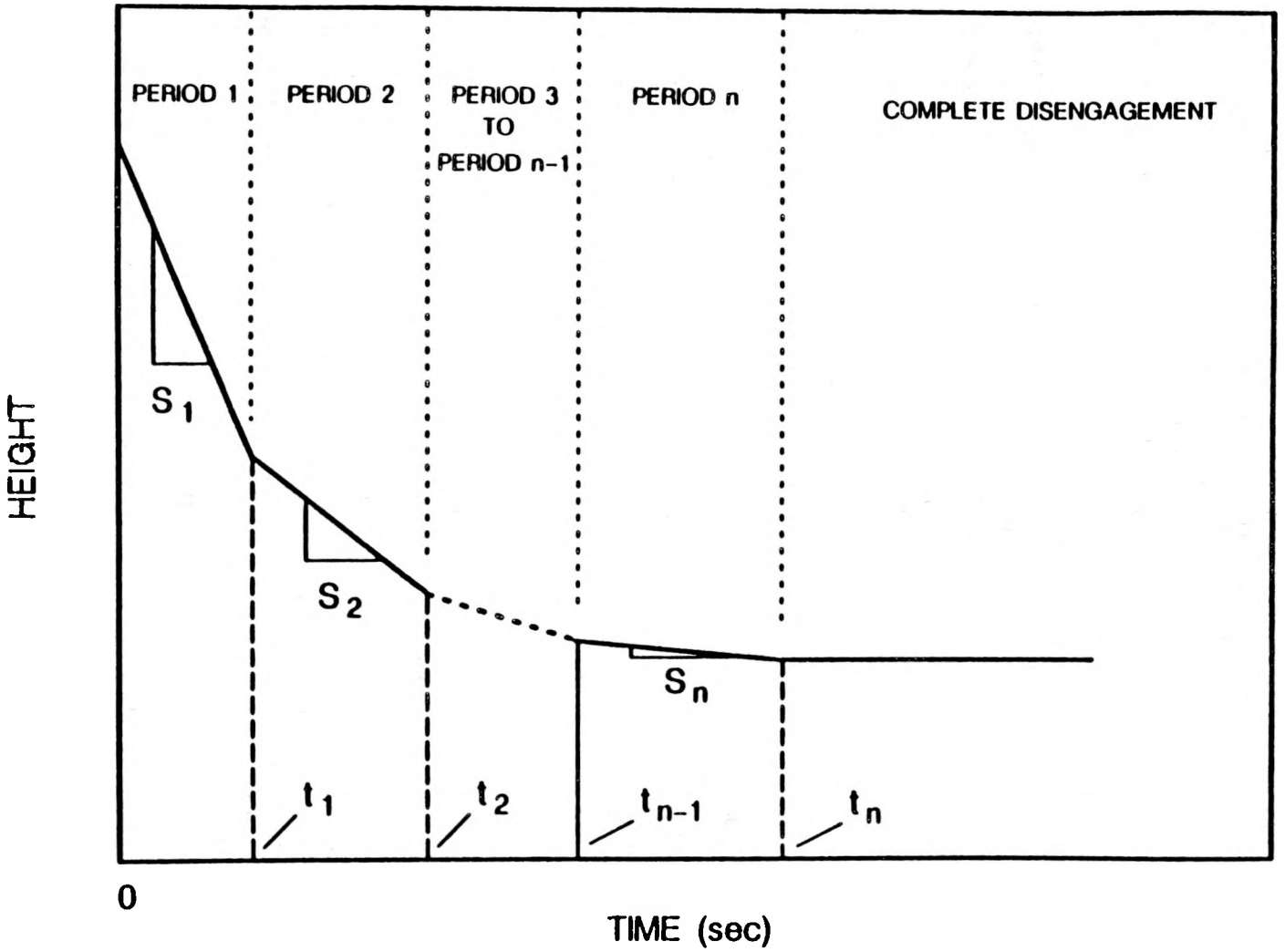

Figure 5.4. Plot of height vs. time for a multimodal distribution (constant rate process).

disengagement, it is possible that strong circulation patterns still exist in the column and the large bubble rise velocities obtained from DGD may not be accurate.

Bubble sizes are estimated from the terminal rise velocity by using appropriate correlations. The correlations used to determine the bubble sizes in the present study are presented in Table 5.1. For the range of rise velocities not covered by these correlations, bubble diameters were obtained by interpolation. Figure 5.5 shows the curve used to determine bubble sizes for FT–300 wax at 265 °C, with the broken line indicating the interpolated region. The correlations by Abou–el–Hassan (1983) and Clift et al. (1978) were used to estimate bubble diameters. The ranges of applicability for these correlations were satisfied for all cases, except for the wax density at 265 °C. At this temperature, the densities of the waxes used in this study (i.e. FT–300 and SASOL) were in the range 660 – 680 kg / m^3, and they are slightly below the range of applicability of the Abou–el–Hassan correlation.

Once the bubble sizes are known, the Sauter mean bubble diameter may be calculated. The definition of the Sauter mean bubble diameter assumes spherical bubbles and is given by

$$d_s = \frac{\sum_{i=1}^{N} n_i d_{Bi}^3}{\sum_{i=1}^{N} n_i d_{Bi}^2} \tag{5.11}$$

where N is the total number of bubble classes, and n_i is total number of bubbles of size d_{Bi}. The number of bubbles of size d_{Bi} may be estimated as follows. The overall gas holdup may be defined as

$$\epsilon_g = \sum_{i=1}^{N} \epsilon_{gi} = \frac{\sum_{i=1}^{N} n_i V_i}{V_t} \tag{5.12}$$

Table 5.1. Correlations for Estimating Bubble Size from Bubble Rise Velocity

Reference	Correlation	Range of applicability
Clift et al. (1978)	$u_b = \left[\frac{2.14\sigma_\ell}{\varrho_\ell d_b} + 0.505 g d_b\right]^{0.5}$	$d_b > 1.3\ mm$
Abou-el-Hassan (1983)	$V = 0.75[log(F)]^2$ $V = velocity\ number = \frac{u_b d_b^{2/3} \varrho_\ell^{2/3}}{\mu_\ell^{1/3} \sigma_\ell^{1/3}}$ $F = flow\ number = \frac{g d_b^{8/3} (\varrho_\ell - \varrho_g) \varrho_\ell^{2/3}}{\mu_\ell^{4/3} \sigma_\ell^{1/3}}$	$710 \le \varrho_\ell \le 1180\ kg/m^3$ $0.233 \le \mu_\ell \le 59 \cdot 1 Pa.s$ $0.015 \le \sigma_\ell \le 0.072\ N/m$ $0.1 \le V \le 40$ $1 \le F \le 10^6$

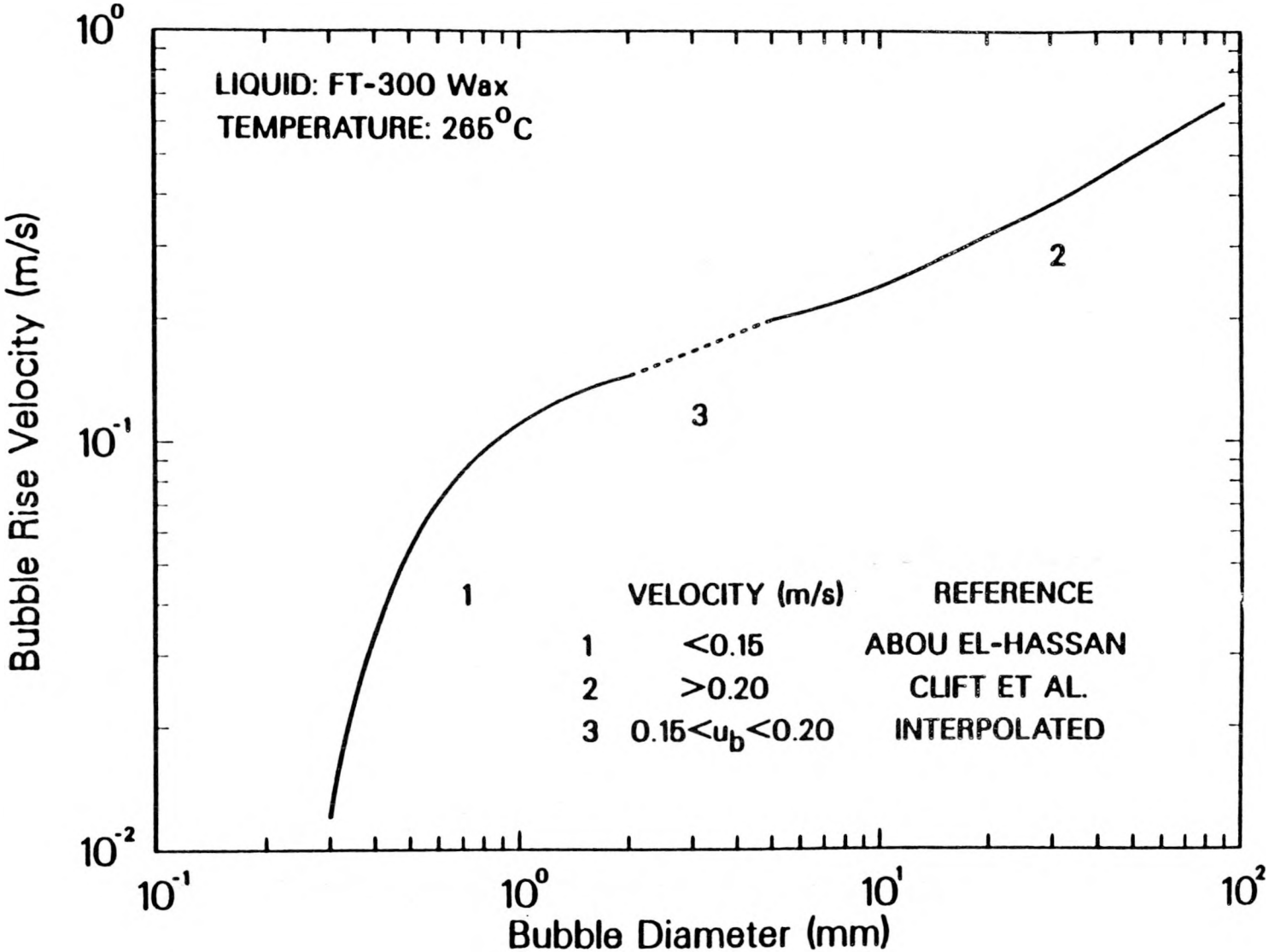

Figure 5.5. Bubble rise velocity vs. bubble diameter correlation for FT-300 wax.

Thus, the number of bubbles in a given bubble class may be written as

$$n_i = \frac{\epsilon_{gi} V_T}{V_i} \tag{5.13}$$

where V_i is the volume corresponding to a bubble of size d_{Bi} and V_T is the total volume of the dispersion below the pressure transducer. Since the volume of an individual bubble is $\pi d_{Bi}^3 / 6$ and the total volume of the dispersion below the pressure transducer is $\pi d_{col}^2 H_{DP} / 4$, Eq. 5.13 may be rewritten as

$$n_i = \frac{3\epsilon_{gi} d_{col}^2 H_{DP}}{2 d_{Bi}^3} \tag{5.14}$$

Substituting the expression for n_i (Eq. 5.14) into the definition of the Sauter mean bubble diameter, Eq. 5.11, the following expression for the Sauter mean bubble diameter is obtained upon rearrangement

$$d_s = \frac{\epsilon_g}{\sum_{i=1}^{N} \epsilon_{gi} / d_{Bi}} \tag{5.15}$$

Data Acquisition and Reduction Procedures

Pressure transducers located at heights of 0.6, 1.3, and 1.9 m above the distributor were used to measure the rate at which the liquid level dropped during the disengagement process. By obtaining data at different heights, knowledge of the axial variation in bubble size distribution may be obtained. After achieving steady state at a given gas velocity ($\approx$ 1.5 hours), the gas flow to the column was shut off using a solenoid valve and the change in the output voltage from the pressure transducer indicators was recorded via the data acquisition system described in Chapter II. Based on our previous work (Bukur et al., 1987a) disengagment was complete within 2 minutes; thus, during the present studies, disengagement data (i.e. output voltages) were acquired for approximately 2 minutes at a sampling frequency of 10 Hz once the gas flow to the

column was terminated. The output voltage from each pressure indicator was converted to pressure (inches of water) using the calibration curves (see Chapter II)

$$\text{P (inches of water)} = \text{SLOPE} * (\text{OUTPUT VOLTAGE}) + \text{INT} \tag{5.16}$$

The pressure, P, may be expressed in "inches of wax" by

$$\text{P (inches of wax)} = \frac{\text{P (inches of water)}}{s_\ell} \tag{5.17}$$

where s_ℓ is the specific gravity of wax. Numerically, the pressure (inches of wax) corresponds to the height of liquid wax above a given pressure transducer.

Typical output voltage versus time data at heights of 0.6, 1.3, and 1.9 m above the distributor from the batch experiment with FT–300 in the 0.05 m ID column at a superficial gas velocity of 0.06 m/s are shown in Figures 5.6a, 5.6b, and 5.6c, respectively. The disengagement profiles at heights of 1.3 and 1.9 m are well defined, but their is a significant amount of oscillations in the disengagement curve acquired at a height of 0.6 m above the distributor. The variation in the disengagement curve at a height of 0.6 m are due to oscillations in the pressure caused by the disengagement of large bubbles from the dispersion. Due to the uncertainty in the disengagement curve at a height of 0.6 m, data obtained at this height were not analyzed.

The original disengagement curve was smoothed by dividing it into 120 equally spaced intervals. This was done by averaging the output voltage for every ten data points, with the exception of the five points at the beginning and end of the disengagement curve. Following this, the slope between successive points were calculated. If successive slopes varied by less than 0.5 %, then the slopes of the two lines were assumed to be the same, and the point common to both lines was omitted, thus reducing the number of bubble classes by one. In general, this reduced the 120 bubble classes to approximately 10 to 20. The output voltage of each data point was then converted to

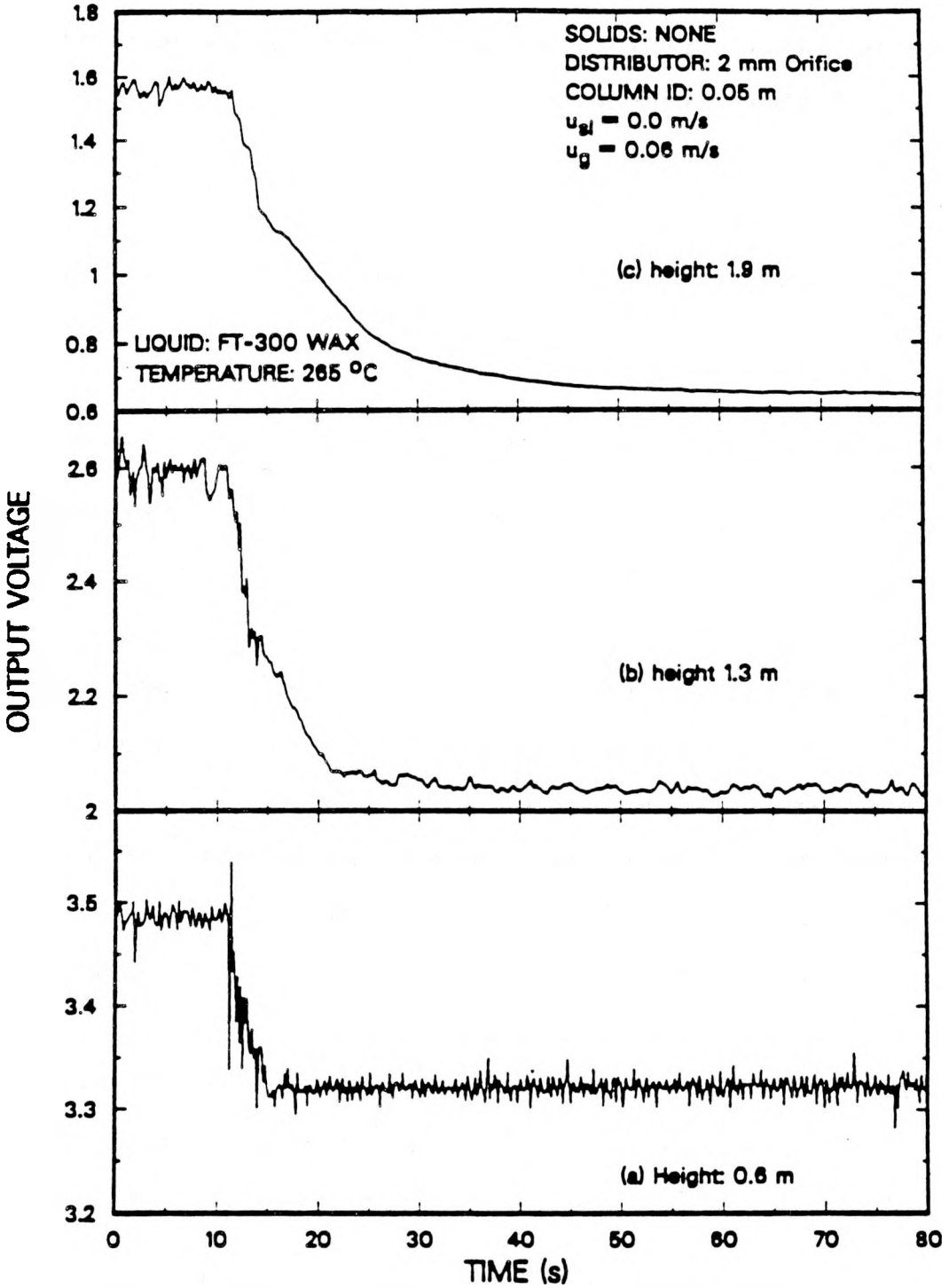

Figure 5.6. Raw pressure transducer signal for DGD analysis from the experiment with FT-300 wax in the small diameter column at heights of (a) 0.6 m; (b) 1.3 m; and (c) 1.9 m above the distributor.

height (inches of wax) by use of Eqs. 5.16 and 5.17. These data (i.e. height vs time) were used to calculate bubble rise velocities and gas holdups for each bubble class via Eqs. 5.9 and 5.10, respectively. Once bubble rise velocities were obtained, bubble sizes were calculated using the correlations presented in Table 5.1. The Sauter mean bubble diameter was obtained from Eq. 5.15. Finally, the specific gas–liquid interfacial area was calculated from Eq. 5.1 using the gas holdup of the dispersion below the pressure transducer.

Discussion of Results

Dynamic gas disengagement measurements were carried out in the two stainless steel columns (0.05 m ID and 0.21 m ID, 3 m tall) during some of the two–phase experiments conducted in the batch mode of operation. DGD data were acquired during two experiments with SASOL wax (experiments 1 and 5 in Table 2.5) and one experiment with FT–300 wax (experiment 30 in Table 2.5) in the large diameter column, and during one experiment with SASOL wax (experiment 29 in Table 2.4) and one experiment with FT–300 wax (experiment 23 in Table 2.4) in the small diameter column. The 2 mm orifice plate distributor was used in the 0.05 m ID column and the 19 x 2 mm distributor was employed in the 0.21 m ID column. All disengagement data for wax were analyzed assuming Case I disengagement.

Figures 5.7 and 5.8 show the disengagement curves at heights of 1.3 and 1.9 m above the distributor plotted as normalized differential height versus time for FT–300 wax and SASOL wax, respectively. The normalized differential height is defined as

$$\text{Norm. Diff. Height} = \frac{H_t(t_i) - H_t(t_n)}{H_t(0) - H_t(t_n)} \qquad i = 1 \text{ to } n \tag{5.18}$$

where $H_t(t_n)$ is the height of the liquid above the pressure transducer at the instant the last small bubble rises above the pressure transducer, $H_t(0)$ is the height of liquid above the pressure transducer immediately prior to interrupting the gas flow (i.e. at

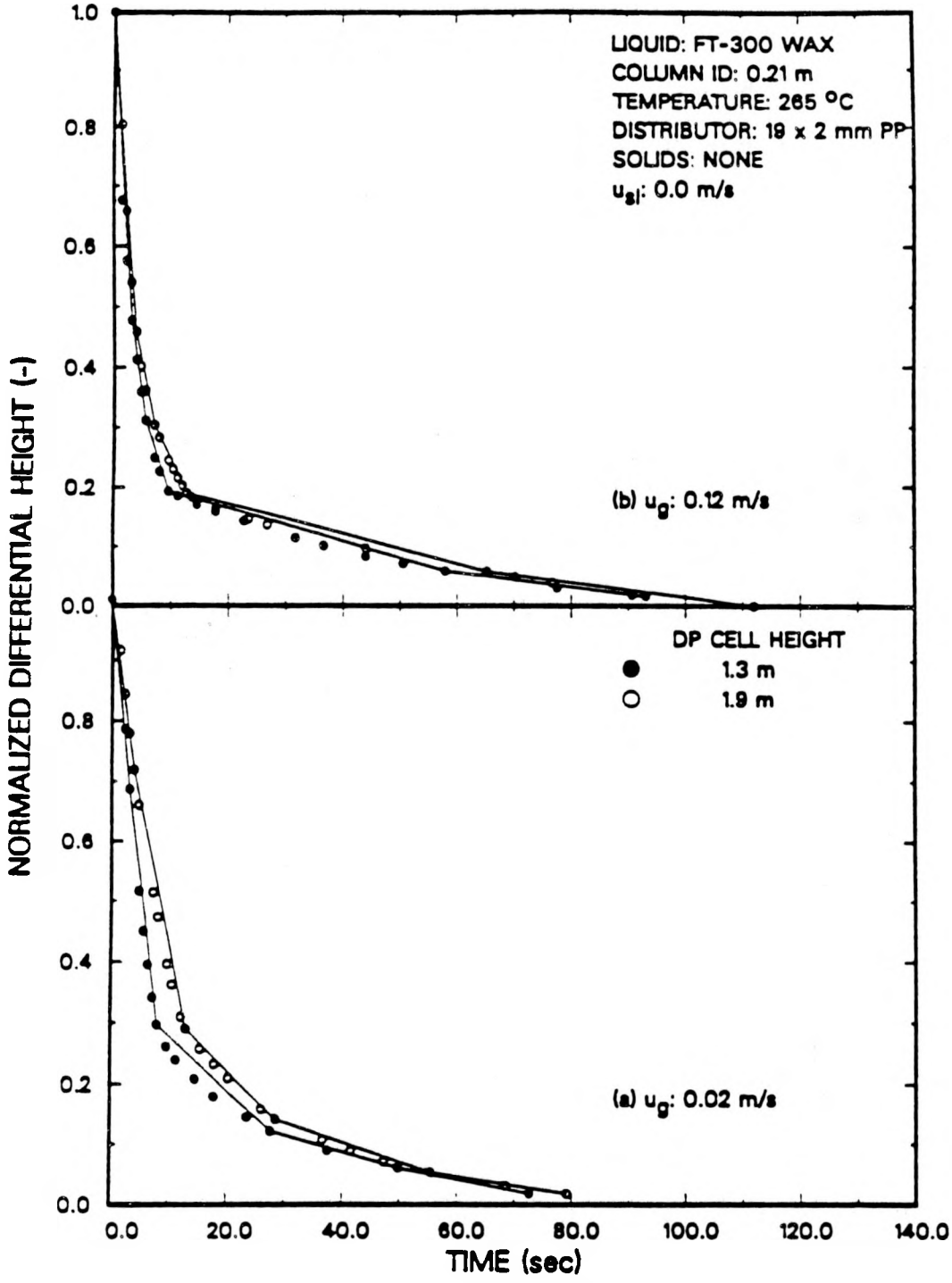

Figure 5.7. Effect of axial position on disengagement (FT-300 wax, (a) u_g= 0 02 m/s; (b) u_g=0.12 m/s).

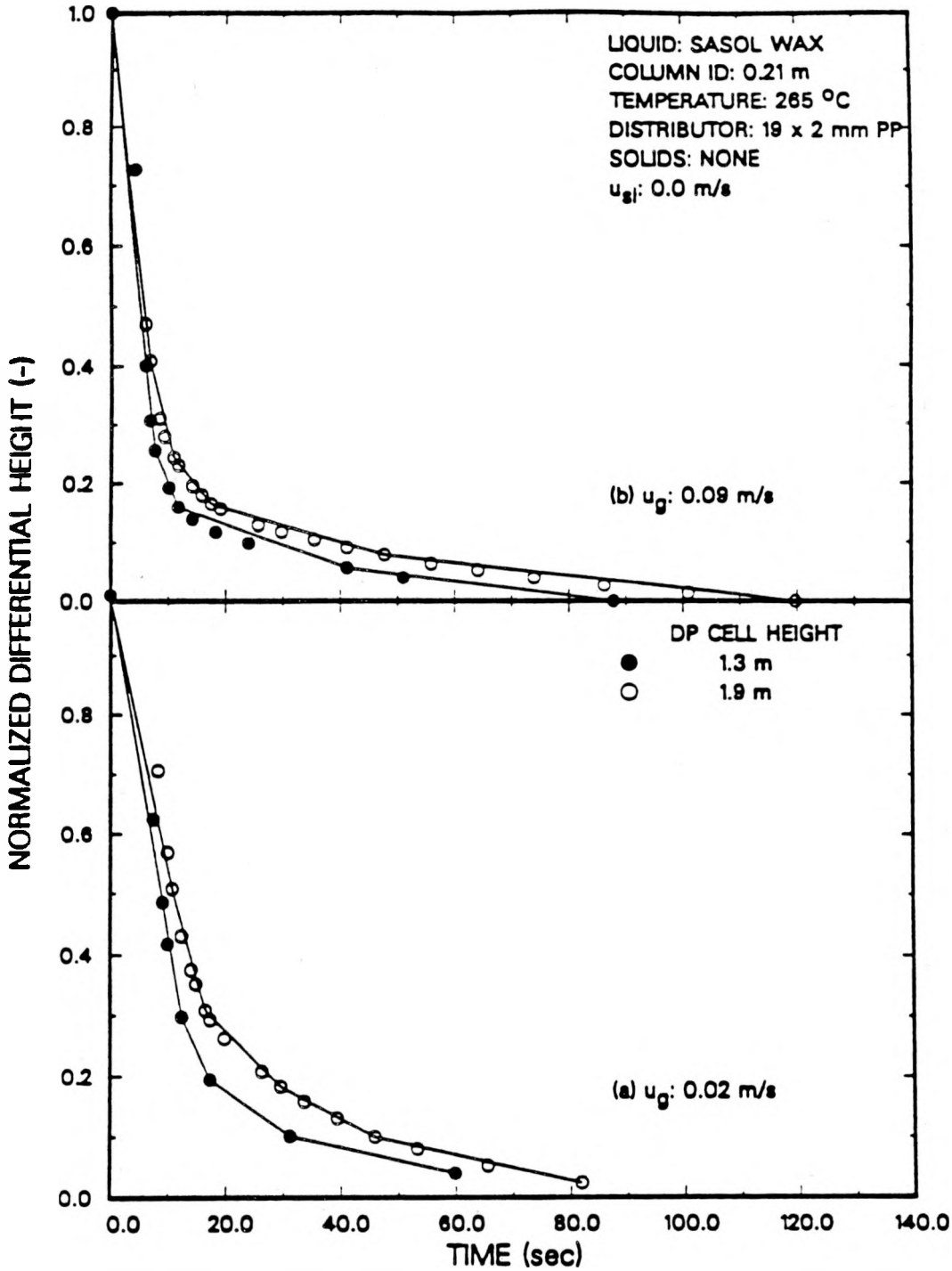

Figure 5.8. Effect of axial position on disengagement (SASOL wax, (a) u_g= 0.02 m/s; (b) u_g=0.09 m/s).

steady state conditions), and $H_t(t_i)$ is the height of liquid above the pressure transducer when the last bubble of size d_{Bi} passes above the pressure transducer. The data from experiments in the large column were also analyzed by dividing the disengagement curve into five intervals (i.e. five bubble classes, lines on Figures 5.7 and 5.8) to see what effect the number of bubble classes used has on the Sauter mean bubble diameter and specific gas–liquid interfacial area. If the dispersion is axially uniform, then the major breakpoints on the two curves (i.e. at heights of 1.3 and 1.9 m) would occur at the same normalized differential height. Also, if bubbles are rising at the same velocity as they rise past heights of 1.3 and 1.9 m, then the curve associated with the DP cell located at 1.9 m should be shifted to the right of the curve associated with the DP cell located 1.3 m. Both the trends mentioned above were observed in all experiments with wax in both the large and small diameter columns.

The gas holdups presented throughout this discussion, unless otherwise noted, correspond to the gas holdup of the dispersion below the measurement location. These gas holdups were obtained using Eq. 2.27, with $n = 3$ (for data obtained at a height of 1.3 m above the distributor) and $n = 4$ (for data obtained at a height of 1.9 m above the distributor). The specific gas liquid interfacial areas and Sauter mean bubble diameters are based on the holdup of the dispersion below the measurement location. Tables 5.2, 5.3, and 5.4 summarize the results obtained from experiments in the large diameter column with FT–300 wax and SASOL reactor wax (decreasing and increasing order of velocities), respectively. The experiment with FT–300 wax was conducted employing a decreasing order of gas velocities. The results presented in the tables for rise velocities, u_{bi}, and fractions of large bubbles f_L were based on the five bubble class analyses. The rise velocity of large bubbles was taken as the largest rise velocity, and the rise velocity of small bubbles was taken as the smallest rise velocity. The medium bubble rise velocity corresponds to the rise velocity of the middle bubble class. Sauter mean bubble

Table 5.2a. DGD Results from the Experiment with FT-300 Wax at a Height of 1.3 m (0.21 m ID Stainless Steel Bubble Column, 265 °C)

u_g (m/s)	ϵ_{go} (-)	u_{bs} (m/s)	u_{bm} (m/s)	u_{bl} (m/s)	f_l (-)	d_s (mm)	d_s^* (mm)	a_s (m^{-1})	a_s^* (m^{-1})
0.02	0.093	0.017	0.168	0.51	0.13	0.92	0.96	607	581
0.04	0.118	0.015	0.168	0.51	0.23	0.95	1.01	745	701
0.08	0.181	0.014	0.126	0.51	0.45	1.12	1.12	970	970
0.12	0.199	0.013	0.137	0.51	0.55	1.33	1.30	898	920

Table 5.2b. DGD Results from the Experiment with FT-300 Wax at a Height of 1.9 m (0.21 m ID Stainless Steel Bubble Column, 265 °C)

u_g (m/s)	ϵ_{go} (-)	u_{bs} (m/s)	u_{bm} (m/s)	u_{bl} (m/s)	f_l (-)	d_s (mm)	d_s^* (mm)	a_s (m^{-1})	a_s^* (m^{-1})
0.02	0.102	0.024	0.151	0.57	0.13	0.92	0.97	665	631
0.04	0.121	0.020	0.162	0.57	0.23	0.92	0.99	789	733
0.08	0.184	0.017	0.142	0.57	0.54	1.26	1.32	876	836
0.12	0.196	0.017	0.151	0.57	0.57	1.37	1.45	858	811

* Denotes values from analysis of all points.

Table 5.3a. DGD Results from the Experiment with SASOL Wax (Decreasing Gas Velocity) at a Height of 1.3 m (0.21 m ID Stainless Steel Bubble Column, 265 °C)

u_g (m/s)	ϵ_{go} (-)	u_{bs} (m/s)	u_{bm} (m/s)	u_{bl} (m/s)	f_l (-)	d_s (mm)	d_s^* (mm)	a_s (m^{-1})	a_s^* (m^{-1})
0.02	0.069	0.023	0.190	0.38	0.34	1.30	1.20	318	345
0.04	0.094	0.015	0.150	0.38	0.56	1.30	1.30	434	434
0.06	0.124	0.013	0.130	0.51	0.63	1.50	1.50	496	496
0.09	0.152	0.015	0.150	0.51	0.65	1.60	1.70	570	540

Table 5.3b. DGD Results from the Experiment with SASOL Wax (Decreasing Gas Velocity) at a Height of 1.9 m (0.21 m ID Stainless Steel Bubble Column, 265 °C)

u_g (m/s)	ϵ_{go} (-)	u_{bs} (m/s)	u_{bm} (m/s)	u_{bl} (m/s)	f_l (-)	d_s (mm)	d_s^* (mm)	a_s (m^{-1})	a_s^* (m^{-1})
0.02	0.074	0.024	0.174	0.38	0.33	1.10	1.10	404	404
0.04	0.109	0.024	0.174	0.38	0.60	1.30	1.40	503	467
0.06	0.130	0.015	0.113	0.45	0.65	1.40	1.50	557	520
0.09	0.154	0.016	0.133	0.56	0.67	1.60	1.60	578	578

* Denotes values from analysis of all points.

Table 5.4a. DGD Results from the Experiment with SASOL Wax (Increasing Gas Velocity) at a Height of 1.3 m (0.21 m ID Stainless Steel Bubble Column, 265 °C)

u_g (m/s)	ϵ_{go} (-)	u_{bs} (m/s)	u_{bm} (m/s)	u_{bl} (m/s)	f_l (-)	d_s (mm)	d_s^* (mm)	a_s (m^{-1})	a_s^* (m^{-1})
0.02	0.079	0.031	0.152	0.52	0.25	1.00	1.00	474	474
0.04	0.100	0.030	0.176	0.51	0.45	1.10	1.20	545	500
0.06	0.141	0.031	0.164	0.57	0.52	1.20	1.24	705	682
0.09	0.156	0.031	0.178	0.57	0.50	1.25	1.28	749	731

Table 5.4b. DGD Results from the Experiment with SASOL Wax (Increasing Gas Velocity) at a Height of 1.9 m (0.21 m ID Stainless Steel Bubble Column, 265 °C)

u_g (m/s)	ϵ_{go} (-)	u_{bs} (m/s)	u_{bm} (m/s)	u_{bl} (m/s)	f_l (-)	d_s (mm)	d_s^* (mm)	a_s (m^{-1})	a_s^* (m^{-1})
0.02	0.083	0.047	0.171	0.43	0.30	1.20	1.30	415	383
0.04	0.122	0.031	0.150	0.49	0.45	1.20	1.20	610	610
0.06	0.145	0.034	0.150	0.49	0.50	1.23	1.25	707	696

* Denotes values from analysis of all points.

diameters and specific gas–liquid interfacial areas are presented assuming five bubble classes and using all points. The Sauter mean bubble diameters and specific gas–liquid interfacial areas were comparable using both types of analyses. Similar results were obtained in the small column with SASOL and FT–300 wax (see Tables 5.5 and 5.6).

Figure 5.9 compares Sauter mean bubble diameters, specific gas liquid interfacial areas and gas holdups at a height of 1.3 m above the distributor for the experiments conducted in the large column (from 5 bubble classes analysis). The specific gas-liquid interfacial area and Sauter mean bubble diameters are based on the gas holdup of the dispersion below the pressure transducer. The gas holdup values from the experiment with FT–300 wax were slightly higher than those obtained from either of the experiments with SASOL wax (see Figure 5.9c). As shown in Figure 5.9a, the Sauter mean bubble diameters for the experiment conducted with FT–300 wax were consistently lower than those for the experiment conducted with SASOL reactor wax employing a decreasing order of gas velocities. In particular, Sauter mean bubble diameters ranged from approximately 1.0 to 1.3 mm for the experiment conducted with FT–300 wax as opposed to 1.3 to 1.6 mm for the experiment conducted in a decreasing order of gas velocities with SASOL reactor wax. However, the Sauter mean bubble diameters from the experiment conducted in an increasing order of gas velocities with SASOL reactor wax were comparable (slightly higher) to those obtained from the experiment conducted with FT–300 wax. The difference in Sauter mean bubble diameters is caused by differences in the fraction of large bubbles. For example, at a gas velocity of 0.09 m/s, the fraction of large bubbles for the experiment conducted in an increasing order of gas velocities was 0.50 whereas it was 0.65 for the experiment conducted in a decreasing order of velocities with SASOL reactor wax (see Tables 5.3a and 5.4a). These results indicate that bubble size distribution is affected by the operating procedure. Specific

Table 5.5a. DGD Results from the Experiment with FT-300 Wax (Increasing Gas Velocity) at a Height of 1.3 m (0.05 m ID Stainless Steel Bubble Column, 265 °C)

u_g (m/s)	ϵ_{go} (–)	u_{bs} (m/s)	u_{bm} (m/s)	u_{bl} (m/s)	f_l (–)	d_s (mm)	d_s^* (mm)	a_s (m^{-1})	a_s^* (m^{-1})
0.02	0.077	0.031	0.152	0.52	0.25	1.38	1.28	334	361
0.04	0.128	0.030	0.176	0.51	0.45	0.94	1.10	768	698
0.06	0.161	0.031	0.164	0.57	0.52	1.22	1.26	790	767
0.09	0.151	0.031	0.178	0.57	0.50	1.27	1.32	570	686

Table 5.5b. DGD Results from the Experiment with FT-300 wax (Increasing Gas Velocity) at a Height of 1.9 m (0.05 m ID Stainless Steel Bubble Column, 265 °C)

u_g (m/s)	ϵ_{go} (–)	u_{bs} (m/s)	u_{bm} (m/s)	u_{bl} (m/s)	f_l (–)	d_s (mm)	d_s^* (mm)	a_s (m^{-1})	a_s^* (m^{-1})
0.02	0.086	0.047	0.171	0.43	0.30	1.09	1.12	471	461
0.04	0.137	0.031	0.150	0.49	0.45	0.90	1.01	902	814
0.06	0.181	0.034	0.150	0.49	0.50	0.90	0.97	1200	1120
0.09	0.200	0.034	0.150	0.49	0.50	1.49	1.38	808	870

* Denotes values from analysis of all points.

Table 5.6a. DGD Results from the Experiment with SASOL Wax (Increasing Gas Velocity) at a Height of 1.3 m (0.05 m ID Stainless Steel Bubble Column, 265 ^{o}C)

u_g (m/s)	ϵ_{go} (-)	u_{bs} (m/s)	u_{bm} (m/s)	u_{bl} (m/s)	f_l (-)	d_s (mm)	d_s^* (mm)	a_s (m^{-1})	a_s^* (m^{-1})
0.02	0.052	0.031	0.152	0.52	0.25	1.40	1.45	220	215
0.04	0.088	0.030	0.176	0.51	0.45	1.80	1.78	290	297
0.06	0.110	0.031	0.164	0.57	0.52	1.81	1.83	350	361
0.09	0.137	0.031	0.178	0.57	0.50	2.10	2.21	390	372

Table 5.6b. DGD Results from the Experiment with SASOL Wax (Increasing Gas Velocity) at a Height of 1.9 m (0.05 m ID Stainless Steel Bubble Column, 265 ^{o}C)

u_g (m/s)	ϵ_{go} (-)	u_{bs} (m/s)	u_{bm} (m/s)	u_{bl} (m/s)	f_l (-)	d_s (mm)	d_s^* (mm)	a_s (m^{-1})	a_s^* (m^{-1})
0.02	0.086	0.047	0.171	0.43	0.30	1.30	1.32	400	391
0.04	0.110	0.031	0.150	0.49	0.45	1.60	1.52	410	434
0.06	0.129	0.034	0.150	0.49	0.50	1.60	1.61	480	481
0.09	0.157	0.034	0.150	0.49	0.50	2.00	2.30	420	410

* Denotes values from analysis of all points.

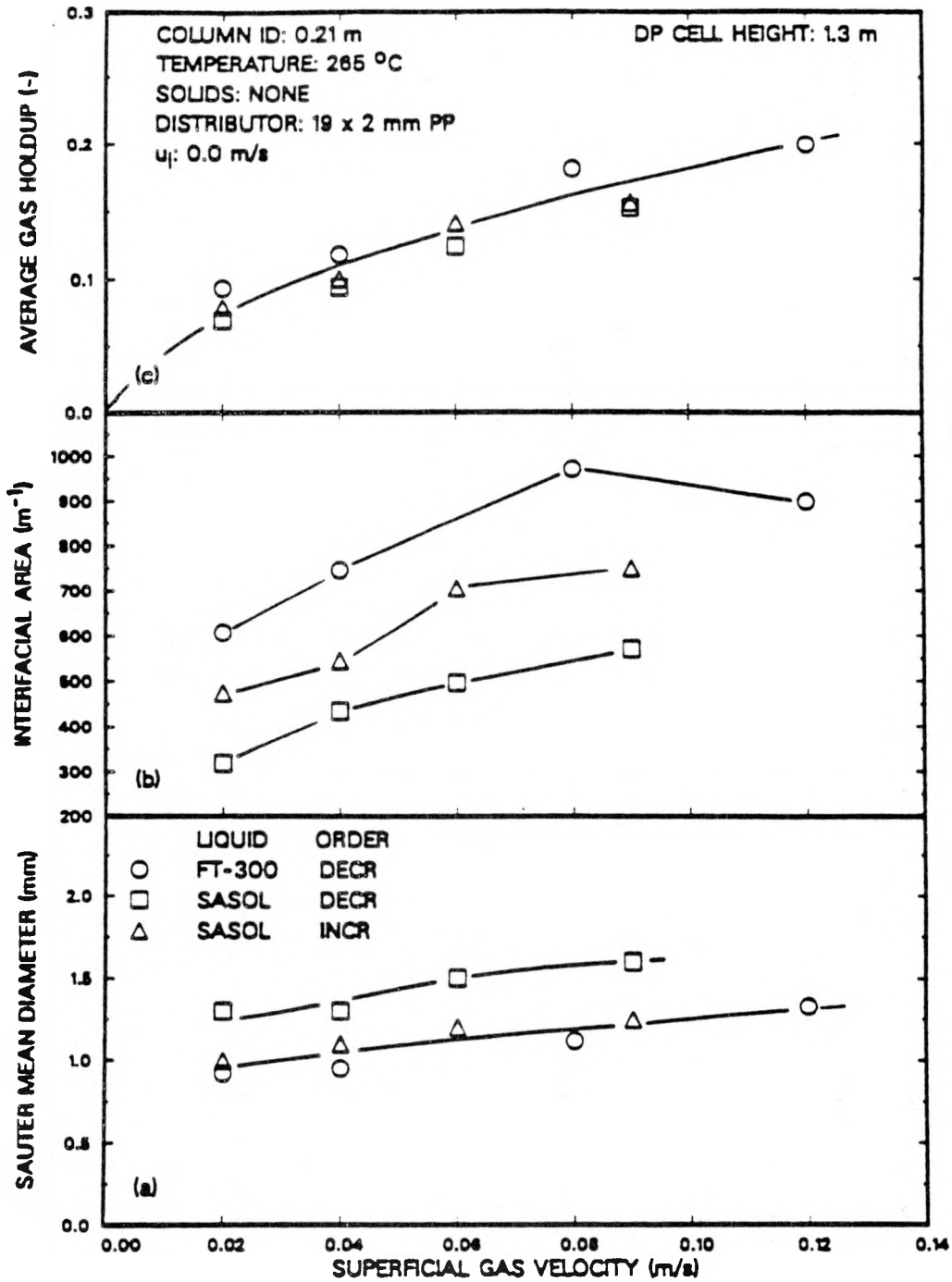

Figure 5.9. Effect of superficial gas velocity and wax type on (a) Sauter mean bubble diameter, (b) specific gas-liquid interfacial area, and (c) gas holdup in the 0.21 m ID column at a height of 1.3 m above the distributor.

gas liquid interfacial areas obtained from the three experiments were substantially different. There was almost a 100 % increase in a_s between the experiment conducted with FT–300 wax and the experiment conducted in a decreasing order of gas velocities with SASOL reactor wax. Similar results were obtained at a height of 1.9 m above the distributor (see Figure 5.10).

Figures 5.11 and 5.12 show results from experiments in the small diameter column at heights of 1.3 and 1.9 m above the distributor. As shown in Chapter II, FT–300 wax produces foam and as a result, the gas holdups with FT–300 wax are considerably larger than those produced with SASOL reactor wax (see Figures 5.11c and 5.12c). These higher gas holdups result in lower Sauter mean bubble diameters (Figures 5.11a and 5.12a), except at a gas velocity of 0.02 m/s, where the Sauter mean bubble diameters obtained for both waxes are comparable. This is expected, since homogeneous bubbly flow exists in the column at this velocity. As the gas velocity is increased to 0.04 m/s, the gas holdup from the experiment with FT–300 is significantly greater than that from the experiment with SASOL wax. This difference is holdup is due primarily to the presence of fine bubbles which accumulate in the uppermost region of the dispersion. This increase in the number of small bubbles associated with FT–300 wax results in a lower Sauter mean bubble diameter (see Figures 5.11a and 5.12a). Specific gas–liquid interfacial areas are shown in Figures 5.11b and 5.12b.

Figure 5.13 shows axial gas holdups from the experiments conducted with FT–300 wax and SASOL wax, at gas velocities of 0.02, 0.04, and 0.09 m/s. Axial gas holdup profiles from the experiment with SASOL wax show a slight increase in gas holdup with increasing height above the distributor (see Figure 5.13b). However, for the experiment with FT–300 wax, the gas holdup in the uppermost region of the column at a gas velocity of 0.04 m/s increases significantly compared to the holdup at lower heights. In particular, at a height of 1.6 m above the distributor, the gas holdup is approximately

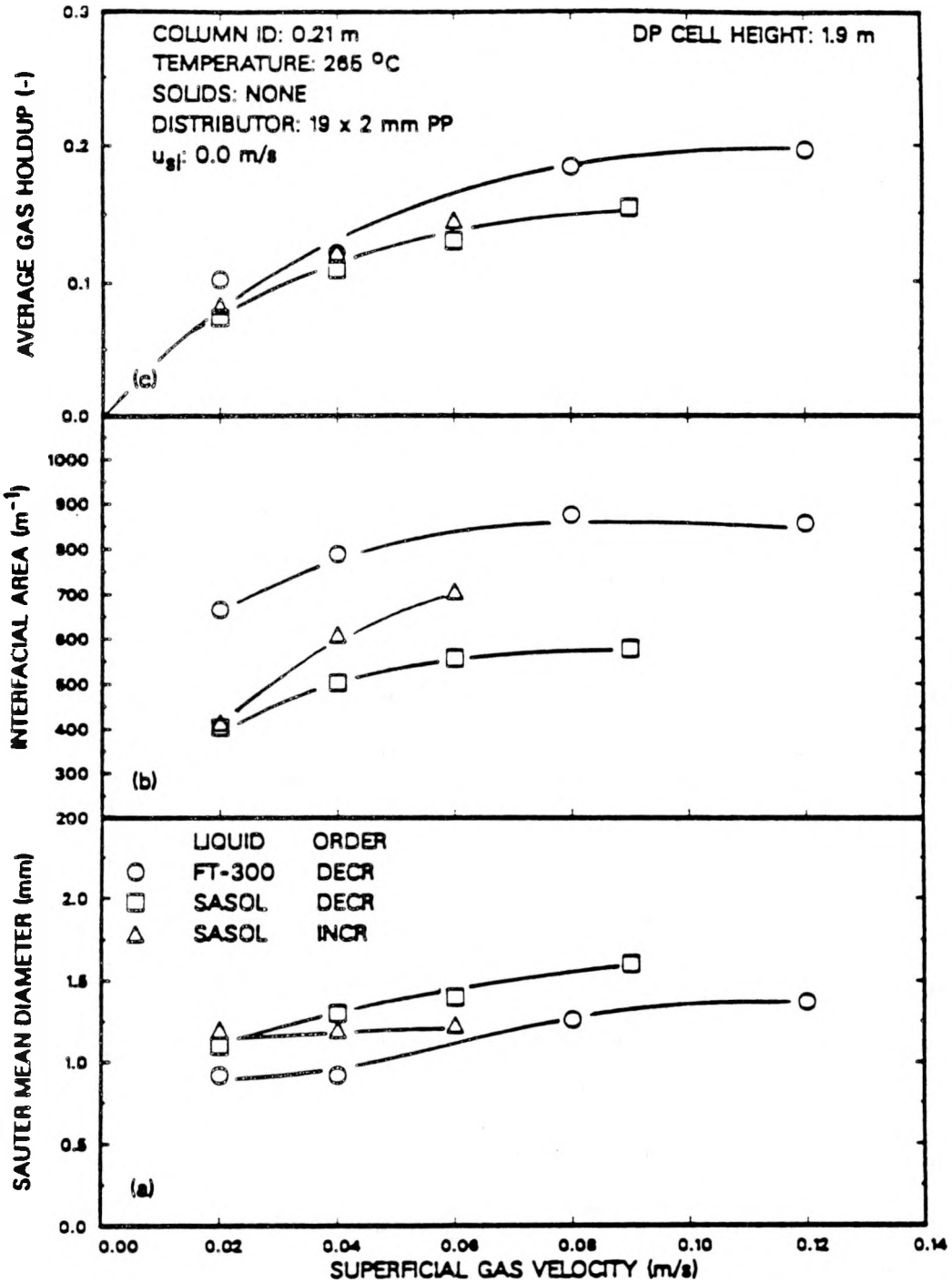

Figure 5.10. Effect of superficial gas velocity and wax type on (a) Sauter mean bubble diameter, (b) specific gas-liquid interfacial area, and (c) gas holdup in the 0.21 m ID column at a height of 1.9 m above the distributor.

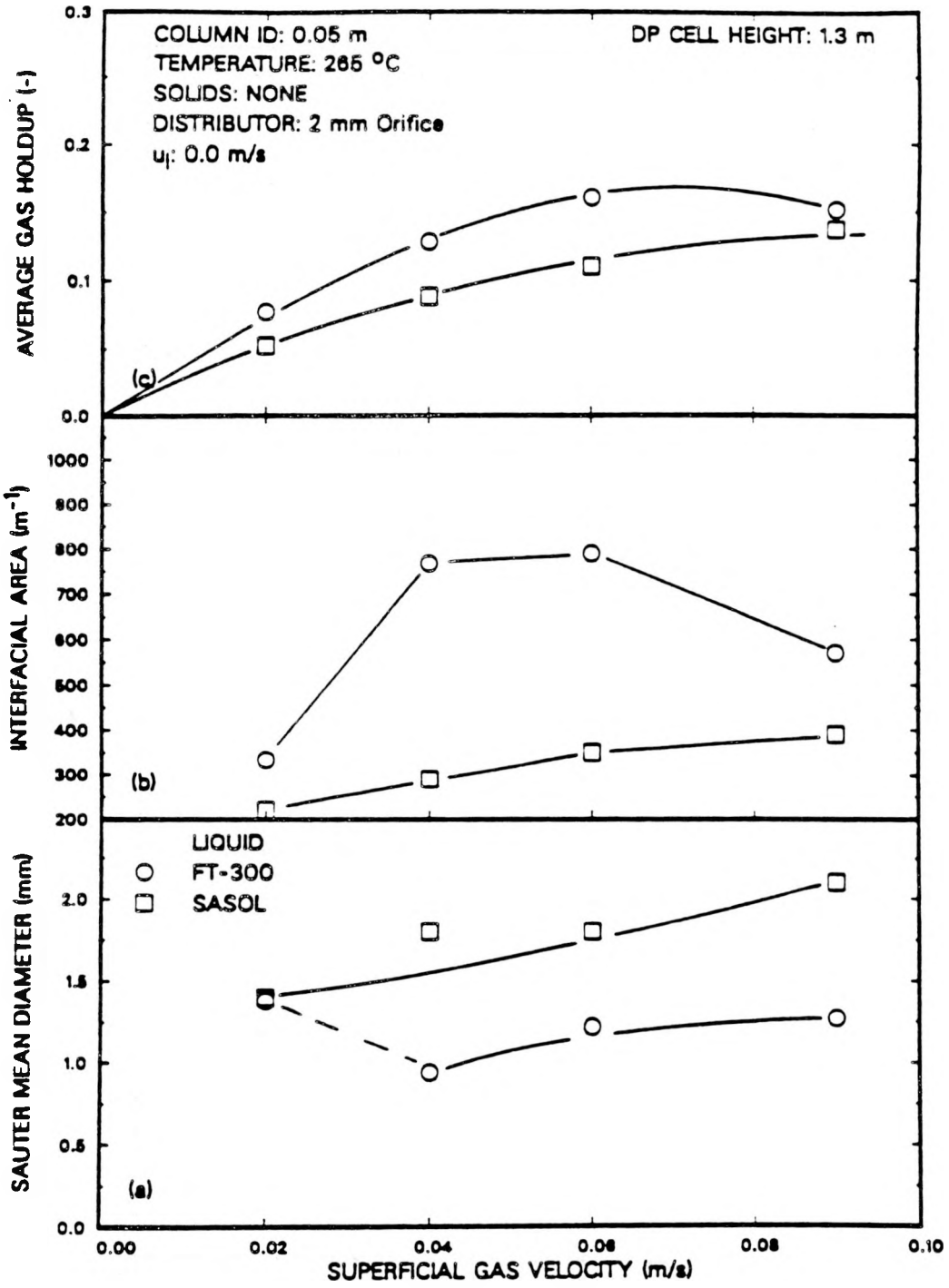

Figure 5.11. Effect of superficial gas velocity and wax type on (a) Sauter mean bubble diameter, (b) specific gas-liquid interfacial area, and (c) gas holdup in the 0.05 m ID column at a height of 1.3 m above the distributor.

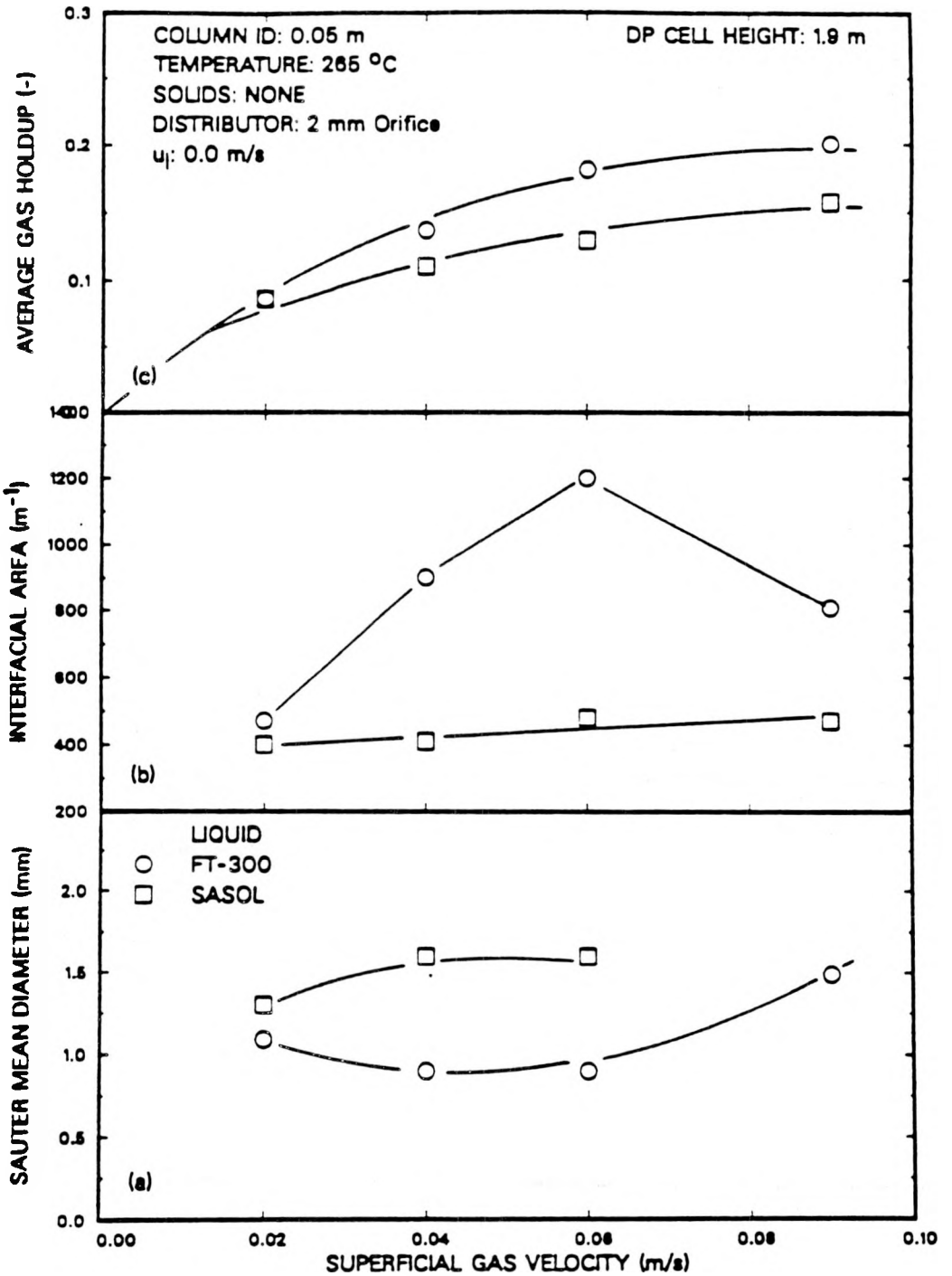

Figure 5.12. Effect of superficial gas velocity and wax type on (a) Sauter mean bubble diameter, (b) specific gas-liquid interfacial area, and (c) gas holdup in the 0.05 m ID column at a height of 1.9 m above the distributor.

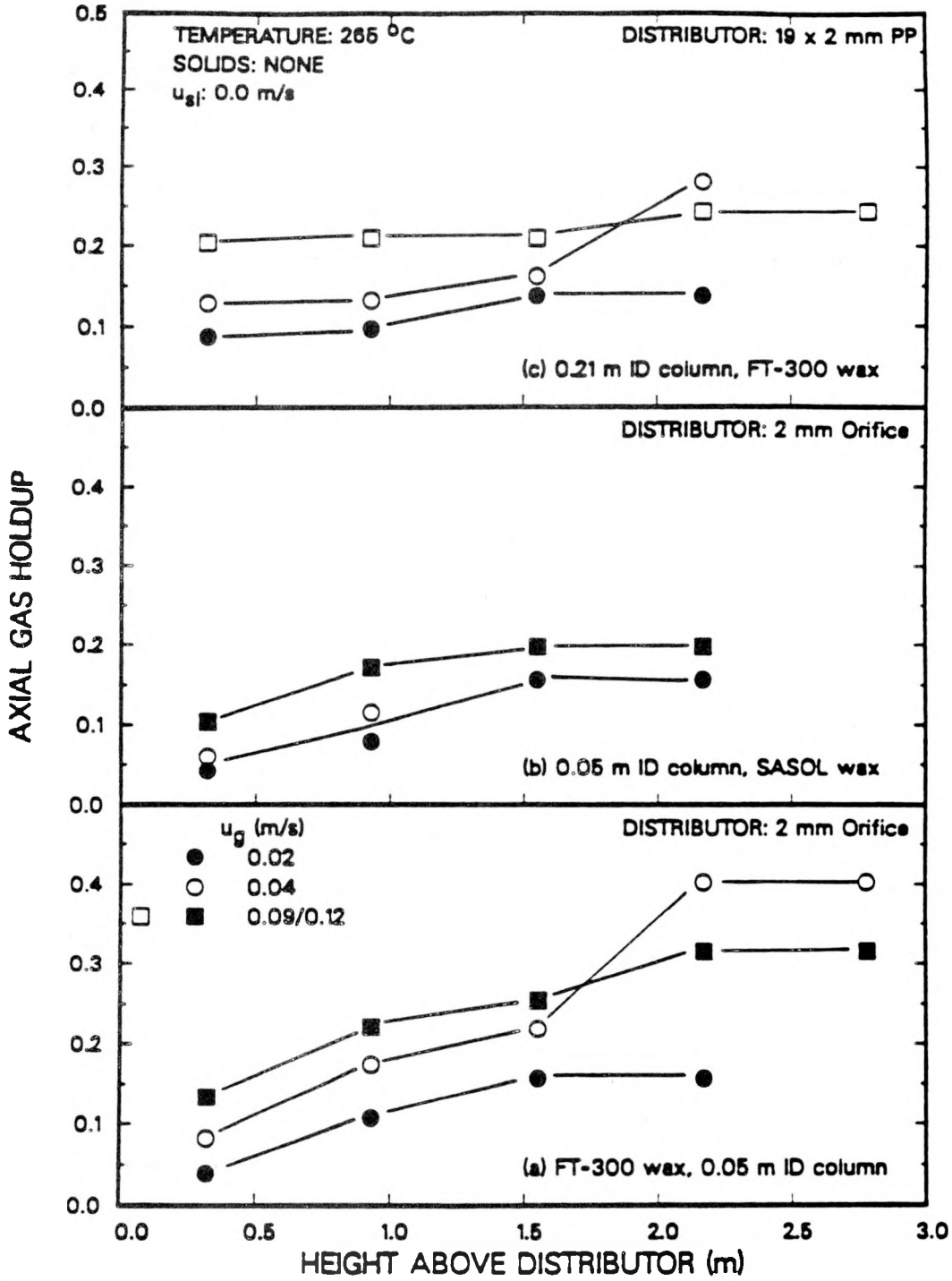

Figure 5.13. Effect of superficial gas velocity on axial gas holdup ((a) 0.05 m ID column, FT-300 wax; (b) 0.05 m ID column, SASOL wax; (c) 0.21 m ID column, FT-300 wax).

0.2; whereas, at a height of 2.2 m above the distributor, the gas holdup is approximately 0.4. At a gas velocity of 0.09 m/s, the foam layer which was present at a gas velocity of 0.04 m/s dissipates and there is a gradual increase in holdup with increasing height above the distributor. With the exception of a gas velocity of 0.02 m/s, the gas holdups with FT–300 wax are higher than those with SASOL wax, particularly at a gas velocity of 0.04 m/s, and as a result, the Sauter mean bubble diameters from the experiment with FT–300 wax are lower than those obtained from the experiment with SASOL reactor wax. The results from this study with FT–300 wax and SASOL reactor wax indicate that the Sauter mean bubble diameter is directly related to the gas holdup (i.e. the higher the gas holdup, the lower the Sauter mean bubble diameter). However, in our studies with other waxes (in the small diameter column) it was found that it is possible to have similar holdup values but significantly different Sauter mean bubble diameters (Bukur et al., 1987c; Patel et al., 1990).

Effect of Axial Position

Figure 5.14 shows the effect of height above the distributor on gas holdup and Sauter mean bubble diameter. The gas holdup values shown in this figure correspond to the average gas holdup below the given pressure transducer. Figures 5.14a and 5.14b show results from the experiments conducted in the large diameter column, and Figures 5.14c and 5.14d show results from experiments conducted in the small diameter column. In the large diameter column, we did not observe a significant difference in gas holdup with axial position, and as a result, there is excellent agreement in gas holdups and Sauter mean bubble diameters obtained at heights of 1.3 and 1.9 m above the distributor. However, in the small column, gas holdup increases with increasing height above the distributor, and as a result, gas holdups are slightly higher at a height of 1.9 m as compared to a height of 1.3 m. This increase in gas holdup with increasing height

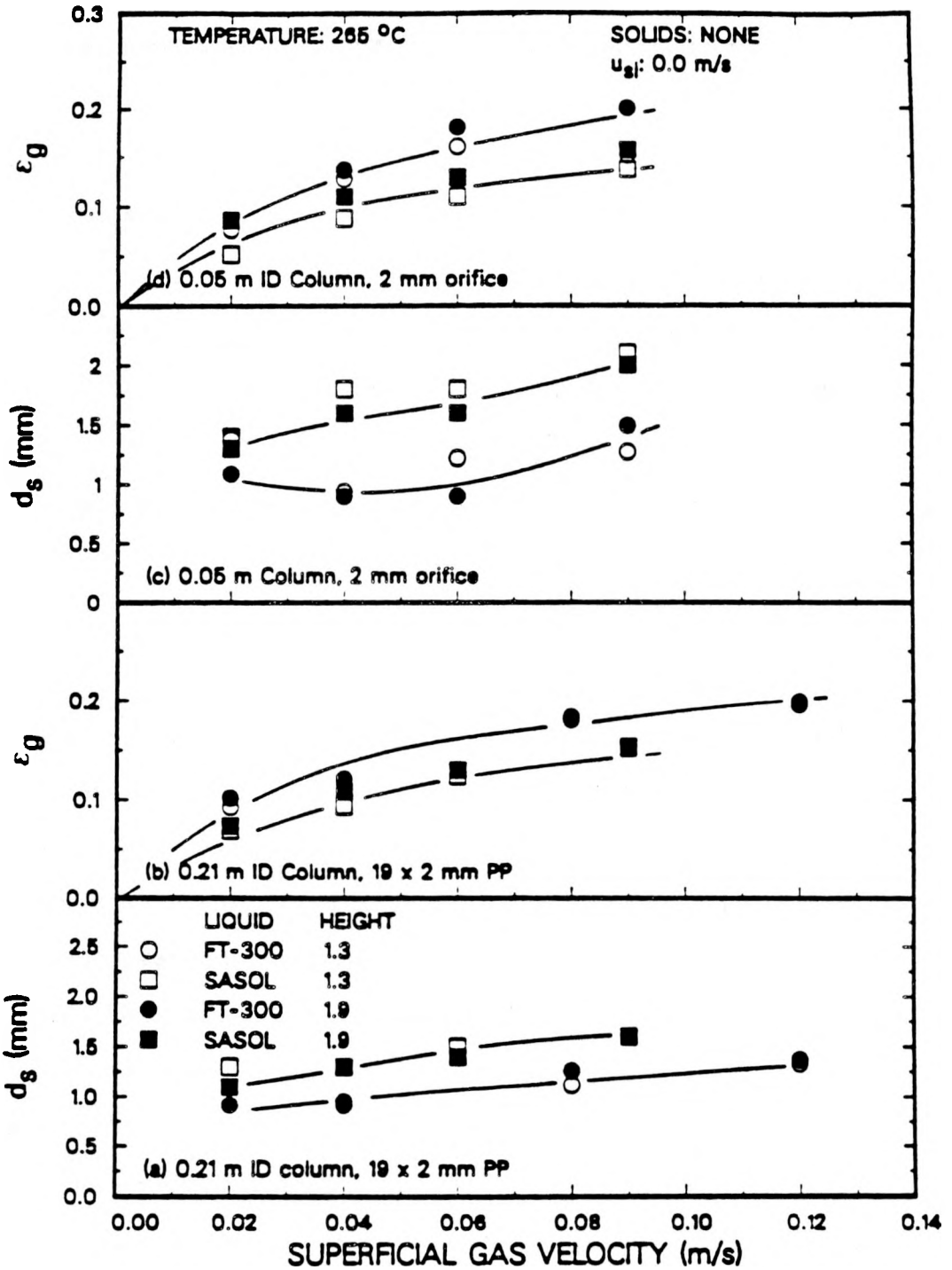

Figure 5.14. Effect of axial position on (a and c) Sauter mean bubble diameter and (b and d) gas holdup in 0.05 and 0.21 m ID bubble columns with wax (decreasing gas velocity - SASOL wax, 0.21 m ID column).

above the distributor results in slightly lower Sauter mean bubble diameters at a height of 1.9 m.

Effect of Column Diameter

Figures 5.15a and 5.15b show the effect of column diameter on the Sauter mean bubble diameter for experiments conducted with FT–300 wax and SASOL reactor wax (decreasing gas velocities) in the 0.05 and 0.21 m ID bubble columns at a height of 1.9 m above the distributor. Sauter mean bubble diameters for experiments conducted with FT–300 wax were similar in both columns for gas velocities less than 0.09 m/s (see Figure 5.15a). This is expected, since very small bubbles are formed with FT–300 at low gas velocities, and as a result, the Sauter mean bubble diameters are similar. At gas velocities greater than 0.09 m/s, the Sauter mean bubble diameter remains fairly constant in the large diameter column. Results from our previous experiments conducted in the small diameter glass column (Patel et al., 1990) indicate that the Sauter mean bubble diameter increases with increasing gas velocity between gas velocities of 0.09 and 0.12 m/s. The differences in trends with increasing gas velocities are due to differences in flow regimes in the 0.21 and 0.05 m ID columns. In the small diameter column, the slug flow regime exists; whereas, in the large diameter column, the churn–turbulent flow regime exists.

The Sauter mean bubble diameters were consistently higher in the small diameter column compared to the large diameter column for the experiments conducted with SASOL wax (see Figure 5.15b). The primary reason for differences in the Sauter mean bubble diameters is due to differences in the flow regimes. The large diameter column operates in the churn–turbulent flow regime and the small diameter column operates in the slug flow regime. The increase in turbulence associated with the large diameter column results in the formation of smaller bubbles.

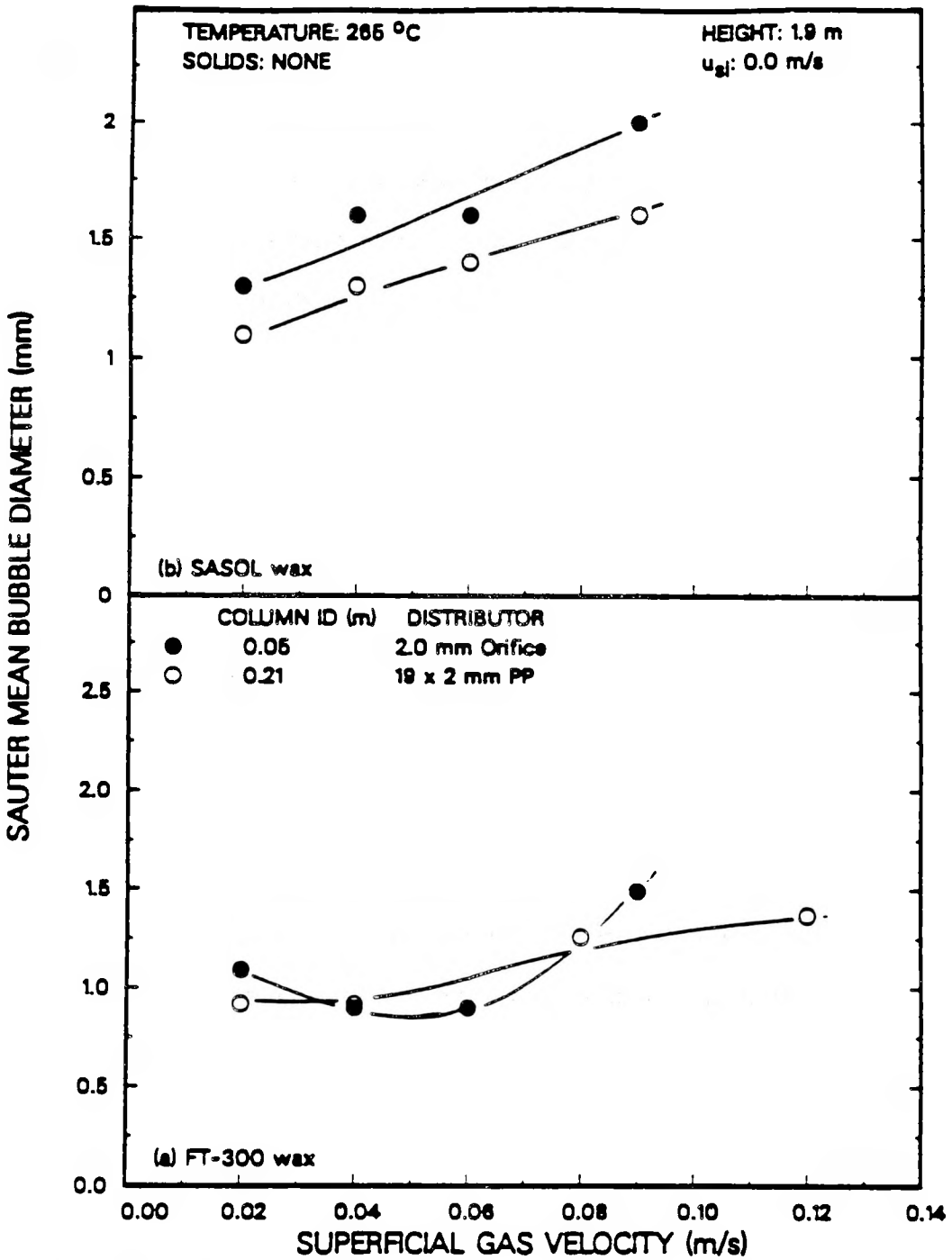

Figure 5.15. Effect of column diameter on Sauter mean bubble diameter for (a) FT-300 wax and (b) SASOL reactor wax - decreasing gas velocity in 0.21 m ID column.

Comparison of Results Obtained in the Glass and Stainless Steel Bubble Columns

The dynamic gas disengagement technique was used to obtain bubble size distributions in both the stainless steel and glass bubble columns. A VCR/video camera system was used to measure the disengagement profile during experiments conducted in the glass column (Bukur et al., 1987a,b; Patel et al., 1990); whereas, pressure transducers were used to measure the disengagement rate in the stainless steel columns. Since disengagement profiles in the glass column were measured for the entire dispersion, only results obtained at a height of 1.9 m above the distributor in the stainless steel columns are used for comparison. Figure 5.16 compares values of d_s and gas holdup from experiments conducted in the large diameter glass and stainless steel columns with FT–300 wax. Results from two experiments in the glass column are shown. There was excellent agreement in Sauter mean bubble diameters in the glass and stainless steel columns when gas holdups were comparable. However, during one experiment in the glass column, a substantial amount of foam was produced and the values of d_s were markedly lower than those obtained in either of the other two experiments.

Figure 5.17 compares d_s values and gas holdups from experiments conducted in the small diameter glass and stainless steel columns. For the experiment conducted in the stainless steel column, the average gas holdup in the entire column, as well as the gas holdup in the column below a height of 1.9 m is shown. The overall gas holdup is substantially greater than that below a height of 1.9 m, indicating the presence of foam in the upper region of the column. While the overall gas holdups in the two columns (glass and stainless steel) were similar for gas velocities greater than 0.02 m/s, the Sauter mean bubble diameters are significantly different. This difference is a result of the data acquisition technique. For the experiment in the glass column, d_s is based on the entire dispersion; whereas, in the stainless steel column, d_s, is based only on the dispersion below a height of 1.9 m. This illustrates one of the problems associated

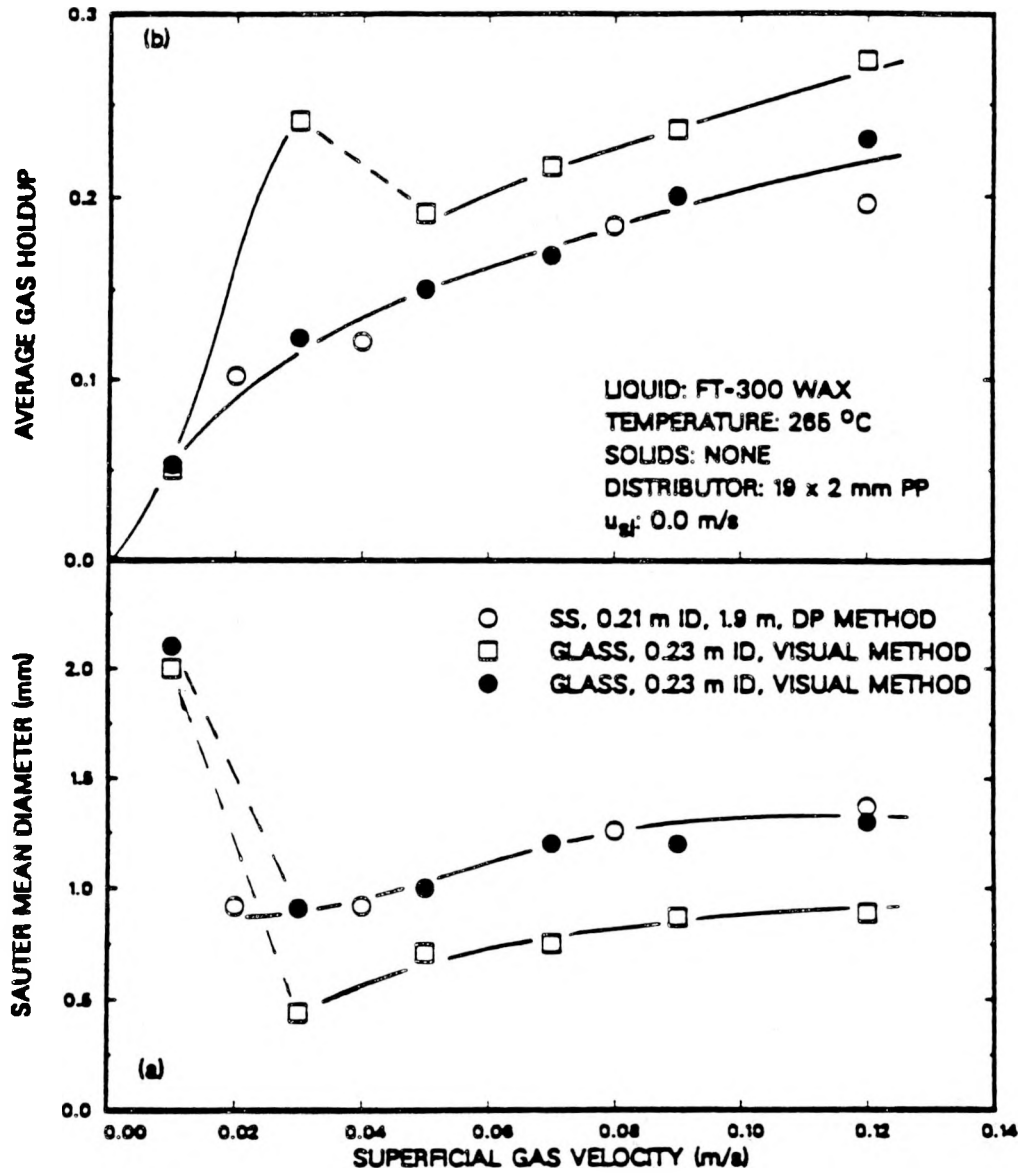

Figure 5.16. Comparison of (a) Sauter mean bubble diameters and (b) gas holdup obtained in the 0.21 m ID stainless steel column (DP method, 1.9 m) and the 0.23 m ID glass column (visual method) with FT-300 wax.

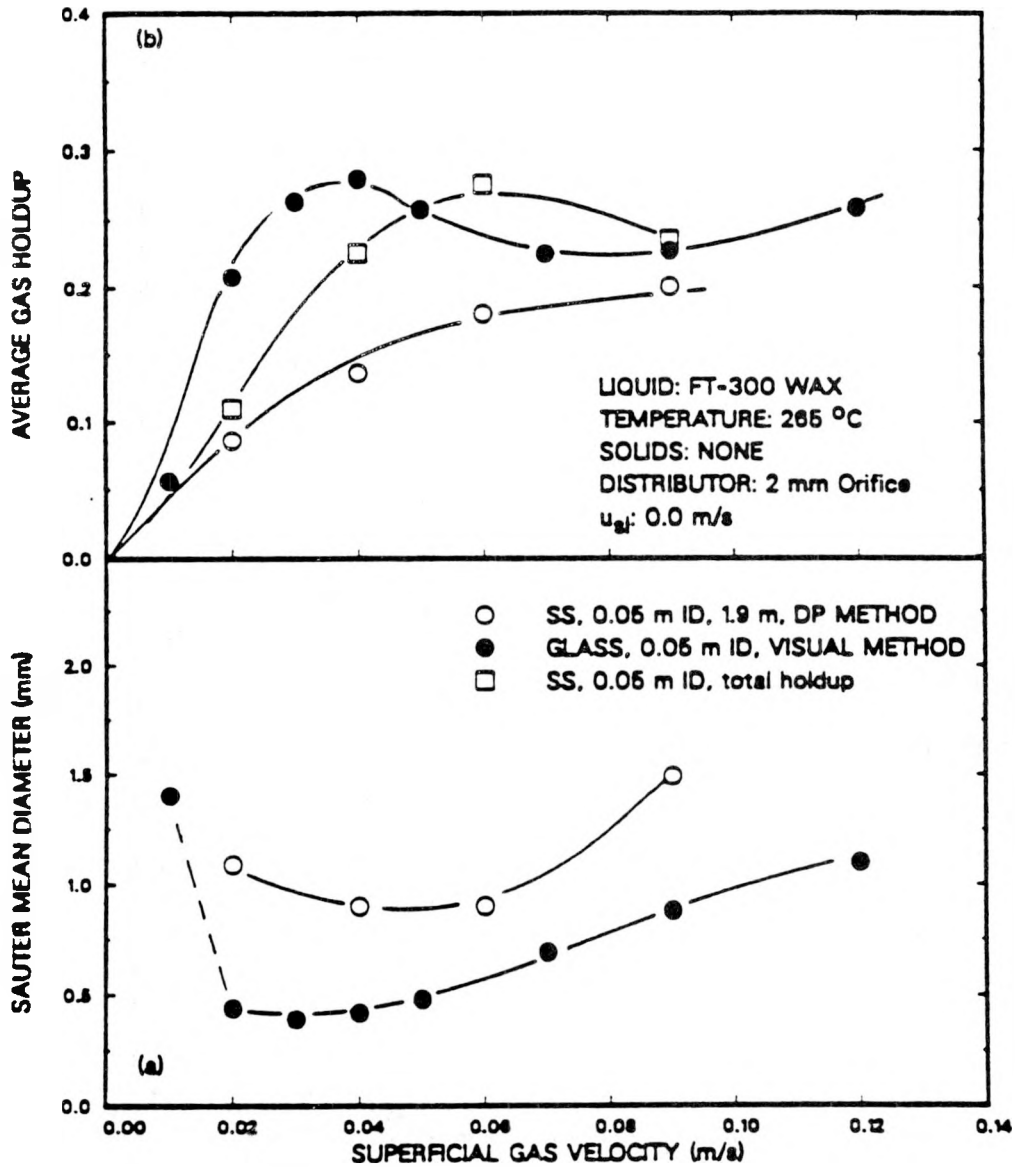

Figure 5.17. Comparison of (a) Sauter mean bubble diameters and (b) gas holdup obtained in the 0.05 m ID stainless steel column (DP method, 1.9 m) and the 0.05 m ID glass column (visual method) with FT-300 wax.

with the DGD technique (i.e. a non–uniform axial gas holdup). For the FT–300 wax system in the small diameter column, the gas holdup remains fairly uniform in the lower region of the column, but increases significantly in the uppermost region of the column for gas velocities between 0.02 and 0.09 m/s. The disengagement rate in the glass column was obtained by recording the drop in dispersion level with time via a VCR/video camera system. Thus, the disengagement profile was based on the entire dispersion. However, in the stainless steel column, the disengagement profile was based only on the dispersion below a given pressure transducer. Hence, the assumption of axial homogeneity is violated for measurements in the glass column, but not for measurements in the stainless steel column. If there is a significant amount of small bubbles located in the uppermost region of the column, which do not disengage continuously (e.g. stable foam), then there will be a bias towards small bubbles which results in a lower Sauter mean bubble diameter. Measurements made with the pressure transducers do not take into account the small bubbles in the uppermost region of the dispersion. However, these bubbles should be included in the overall Sauter mean bubble diameter. Thus, the actual values of d_s are probably within the range of values shown in Figure 5.17.

Figure 5.18 compares Sauter mean bubble diameters and gas holdups obtained from experiments conducted with SASOL wax in the small diameter glass and stainless steel columns. As stated earlier, SASOL wax does not produce foam, and as a result, the axial gas holdups remained fairly uniform. Thus, it is not surprising that Sauter mean bubble diameters and gas holdups measured using different techniques in the two columns (i.e. video/VCR - glass column; pressure transducers - stainless steel column) are in excellent agreement.

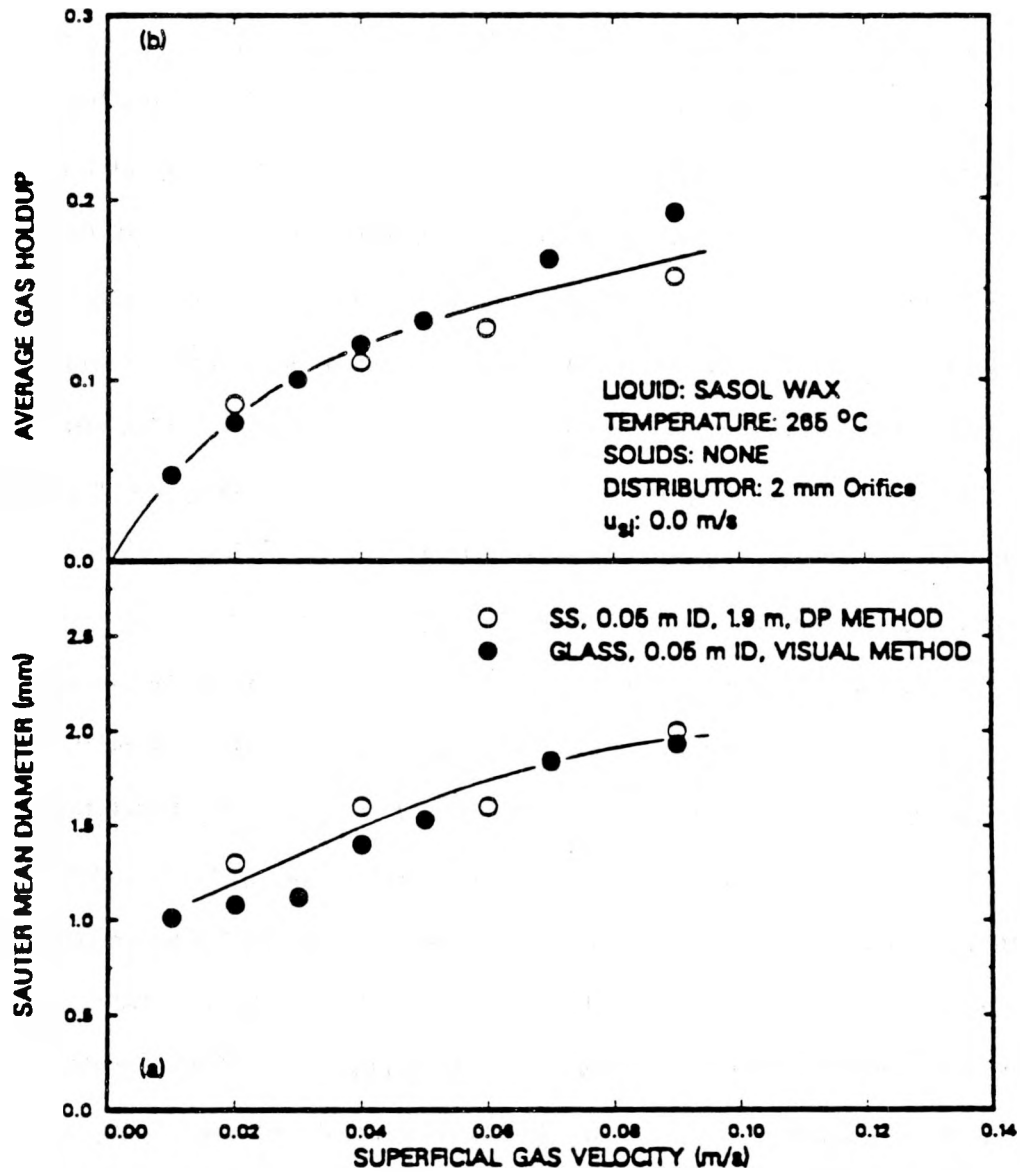

Figure 5.18. Comparison of (a) Sauter mean bubble diameters and (b) gas holdup obtained in the 0.05 m ID stainless steel column (DP method, 1.9 m) and the 0.05 m ID glass column (visual method) with SASOL wax.

VI. FLOW REGIME CHARACTERIZATION

Pressure signals and nuclear density gauge signals were recorded during several experiments in both the 0.05 m ID and 0.21 m ID bubble columns. Statistical analysis of the pressure fluctuations and density gauge fluctuations was used to determine flow regimes and flow regime transitions. Wall pressure measurements were made at heights of 0.08, 0.61, 1.22, 1.83, and 2.44 m above the distributor during experiments conducted in both columns. In the 0.05 m ID bubble column, density gauge measurements were made at a fixed height (1.5 m above the distributor); whereas, in the large diameter column, density gauge measurements were made at heights of 0.9, 1.5, and 1.7 m above the distributor. We developed the necessary software that would allow us to do time series analysis of the signals on the Zenith-248 AT compatible computer in our laboratory. The same computer is also interfaced to the data acquisition system (see Chapters II and III) that was used to record the pressure and density gauge fluctuations.

Theoretical Background

Statistical analysis of pressure fluctuations has been used in the past to determine transitions between flow regimes in both two–phase and three–phase bubble columns and fluidized beds. Various techniques may be used to determine flow regimes and flow regime transitions. The two most commonly used designs involving pressure transducers are: (1) measurement of absolute pressure fluctuations and (2) measurement of differential pressure fluctuations. For analysis of systems which operate in the slug flow regime, differential pressure fluctuations can provide more detailed information, and a more accurate measure of the transition from bubbly to slug flow, slug flow to annular flow, and annular flow to mist flow. Differential pressure measurements have generally been limited to two–phase systems (e.g., Ishigai et al., 1965a,b; Lin and Hanratty, 1987;

Matsui, 1984; Miyazaki, et al. 1973; Akagawa, et al. 1971a, b, c). These measurements may be used to determine instantaneous fluctuations in void fraction. The signals returned from differential transducers have the same characteristics as those obtained from a nuclear density gauge or a probe.

Surface pressure fluctuations may be detected with various types of pressure measurement equipment (e.g., pitot tubes, surface mounted transducers, microphones, transducers connected by an external tube, etc.). One drawback associated with surface mounted and tube mounted transducers is that they respond to fluctuations occurring not only in the boundary layer, but also to fluctuations beyond the boundary layer. The tube mounted transducers also suffer from signal delay governed by the length of the tube and the velocity of sound in the medium (Lee, 1983). With tube mounted transducers, it is usually difficult to obtain data over the entire range of frequencies. In general, data obtained from tube mounted transducers will be limited to low frequency fluctuations in the system. For our purpose, this should be sufficient since we are interested in detecting the onset of slug flow.

As discussed by Glasgow et al. (1984), the passage of a buoyant bubble can produce three distinct response characteristics: (1) sound of approach (observable if rapidly rising bubbles are present), (2) pressure field around the object, and (3) wake or vortex street behind the object. Our pressure transducers will only detect fluctuations caused by changes in the pressure field as a bubble passes the surface of the tube (i.e. low frequency oscillations). Even if our system was sensitive enough to detect fluctuations caused by the wakes of bubbles, it would be very difficult, if not impossible, to distinguish between these fluctuations and those created by the pressure field around the bubble.

Three different statistical techniques are commonly employed to determine flow regimes and flow regime transitions from pressure transducer measurements. The statistical analysis involves the use of the power spectral density function (psd), the mean

square error of the pressure fluctuations (MSE), and the probability density function (pdf). The pdf is used extensively in the analysis of signals obtained from differential transducers, nuclear density gauges, and probes. Flow regimes and flow regime transitions cannot be determined directly from pdf's for data obtained from absolute pressure measurements (e.g. Fan et al., 1981; Matsui, 1984,1986; Akagawa et al., 1971a,b,c).

For data from differential pressure measurements and nuclear density gauge measurements, the pdf has significantly different characteristics for different flow regimes. In bubbly flow the pdf is concentrated near a pressure difference (or count rate) corresponding to low gas hold–up. However, when slugs begin to appear, two peaks (or regions) are observed on the pdf curve, one corresponding to low hold–up and the other corresponding to high hold–up. The low hold–up region corresponds to the liquid slugs and the high hold–up region corresponds to the gas slugs. In annular flow, the low hold–up peak disappears and only the peak corresponding to high gas hold–up is observed (Matsui, 1984).

As mentioned previously, the pdf of an absolute pressure signal cannot be used as a direct measure of flow regime transitions. However, the pdf of an absolute pressure signal will broaden as turbulence increases (Patel, 1985). In other words, the variance of the pressure fluctuations in the column changes with gas and liquid velocities, and this change is reflected by an increase or decrease in the variance of the pdf. Two quantities which have found some use in determining flow regime transitions and changes in turbulence are the mean square error (MSE) and root mean square (RMS) of the pressure fluctuations. The MSE is defined as:

$$MSE = \frac{\left[\sum (P_i - \overline{P})^2 / N\right]^{1/2}}{\overline{P}} \qquad i = 1, \ldots, N \tag{6.1}$$

where N is the total number of data points, P_i is the pressure corresponding to data point i, and $\overline{P}$ is the average pressure defined as:

$$\overline{P} = \frac{\sum P_i}{N} \qquad i = 1, \ldots, N$$

Fan et al. (1984) had reasonable success in using this quantity to determine flow regime transitions in a three–phase fluidized bed. Lee (1983) used the RMS, defined as :

$$RMS = (MSE)(\overline{P}) \tag{6.2}$$

to obtain a qualitative description of turbulence in an air lift bubble column.

Two other statistical quantities which are sometimes used are the autocorrelation function and the power spectral density function (psd). The psd is the Fourier transform of the autocorrelation function. The autocorrelation function is the normalized autocovariance function. The autocovariance function gives an indication of how the dependence between adjacent values in a stochastic process changes with lag (u) and is defined as (Jenkins and Watts, 1968):

$$\gamma_{xx}(u) = E[(x(t) - \mu)(x(t+u) - \mu)] = cov[x(t), x(t+u)] \tag{6.3}$$

where E[y] is the expected value of y, cov is the covariance, μ is the mean of the time series, x is the measured quantity (pressures for our case), and u is the lag between observations. The autocorrelation function is given by:

$$\rho_{xx}(u) = \frac{\gamma_{xx}(u)}{\gamma_{xx}(0)} \tag{6.4}$$

where $\gamma_{xx}(u)$ is the autocovariance function evaluated at lag u and $\gamma_{xx}(0)$ is the autocovariance function evaluated at lag 0, or more simply, the variance of the time series. Thus, the RMS is the square root of the autocovariance function evaluated at lag 0, and the MSE is the square root of the autocovariance function evaluated at lag 0 divided

by the mean of the time series (or, for our case, the mean of the pressure fluctuations or density gauge fluctuations).

Fourier transforms are used to approximate the time series. A series of periodic functions may be used to approximate a non–periodic signal. One such series is the Fourier series, in which the periodic functions are sines and cosines. Thus, the Fourier series may be used to approximate the actual pressure signal. In essence, we are fitting the raw signal to a Fourier series. From this type of a fit, we gain information on the periodicity of the signal. Fourier series have the important property that an approximation consisting of a given number of terms achieves the minimum mean square error between the signal and approximation, and also, since they are orthogonal, the coefficients may be determined independently of one another. The sample spectrum is the Fourier transform of the sample autocovariance function. It shows how the average power or variance of the signal is distributed over frequency. Fourier analysis breaks down when applied to time series because it is based on the assumption of fixed amplitudes, frequencies, and phases. Thus, the sample spectrum of a time series can be quite erratic in nature. However, if we treat the sample spectrum as a random variable, and examine its moments, we will be able to explain the erratic behavior. The power spectrum is defined as the first moment, or mean, of the sample spectrum. The power spectral density function is a normalized version of the power spectrum. The psd is the Fourier transform of the autocorrelation function and is defined by (Jenkins and Watts, 1968):

$$P(f) = \int_{-\infty}^{\infty} \rho_{xx}(u)\exp(-j2\pi fu)du \qquad (6.5)$$

Thus, all three quantities (i.e., RMS or MSE, autocorrelation and psd) are related. For our data, we will only use the MSE and psd to show qualitatively, the transitions between flow regimes for various experimental data.

Taitel et al. (1981) presented various correlations for the prediction of flow regime transitions in two–phase gas–liquid flow. By treating our three–phase system as a two–phase system (i.e., using slurry properties in place of liquid properties), we can use Taitel et al.'s correlations to obtain approximate values for the transitions between bubbly and slug flow in the 0.05 m ID bubble column. According to Taitel et al., for our system and range of operating conditions in the 0.05 m ID bubble column, there are two possible flow regimes which can exist, bubbly and slug flow. Taitel et al. also present a correlation for describing the entrance region in which mixing (i.e. churn flow) will exist due to the incoming gas (i.e., in the lower section of the column there will be churn flow, but towards the top of the column slug flow will exist).

According to Taitel et al., bubbly flow will not exist if the following correlation is satisfied:

$$\left[\frac{\rho_{s\ell}^2 g D_{col}^2}{(\rho_{s\ell}-\rho_g)\sigma}\right]^{1/4} \leq 4.36 \qquad (6.6)$$

where $\rho_{s\ell}$ is the density of the slurry, D_{col} is the column diameter, ρ_g is the density of the gas, and σ is the surface tension of the liquid. Note that in their original correlation they used the density of the liquid and not the density of the slurry. For the small diameter bubble column, the quantity on the left hand side of Eq. 6.6 ranges from approximately 5.2 to 5.5. Thus, for our system, according to Taitel et al., it is possible to observe the bubbly regime.

Assuming that the transition to slug flow occurs when the gas hold–up is approximately 25 %, Taitel et al. propose that the following correlation can be used to determine the transition to slug flow:

$$U_{s\ell} = 3.0U_g - 1.15\left[\frac{g(\rho_{s\ell}-\rho_g)\sigma}{\rho_{s\ell}^2}\right]^{1/4} \qquad (6.7).$$

where $U_{s\ell}$ is the superficial slurry velocity and U_g is the superficial gas velocity at which the transition takes place. For the various systems and operating conditions used in

this study, the transition from the bubbly to slug flow regime should occur between gas velocities of 0.048 and 0.056 m/s.

Taitel et al. also present a correlation for predicting the entry region over which churn flow will exist. In this region, it is assumed that short Taylor bubbles are created. Two of these coalesce to form a "large" Taylor bubble (or slug). The entry region is the region in which this coalescence takes place and is defined by:

$$\frac{l_e}{D_{col}} = 40.6\left[\frac{U_m}{\sqrt{gD_{col}}} + 0.22\right] \tag{6.8}$$

For our system, the entry length, l_e ranges from approximately 0.7 m at a gas velocity of 0.06 m/s to 1.0 m at a gas velocity of 0.12 m/s. Thus, if Taitel et al.'s correlations (i.e., Eqs. 6.7 and 6.8) hold true for our system, we should observe a transition to slug flow between gas velocities of 0.04 and 0.06 m/s for all experiments, and furthermore, we should not observe slugs in the lower (0.7 to 1.0 m) section of the bubble column.

The range of gas velocities at which the transition from bubbly to slug flow occurs based on the correlations presented by Taitel et al., agrees with the range of velocities predicted by Deckwer et al., 1980 (see Figure 2.12). Based on the flow regime map presented by Deckwer et al., the transition from the bubbly to churn–turbulent flow regime in the 0.21 m ID bubble column occurs between gas velocities of 0.04 and 0.07 m/s.

Discussion Of Results

Wall pressure fluctuations and nuclear density gauge fluctuation measurements were made in both the small diameter and large diameter stainless steel bubble columns. Raw output (i.e. voltages) from the density gauges and pressure transducers were recorded on the Zenith AT personal computer. The data were then analyzed to obtain the MSE, pdf, and psd. The spectral density functions, psd, were obtained using the IMSL routine PFFT.

Figures 6.1a and 6.1b show typical raw signals from the nuclear density gauge obtained during experiments in the 0.05 m ID bubble column at gas velocities of 0.02 and 0.06 m/s, respectively. The large peaks in each figure correspond to the passage of large bubbles across the beam path of the density gauge. The regularity of the large peaks is significantly different at the two gas velocities. At 0.02 m/s, the large peaks appear randomly and also are less frequent; however, at a gas velocity of 0.06 m/s, they appear at an increased regularity, and also have a relatively higher intensity (amplitude) than those at 0.02 m/s. This regularity indicates the presence of slugs in the dispersion at a gas velocity of 0.06 m/s. At the lower gas velocity (0.02 m/s), the bubbles are smaller and are randomly dispersed in the flow field. Additionally, the lower amplitude of the oscillations at this gas velocity is indicative of the larger liquid fraction at 0.02 m/s relative to that at 0.06 m/s. Figure 6.2 shows typical density gauge fluctuations during experiments in the 0.21 m ID column. The large peaks in Figures 6.2a and 6.2b correspond to the passage of large bubbles through the beam of radiation at gas velocities of 0.02 and 0.12 m/s, respectively. The fluctuations at a gas velocity of 0.02 m/s in the 0.21 m ID column appear similar to those in the 0.05 m ID column at the same velocity. However, at a gas velocity of 0.12 m/s in the 0.21 m ID column, peaks appear randomly; whereas, in the 0.05 m ID column the peaks occur regularly during slug flow (see Figure 6.1b). This non–regularity in peaks at a relatively high gas velocity indicates the presence of the churn–turbulent flow regime. At a gas velocity of 0.12 m/s, the amplitude of the peaks is higher than at a gas velocity of 0.02 m/s, thus indicating the presence of either larger bubbles or swarms of bubbles at this velocity.

Figures 6.3 and 6.4 show typical probability density functions of the pressure signals in the 0.05 and 0.21 m ID column, respectively. Figures 6.3a and 6.4a correspond to the homogeneous bubbly regime. The homogeneous bubbly regime is characterized by a narrow density distribution function. As the gas flow is increased, the pressure variation

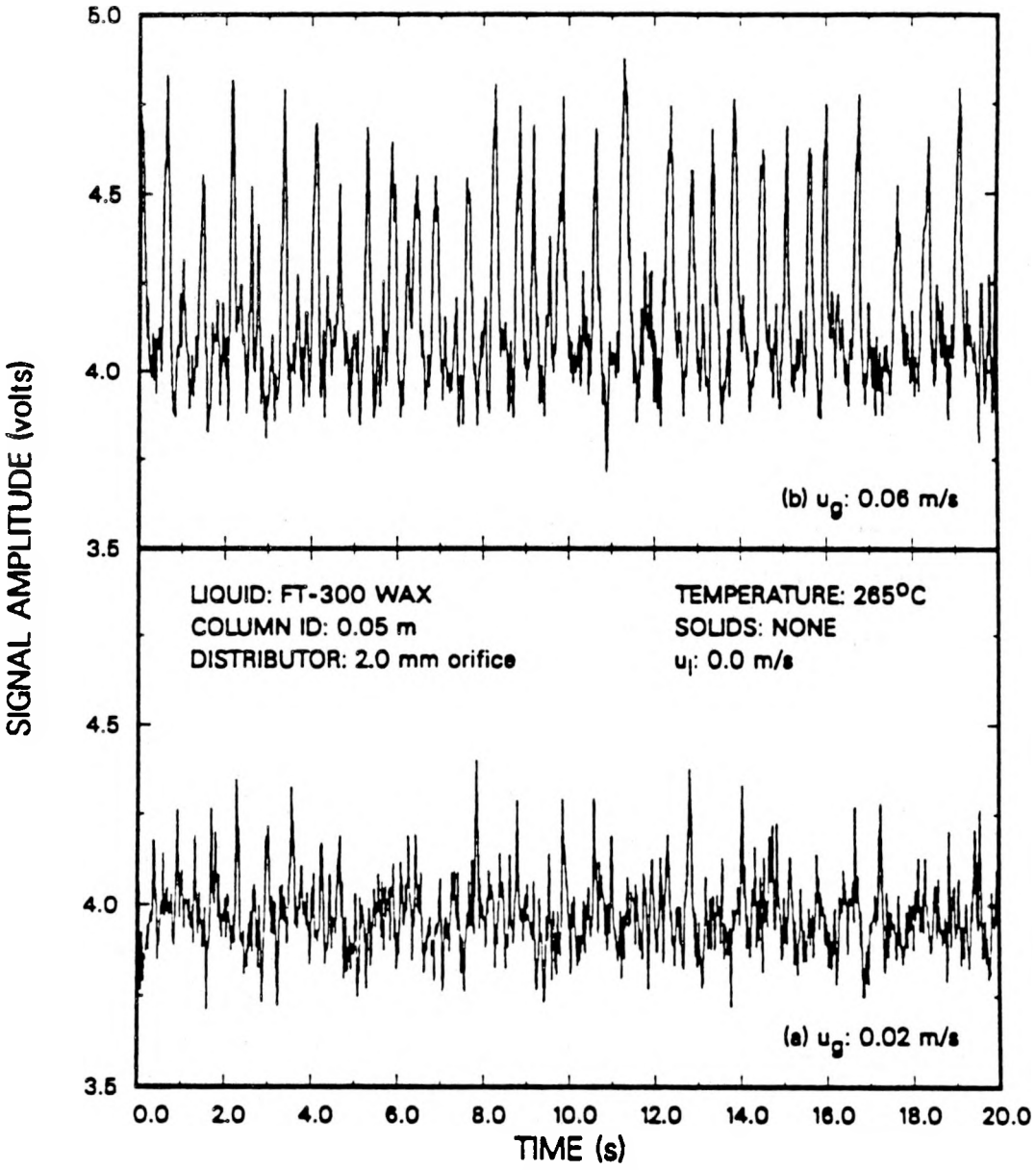

Figure 6.1. Typical raw signals from the nuclear density gauge apparatus during experiments in the 0.05 m ID bubble column.

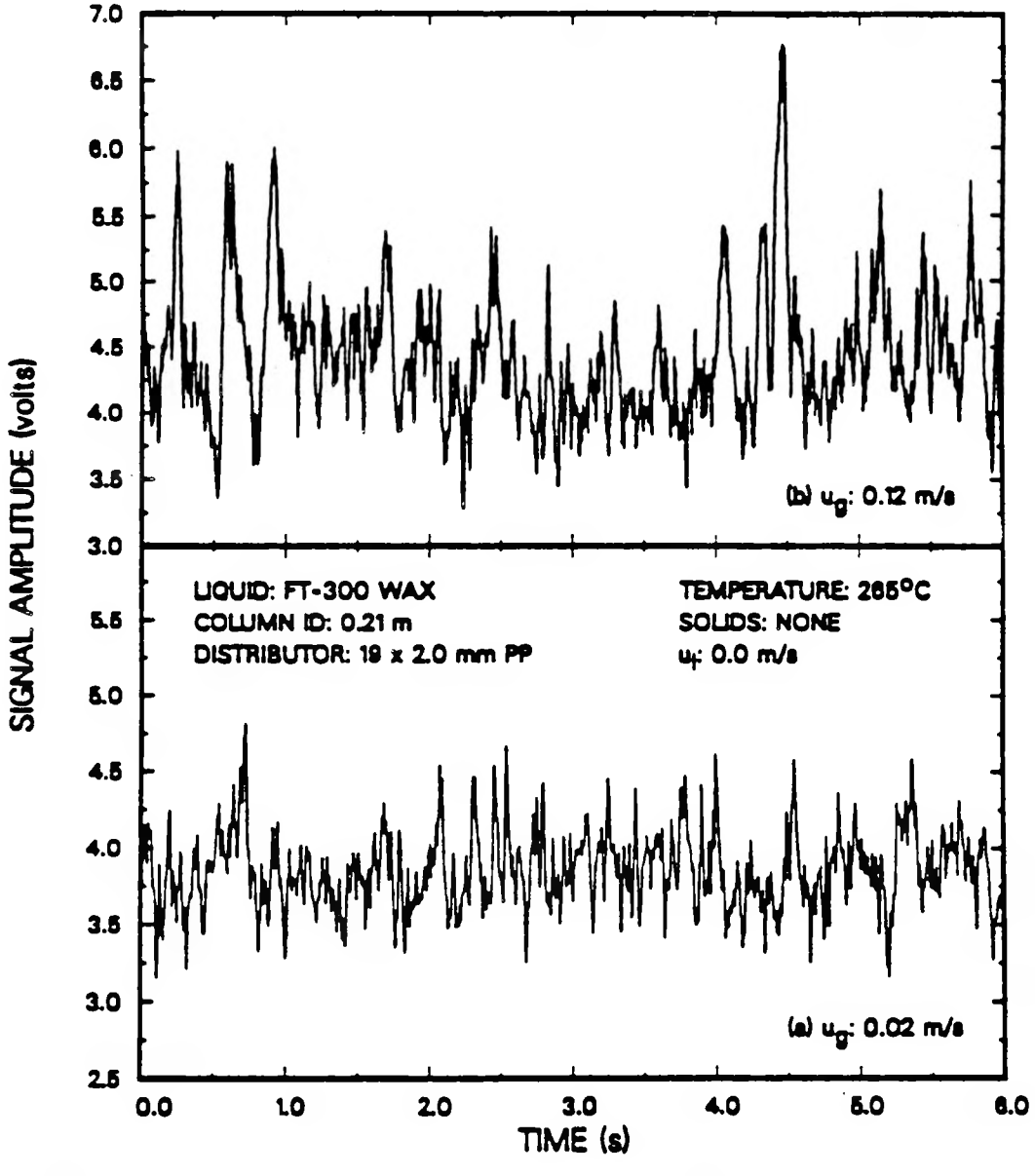

Figure 6.2. Typical raw signals from the nuclear density gauge apparatus during experiments in the 0.21 m ID bubble column.

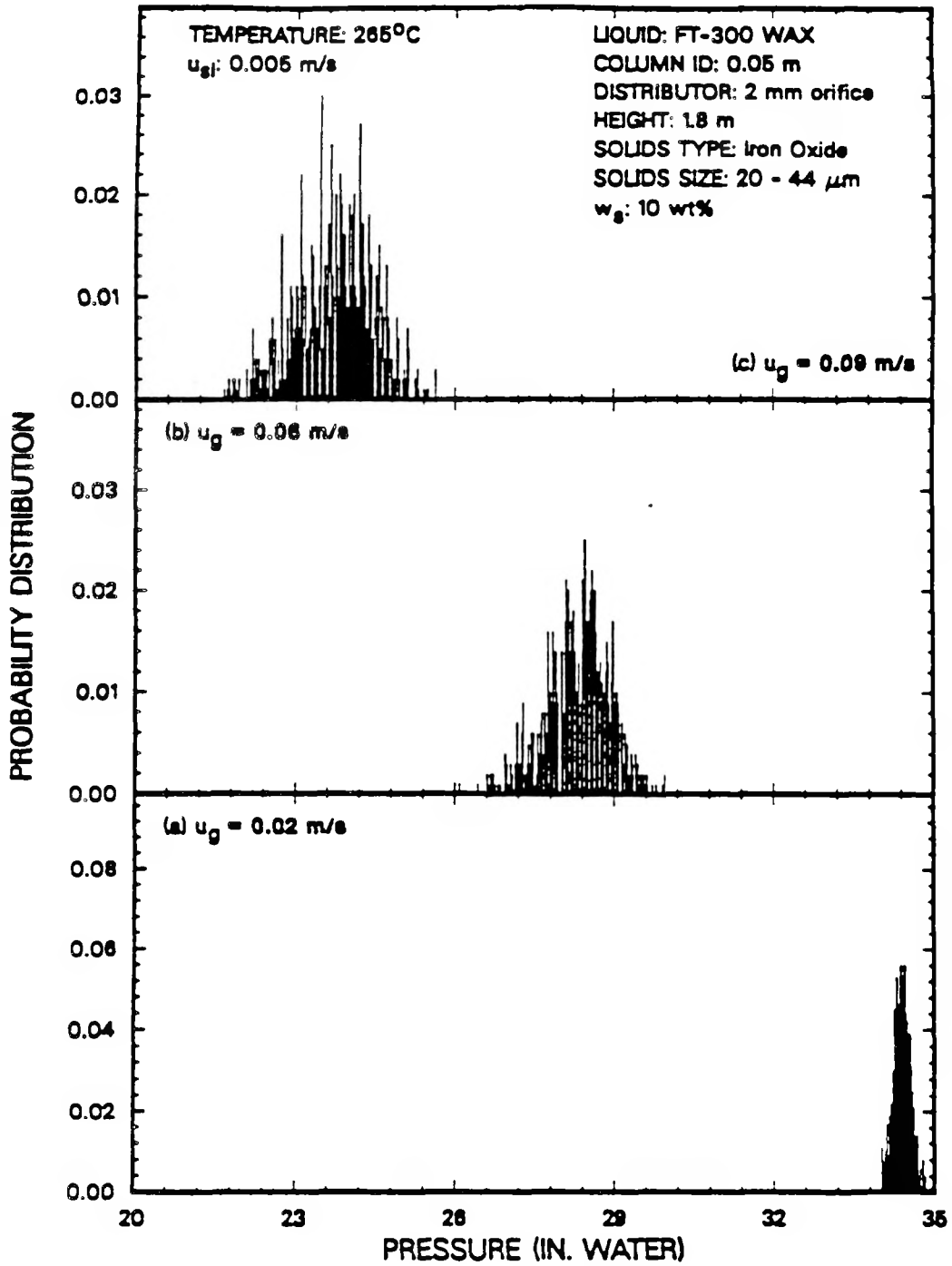

Figure 6.3. Effect of superficial gas velocity on the probability density function from the pressure transducer in the 0.05 m ID bubble column at a height of 1.8 m above the distributor.

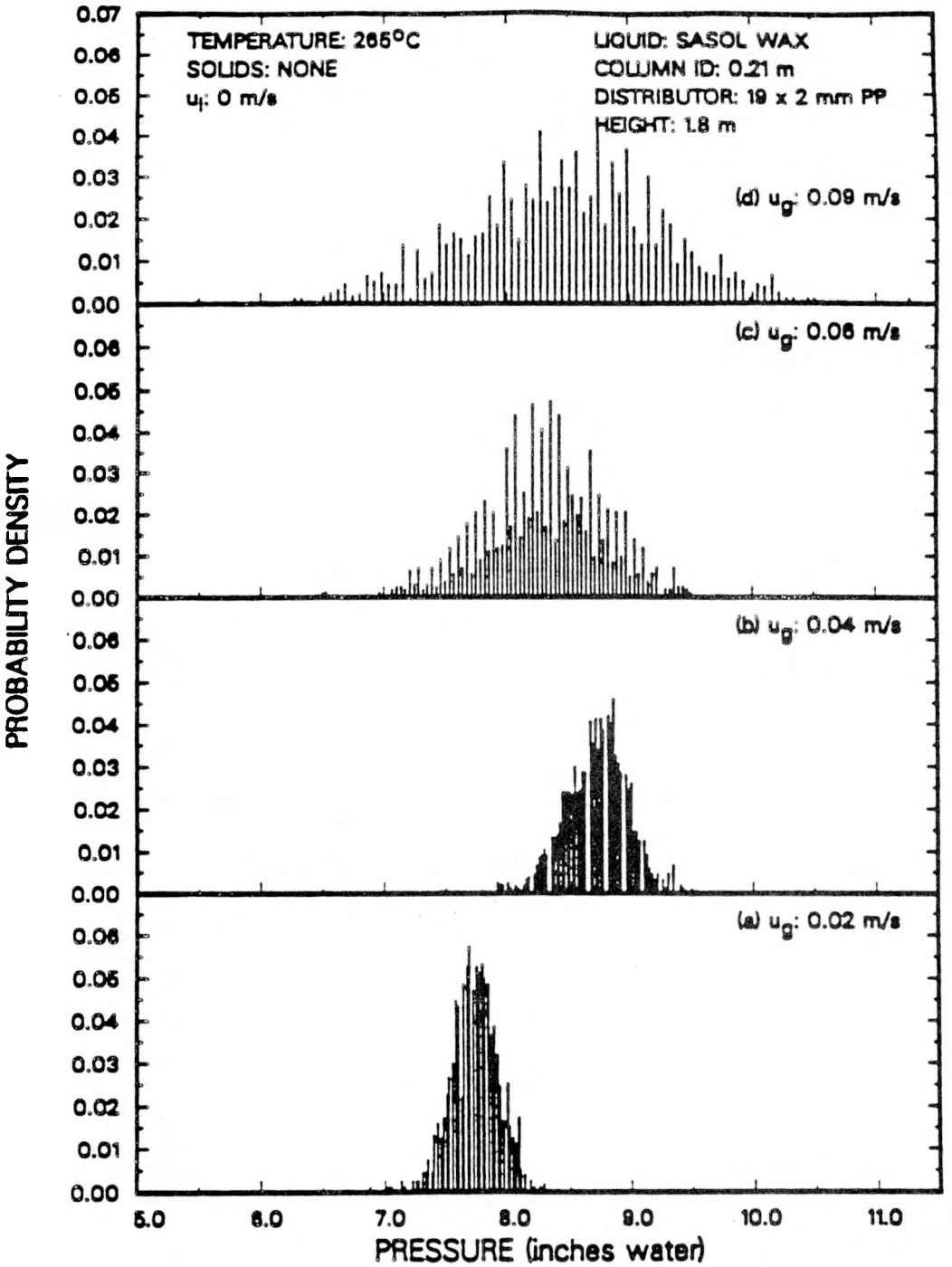

Figure 6.4. Effect of superficial gas velocity on the probability density function from the pressure transducer in the 0.21 m ID bubble column at a height of 1.8 m above the distributor.

increases. As the gas flow is increased to 0.04 m/s, the variation in pressure begins to increase in the 0.21 m ID column (see Figure 6.4b). This slight increase may correspond to the transition regime between bubbly and churn–turbulent flow. At gas velocities of 0.06 and 0.09 m/s in both columns, the variation in pressure increases significantly, indicating the presence of slug flow in the small diameter column and churn–turbulent flow in the large diameter column.

Typical probability density functions from the nuclear density gauges, associated with experiments in the small diameter and large diameter bubble columns, are shown in Figures 6.5 and 6.6, respectively. As mentioned previously, nuclear density gauge fluctuations correspond to fluctuations in gas holdup. The distribution at a gas velocity of 0.02 m/s in both columns has the shape of a normal distribution and can be associated with the homogeneous bubbly regime. As the gas velocity is increased in the small diameter column, the Gaussian distribution becomes skewed to the right (e.g. u_g=0.04 m/s). At a gas velocity of 0.06 m/s, the formation of a second peak is evident at the right hand end of the distribution, and this is exemplified at 0.09 m/s (see Figures 6.5c and 6.5d). An increase in peak intensity corresponds to an increase in the volume fraction of gas. Thus, the second peak at gas velocities of 0.06 and 0.09 m/s corresponds to the presence of slugs. In the large diameter column at gas velocities of 0.08 and 0.12 (see Figures 6.6b and 6.6c, respectively), the distribution becomes skewed to the right also. However, the second peak is not formed. This is expected, since in the churn–turbulent flow regime, the passage of large bubbles is not as regular as it is in the slug flow regime.

Flow Regime Transitions Based on the MSE

MSE were calculated from the raw pressure signal data for all runs conducted in the 0.05 m ID column. In general, the MSE increased with increasing gas velocity and with increasing height above the distributor, but decreased with increasing liquid velocity.

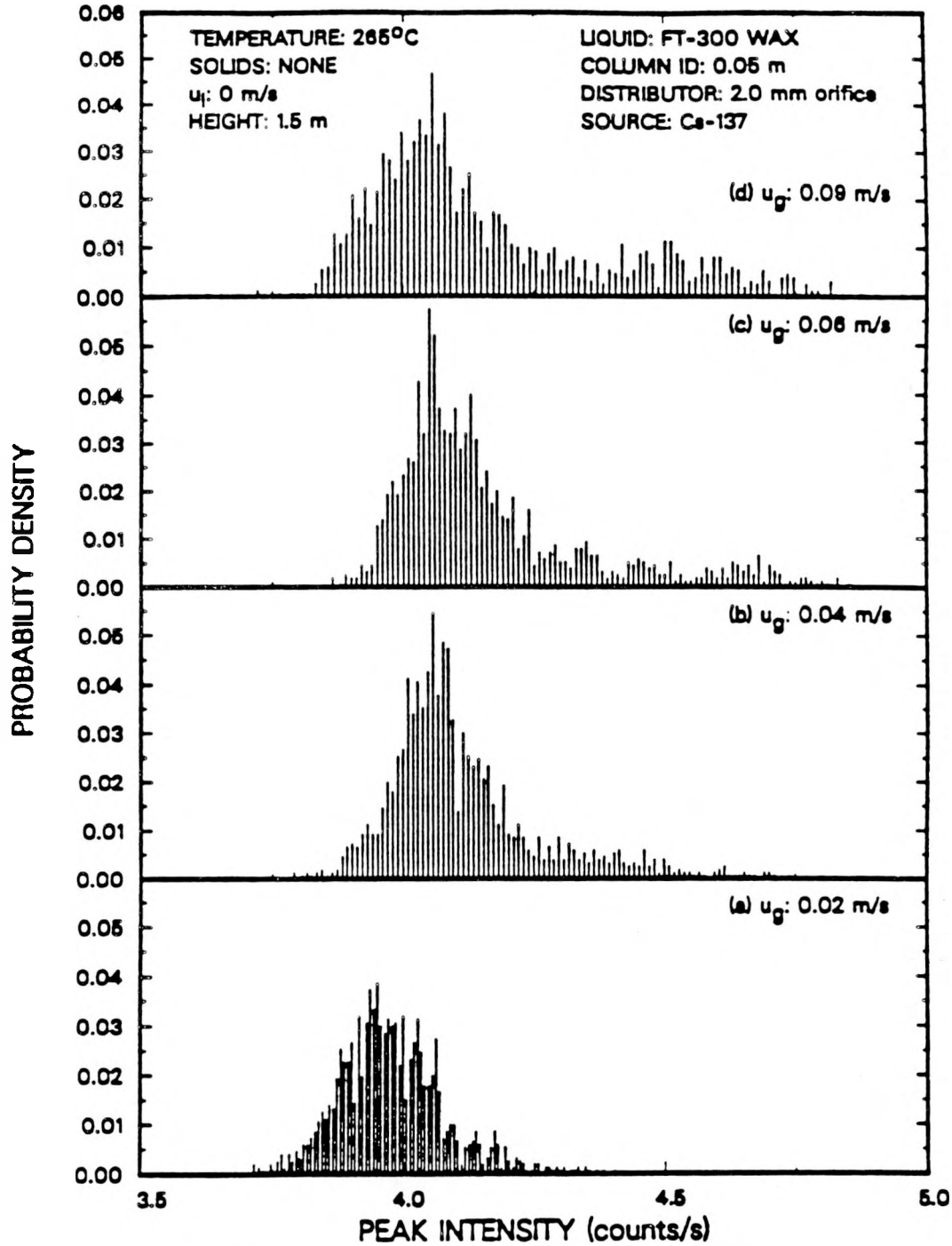

Figure 6.5. Effect of superficial gas velocity on the probability density function from the nuclear density gauge using the Cesium-137 source in the 0.05 m ID bubble column at a height of 1.5 m above the distributor.

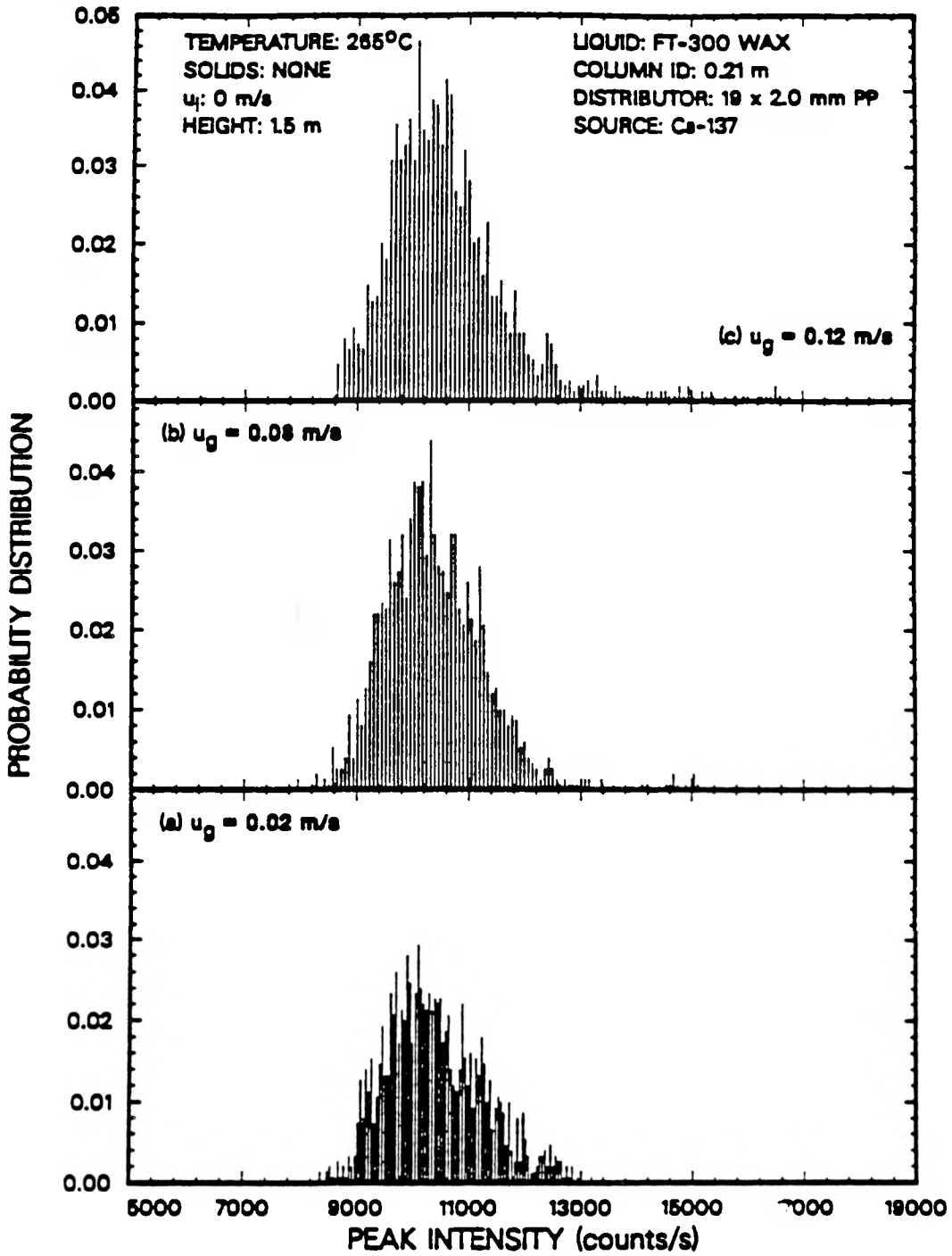

Figure 6.6. Effect of superficial gas velocity on the probability density function from the nuclear density gauge using the Cesium-137 source in the 0.21 m ID bubble column at a height of 1.5 m above the distributor.

Figure 6.7 shows the MSE obtained at a height of 1.2 m for experiments conducted with 0 – 5 μm silica particles at slurry velocities of 0, 0.005, and 0.02 m/s. At low gas velocities (i.e., $u_g \leq 0.06$ m/s, the MSE of the pressure fluctuations is essentially the same for all three experiments. However, at gas velocities of 0.09 and 0.12 m/s the MSE of the pressure fluctuations are significantly different for the various experiments. The MSE for the experiment conducted in the batch mode of operation is significantly higher than those for the other two runs, which were conducted in the continuous mode of operation. This increase in MSE for the batch experiment may be attributed to an increase in turbulence at the top of the dispersion due to fluctuations caused by slugs exiting the slurry. The MSE for the experiment conducted using a superficial slurry velocity of 0.005 m/s was higher than that for the experiment conducted using a superficial slurry velocity of 0.02 m/s. Increasing the liquid velocity causes a decrease in pressure fluctuations. This decrease in the variance of pressure fluctuations with increasing slurry flow rate may be attributed to two factors: (1) the relative velocity between the gas and slurry decreases with increasing slurry velocity and (2) the static height of the slurry above a given pressure port does not fluctuate as much during a continuous run as it does during a batch run. In Figure 6.7 there is a distinct change in the slope of the curves between gas velocities of 0.02 to 0.04 m/s and 0.06 to 0.12 m/s (i.e. the slopes of curves between gas velocities of 0.06 and 0.12 m/s are greater than the slopes of the curves between gas velocities of 0.02 and 0.04 m/s).. This change in slope may be attributed to a change in the flow regime from bubbly to slug flow. It appears that the transition occurs somewhere between gas velocities of 0.04 and 0.06 m/s for all three experiments. Similar trends were observed in all other experiments conducted. This result agrees with the transition velocities predicted from Taitel et al.'s correlation (i.e., Eq. 6.7).

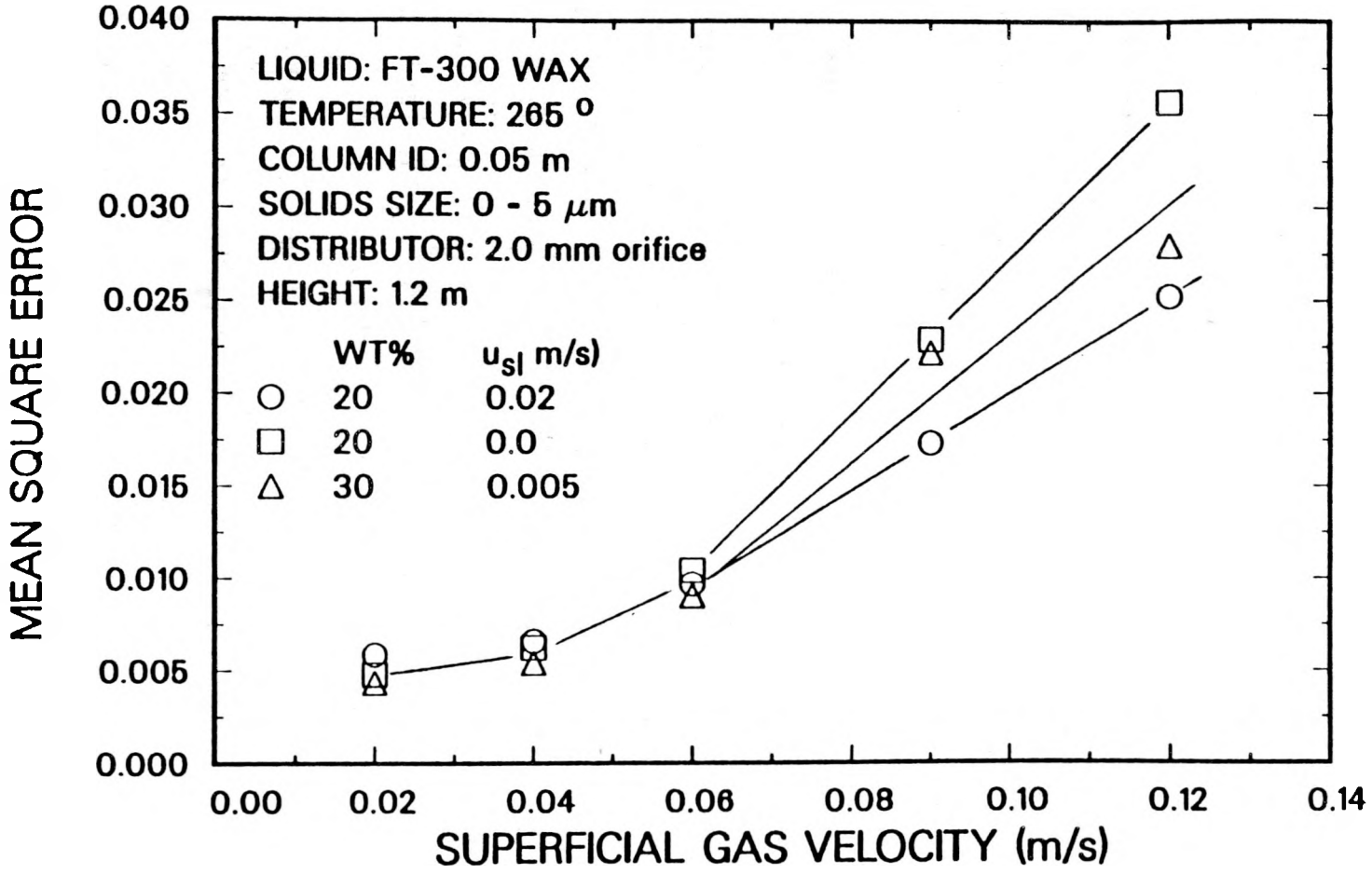

Figure 6.7. Effect of slurry flow rate on the mean square error of pressure fluctuations at the wall (FT-300 wax, 265 °C, 0 - 5 μm silica, 0.05 m ID column, 1.2 m above the distributor).

Figure 6.8 shows the effect of height above the distributor on the MSE at various gas velocities for the batch experiment shown in Figure 6.7. In general, the MSE increases with increasing u_g for all pressure transducers. One interesting trend was the decrease in the MSE between heights of 0.08 and 0.6 m above the distributor. We cannot be certain of the cause for the decrease in MSE at gas velocities of 0.09 and 0.12 m/s. One possible explanation is that the increase in oscillations at a height of 0.08 m is due to the increase in turbulence near the distributor caused by the increase in the gas velocity. The sharp changes in the slope of the MSE curve between heights of 0.6 and 1.2 m at gas velocities of 0.06, 0.09, and 0.12 m/s indicates that slugs begin appearing in the column somewhere between these heights. At gas velocities of 0.02 and 0.04 m/s, there is a slight change in the slope of the MSE curve between heights of 1.2 and 1.8 m, indicating the presence of large bubbles. This result agrees with the prediction of Eq. 6.8, i.e., slugs will not develop in the bottom part of the column.

Figure 6.9 show the effect of superficial gas velocity on the MSE of the pressure fluctuations for the same experiment. At heights of 0.08 and 0.6 m, we do not observe a transition to slug flow; however, the change in slope of the MSE curve for at a height of 1.2 m between gas velocities of 0.04 and 0.06 m/s indicates a transition to slug flow between these velocities. On the other hand, the slope of the MSE curve at a height of 1.8 m above the distributor does not change significantly, indicating that large bubbles are present at all velocities at this height.

Results obtained from experiments with large iron oxide particles showed similar trends in the MSE with gas velocity and height above the distributor. In general, for all experiments in which pressure fluctuations were obtained, the transition between bubbly and slug flow occurred somewhere between gas velocities of 0.04 and 0.06 m/s. Also, slugs were not observed below a height of 0.6 m above the distributor.

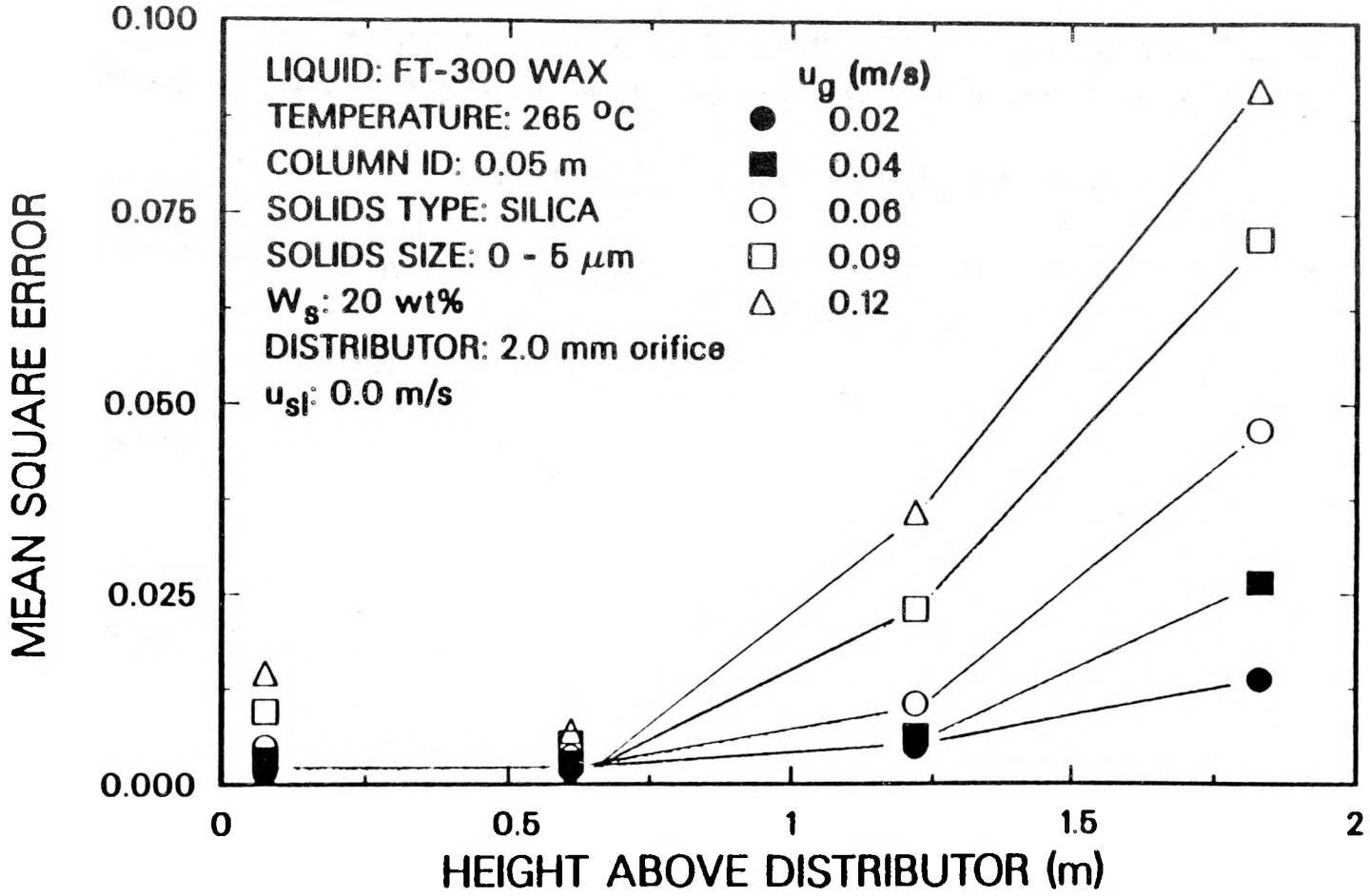

Figure 6.8. Effect of height above the distributor on the mean square error of pressure fluctuations at the wall (FT-300 wax, 265 °C, 20 wt% 0 - 5 μm silica, 0.05 m ID column, u_{sl} = 0.0 m/s).

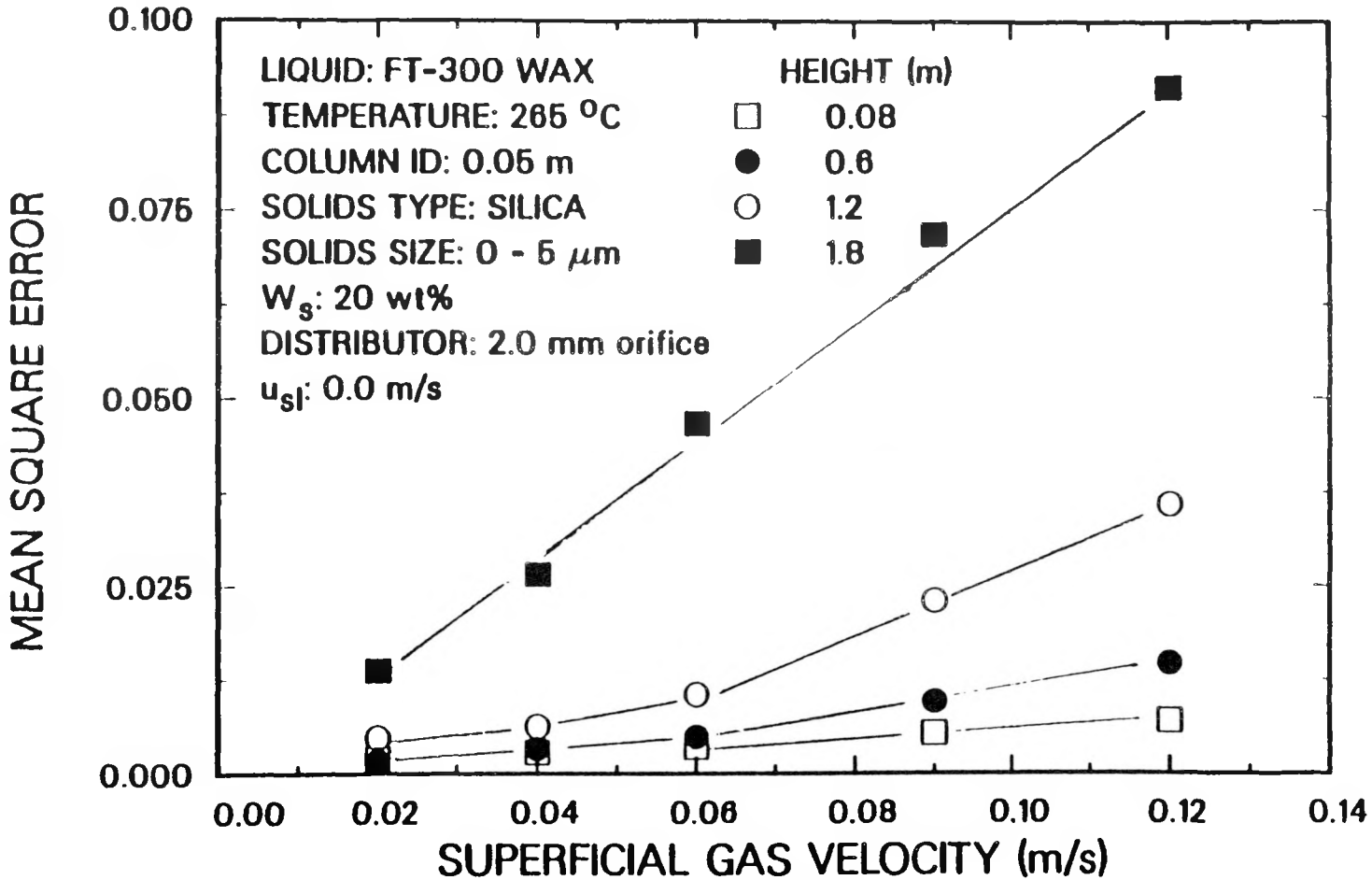

Figure 6.9. Effect of superficial gas velocity on the mean square error of pressure fluctuations at the wall (FT-300 wax, 265 °C, 20 wt% 0 - 5 μm silica, 0.05 m ID column, u_{sl} = 0.0 m/s).

MSE were calculated from both nuclear density gauge signals and raw pressure signals in the 0.21 m ID column for several experiments. In general, the MSE increased with increasing gas velocity but decreased slightly with increasing height above the distributor. Figure 6.10 shows the effect of superficial gas velocity on MSE for nuclear density gauge fluctuations at liquid velocities of 0.005 and 0.02 m/s using the perforated plate distributor and 0.005 m/s using the bubble cap distributor with SASOL reactor wax. An increase in the MSE of nuclear density fluctuations indicates an increase in the variation of gas holdup. For the experiments with the perforated plate distributor there is essentially no effect of liquid flow rate on MSE. However, the MSE of the density gauge fluctuations from the experiment conducted with the bubble cap distributor were significantly lower than those obtained during the experiments with the perforated plate distributor at gas velocities of 0.06 and 0.09 m/s. The lower MSE associated with the bubble cap distributor indicate the presence of a more uniform distribution (i.e. fewer larger bubbles). These results help substantiate the claim that smaller bubbles are formed with the bubble cap distributor due to its geometry. MSE from all experiments were essentially the same at gas velocities of 0.02 and 0.04 m/s. There is a change in the slope of the curves between gas velocities of 0.04 and 0.06 m/s for the experiments conducted with the perforated plate distributor and between gas velocities of 0.06 and 0.09 m/s for the experiment conducted with the bubble cap distributor. The change in slope indicates the transition from the homogeneous bubbly regime to the churn–turbulent flow regime. Similar trends were observed in other experiments. The transition velocities from the bubbly to churn–turbulent flow regime are within the range of velocities given by Deckwer et al. (1980).

Figure 6.11 shows the effect of axial position on the MSE of the pressure fluctuations for the batch experiment conducted with SASOL wax in the 0.21 m ID column. At gas velocities of 0.02 and 0.04 m/s, the MSE of the pressure fluctuations was essentially

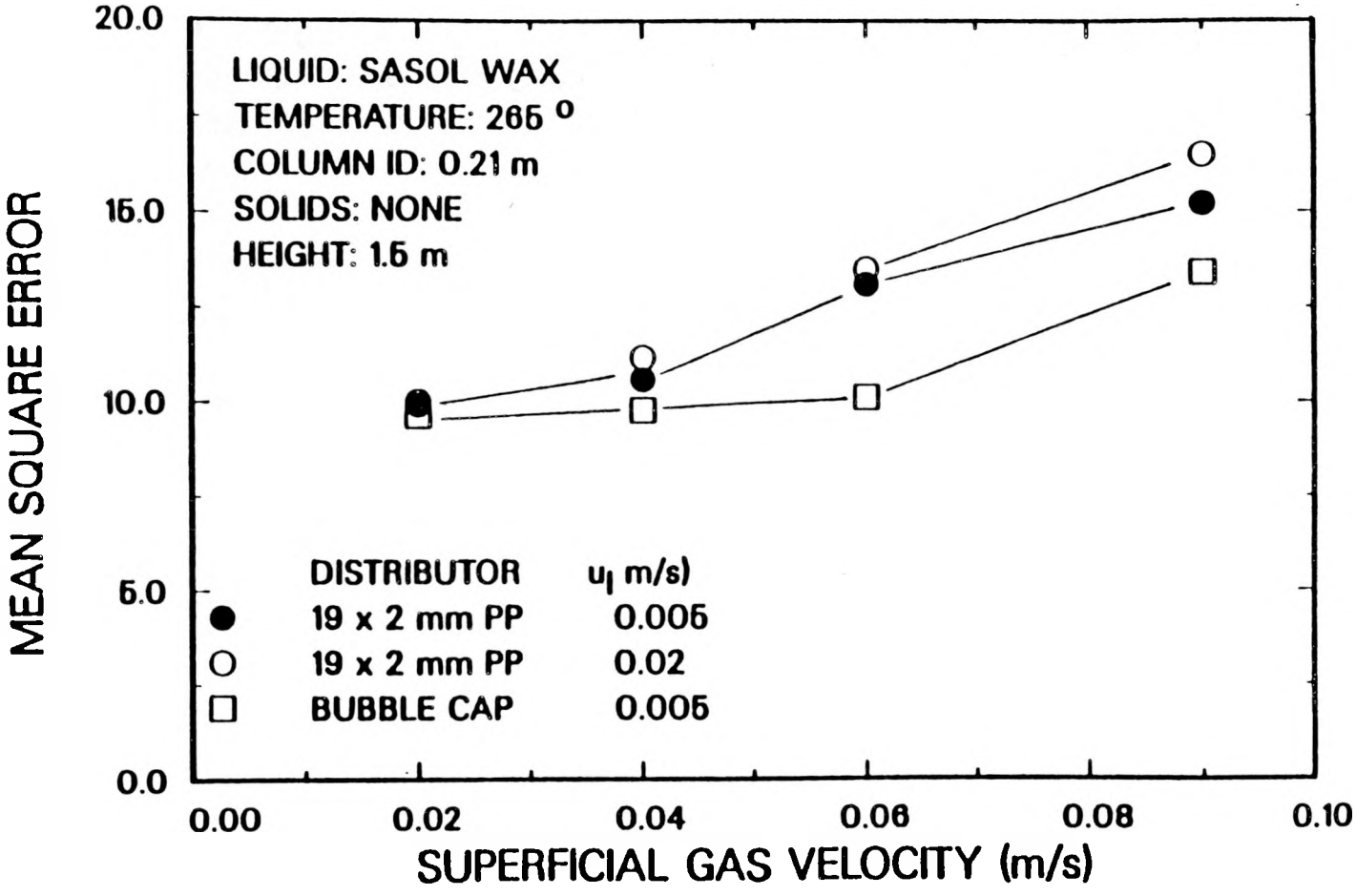

Figure 6.10. Effect of slurry flow rate and distributor on the mean square error of nuclear density gauge fluctuations (SASOL wax, 265 °C, 0.21 m ID column, Cesium-137 source, 1.5 m above the distributor).

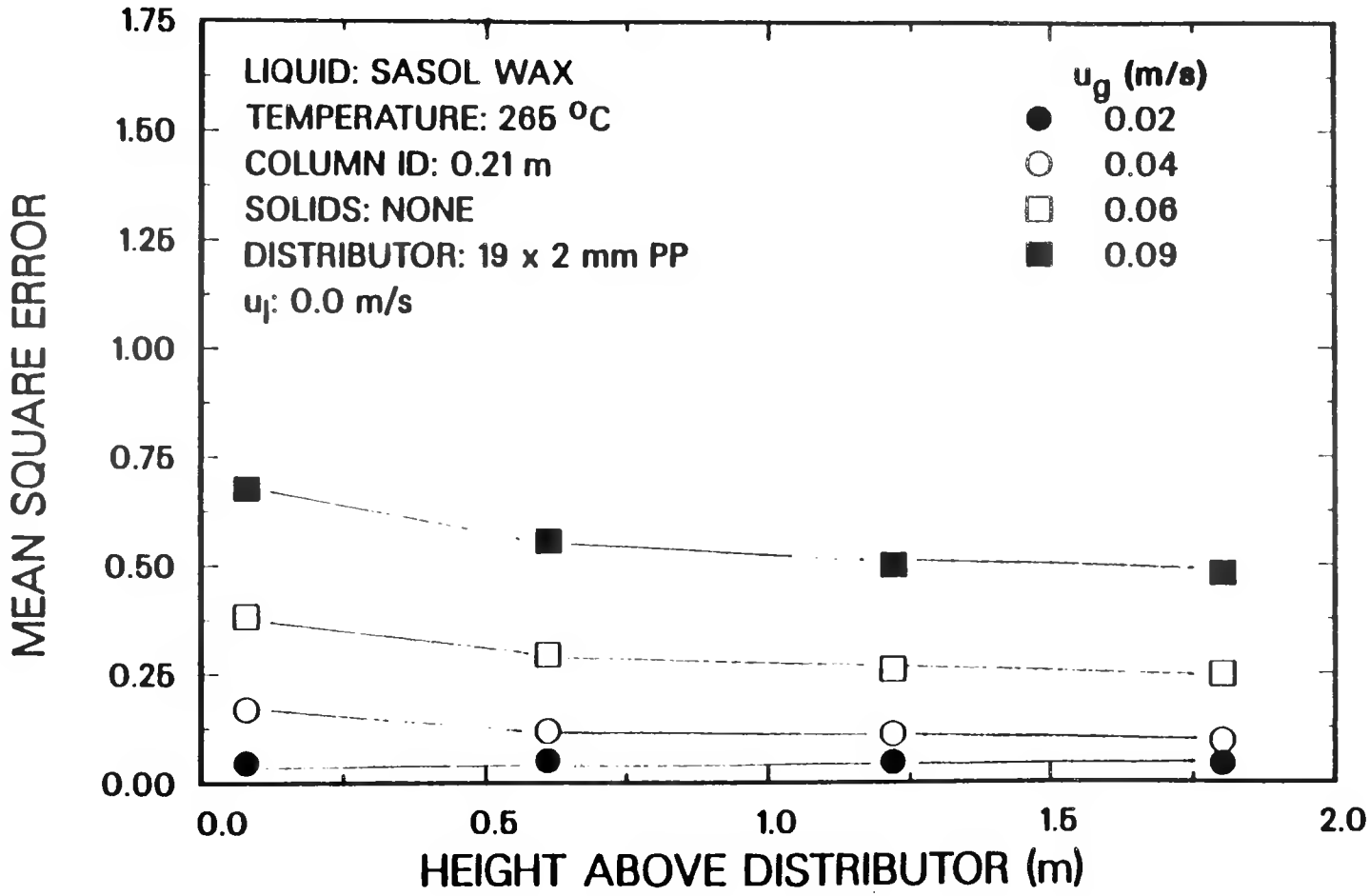

Figure 6.11. Effect of height above the distributor on the mean square error of pressure fluctuations at the wall (SASOL wax, 265 °C, 0.21 m ID column, u_l = 0.0 m/s).

the same at all heights, indicating the presence of the homogeneous bubbly regime. At gas velocities of 0.06 and 0.09 m/s, we observed a slight decrease in the MSE of the pressure fluctuations between heights of 0.08 and 0.6 m above the distributor. A similar trend was observed in the small diameter column (see Figure 6.8). However, in the small diameter column, the MSE increased significantly between heights of 0.6 and 1.2 m above the distributor, but in the large diameter column, it remained essentially constant. The lack of variation in the MSE with column height indicates that there is a minimal amount of axial variation in the flow patterns. We also observed uniform axial gas holdup profiles and bubble size distributions in the large diameter column, which agrees with these results. This type of behavior is representative of the churn–turbulent flow regime.

The effect of superficial gas velocity on the MSE of pressure fluctuations is shown in Figure 6.12 for the batch experiment with SASOL wax in the 0.21 m ID column. As expected, there is an increase in the MSE with increasing gas velocity. The change in slope between gas velocities of 0.04 and 0.06 m/s may be attributed to the transition from the bubbly to the churn–turbulent flow regime. These results are in agreement with those obtained from MSE analysis of nuclear density fluctuations.

Flow Regime Transitions Based on the PSD

Pressure signals and nuclear density gauge signals required high pass filtering. Slow changes in the mean of the signal, unrelated to higher frequency hydrodynamic phenomena, gave rise to a heavy low frequency bias in the psd and autocorrelation functions (Weimer et al., 1985) . To avoid this, the first difference of the time series corresponding to the fluctuations was used before spectra were obtained. The first difference is defined as (Jenkins and Watts, 1968):

$$P'_t = P_{t+\Delta t} - P_t \qquad (6.9)$$

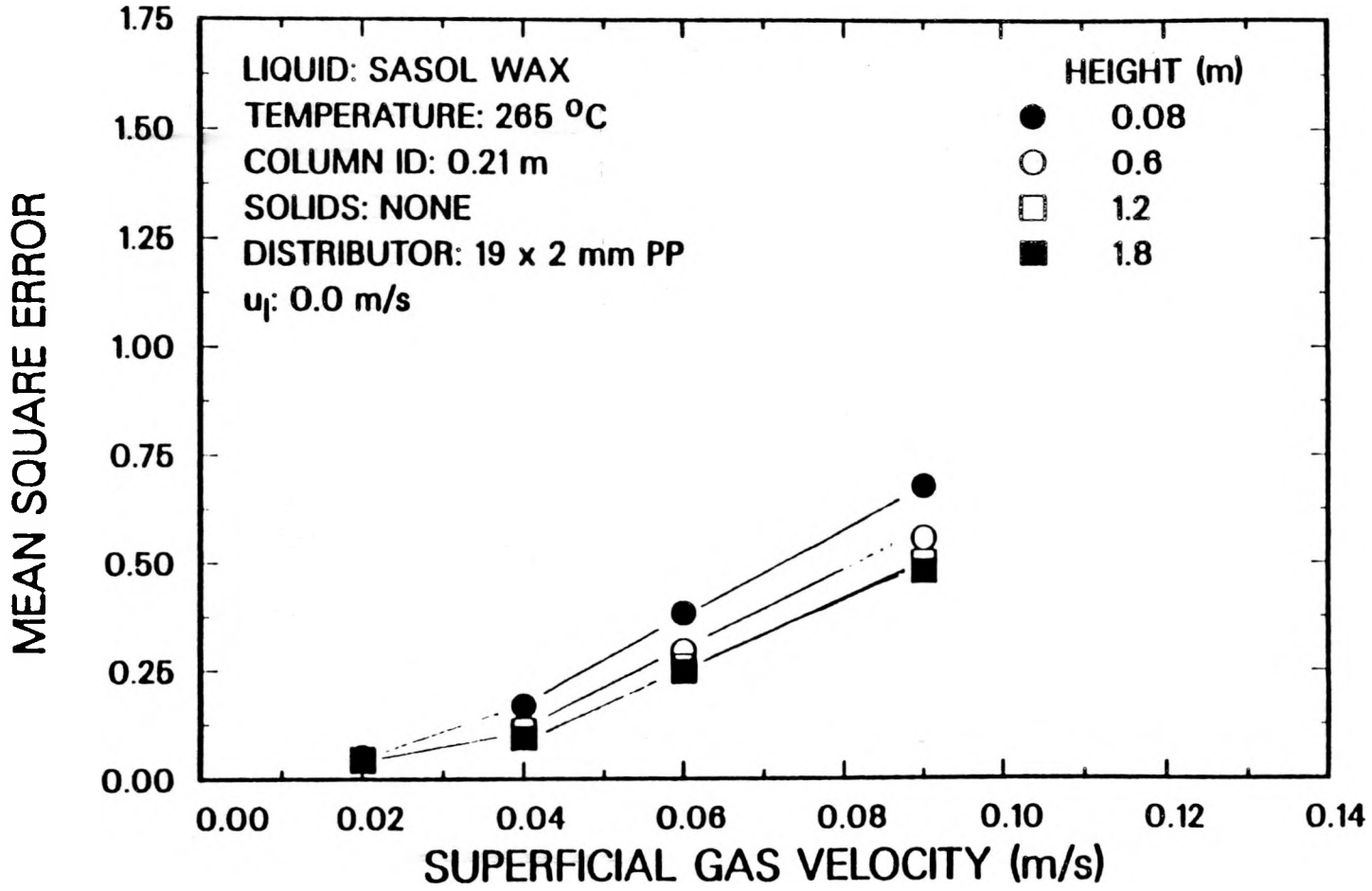

Figure 6.12. Effect of superficial gas velocity on the mean square error of pressure fluctuations at the wall (SASOL wax, 265 °C, 0.21 m ID column, u_l = 0.0 m/s).

where P corresponds to the pressure or nuclear density gauge signal and Δt corresponds to the time difference between two successive measurements. For example, if data was acquired at a rate of 100 Hz, then Δt would correspond to 0.01 sec. The psd was obtained from the new time series, P'_t. The psd of data from experiments with small silica particles and large iron particles in the small diameter column were obtained. The results from these calculations were used to determine flow regime transitions and slug frequencies. Likewise, the psd of data from experiments in the large diameter column in the absence of solids were obtained. These results were used to determine the transition from the bubbly to churn–turbulent flow regime.

Figure 6.13 show spectra of pressure signals obtained at a height of 1.8 m at different gas velocities in the 0.05 m ID column at a superficial slurry velocity of 0.02 m/s. The psd are fairly broad at a gas velocity of 0.02 and 0.04 m/s, with frequencies ranging from 2.5 to 10 Hz. For $u_g \geq 0.06$ m/s, the dominant frequency is in the range 2.5 to 5 Hz. The shift in frequency is indicative of the onset of slug flow between gas velocities of 0.04 and 0.06 m/s. Also, the intensity of the psd increases with increasing gas velocity; a similar trend was observed with the MSE (i.e. MSE increased with increasing gas velocity).

The spectra from transducers at heights of 0.6, 1.2, and 1.8 m above the distributor at a gas velocity of 0.12 m/s for the batch experiment conducted with 20 wt% 20 – 44 μm iron oxide particles in the 0.05 m ID column are shown in Figure 6.14. The dominant frequency observed at a height of 0.6 m above the distributor is 5 Hz; whereas, the dominant frequency at heights of 1.2 and 1.8 m is 2.5 Hz. This shift from 5 Hz to at the bottom of the column to 2.5 Hz at the top of the column is an indication of coalescence which may be taking place. Similar results were observed for the batch experiment with small silica (see Figure 6.15). For experiments conducted in the glass column we observed slug frequencies in the range 2 to 3 Hz at the top of the column

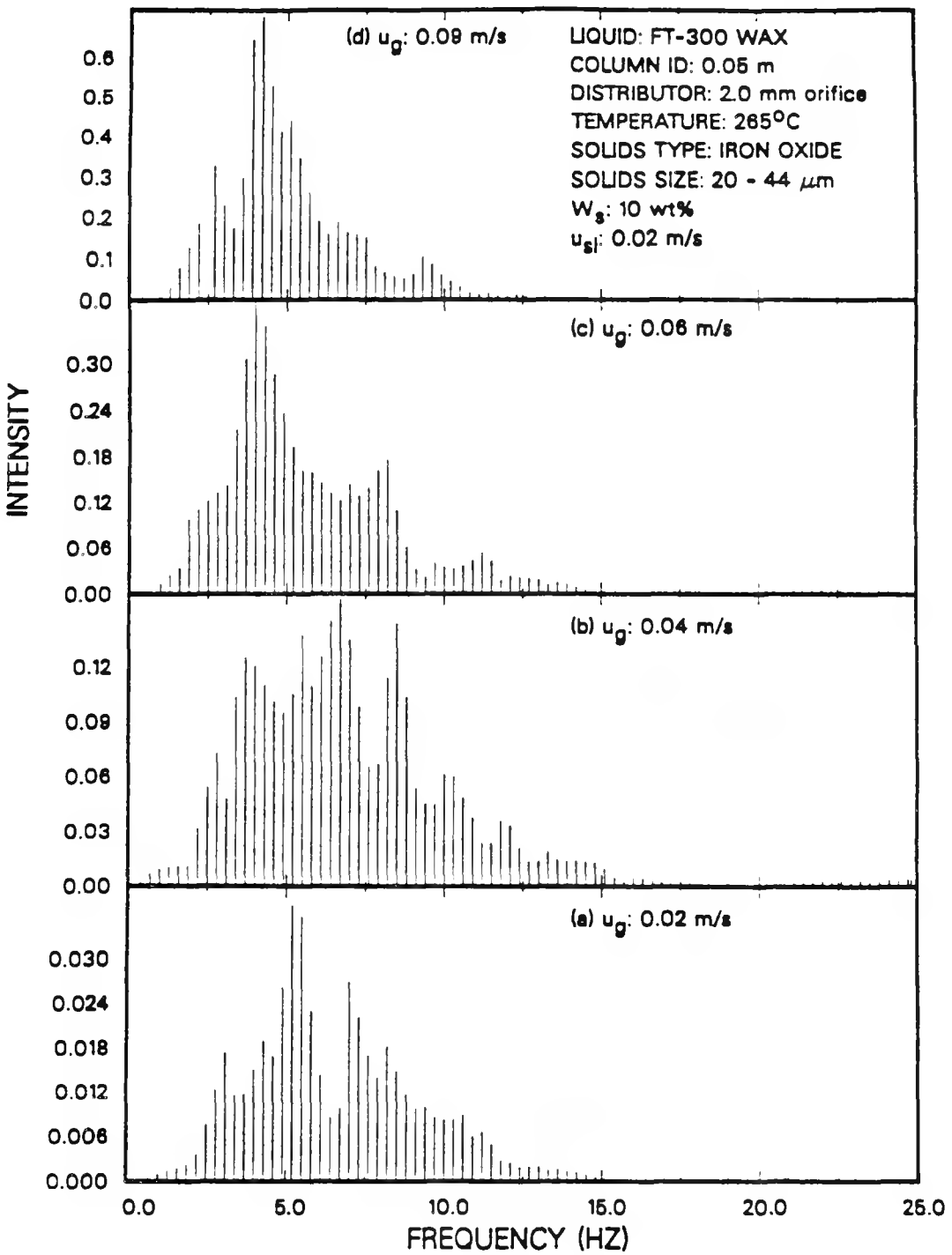

Figure 6.13. Effect of superficial gas velocity on the power spectral density function for pressure fluctuations at the wall (FT-300 wax, 265 °C, 0.05 m ID column, 10 wt% 20 - 44 μm iron oxide, u_{sl} = 0.02 m/s, height = 1.8 m).

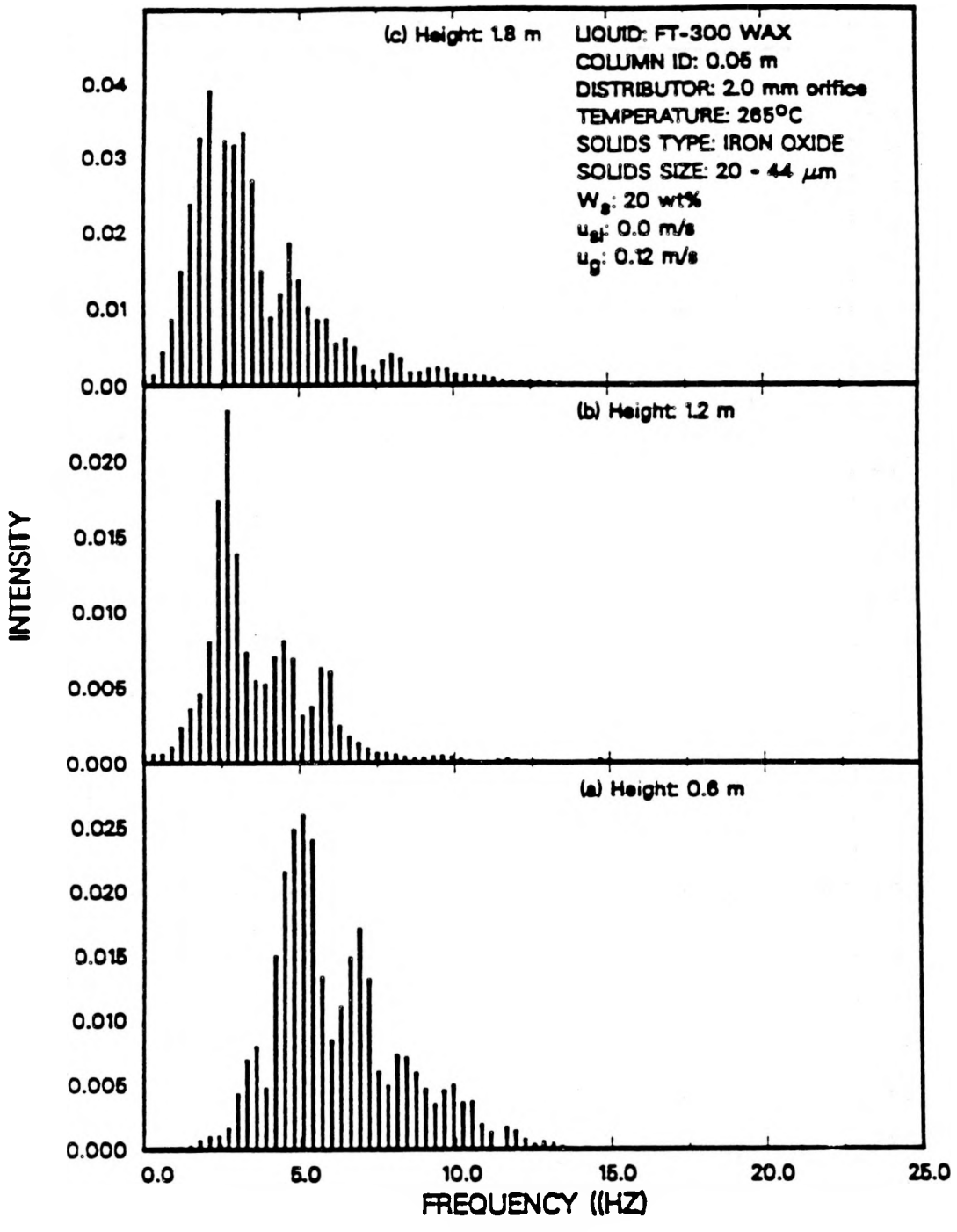

Figure 6.14. Effect of height above the distributor on the power spectral density function for pressure fluctuations at the wall (FT-300 wax, 265 °C, 0.05 m ID column, 20 wt% 20 - 44 μm iron oxide, u_{sl} = 0.0 m/s, u_g = 0.12 m/s).

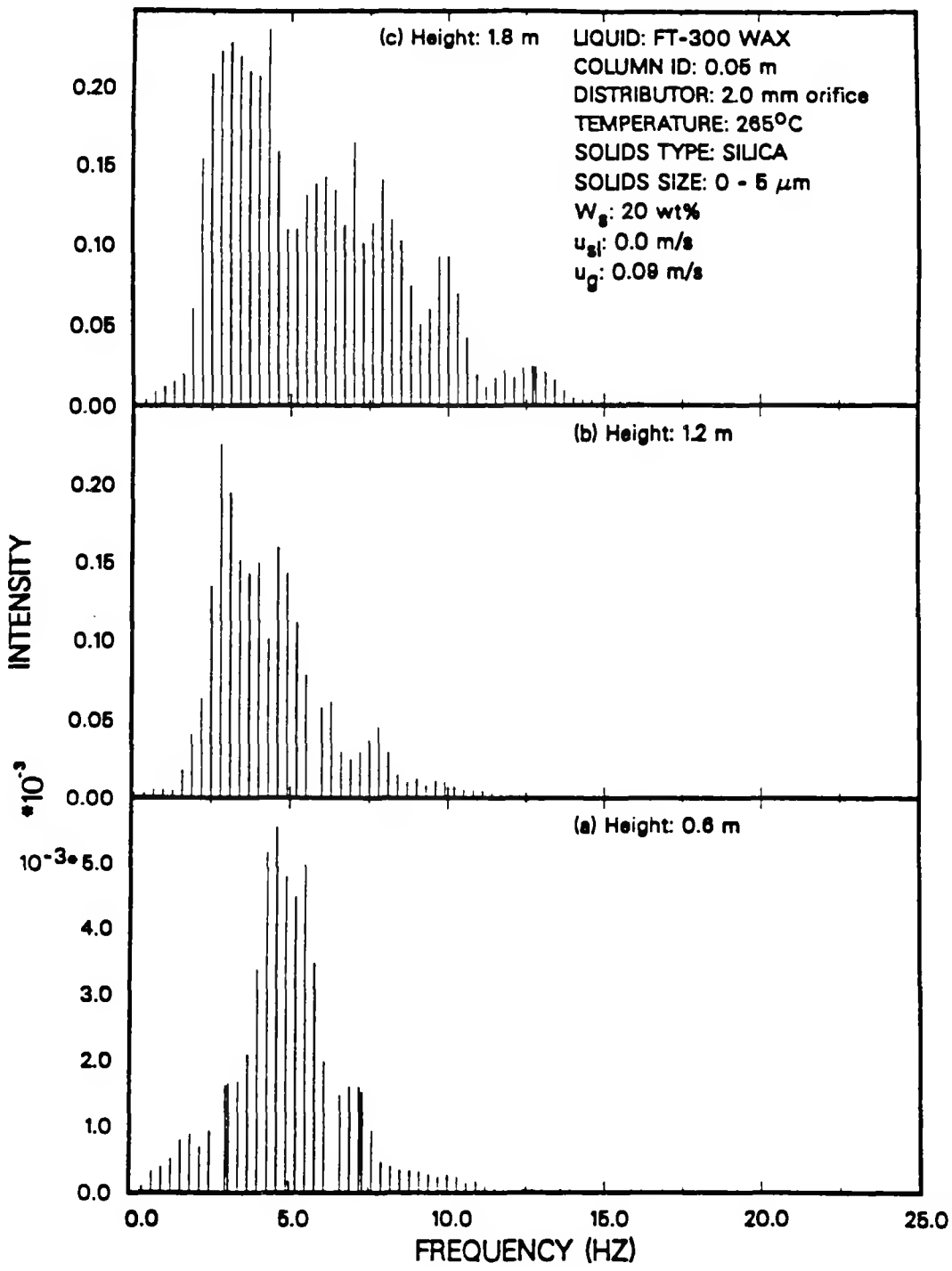

Figure 6.15. Effect of height above the distributor on the power spectral density function for pressure fluctuations at the wall (FT-300 wax, 265 °C, 0.05 m ID column, 20 wt% 0 - 5 μm silica, u_{sl} = 0.0 m/s, u_g = 0.09 m/s)

for gas velocities of 0.07, 0.09, and 0.12 m/s. At the bottom of the column, we have more frequent, smaller slugs, whereas, towards the top of the column, two small slugs coalesce to form a single large slug. This type of behavior has been observed visually in our two–phase experiments conducted in the glass column. This also agrees with the description proposed by Taitel et al. (1981) which was used in their correlation for determining the entry region over which churn flow exists.

Thus, for experiments conducted in the small stainless steel column in the batch mode of operation, the dominant slug frequency is approximately 2.5 Hz at the top of the column. Coalescence of small slugs to form large slugs occurs between a height of 0.6 m and 1.2 m above the distributor.

Figure 6.16 shows the effect of superficial gas velocity on the psd of the nuclear density gauge fluctuations from the batch experiment with FT–300 wax (without solids) in the small diameter column at gas velocities of 0.02, 0.04, 0.06, and 0.09 m/s. The four plots at the four different gas velocities indicate the progressive movement of the dominant frequency to the left (towards lower values) with an increase in gas velocity. These results show that the spectra are narrower at higher gas velocities (u_g=0.06 and 0.09 m/s) than they are at lower velocities. This behavior in the frequency spectrum is indicative of the change in flow regime in the bubble column. At low gas velocities, the homogeneous bubbly regime prevails and goes through a transition before approaching the slug flow regime at a gas velocity of 0.06 m/s. The dominant frequency at a gas velocity of 0.02 m/s is in the range 7.5 to 10 Hz, and shifts to the range 2.5 to 5 Hz at 0.04 m/s, and finally approaches 2.5 Hz as slug flow develops at 0.06 m/s. The definite shift in the dominant frequency observed between gas velocities of 0.04 and 0.06 m/s which was observed in all experiments indicates that slug flow begins somewhere between these two velocities. As mentioned previously, the same transition region was observed in experiments with the silica particles using MSE analysis (see Figure 6.9).

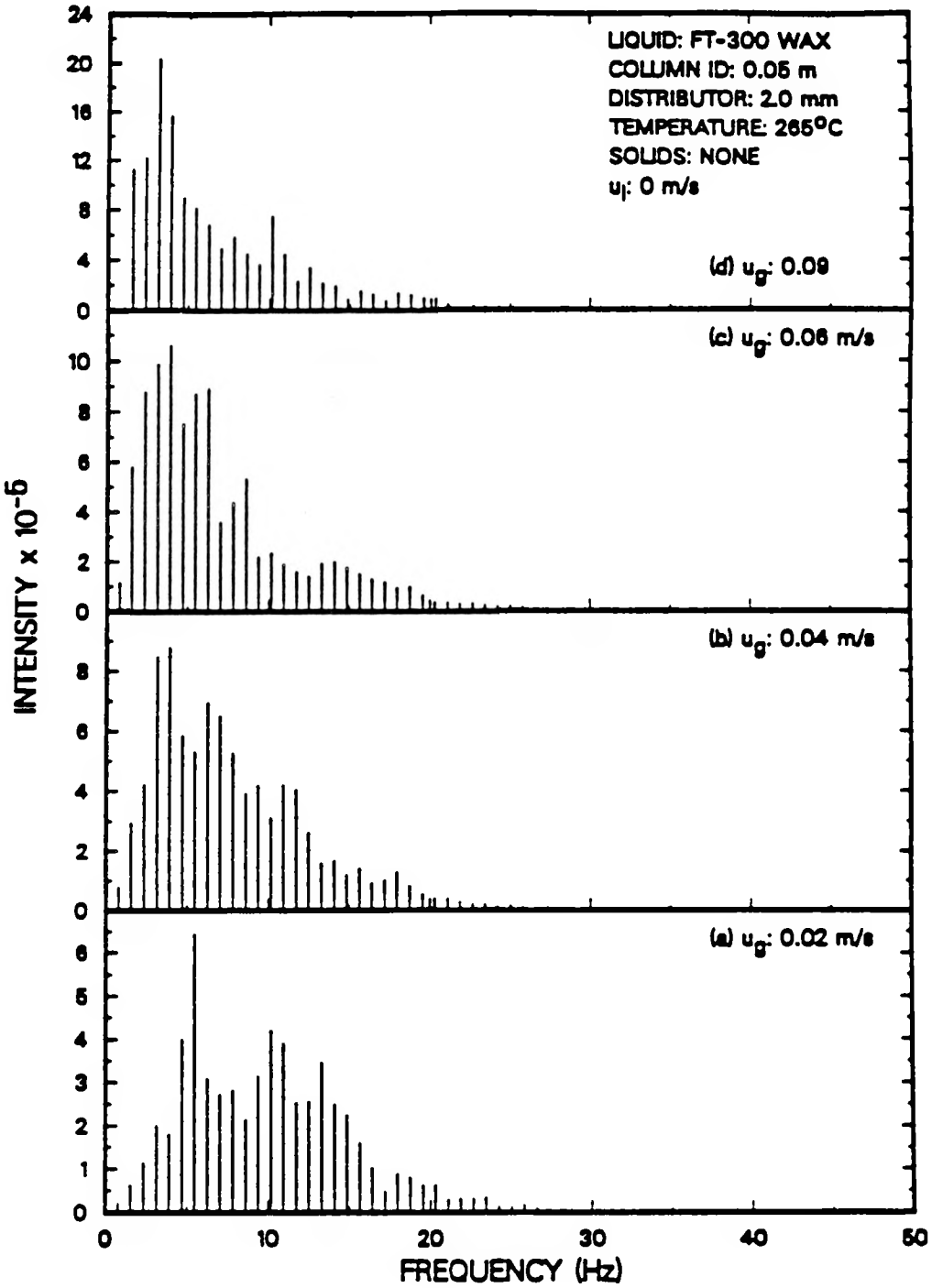

Figure 6.16. Effect of superficial gas velocity on the power spectral density function from the nuclear density gauge (FT-300 wax, 265 °C, 0.05 m ID column u_l = 0.0 m/s, Cesium-137, height = 1.5 m).

Hence, both MSE and psd analysis may be used to determine the transition from bubbly to slug flow. In addition, the psd may be used to determine slug frequency. Results obtained from statistical analysis results are in agreement with predictions from Taitel et al.'s correlations. Also, they are consistent with our visual observations in the small glass column.

The effect of superficial gas velocity on the power spectra for pressure signals obtained from the batch experiment with SASOL reactor wax (no solids) in the 0.21 m ID column at heights of 0.08 and 1.8 m above the distributor are shown in Figures 6.17 and 6.18, respectively. In the vicinity of the distributor, two characteristic psd peaks are observed (see Figure 6.17). The bimodal distribution may be indicative of the coalescence near the distributor. The intensity of the low frequency peak increases significantly with increasing gas velocity, which implies the formation of larger, less frequent bubbles in the vicinity of the distributor. At a height of 1.8 m above the distributor, a single peak in the psd is observed. The single peak is representative of a stable flow pattern (i.e. stable bubble size). As the gas flow rate is increased from 0.02 to 0.04 m/s, there is a definite shift in the frequency of the psd (12 Hz at 0.02 m/s to 8 - 10 Hz at 0.04 and 0.06 m/s). This shift in the dominant frequency between gas velocities of 0.02 and 0.04 m/s represents the transition from bubbly to the churn–turbulent flow regime.

Figures 6.19 and 6.20 show the effect of height above the distributor on the psd for the same experiment at gas velocities of 0.02 and 0.06 m/s, respectively. At both velocities, the bimodal distribution prevails at heights of 0.08 and 0.6 m. As mentioned above, the bimodal distribution is characteristic of the entry region over which bubble coalescence and breakup occurs. At heights of 1.2 and 1.8 m above the distributor, we no longer observe the bimodal distribution, thus indicating the presence of fully developed flow.

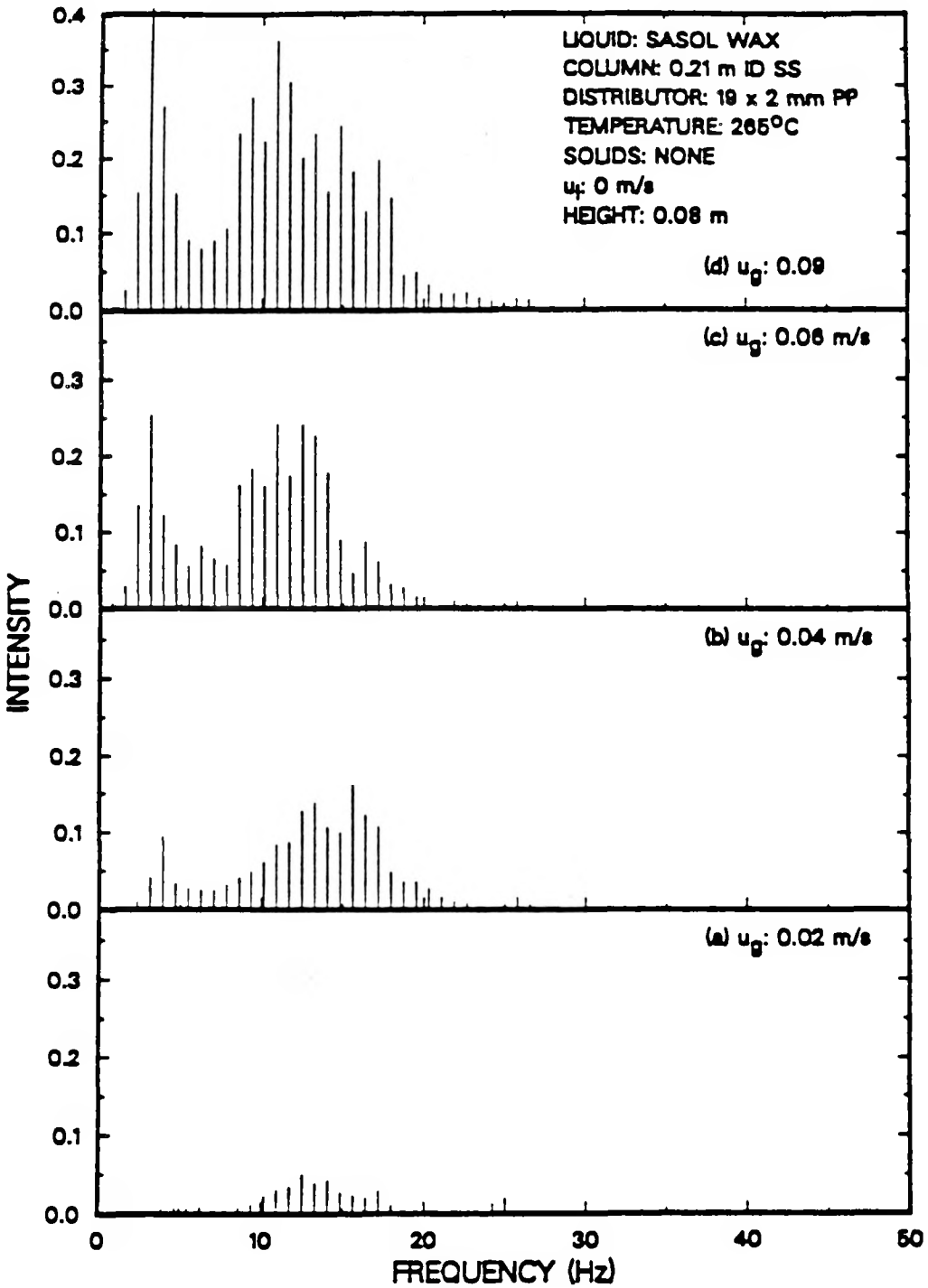

Figure 6.17. Effect of superficial gas velocity on the power spectral density function for pressure fluctuations at the wall (SASOL wax, 265 °C, 0.21 m ID column, u_l = 0.0 m/s, height = 0.08 m).

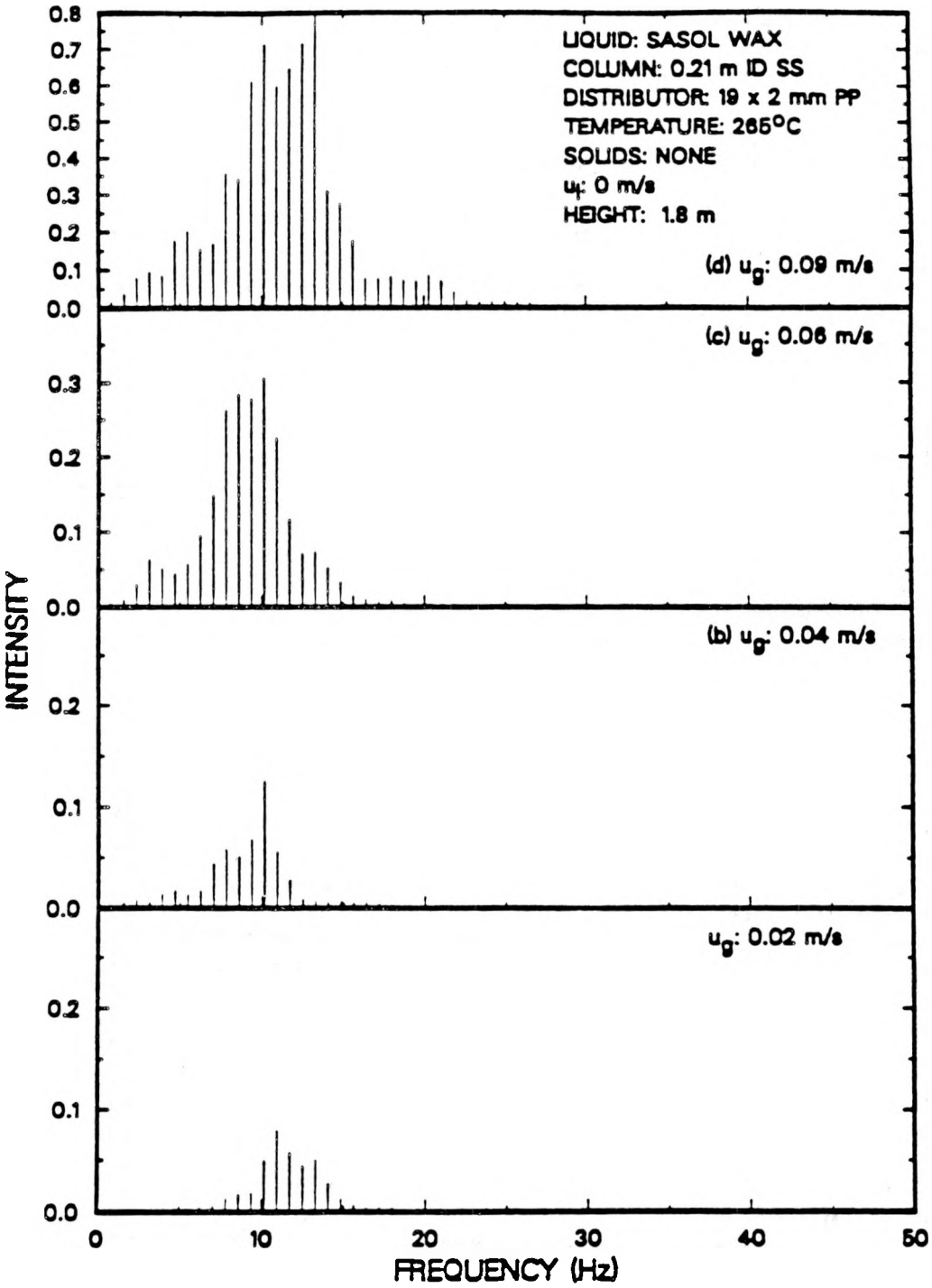

Figure 6.18. Effect of superficial gas velocity on the power spectral density function for pressure fluctuations at the wall (SASOL wax, 265 °C, 0.21 m ID column, u_l = 0.0 m/s, height = 1.8 m).

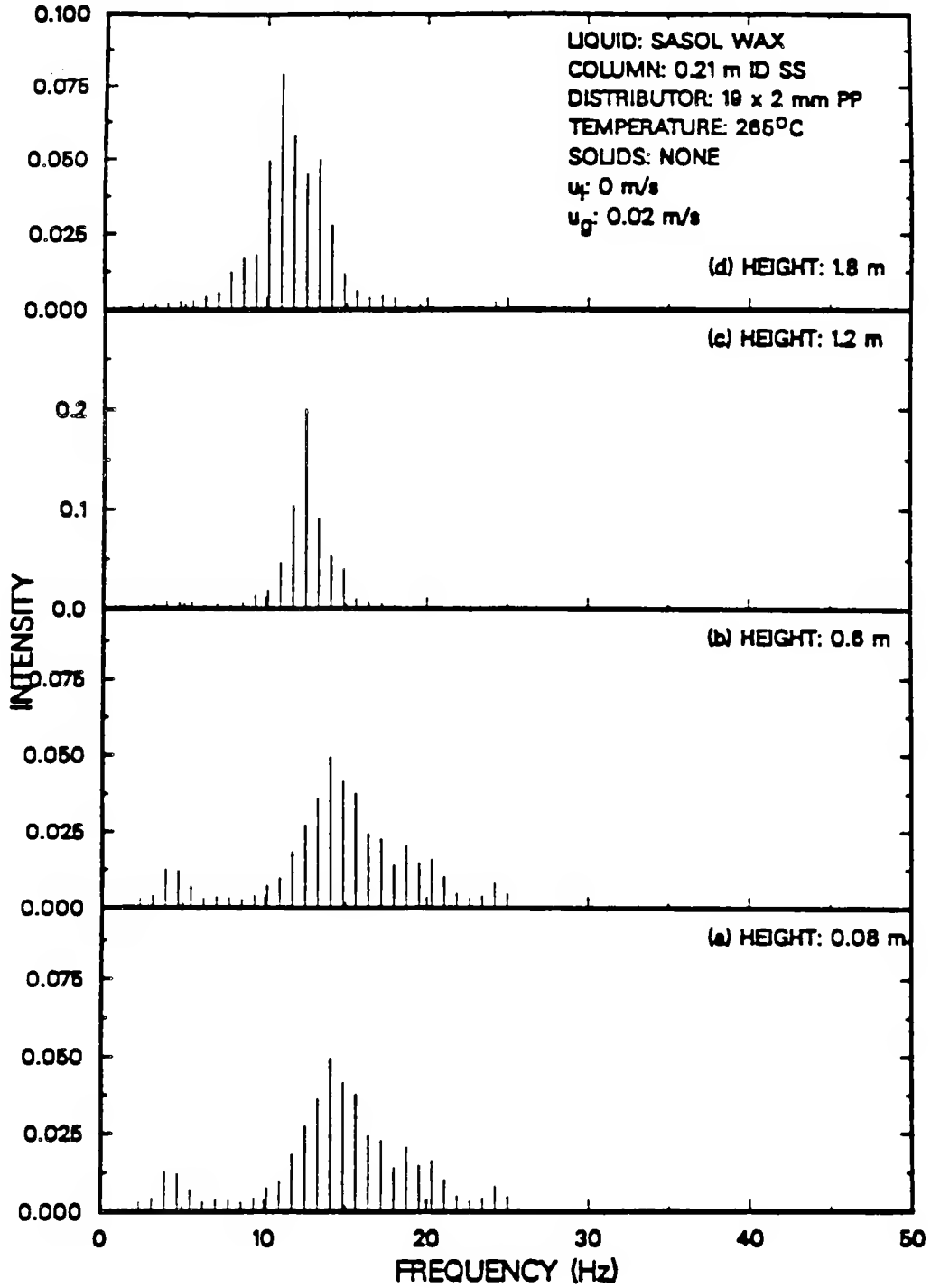

Figure 6.19. Effect of height above the distributor on the power spectral density function for pressure fluctuations at the wall (SASOL wax, 265 °C, 0.21 m ID column, u_l = 0.0 m/s, u_g = 0.02 m/s).

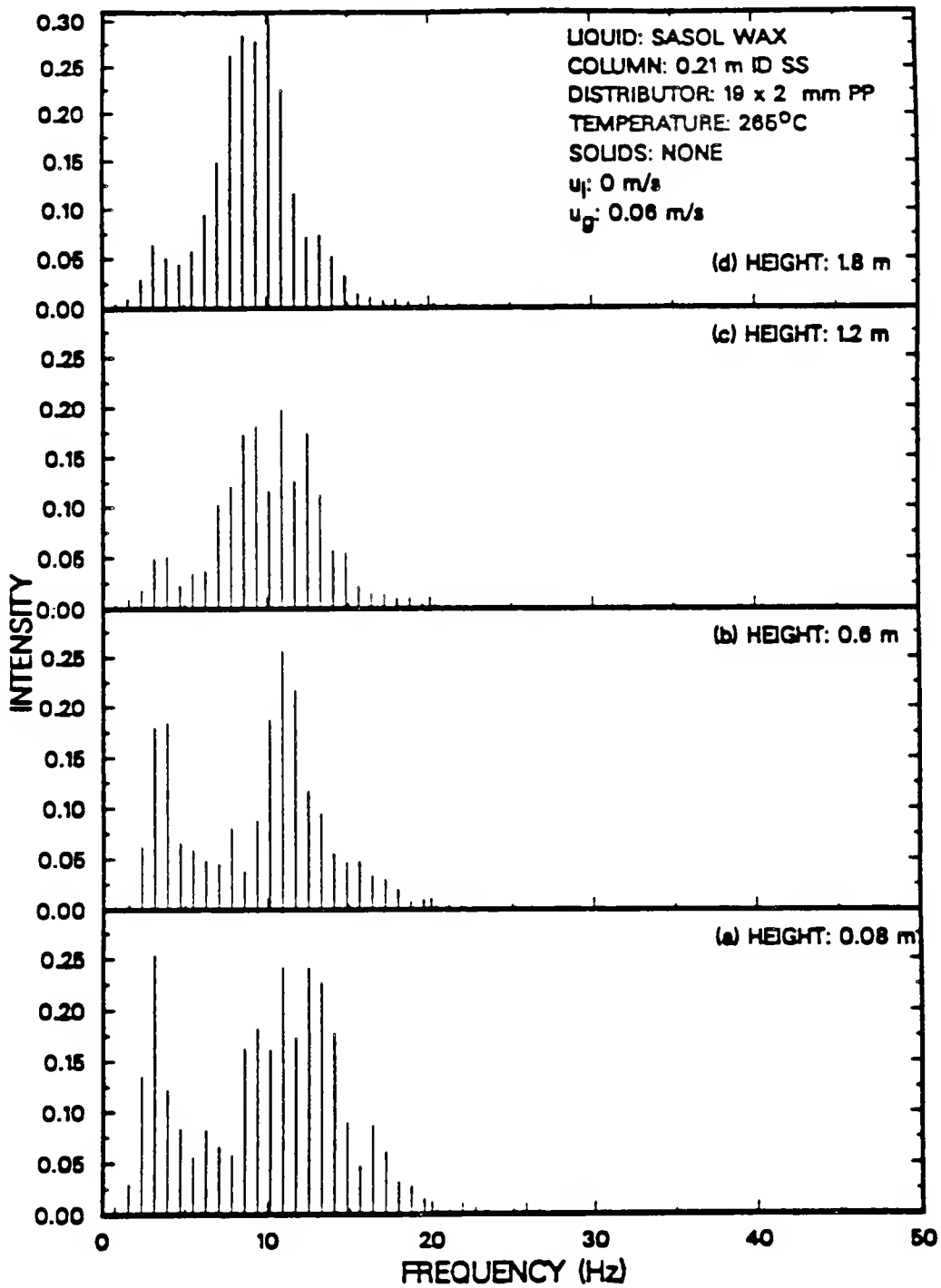

Figure 6.20. Effect of height above the distributor on the power spectral density function for pressure fluctuations at the wall (SASOL wax, 265 °C, 0.21 m ID column, u_l = 0.0 m/s, u_g = 0.06 m/s).

Figure 6.21 shows the effect of superficial gas velocity on the psd of nuclear density gauge fluctuations from the batch experiment with FT–300 wax in the 0.21 m ID column at a height of 1.5 m above the distributor. At a gas velocity of 0.02 m/s, the psd is fairly broad, which indicates the presence of the homogeneous bubbly regime. As the gas velocity is increased, the psd appears to become narrower and there is a shift in the dominant frequency towards the left (i.e. lower frequency). In the homogeneous bubbly regime, there is not a dominant frequency; however, in the churn–turbulent flow regime, large bubbles are produced which pass by the transducer at regular intervals (i.e. the dominant frequency). At a gas velocity of 0.02 m/s the frequency primarily ranges from 6 to 12 Hz; whereas, at gas velocities of 0.04 and 0.08 m/s, the dominant frequency is approximately 6 Hz. This shift in the frequency of the psd represents a transition from the bubbly flow regime to the churn–turbulent flow regime. The transition to the churn–turbulent flow regime in the neighborhood of 0.04 m/s is in agreement with our results obtained using the MSE approach. Also, the transition velocity is within the range of velocities presented by Deckwer et al. (1980).

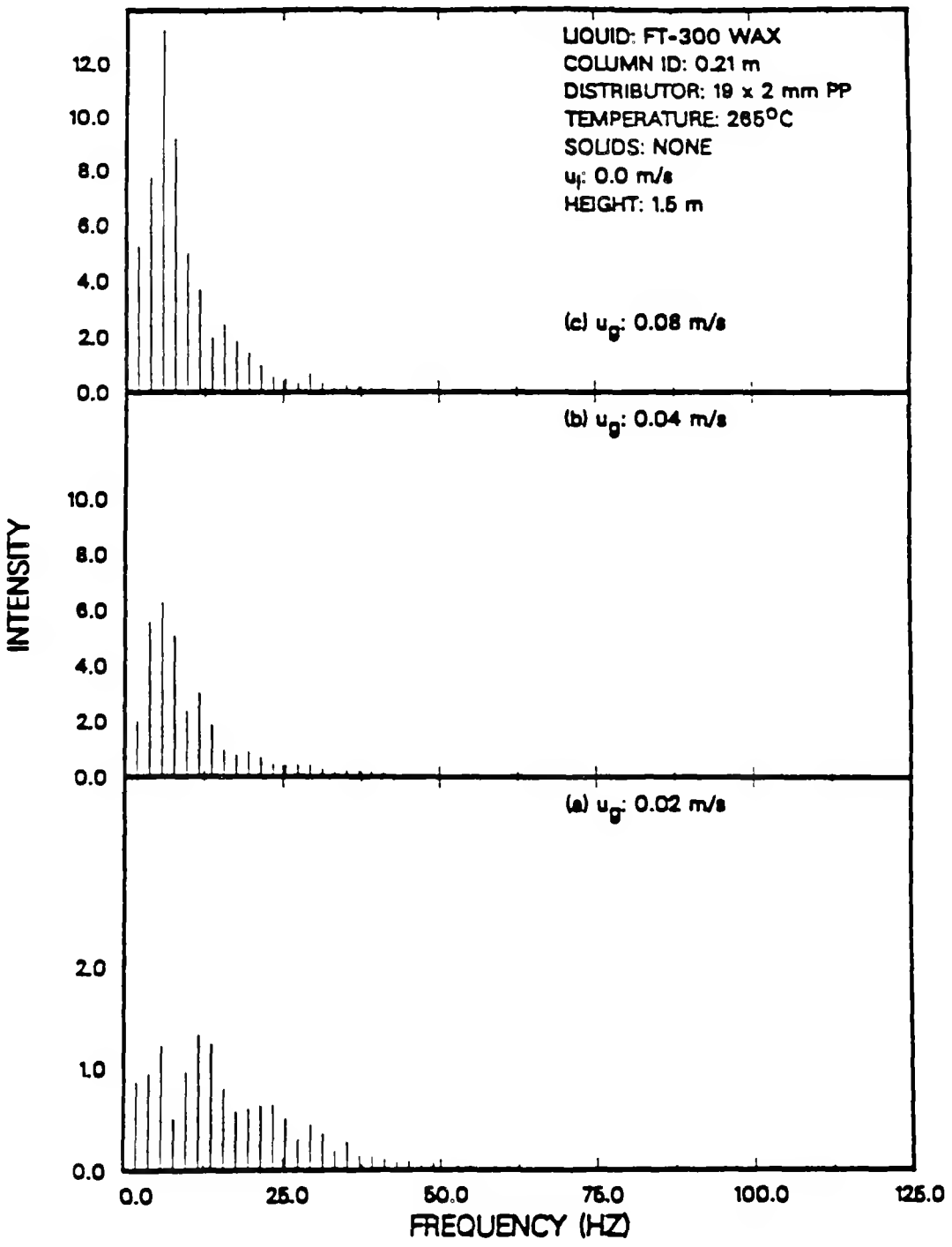

Figure 6.21. Effect of height above the distributor on the power spectral density function for nuclear density gauge fluctuations (FT-300 wax, 265 °C, 0.21 m ID column, Cobalt-60, height=1.5 m).

VII. NOMENCLATURE

a_s = specific gas–liquid interfacial area, m^2 / m^3

A_i = atomic mass of species i, Chapter III, kg/kmole

Ar = Archimedes number

A_L = cross sectional area of the column occupied by large bubbles, m^2

A_s = cross sectional area of the column occupied by small bubbles, m^2

A_{s_i} = area of region i, defined by Eq. 3.39, m^2

A_x = cross sectional area of the column, m^2

A_x = cross sectional area of the absorbing media, Chapter III, m^2

a = slope of pressure transducer calibration curve, inches water/volts

b = intercept of pressure transducer calibration curve, inches water

Bo = Bond number

B = number of photons crossing a unit area per unit time

B_o = incident number of photons crossing a unit area per unit time

B_i = number of photons crossing a unit area per unit time for source i

B_{oi} = incident number of photons crossing a unit area per unit time for source i

C_s = solids concentration, kg/m^3

C_s^B = solids concentration at the bottom of the dispersion, kg/m^3

C_s^f = solids concentration in the feed, kg/m^3

d = distance through the column, m

d_{Bi} = size of bubble i, m

d_c = column diameter, m

d_{col} = column diameter, m

d_i = distance through the column at position i, m

d_p = particle diameter, m

d_s = Sauter mean bubble diameter, m

E_s = axial dispersion coefficient, m^2/s

$f_{d_{ij}}$ = volume fraction of the dispersion between pressure ports i and j

f_{o_i} = fraction of the incident beam passing through phase i

Fr_g = Froude number = $\frac{u_g}{\sqrt{g d_{col}}}$

f_s = fraction of the cross sectional area occupied by small bubbles

g = gravitational accelerational constant, 9.81 m/s^2

H_{DP} = height of the pressure transducer, m

$H_t(t)$ = height of liquid above the presure transducer at time t, m

$H_t(0)$ = height of liquid above the presure transducer at time t=0, m

h = height, m

h_s = static liquid height, m

h_{exp} = expanded height, m

I = intensity of radiation

I_o = initial intensity of radiation

l_e = entry length, cm

L = expanded height of the dispersion, m

MSE = mean square error, defined by Eq. 2.36

$m_{s\ell}$ = weight of solidified slurry sample, kg

m_1 = weight of structure + sample, kg

m_2 = weight of structure + sample immersed in acetone, kg

N = number of data points

n_i = number of bubbles of size i

psd = power spectral density function

P = pressure, inches water

P = Fourier transform of the autocorrelation function

$\overline{P}$ = average pressure

P_i = pressure

P_n = probability associated with a Poisson process, defined by Eq. 3.29

Pe_p = particle Peclet number = $\frac{u_g d_{col}}{E_s}$

r_c = column radius, m

r_{pos_i} = radial position measured from the center of the column, defined by Eq. 3.38, m

S_c = scale factor used in Eq. 3.34

$s_{d_{ij}}$ = specific gvavity of the dispersion between pressure ports i and j

s_ℓ = specific gvavity of the liquid

$s_{s\ell_{ij}}$ = specific gvavity of the slurry between pressure ports i and j

Re_g = Reynolds number = $\frac{u_g d_{col} \rho_\ell}{\mu_\ell}$

Re_p = particle Reynolds number = $\frac{u_T d_p \rho_\ell}{\mu_\ell}$

RMS = root mean square, defined by Eq. 6.2

t = time, s

u = lag

u_{bs} = rise velocity of small bubbles, m/s

u_{bL} = rise velocity of large bubbles, m/s

u_g = superficial gas velocity, m/s

u_ℓ = superficial liquid velocity, m/s

u_p = hindered settling velocity of particles, m/s

u_r = bubble rise velocity, Eq. 2.28, m/s

$u_{s\ell}$ = superficial slurry velocity, m/s

$u'_{s\ell}$ = = $\frac{u_{s\ell}}{(1-\epsilon_g)}$ in Eq. 4.3, m/s

u_T = terminal rise velocity of a single particle in an infinite medium, m/s

$V(t)$ = volume of liquid above the pressure transducer at time t, m^3

V_i = volume of component i, defined by Eq. 3.11, m^3

$V_L(t)$ = volume of large bubbles that rise above the pressure transucer at time t, m^3

$V_{liq}(t)$ = volume of liquid displaced during Period I of disengagement, m^3

V_o = volume of liquid above the pressure transducer at time t=0, m^3

$V_\ell(t)$ = volume of the liquid entering the dispersion at time t, m^3

$V_{s\ell}$ = volume of solidified slurry, defined by Eq. 2.4, m^3

$V_s(t)$ = volume of small bubbles that rise above the pressure transucer at time t, m^3

V_T = total volume of the slurry, m^3

V_{ij} = volume of the slurry in section ij, m^3

w_i = weighting factor, defined by Eq. 3.40

W_{acet} = weight of acetone displaced, defined by Eq. 2.3, kg

We = Weber number, defined by Eq. 2.28

x = dimensionless height above the distributor, Chapter IV, m

x_i = thickness of species i, Chapter III, m

Z_i = atomic number of species i, Chapter III

Greek Letters

Δh_{ij} = height between preessure ports i and j, inches

ΔI = change in intensity of radiation

ΔP_{ij} = pressure drop across ports i and j, inches water

Δt = time interval, sec

Δx = thickness of the absorbing media, m

ϵ_g = average gas holdup

ϵ_{goL} = volume fraction of large bubbles at steady state

ϵ_{gos} = volume fraction of small bubbles at steady state

$\epsilon_{g_{ax}}$ = axial gas holdup

$\epsilon_{g_{ij}}$ = gas holdup between pressure ports i and j

ϵ_{ℓ} = average liquid holdup

$\epsilon_{\ell_{ij}}$ = liquid holdup between pressure ports i and j

ϵ_{meas} = measured gas holdup

ϵ_{pred} = predicted gas holdup

ϵ_{r_i} = radial gas holdup at location i

ϵ_{s} = average solids holdup

$\epsilon_{s_{ij}}$ = solids holdup between pressure ports i and j

γ_{xx} = autocovariance function

κ_i = Compton scattering coefficient of component i, Chapter III, m^{-1}

μ = mean of the time series, Chapter IV

μ_{ℓ} = liquid viscosity, Chapter II, kg/m-s

$\mu_{s\ell}$ = slurry viscosity, Chapter II, kg/m-s

μ_i = attenuation coefficient of species i, Chapter III, m^{-1}

μ_{ij} = attenuation coefficient of species i associated with source j, Chapter III, m^{-1}

ω_s = weight fraction of solids

ρ_i = density of the component i, kg/m^3

ρ_{acet} = density of acetone, kg/m^3

ρ_d = density of the dispersion, kg/m^3

ρ_g = density of the gas, kg/m^3

ρ_p = particle density, kg/m^3

ρ_s = density of solids, kg/m^3

$\rho_{s\ell}$ = density of the solidified slurry, kg/m^3

ρ_w = density of solidified wax, kg/m^3

ρ_{water} = density of water, kg/m^3

ρ_{xx} = autocorrelation function

σ_ℓ = surface tension of the liquid, N/m

σ_i = Compton scattering coefficient of component i, Chapter III, m^{-1}

τ_i = Compton scattering coefficient of component i, Chapter III, m^{-1}

Φ_ℓ = volume fraction of liquid in the slurry

$\overline{\Phi_\ell}$ = average volume fraction of liquid in the slurry

Subscripts

1,2,... = component number

g = gas

ℓ = liquid

sℓ = slurry

s = solids

T = total

VIII. LITERATURE CITED

Abou–el–Hassan, M.E., "A Generalized Bubble Rise Velocity Correlation," *Chem. Eng. Commun.*, **22**, 243 (1983)

Abouelwafa, M.S.A., and E.J.M. Kendall, "The Measurement of Component Ratios in Multiphase Systems Using Gamma–Ray Attenuation," *J. Phys. E: Sci. Instrum.*, **13**, 341 (1980)

Akagawa, K., H. Hamaguchi, and T. Sakaguchi, "I. Studies on the Fluctuation of Pressure Drop in Two-Phase Slug Flow," *Bulletin of JSME*,**14**, 447 (1971a)

Akagawa, K., H. Hamaguchi, and T. Sakaguchi, "II. Studies on the Fluctuation of Pressure Drop in Two-Phase Slug Flow," *Bulletin of JSME*,**14**, 455 (1971b)

Akagawa, K., H. Hamaguchi, and T. Sakaguchi, "III. Studies on the Fluctuation of Pressure Drop in Two-Phase Slug Flow," *Bulletin of JSME*,**14**, 462 (1971c)

Akita, K., and F. Yoshida, "Bubble Size, Interfacial Area, and Liquid–Phase Mass Transfer Coefficient in Bubble Columns," *Ind. Eng. Chem. Proc. Des. Dev.*, **13**, 84 (1974)

Albal, R.S., Y.T. Shah, N.L. Carr, and A.T. Bell, "Mass Transfer Coefficients and Solubilities for Hydrogen and Carbon Monoxide under Fischer–Tropsch Conditions," *Chem. Eng. Sci.*, **39**,905 (1984)

Attix, F.H., *Radiation Dosimetry, Volume I: Fundamentals*, Academic Press, New York (1968)

Bach, H.F., and T. Pilhofer, "Variation of Gas Holdup in Bubble Columns with Physical Properties of Liquids and Operating Parameters of Columns," *Ger. Chem. Eng.*, **1**, 270 (1978)

Badjugar, M.N., A. Deimling, B.I. Morsi, and Y.T. Shah, "Solids Distribution in a Batch Bubble Column," *Chem. Eng. Commun.*, **48**, 127 (1986)

Bartholemew, R.N., and R.M. Casagrande, "Measuring Solids Concentrations in Fluidized Systems by Gamma–Ray Absorption," *Ind. Eng. Chem.*, **3**, 428 (1957)

Basov V.A., V.I. Markheuka, T. Kh. Melik-Akhnazarov, and D.I. Orochko, "Investigation of the Structure of a Non–Uniform Fluidized Bed," *Int. Chem. Eng.*, **9**, 263 (1969)

Baumgarten, P.K., and R.L. Pigford, "Density Fluctuations in Fluidized Beds," *AIChE J.*, **6**, 115 (1960)

Bernatowicz, H., D. Gansmiller, and S. Wolff, "Final Report for the Development of a Three Phase Fraction Meter for Use at the SRC–1 Facility in Wilsonville, Alabama," Final Report to the Department of Energy for Contract Number DE-AC22-82PC50031 (1987)

Bhatia, V.K., K.A. Evans, and N. Epstein, "Effect of Solids Wettability on Expansion of Gas–Liquid Fluidized Beds," *Ind. Eng. Chem. Proc. Des. Dev.*, **11**, 151 (1972)

Buchholz, R., and K. Schugerl, "Bubble Column Bioreactors," *Europ. J. Appl. Micro.*, **6**, 301 (1979)

Buchholz, R., J. Tsepetonides, J. Steinemann, and U. Onken, "Influence of Gas Distribution on Interfacial Area and Mass Transfer in Bubble Columns," *Ger. Chem. Eng.*, **6**, 105 (1983)

Bukur, D.B., D. Petrovic, and J.G. Daly, "Hydrodynamics of Fischer–Tropsch Synthesis in Slurry Bubble Column Reactors," *Proc. DOE Indirect Liquefaction Contractors' Mtg.*, Houston, TX, 479 (1985)

Bukur, D.B., and V.R. Kumar, "Effect of Catalyst Dispersion on Performance of Slurry Bubble Column Reactors," *Chem. Eng. Sci.*, **41**, 1435 (1986)

Bukur, D.B., J.G. Daly, S.A. Patel, M.L. Raphael, and G.B. Tatterson, "Hydrodynamics of Fischer–Tropsch Synthesis in Slurry Bubble Column Reactors," Final Report to the Department of Energy for Contract Number DE-AC22-84PC70027 (1987a)

Bukur, D.B., D. Petrovic, and J.G. Daly, "Flow Regime Transitions in a Bubble Column with a Paraffin Wax as the Liquid Medium," *Ind. Eng. Chem. Res.*, **26**, 1087 (1987b)

Bukur, D.B., S.A. Patel, and M.L. Raphael, "Hydrodynamic Studies in Fischer–Tropsch Derived Waxes in a Bubble Column," *Chem. Eng. Commun.*,**60**,63 (1987c)

Bukur, D.B., and J.G. Daly, "Gas Hold-up in Bubble Columns for Fischer–Tropsch Synthesis," *Chem. Eng. Sci.*, **42**, 2967 (1987)

Calderbank, P.H., and M.B. Moo-Young, "The Continuous Phase Heat and Mass Transfer Properties of Dispersions," *Chem. Eng. Sci*, **16**, 39 (1961)

Calderbank, P.H., F. Evans, R. Farley, G. Jepson, and A. Poll, "Rate Processes in the Catalyst-Slurry Fischer–Tropsch Reaction," *Catalysis in Practice - Instn. Chem. Engs.*, 66 (1963)

Chan, A.M.C., and S. Banerjee, "Design Aspects of Gamma Densitometers for Void Fraction Measurements in Small Scale Two–Phase Flows," *Nucl. Instr. Meth.*, **190**, 135 (1981)

Clift, R., J.R. Grace, and M.E. Weber, *Bubble Drops and Particles*, Academic Press, New York, 171, 236 (1978)

Cova, D.R., "Catalyst Suspension in Gas Agitated Tubular Reactors," *Ind. Eng. Chem. Proc. Des. Dev.*, **5**, 20 (1966)

Deckwer, W.D., Y. Louisi, A. Zaidi, and M. Ralek, "Hydrodynamic Properties of the

Fischer–Tropsch Slurry Process," *Ind. Eng. Chem. Proc. Des. Dev.*, **19**, 699 (1980)

Deimling, A., B.M. Karandikar, Y.T. Shah, and N.L. Carr, "Solubility and Mass Transfer of CO and H_2 in Fischer–Tropsch Liquids and Slurries," *Chem. Eng. J.*, **29**, 127 (1984)

de Vries, R.J., W.P.M. Van Swaaij, C. Mantovani, and A. Heijkoop, "Design Criteria and Performance of the Commercial Reactor for the Shell Chlorine Process," *Proc. 5th Europ. Symp. Chem. Reaction Eng.*, Amsterdam, B9,59 (1972)

El-Halwagi, M.M., and A. Gomezplata, "An Investigation of Solids Distribution Mixing, and Contacting Characteristics of Gas–Solid Fluidized Beds," *AIChE J.*, **13**, 503 (1967)

Evans R.D., *The Atomic Nucleus*, McGraw–Hill, New York (1955)

Fan, L.S., S. Satija, and K. Wisecarver, "Pressure Fluctuation Measurements and Flow Regime Transitions in Gas-Liquid-Solid Fluidized Beds," Paper 67E presented at AIChE Annual Meeting, San Francisco (1984).

Fan, L.S., *Gas–Liquid–Solid Fluidization Engineering*, Butterworth Publishers, Stoneham, MA (1989)

Fan, L.T., C.J. Lee, and R.C. Bailie, "Axial Solids Distribution in Gas–Solid Fluidized Beds," *AIChE J.*, **8**, 239 (1962)

Fan, L.T., T.C. Ho, S. Hiraoka, and W.P. Walawender, "Pressure Fluctuations in a Fluidized Bed," *AIChE J.*, **27**, 388 (1981)

Farley, R., and D.J. Ray, "Gamma Radiation Absorption Measurements of Density and Gas Holdup in a Three Phase Catalytic Reactor," *Brit. Chem. Eng.*, **9**, 830 (1964)

Gibson, E.J., J. Rennie, and B.A. Say, "The Use of Gamma Radiation in the Study of the Expansion of Gas–Liquid Systems," *Int. J. of Appl. Rad. Iso.*, **2**, 129 (1957)

Gidaspow D., C. Lin, and Y.C. Seo, "Fluidization in Two–Dimensional Beds with a Jet. 1. Experimental Porosity Distributions," *Ind. Eng. Chem. Fundam.*, **22**, 187 (1983)

Glasgow, L.A., L.E. Erickson, C.H. Lee, and S.A. Patel, "Wall Pressure Fluctuations and Bubble Size Distributions at Several Positions in an Airlift Fermentor," *Chem. Eng. Commun.*, **29**, 34 (1984)

Godbole, S.P., M.F. Honath, and Y.T. Shah, "Holdup Structure in Highly Viscous Newtonian and Non–Newtonian Solutions in Bubble Columns," *Chem. Eng. Commun.*, **16**, 119 (1982)

Godbole, S.P., A. Schumpe, Y.T. Shah, and N.L. Carr, "Hydrodynamics and Mass Transfer in Non–Newtonian Solutions in a Bubble Column," *AIChE J.*, **30**, 213 (1984)

Gray, D., M. Lytton, M. Neworth, and G. Tomlison, "The Impact of Developing Technology on Indirect Liquefaction," Final Report to the Department of Energy for Contract Number EF-77-C-01-2738 (1980)

Gupte, K.M., J. Smith, T.M. Leib, and J.C.W. Kuo, "Fischer–Tropsch Bubble Column Hydrodynamics", *Proc. of the Fourth DOE Contractors' Conference on Indirect Liquefaction*, Washington, PA (1984)

Hatate, Y., H. Nomura, T. Fujita, S. Tajiri, N. Hidaka, and A. Ikari, "Gas Holdup and Pressure Drop in Three–Phase Vertical Flows of Gas–Liquid–Fine Solid Particles System," *J. Chem. Eng. Jap.*, **19**, 56 (1986)

Heijnen J.J, and K. Van't Riet, "Mass Transfer, Mixing and Heat Transfer Phenomena in Low Viscosity Bubble Column Reactors," *Chem. Eng. J.*, **28**, B21 (1984)

Hughmark, G.A., "Holdup and Mass Transfer in Bubble Columns," *Ind. Eng. Chem. Pro. Des. Dev.*, **6**, 218 (1967)

Ishigai, S., M. Yamane, and K. Roko, "Measurement of Component Flows in a Vertical Two–Phase Flow by Making Use of the Pressure Fluctuation: Part I," *Bull. of JSME*, **8**, 375 (1965a)

Ishigai, S., M. Yamane, and K. Roko, "Measurement of Component Flows in a Vertical Two–Phase Flow by Making Use of the Pressure Fluctuation: Part II," *Bull. of JSME*, **8**, 383 (1965b)

Jasper, J, "The Surface Tension of Pure Liquid Compounds," *J. Phys. Chem. Ref. Data*, **1**, 841(1972)

Jenkins, G.M., and D.G. Watts, *Spectral Analysis and Its Applications*, Holden Day, San Francisco (1968)

Kara, S., B. Kelkar, Y.T. Shah, and N.L. Carr, "Hydrodynamics and Axial Mixing in a Three–Phase Bubble Column," *Ind. Eng. Chem. Proc. Des. Dev.*, **21**, 584 (1982)

Kato, Y., A. Nishiwaki, T. Fukuda, and S. Tanaka, "The Behavior of Suspended Solid Particles and Liquid in Bubble Columns," *J. Chem. Eng. Jap.*, **5**, 112 (1972)

Kelkar, B.G., S.P. Godbole, M.F. Honath, Y.T. Shah, N.L. Carr, and W.D. Deckwer, "Effect of Addition of Alcohols on Gas Holdup and Backmixing in Bubble Columns," *AIChE J.*, **29**, 361 (1983)

Kelkar, B.G., Y.T. Shah, and N.L. Carr, "Hydrodynamics and Axial Mixing in a Three–Phase Bubble Column," *Ind. Eng. Chem. Proc. Des. Dev.*, **23**, 308 (1984)

Kim, S.D., C.G.J. Baker, and M.A. Bergougnou, "Bubble Characteristics in Three–Phase Fluidized Beds," *Chem. Eng. Sci.*, **32**, 1299 (1977)

Kolbel, H., and M. Ralek, "The Fischer–Tropsch Synthesis in the Liquid Phase," *Catal. Rev. Sci. Eng.*, **21**, 225 (1980)

Krambeck, F.J., A.A. Avidan, C.K. Lee, and M.N. Lo, "Predicting Fluid Bed Reactor Efficiency Using Adsorbing Gas Tracers," Paper Presented at AIChE Annual Meeting, Chicago, (1985)

Kuo, J.C.W., "Two-Stage Process for Conversion of Synthesis Gas to High Quality Transportation Fuels," Final Report to the Department of Energy for Contract Number DE-AC22-83PC60019 (1985)

Lassahn G.D., "Two–Phase Flow Velocity Measurements Using Radiation Intensity Correlation," *ISA Trans.*, **15**, 297 (1975)

Ledakowicz, S., H. Nettelhoff, R. Kokuun, and W.D. Deckwer, "Kinetics of the Fischer–Tropsch Synthesis in Slurry Phase on Promoted Iron Catalyst," *Ind. Eng. Chem. Fundam.*, **23**, 510 (1984)

Lee, C.H., *Dynamics of Bubble Size Distribution and Wall Pressure Fluctuations in Airlift Fermentors,* Masters Thesis, Kansas State University, Manhattan (1983)

Lee, Y.H., Y.J. Kim, B.G. Kelkar, and C.B. Weinberger, "A Simple Digital Sensor for Dynamic Gas Holdup Measurements in Bubble Columns," *Ind. Eng. Chem. Fund.*, **24**, 105 (1985)

Lin, P.Y., and T.J. Hanratty, "Detection of Slug Flow from Pressure Measurements," *Int. J. of Mult. Flow*, **13**, 13 (1987)

Matsui, G., "Identification of Flow Regimes in Vertical Gas–Liquid Two–Phase Flow Using Differential Pressure Fluctuations," *Int. J. of Mult. Flow*, **10**, 711 (1984)

Matsui, G., "Automatic Identification of Flow Regimes in Vertical Two–Phase Flow Using Differential Pressure Fluctuations," *Nucl. Eng. Des.*, **95**, 221 (1986)

Miyazaki, K., K. Isogai, Y. Fujii-e, and T. Suita, "Measurement of Propagation Velocities of Pressure and Void By Cross Correlation Fluctuations in Nitrogen–Water Flow," *J. of Nucl. Sci. Tech.*, **10**, 323 (1973)

Murray P., and L.S. Fan, "Axial Solids Distribution in Slurry Bubble Columns," *Ind. Eng. Res.*, **28**, 1697 (1989)

O'Dowd, W., D.N. Smith, J.A. Ruether, and S.C. Saxena, "Gas and Solids Behavior in a Baffled and Unbaffled Slurry Bubble Column," *AIChE J.*, **33**, 1959 (1987)

Orcutt, J.C., and B. H. Carpenter, "Bubble Coalescence and Simulation of Mass Transport and Chemical Reaction in Gas Fluidized Beds," *Chem. Eng. Sci*, **26**, 1049 (1971)

Ouyang C.J.P., and G.B. Tatterson, "The Effect of Distributors on Two–Phase and Three–Phase Flows in Vertical Columns," *Chem. Eng. Commun.*, **49**, 197 (1987)

Parulekar, S.J., and Y.T. Shah, "Steady State Behavior of Gas–Liquid–Solid Fluidized Bed Reactors," *Chem. Eng. J.*, **20**, 21 (1980)

Patel, S.A.,*Investigation of Two–Phase Flow Structures in an Airlift Fermentor*, PhD Dissertation, Kansas State University, Manhattan (1985)

Patel, S.A., J.G. Daly, and D.B. Bukur, "Holdup and Interfacial Area Measurements Using Dynamic Gas Disengagement," *AIChE J*, **35**, 931 (1989)

Patel, S.A., J.G. Daly, and D.B. Bukur, "Bubble-Size Distributions in Fischer–Tropsch Derived Waxes in Bubble Columns," *AIChE J*, **36**, 93 (1990)

Perry, and Chilton, *Chemical Engineers Handbook*, McGraw–Hill, New York (1983)

Peter, S., and M. Weinert, "Uber die Loslichkeit von H_2, CO, CO_2, and Wasserdampf in flussigen Kohlenwasserstoffen," *Z. Physik. Chem.*, **5**, 114 (1955)

Petrick, M., and B.S. Swanson, "Radiation Attenuation Method of Measuring Density of a Two–Phase Fluid," *Rev. of Sci. Instr.*, **29**, 1079 (1958)

Quicker, G., and W.D. Deckwer, "A Further Note on Mass Transfer Limitations in the Fischer–Tropsch Slurry Process," *Chem. Eng. Sci.*, **36**, 1577 (1981)

Rabiger, N., "Die Auswirkung von Feststoffpartikein auf den Gasgehalt in einem von oben begasten Schlaufenreaktor," *Chem. Ing. Tech.*, **57**, 248 (1985)

Reilly, I.G., D.S. Scott, T. De Bruijn, A. Jain, and J. Piskorz, "A Correlation for Gas Holdup in Turbulent Coalescing Bubble Columns," *Can. J. Chem. Eng.*, **64**, 705 (1986)

Rodden, J.B., "Diffusion Coefficients for Several Dilute Solutes in n-Eicosane, n-Octacosane, and Fischer–Tropsch Wax," PhD Dissertation, Texas A&M University (1988)

Rodden, J.B., C. Erkey, and A. Akgerman, "Mutual Diffusion Coefficients for Several Dilute Solutes in n-Octacosane and the Solvent Density at 371–534 K," *J. Chem. Eng. Datai*, **33**, 450 (1988)

Sada, E., H. Kumazawa, C. Lee, and T. Iguchi, "Gas Holdup and Mass Transfer Characteristics in a Three–Phase Bubble Column," *Ind. Eng. Chem. Proc. Des. Dev.*, **25**, 472 (1986)

Sanders, E., S. Ledakowicz, and W.D. Deckwer, "Fischer–Tropsch Synthesis in Bubble Column Slurry Reactors of Fe/K Catalyst," *Can. J. Chem. Eng.*, **64**, 133 (1986)

Sauer, T., and D.C. Hempel, "Fluid Dynamics and Mass Transfer in a Bubble Column with Suspended Particles," *Chem. Eng. Tech.*, **10**, 180 (1987)

Saxena, S.C., D. Patel , D.N. Smith, and J.A. Ruether, "An Assessment of Experimental Techniques for the Measurement of Bubble Size in a Bubble Slurry Reactor as Applied to Indirect Coal Liquefaction," *Chem. Eng. Commun.*, **63**, 87 (1988)

Schumpe, A., and W.D. Deckwer, "Gas Holdups, Specific Interfacial Areas, and Mass Transfer Coefficients of Aerated Carboxymethyl Cellulose Solutions in a Bubble Column," *Ind. Eng. Chem. Proc. Des. Dev.*, **21**, 706 (1982)

Schumpe, A., and A. Grund, "The Gas Disengagement Technique for Studying Gas Holdup Structure in a Bubble Column," *Can. J. Chem. Eng.*, **64**, 891 (1986)

Seo, Y.C., and D. Gidaspow, "An X–Ray–Gamma–Ray Method of Measurement of Binary Solids Concentrations and Voids in Fluidized Beds," *Ind. Eng. Chem. Res.*, **26**, 1622 (1987)

Shah, Y.T., B.G. Kelkar, S.P. Godbole, and W.D. Deckwer, "Design Parameter Estimations for Bubble Column Reactors," *AIChE J*, **28**, 353 (1982)

Shah, Y.T., S. Joseph, D.N. Smith, and J.A. Ruether, "On the Behavior of the Gas Phase in a Bubble Column with Ethanol–Water Mixtures," *Ind. Eng. Chem. Proc. Des. Dev.*, **24**, 1140 (1985)

Smith, D.N., and J.A. Ruether, "Dispersed Solid Dynamics in a Slurry Bubble Column Reactor," *Chem. Eng. Sci.*, **40**, 741 (1985)

Smith, J., K.M. Gupte, T.M. Leib, and J.W.C. Kuo, "Hydrodynamics Studies of Fischer–Tropsch Bubble Column Systems," Paper Presented at the AIChE Summer National Meeting, Philadelphia, (1984)

Sriram, K., and R. Mann, "Dynamic Gas Disengagement: a New Technique for Assessing the Behavior of Bubble Columns," *Chem. Eng. Sci.*, **32**, 571 (1977)

Taitel, Y., D. Bornea, and A.E. Dukler, "Modeling Flow Pattern Transitions for Steady Upward Gas–Liquid Flow in Vertical Tubes," *AIChE J.*, **27**, 1043 (1981)

Thompson, G.J., M.L. Riekena, and A.G. Vickers, "Comparison of Fischer–Tropsch Reactor Systems," Final Report to the Department of Energy for Contract Number DE-AC01-78ET 10159 (1981)

Tsao, T.R., "Results of LaPorte Liquid Phase Methanol PDU Unit," Proc. of Fourth DOE Contractors' Conference on Indirect Liquefaction, Washington, PA (1984)

Vermeer, D.J., and R. Krishna, "Hydrodynamics and Mass Transfer in Bubble Columns Operating in the Churn–Turbulent Regime," *Ind. Eng. Chem. Proc. Des. Dev.*, **20**, 475 (1981)

Weimer, A.W., D.C. Gyure, and D.E. Cough, "Application of a Gamma Radiation Density Gauge for Determining Hydrodynamic Properties of Fluidized Beds," *Powder Tech.*, **44**, 179 (1985)

Ying D.H.S., R. Sivasobramanian, and E.N. Givens, "Gas/Slurry Flow in Coal Liquefaction Processes," Final Report to the Department of Energy for Contract Number Fe–14801–3 (1980)

Zaidi, A., Y. Louisi, M. Ralek, and W.D. Deckwer, "Mass Transfer in the Liquid Phase Fischer–Tropsch Synthesis," *Ger. Chem. Eng.*, **2**, 94 (1979)

Zheng, C., B. Yao, and Y. Feng, "Flow Regime Identification and Gas Holdup of Three–Phase Fluidized Systems," *Chem. Eng. Sci.*, **43**, 2195 (1988)

Zigrand, D.J., and N.D. Sylvester, "An Explicit Equation for Particle Settling Velocities in Solid–Liquid Systems," *AIChE J.*, **27**, 1043 (1980)

IX. ACKNOWLEDGEMENT

We are grateful to Mike Noak and Randy Marek for their help with design and construction of experimental apparatus, and to Manne Ramakrishna for his technical assistance with the preparation of the final report. SASOL reactor wax was supplied by Sasol Technology Ltd. of South Africa, through Dr. Ben Jager.

☆U.S. GOVERNMENT PRINTING OFFICE: 1991 - 548 - 138/40037